2018

Spray and Combustion Studies of High Reactivity Gasoline in Comparison to Diesel under Advanced Compression Ignition Engine Conditions

Meng Tang
Michigan Technological University, mengt@mtu.edu

SPRAY AND COMBUSTION STUDIES OF HIGH REACTIVITY GASOLINE IN COMPARISON TO DIESEL UNDER ADVANCED COMPRESSION IGNITION ENGINE CONDITIONS

By

Meng Tang

A DISSERTATION

Submitted in partial fulfillment of the requirements for the degree of

DOCTOR OF PHILOSOPHY

In Mechanical Engineering – Engineering Mechanics

MICHIGAN TECHNOLOGICAL UNIVERSITY

2018

This dissertation has been approved in partial fulfillment of the requirements for the Degree of DOCTOR OF PHILOSOPHY in Mechanical Engineering – Engineering Mechanics.

Department of Mechanical Engineering – Engineering Mechanics

Dissertation Co-Advisor:	*Dr. Jeffrey D. Naber*
Dissertation Co-Advisor:	*Dr. Seong-Young Lee*
Committee Member:	*Dr. David R. Shonnard*
Committee Member:	*Dr. Jaclyn E. Johnson*
Department Chair:	*Dr. William W. Predebon*

Table of Contents

List of figures

List of tables

Author contribution statement

This dissertation contains several publications developed in collaboration with colleagues, listed as follows:

- Chapter 4.1 was published as a conference paper at the 2017 ILASS Americas conference. I was the first author and led the experimental work, performed data analyses, and wrote the manuscript. My coauthors Jiongxun Zhang and Tyler Menucci supported the experimental work. Henry Schmidt led the development of the experimental hardware. Dr. Jeffrey Naber, Dr. Seong-Young Lee, and Tom Tzanetakis proofread the manuscript.
- Chapter 4.2 was published as a conference paper at the 2017 ILASS Americas conference. I was the second author and led the experimental work. Jiongxun Zhang was the first author, he supported the experimental work, led the data analyses and wrote the manuscript. Tyler Menucci supported the experimental work. Henry Schmidt led the development of the experimental hardware. Dr. Jeffrey Naber, Dr. Seong-Young Lee, and Tom Tzanetakis proofread the manuscript.
- Chapter 4.3 was extended based on a published conference paper at the 10th U.S. National Combustion Meeting. I was the first author and led the experimental work, performed data analyses, and wrote the manuscript. My coauthors Jiongxun Zhang and Tyler Menucci supported the experimental work. Henry Schmidt led the development of the experimental hardware. Dr. Jeffrey Naber, Dr. Seong-Young Lee, and Tom Tzanetakis proofread the manuscript.
- Chapter 5 was published as an SAE Technical Paper 2018-01-0304. I was the first author and led the experimental work, performed data analyses, developed the correlation, ran CFD simulations, and wrote the manuscript. Yuanjiang Pei supported in running CFD simulations and planning the scope of work, Shaoping Quan integrated the correlation into the CFD software Converge, Yu Zhang, Tom Tzanetakis, Michael Traver, David Cleary, Dr. Jeffrey Naber, and Dr. Seong-Young Lee proofread the manuscript and provided comments.
- Chapter 6 has been accepted (ASME ICEF 2018-9696) at the ASME 2018 Internal Combustion Engine Fall Technical Meeting. I was the first author and led the experimental work, performed data analyses, ran part of the CFD simulations, and wrote the paper. Yuanjiang Pei ran the other part of the CFD simulations, and provided suggestions on the scope of work. Yu Zhang, Michael Traver, David Cleary, Zhaoyu Luo, Dr. Jeffrey Naber, and Dr. Seong-Young Lee proofread the manuscript and provided comments.

Acknowledgements

The work contained in this dissertation and during my doctoral candidacy was made possible through many funded projects. Acknowledgement is provided to Saudi Aramco and King Abdullah University of Science and Technology for funding the work in this dissertation through the FUELCOMM II program. Funding for other projects were made possible through the National Science Foundation Sustainable Energy Pathways Program (#1230803), John Deere, and Fiat Chrysler Automobiles. The Graduate School at Michigan Technological University is acknowledged for providing the funds through the Doctoral Finishing Fellowship.

I would like to send my deepest respect and gratitude to Dr. Jeffrey Naber, who has been my advisor since the spring semester of 2012. The journey of researches started with a Master's project focusing on a diesel injector nozzle design improvements using CFD simulations. I gained the privilege to work on experimental projects in the Combustion Vessel Laboratory since the summer semester of 2013. Throughout the years, I greatly benefitted from the technical discussions, which prepared my mindset towards being a researcher. His expertise and guidance on problem solving provided great support during the difficult times in the experiments. His breadth of knowledge and experience, dedication, and work ethic has inspired me both personally and professionally to become a better researcher and collaborator.

I would like to express my sincere appreciation and gratitude to Dr. Seong-Young Lee, who has been my co-advisor since the fall semester of 2014. As early as 2013, Dr. Lee assisted my Master's project by providing me with access to the Converge CFD software and the workstation to run simulations. His level of dedication to work has been inspirational and greatly motivated myself to overcome the challenges in the research. His encouragement in scientific publishing and participation in professional conferences established my confidence in the academic world.

I am very grateful for having the privilege to have Dr. David Shonnard to serve on my doctoral advisory committee since the summer semester of 2015. Dr. Shonnard led the NSF-SEP program, through which I had the first opportunity to lead the planning and execution of an experimental project. This has given me much confidence and invaluable experience for all the subsequent projects in my doctoral career.

I owe many thanks to Dr. Jaclyn Johnson, who has served on my doctoral advisory committee since the summer semester of 2015. As early as 2012, Dr. Johnson provided me with the experimental data for calibrating the CFD model. She has offered a great deal of help and assistance with respect to the lab operation, data processing, and project coordination. She has always been very productive and responsive, which greatly motivated myself to improve my project management skills.

I would like to give special thanks to Aramco Research Center – Detroit for having me as an intern. My supervisor Michael Traver provided very useful career suggestions. Tom

Tzanetakis offered valuable assistance in recruiting and coordinating the bi-weekly project meetings. Yuanjiang Pei offered great help on the numerical studies with his expertise on CFD simulations. Discussions with Yu Zhang greatly improved my understanding on the technological development of engines.

I am very fortunate to have some of the best colleagues to support my journey on the doctoral study. Advanced Energy Research Building (AERB) staff Henry Schmidt and William Atkinson were very helpful in managing the projects. I gained invaluable experience on the lab operation and the basics of the different diagnostics from the collaborations with Anqi Zhang, Khanh Cung, and Meghraj Bhagat. My colleagues Abdul Moiz, Kyle Yeakle, Jiongxun Zhang, Tyler Menucci, Xiucheng Zhu, Le Zhao, Zhihao Zhao, Niranjan Miganakallu, and Mary Pourhasanzadeh provided great assistance for all the work and strong support during those difficult times. Those good old times spent with friends will never be forgotten, and I would like to give my appreciation to Yanyu Wang, Wei Chen, Hao Wu, Yun Wang, Xin Wang, Zhuyong Yang, Luting Wang, Chong Cao, Xin Diao, Xuebin Yang, and many others.

Last but not least, special thanks and credits belong to my parents, Yuxin Tang, and Yuling Cui, for their long time unconditional love, and financial support, without which a doctoral degree would not be possible. Moreover, I cannot show enough gratitude and appreciation to the journey that brought Peipei Lin to be my wife. Her love, understanding, and support empowered myself through the challenging yet meaningful life of a doctoral candidate.

List of abbreviations

AMR	Adaptive mesh refinement
aTDC	after top dead center
BMEP	Brake mean effective pressure
CAFÉ	Corporate average fuel economy
CARB	California Air Resource Board
CCD	Charge-coupled device
CCD	Charge-coupled device
CFD	Computational fluid dynamics
CI	Compression ignition
ECN	Engine Combustion Network
EGR	Exhaust gas recirculation
EGR	Exhaust gas recirculation
EOI	End of injection
EPA	Environmental Protection Agency
EV	Electric vehicles
EVC	Exhaust valve close
FBP	Final boiling point
FIR	Finite impulse response
fps	Frames per second
GCI	Gasoline compression ignition
GDI	Gasoline direct injection
GHG	Greenhouse gas
HCCI	Homogeneous charge compression ignition
HFRR	High-frequency reciprocating rig
IBP	Initial boiling point
IMEP	Indicated mean effective pressure
IMEP	Indicated mean effective pressure
IVO	Intake valve open
IXT	Intensity-aXial-Time
KH-RT	Kelvin Helmholtz – Rayleigh Taylor
LED	Light emitting diode
LES	Large eddy simulation
LOL	Lift-off length
LTC	Low temperature combustion
MON	Motor octane number
MOSFET	Metal-oxide-semiconductor field-effect transistor
mpg	miles per gallon

MPRR	Maximum pressure rise rate
MULDIC	MULtiple stage Diesel Combustion
NATO	North Atlantic Treaty Organization
NHTSA	National Highway Traffic and Safety Adminsitration
NRMSD	Normalized root mean square difference
NRMSD	Normalized root mean square difference
NTC	No time encounter
NVO	Negative valve overlap
PAH	Polycyclic-aromatic hydrocarbon
PCCI	Premixed charge compression ignition
PM	Particulate mimic
PPCI	Partially-premixed compression ignition
PRF	Primary reference fuel
RANS	Reynolds-averaged Navier-Stokes
RCCI	Reactivity-controlled compression ignition
RON	Research octane number
rpm	Revolutions per minute
SI	Spark ignition
SINL	Spatially-integrated natural luminoisty
SLOL	Soot lift-off length
SNL	Sandia National Laboratories
SOI	Start of injection
TDC	Top dead center
TISINL	Time-integrated, spatially-integrated natural luminosity
UHC	Unburned hydrocarbon
ULSD	Ultra-low sulfur diesel
ULSD	Ultra-low sulfur diesel
VVT	Variable vale timing
WSC	Wear scar diameters
Z – T	Mixture fraction – temperature

Abstract

Gasoline compression ignition (GCI) technology has demonstrated great potentials in improving fuel economy and reducing engine-out NO_x and particulate matter emissions. Development and application of the GCI technology on multi-cylinder engines require both fundamental understandings of the gasoline spray combustion characteristics and accurate numerical tools. Due to the large differences in the thermo-physical and the chemical properties between gasoline and diesel range fuels, differences in the spray combustion characteristics between gasoline and diesel is expected. Reports on the gasoline spray combustion characteristics under conditions relevant to medium to heavy-duty engines are scarce and this dissertation aims to fill in this knowledge gap.

Experimental work were performed in a constant volume combustion vessel. Non-reacting sprays under low and high ambient charge gas temperatures and reacting sprays were performed using a high reactivity gasoline (research octane number 60) and ultra-low sulfur diesel. The experimental work were designed to isolate the effect of several important fuel properties on spray and combustion. The experimentally investigated spray combustion characteristics include spray dispersion, vapor penetration, liquid penetration, ignition, flame lift-off, and natural luminosity. These experiments provided evidence behind the lower particulate matter emissions benefit of gasoline.

A transient spray cone angle correlation was developed based on the experimental measurements. The correlation was developed to improve the description of fuel-air mixing in computational fluid dynamic (CFD) simulations. The correlation was integrated with CFD simulations and the benefits of using a transient spray cone angle profile were demonstrated.

Reacting spray CFD simulations were performed and validated extensively against the experimental spray characteristics on ignition, flame lift-off, soot natural luminosity, and external published local soot concentration measurements. The CFD simulations provided additional understanding of the soot emission processes to complement experimental measurements.

1 Introduction

1.1 Background and Motivation

The internal combustion engine is dominating the propulsion technology in vehicles. Currently, petroleum oils account for 94-95% of the total global transport fuels demand (BP 2018, ExxonMobil 2016), and 89% in the United States domestic market (USEIA 2016). Growth in the population and the economy is projected to lead to growing demands of transportation. In a U.S. Energy Information Administration projection through 2050, the miles traveled by light duty vehicles are projected to increase by 18% from 2.8 trillion miles to 3.3 trillion miles, and the miles traveled by truck vehicles are projected to increase by 50% from 384 billion miles to 569 billion miles (USEIA 2016). Global passenger transportation demands are also expected to double by 2040 (BP 2018).

This growing demand in transportation is unlikely to be met by electric vehicles (EV). The electric vehicle fleet size, though has been growing at a year-over-year rate over 50% in recent years and reached 2 million in 2016, still only comprises of 0.2% of the global fleet of light duty vehicles. BP projects that the global passenger car fleet will double its size to 2 billion by 2040, with over 300 million EVs, which is 15% (BP 2018). Thus engine powered vehicles are still the powerhouse for passenger transportation in the near future.

Future development of vehicle propulsion technologies is heavily influenced by fuel economy and emission regulations by different government agencies, aimed at improving vehicle efficiencies and reducing greenhouse gas/pollutant emissions. For example, the U.S. National Highway Traffic and Safety Administration (NHTSA) and the Environmental Protection Agency (EPA) jointly issued regulations on the Corporate Average Fuel Economy (CAFE) and Greenhouse Gas (GHG) emissions regulations. The CAFE standard (NHTSA 2012) for passenger cars and light trucks during 2017-2021 would require a fleet economy of 40.3-41.0 miles per gallon (mpg) be achieved by 2021. The GHG standard (EPA 2012) for passenger cars and light trucks during 2017-2025 would result in a fleet emission of 163 grams/mile of CO_2, which is equivalent to 54.5 mpg. Additionally, the EPA and California Air Resource Board (CARB) also regulates the tailpipe and evaporative emissions, such as non-methane organic gases, NO_x, particulate matter, CO, and HCHO.

With the growing transportation demands, ever increasing fuel economies, and the electrifications in vehicle propulsions, it is expected that oil share in the transportation fuel demand will decrease to 84% (BP 2018) and 89% (ExxonMobil 2016) on the global market, and to 70% on the US market. Specifically in the US, improvements in fuel economy standards is expected to decrease motor gasoline consumption by 31% through 2050, and maintain similar levels of diesel consumption to current times.

Continuous improvements in the internal combustion engine technology is clearly needed given the trends of transportation demands and fuel economy regulations. Advances in

spark ignition (SI) engine technologies includes, but unlimited to: gasoline direct injection, variable valve timing and lift, combustion chamber designs, reduced friction, lean-burn gasoline engines, and downsizing. Compression ignition (CI) engines are mostly diesel engines, and advances in the diesel engines are emission reductions due to the emission regulations, as well as fuel economy improvements. Fuels and engines co-optimization is a technical pathway that draws growing attentions in improving engine efficiency and fuel supply diversifications. Low temperature combustion (LTC) strategies apply to both SI and CI engines and can be realized through homogeneous charge compression ignition (HCCI), premixed charge compression ignition (PCCI), partially-premixed compression ignition (PPCI), and reactivity-controlled compression ignition (RCCI).

Gasoline compression ignition (GCI) is a technology that combusts gasoline in a compression ignition engine. CI engines' higher thermal efficiencies benefit from the higher compression ratios compared to SI engines. High reactivity fuels that can be compression ignited are used on CI engines, for example, diesel. However, the short period of time from the fuel injection to ignition, also known as the ignition delay, limits the degree of fuel air mixing, and this leads to the high levels of particulate matter and NO_x emissions. By lowering the fuel reactivity, longer ignition delays can be achieved that allow more time for fuel air mixing, and thus lower levels of pollutant emissions can be potentially achieved. This technology offers great potentials in reducing the tailpipe emissions from CI engines because current CI engines are equipped with additional exhaust after-treatment systems that are costly.

In addition to the mentioned benefits, challenges of the GCI technology considering its applications in heavy-duty engines includes, but not limited to:

1. Combustion instabilities under cold start and low load operations.
2. High unburned hydrocarbons and CO emissions in the exhaust, resulting from incomplete combustion under cold start and low load conditions, is challenging for the exhaust oxidation catalyst (Zhang, Kumar, et al. 2018).
3. Air handling system design for multi-cylinder engines. High levels of boost pressure is needed with exhaust gas recirculation (EGR) to maintain lean combustion. While this has been demonstrated for single cylinder engines, the requirement for the air handling system is more difficult to be met by production boosting systems without high penalties on the back pressure (Kumar et al. 2017).

1.2 Goals and Objectives

For medium to heavy duty CI engine applications, the mixing-controlled spray combustion dominates the majority of the combustion event. This complex process involves spray injection, liquid atomization, vaporization, fuel-air mixing, ignition, combustion, soot formation and oxidation. These processes are affected by various fuel thermos-physical properties and chemical kinetic characteristics. Thermo-physical property effects are reflected through the spray injection processes, for example, fuel density affects the momentum exchange with the ambient gas and thus affects the spray penetration, fuel

viscosity affects the atomization processes, and volatility affects the vaporization behavior. Chemical kinetics characteristics, like fuel reactivity and component chemical classes, affect ignition and soot formation characteristics, etc. A list of fuel properties of ultra-low sulfur diesel (ULSD) and high reactivity gasoline is given in Table 1.1. In summary, gasoline has lower density, lower reactivity, lower viscosity, lower aromatics content, lower boiling ranges, and higher net heating value compared to ULSD. These differences in fuel properties are expected to result in vast differences in the spray injection, combustion and soot emission processes.

Table 1.1. Fuel properties comparisons between ULSD and high reactivity gasoline.

Fuel	ULSD	High React. Gasoline
Density (kg/m^3)	848	705
Cetane Number	44.2	33.7
RON/MON	N/A	58.8 / 57.9
Kinematic Viscosity (cSt)	2.25	0.58
Carbon (wt%)	86.8	84.9
Hydrogen (wt%)	13.2	15.1
Aromatics(vol%)	28.2	9.1
IBP (˚C)	173.3	32.3
10% Dist. (˚C)	214.4	58.2
50% Dist. (˚C)	267.8	94.4
90% Dist. (˚C)	315.0	124.0
FBP (˚C)	346.7	139.7
Net Heat Value (MJ/kg)	42.8	43.4

The research community has conducted numerous researches on the spray combustion of diesel and many fuels alike, including jet fuels (Jing, Roberts, and Fang 2015), biodiesel or fatty acid methyl esters (Chong and Hochgreb 2015, Abdul Malik et al. 2017), Fischer-Tropsch fuel (Ochoterena et al. 2008), direct coal liquefaction (Pei, Qin, et al. 2017). These fuels are closer to diesel fuel property ranges and are readily used as drop-in fuels or alternative fuels. Gasoline's vastly different properties, in particular volatilities and fuel reactivity, may present other important differences on spray flame characteristics than ULSD or diesel-like fuels that could be potentially used for developing spray injection, engine piston bowl shapes, and combustion strategies.

Therefore, the first goal of this work is to experimentally understand the fundamental characteristics of the spray combustion of a high reactivity gasoline with a research octane number (RON) of 60, in comparison to ULSD. Experiments will be done in a constant volume combustion vessel with optical access. To isolate the fuel property effects on the physical processes and chemical kinetic processes, spray experiments will be carried out under both non-reacting and reacting ambient conditions. Specifically, non-reacting experiments will be carried out under low ambient temperatures that prevent spray plume vaporization, i.e. non-vaporizing conditions, and under high ambient temperatures that are similar to engine in-cylinder temperatures to facilitate vaporization, i.e. vaporizing

conditions. Through these experiments a variety of spray characteristics are measured, including spray vapor and liquid penetrations, spray cone angles, ignition delays, lift-off lengths, and soot natural luminosities, using optical and pressure-based diagnostics. Spray characteristics will be compared, and the effects of key fuel properties will be analyzed through established spray correlations to gain quantitative understanding of fuel effects.

The second goal of this work is to enable accurate computational fluid dynamics (CFD) simulations for the high-reactivity gasoline under conditions typical of medium to heavy duty CI engine operations. Through this goal, further understanding of the combustion and soot emission processes that is not easily interpreted through experimental diagnostics can be obtained. In addition, improved spray mixing predictions in CFD simulations will be facilitated through the development of a spray cone angle correlation, based on experimental measurements. Spray mixing is strongly correlated with the spray cone angles and an accurate description of the mixture formation is important for subsequent processes of ignition, combustion, and emissions. Use of this correlation is an advancement over established spray angle correlations in these areas: (1) more accurate description of the spray cone angle history, (2) more accurate spray cone angle inputs for engine simulations as a function of charge gas densities induced by piston movements, (3) first effort in the development of a spray cone angle correlation for gasoline spray injection using a heavy duty injector under injection pressures typical of CI engine operations.

The aforementioned goals will be accomplished through these following tasks:

1. Perform experimental studies using gasoline and ULSD in the constant volume combustion vessel, using optical diagnostics including Schlieren/shadowgraphy technique, Mie scattering, OH* chemiluminescence, natural luminosity, and a pressure sensor mounted in the vessel.
2. Develop data processing methods and programs to interpret the images and the pressure signals to obtain the spray characteristics.
3. Analyze spray results using existing vapor and liquid penetration correlations to obtain quantitative understanding of the spray mixing process and establish the relationship between the mixing processes and ignition characteristics.
4. Perform CFD simulations of high reactivity gasoline and ULSD spray combustion. Validate the CFD models with respect to key spray characteristics, including liquid and vapor penetrations, ignition delays, lift-off lengths, and soot natural luminosity characteristics.
5. Investigate the detailed soot emission processes from CFD simulation results and understand the fuel effects.
6. Develop spray cone angle correlations for both high reactivity gasoline and ULSD, based on measured non-reacting, non-vaporizing spray cone angle profiles. Validate the correlation.
7. Implement the spray cone angle correlation in CFD simulations and compare simulation results using the correlation against results using constant spray cone angle inputs.

2 Literature Review

This chapter provides a review of the low temperature combustion concept, with a focus on recent progresses on the gasoline compression ignition technology. Research and development both on engines and the fundamental spray combustion will be covered.

2.1 Diesel Combustion Overview

Diesel engine combustion is largely through a mixing controlled diffusion flame. Diesel fuel is injected into the cylinders when the piston is near the top dead center (TDC), using multi-hole nozzles with sizes on the order of 100 micrometers. High injection pressures on the order of 100-300 MPa are used. The sprays are finely atomized from the high pressure injection and forms a cone shape as illustrated by the non-reacting, non-vaporizing spray in Figure 2.1. The spray jet entrains the ambient gas and grows both axially and radially, and this leads to the dilution of the spray jet as it proceeds towards downstream.

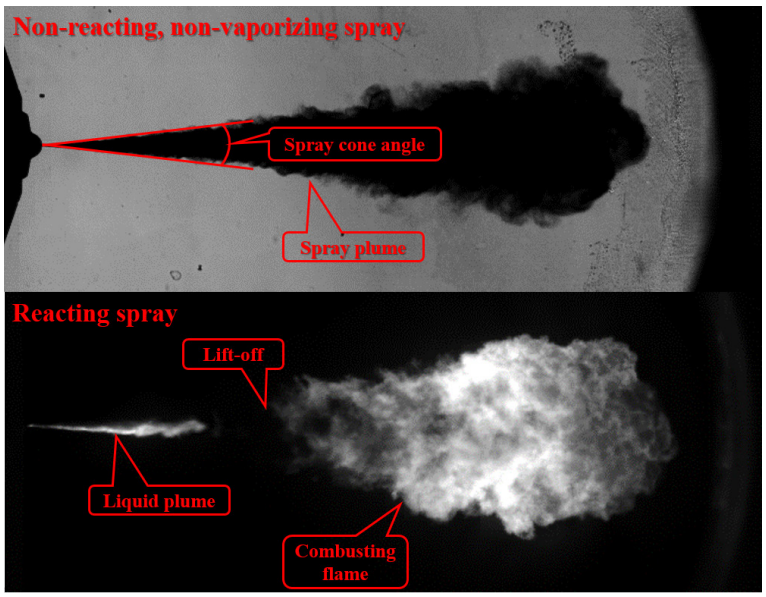

Figure 2.1. Illustration of typical diesel sprays under a non-reacting, non-vaporizing environment, and a combusting environment.

The gas in the engine cylinders near top dead center is hot. The spray jet mixes with the entrained ambient hot gas and increases local jet temperatures. Fuel droplets are vaporized and form fuel air mixtures. Under these conditions, the spray jet only exhibit a liquid core, which is surrounded by vaporized fuel-gas mixtures, as shown by the reacting spray in Figure 2.1. Downstream of the liquid core, the gaseous mixture continues to entrain ambient hot gases and the local jet temperature increases to ignite the combustible mixture. A lifted flame is characteristic of diesel spray combustion in diesel engines. The flame stabilizes around a location which results from both auto-ignition and flame propagation

(Pickett, Siebers, and Idicheria 2005). Downstream of the lift-off location, the flame develops.

Due to the high reactivity of diesel, denoted by its high cetane numbers (usually > 40), compression ignition occurs very shortly after the injection, which means very limited premixed combustion occurs. Injection durations are usually longer than the auto-ignition delay, which is the duration from the start of injection to the onset of auto-ignition. Thus diesel spray combustion is usually dominated by diffusion combustion.

NO_x is produced mainly through a thermal mechanism process, whereby its production rate grows exponentially with temperature (Plee et al. 1982, Ladommatos et al. 1996). Peak combustion temperatures occurs under a fuel-air stoichiometric mixture, which is mostly distributed on the periphery of a flame. This is where the highest level of NO_x occurs in a combusting flame, although NO_x may be produced toward a later time during spray combustion and even after the end of injection (Dec 1997).

Soot is produced in fuel rich regions, where the temperatures are below the peak combustion temperature. Low concentrations of soot are formed downstream of the flame lift-off location, where the soot sizes are small. The low concentration soot fills in a large portion inside the diffusing flame, except for the head region in the jet where vortices occur and the highest soot concentrations and largest soot particle sizes are present. The diffusion flame is where the highest levels of OH radicals occur, which is the main pathway for soot oxidation (Dec 1997). The combusting flame as shown in Figure 2.1 is the natural luminosity produced by the incandescing soot particles which is highly dependent on the soot particle temperatures and soot volume fractions (Mueller and Martin 2002). Soot formation and oxidation rates are also highly dependent on the ambient temperature and O_2 levels. Higher temperatures and O_2 levels are associated with higher rates of soot formation and even higher rates of soot oxidation (Huestis, Erickson, and Musculus 2007).

The process above describes a typical diesel spray as presented by Figure 2.1, although a variety of parameters, including nozzle specifications, and ambient gas conditions, will influence the flame in different ways that may lead to an overlap of the downstream extent of liquid jet and the upstream extent of the flame. The general processes of the spray combustion still proceeds as described.

The above discussion also shows that the cause of the classic NO_x – soot tradeoff originates from the dependence of NO_x and soot processes on the ambient gas temperature and O_2 levels. Increasing the ambient gas temperatures and O_2 levels leads to increases in the NO_x emissions, where soot emission decreases because soot oxidation increases faster than soot formation. Decreasing the ambient gas temperatures and O_2 levels leads to decreases in NO_x emissions, at the expense of higher soot emissions because soot oxidation slows down faster than soot formation. The pathway of a typical diesel spray combustion described above is depicted in Figure 2.2. The equivalence ratio is defined as the actual fuel-air ratio (mass-based) over the stoichiometric fuel-air ratio (mass-based).

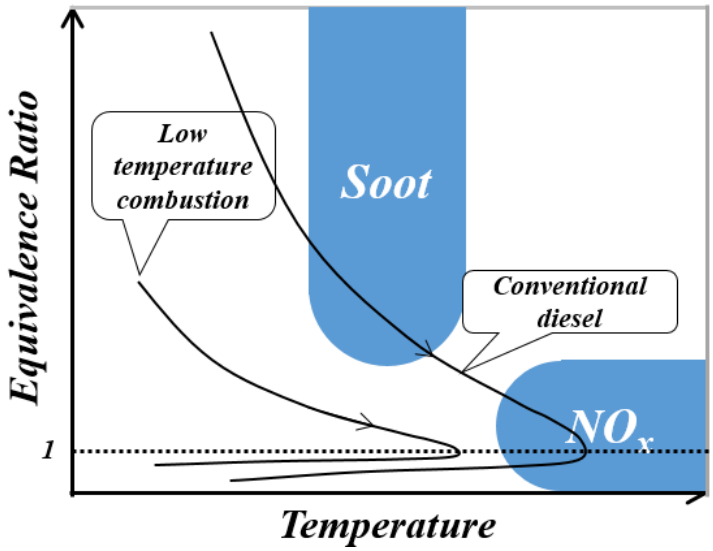

Figure 2.2. Illustration of typical conventional diesel spray combustion pathways and low temperature combustion pathways relative to high soot and NO_x emissions regions on an equivalence ratio – temperature space. Adapted from (Pickett and Siebers 2004a, Kitamura et al. 2002).

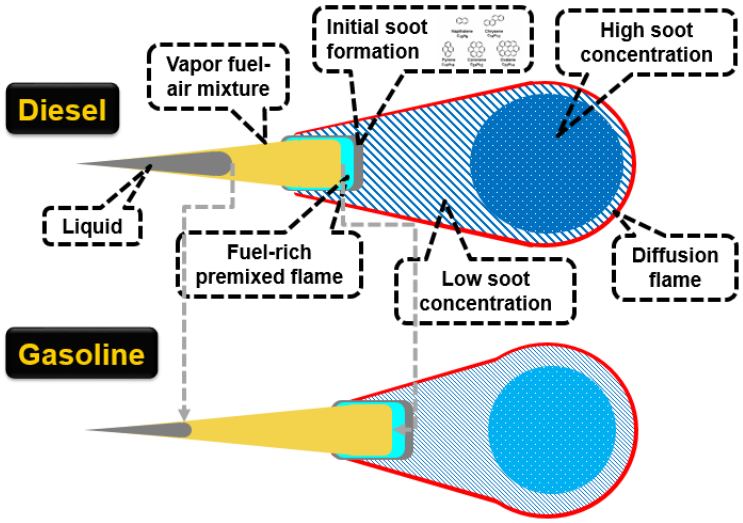

Figure 2.3. Hypothesized conceptual model for combusting diesel and gasoline flames. Adapted from (Dec 1997).

John Dec proposed a model to conceptually demonstrate the structure of a combusting diesel spray (Dec 1997), which is adapted and reproduced in Figure 2.3. A conceptual gasoline spray flame is hypothesized and provided based on the fuel property differences listed in Table 1.1. Due to the higher volatility, gasoline spray flames are expected to exhibit shorter liquid penetrations than ULSD. The lower fuel reactivity of RON 60 gasoline compared to ULSD is expected to lead to slower ignitions, thus resulting in longer

flame lift-off locations. Reduced soot concentration is expected from RON 60 gasoline spray flames, due to higher levels of premixing and the lower aromatics content of gasoline.

2.2 Low Temperature Combustion Concept Overview

To overcome the NO_x – soot tradeoff, one of the effective pathways is to pursue a low temperature combustion (LTC) strategy, where NO_x productions reduce with lower flame temperatures. Soot productions are reduced through better mixing and through an increased portion of premixed combustion relative to the diffusion combustion. One of the LTC pathways is shown in Figure 2.2, which features lower peak combustion temperature and lower overall equivalence ratio, as a result of enhanced mixing relative to conventional diesel spray combustion. However, there are other ways which feature different mixture and combustion characteristics that exhibit a different pathway than the LTC pathway shown in Figure 2.2.

2.2.1 Homogeneous Charge Compression Ignition

Early introduction of the LTC concept are through the form of homogeneous charge compression ignition (HCCI) processes (Onishi et al. 1979, Noguchi et al. 1979, Najt and Foster 1983). HCCI combustion operates on overall lean and homogeneous fuel air mixture, which is through either port induction, or direct injection during the intake stroke or early compression stroke. Similar to CI engines, HCCI engines operates un-throttled and on higher compression ratios than SI engines, thus overcoming the throttle loss the lower efficiency of SI engines. Lower combustion temperature also reduces heat transfer loss compared to CI engines. Ignition events are kinetically driven, and are sensitive to ambient gas temperature and pressures, which are difficult to control. Due to the fast combustion of a homogeneous mixture, a high maximum pressure rise rate (MPRR) and thus excessive combustion noise are often associated with high load HCCI operations. These limit HCCI operations to low load conditions. Recent development of HCCI utilizes temperature and mixture equivalence ratio gradients in the cylinder for better control of the ignition processes (Yang et al. 2011), although the mixture is still locally lean.

2.2.2 Partially Premixed Compression Ignition

Another way to realize the LTC concept is generally termed partially premixed compression ignition (PPCI), and the premixedness is in between HCCI and conventional diesel combustion, as the name suggests. PPCI covers a range of different combustion strategies, including but not limited to injection strategies, and fuel selections.

To create the partially premixed mixture, injection timings are retarded relative to HCCI operations to either before TDC and during mid to late compression stroke (Keeler and Shayler 2008), or after TDC and early in the expansion stroke (Kimura et al. 1999). The duration of injection and the start of combustion are usually separate to allow improved mixing, which are achieved through exhaust gas recirculation (EGR), and short injection

durations. However, under high-loads, an overlap between the duration of injection and the start of combustion still occurs (Noehre et al. 2006). The mixture in PPCI operations is locally rich, and overall richer than HCCI mixtures. Lower gas temperatures are achieved with both strategies, and with increased proportions of premixed mixture, both NO_x and soot emissions reductions are achieved. However, CO and unburned hydrocarbons (UHC) may become excessive due to incomplete combustion. This negatively influences the combustion efficiency and results in increased fuel consumption relative to conventional diesel engine operations (Cho et al. 2009). One of the possible solutions to the incomplete combustion is to use EGR, which was demonstrated to increase the combustion efficiency beyond 99% with an EGR rate of up to 62% (Manente et al. 2010).

Multiple injections is another injection strategy for PPCI operations. A multiple premixed compression ignition (MPCI) strategy was proposed by (Yang et al. 2012), where injection and combustion occur in a sequence of "spray-combustion-spray-combustion" with separations between spray and combustion for ideal operations. The spray events can be repeated three or more times. MPCI better controls the excessive MPRR in HCCI or PPCI operations, and the pollution emission processes can be controlled within each combustion events. Multiple injections are also experimented by (Borgqvist et al. 2013), where the fuel injection quantity distribution between the two injections and the dwell time were optimized.

PPCI operations are compatible with a range of fuels. Diesel fuels are optimized to work with CI engines and can also be used to work with PPCI operations. Diesel PPCI operation showed that the classic NO_x and soot trade-off in conventional CI engines were prevented, however, at the expense of higher CO and UHC emissions and reduced combustion efficiency (Noehre et al. 2006). Other important findings include: (1) EGR reduced soot emission levels, (2) high swirl was associated with low soot emissions, and (3) boosting intake was effective in broadening PPCI operation ranges. Diesel PPCI operations usually employs injections later during the compression cycle to avoid (1) early auto-ignition during the compression stroke that leads to reduced efficiency (Dronniou et al. 2005), and (2) wall impingement and wetting due to diesel fuel's low volatility, which may become a source of soot emissions.

PPCI or HCCI operations on fuels other than diesel was possible. PPCI with gasoline was able to achieve advanced injection timings compared to diesel due to its high volatility (Kalghatgi, Risberg, and Ångström 2006). The resistance to auto-ignition by gasoline's lower reactivity also promoted premixedness of gasoline even for injections near the TDC, compared to diesel. This results in low NO_x and soot emissions by gasoline relative to diesel. Fuel property effects were discussed with respect to HCCI combustion by (Bessonette et al. 2007), and it was concluded that a reduced ignitability as measured by the derived cetane number was conducive for increasing the operating load range, while fuel volatility and fuel chemistry effects were minor in comparison. Fuel volatility and chemical composition effects on NO_x, UHC, and CO were negligible, while diesel fuels produced higher levels of PM emissions. Similar thermal efficiencies were achieved compared to conventional CI engines.

Dual fuel operations is a technical pathway alternative to PPCI with EGR operations, which is aimed at controlling PPCI ignition events and the excessive MPRR. The downside of EGR, however, is associated with its lower thermal efficiency, reduced maximum engine power, and unstable transient EGR operations (Inagaki et al. 2006). Fuels with different reactivity can be harnessed to gain effective control of the ignition process, as demonstrated by (Inagaki et al. 2006) through the use of high (iso-pentane or iso-octane) and low (n-pentane, or n-hexane, or n-heptane) reactivity fuels. However, the burning rate cannot be controlled by regulating the dual-fuel ratio from (Inagaki et al. 2006). Dual fuel operations with other fuels were also possible, like diesel – natural gas (Ansari et al. 2016), and diesel – gasoline (Hanson et al. 2012).

Previous discussions provided an overview of the LTC concept and several technical pathways, from HCCI to PPCI. Specifically, PPCI can be realized by different injection strategies and fuels. Specifically, PPCI operations with gasoline and dual fuels can be termed as gasoline compression ignition (GCI) and reactivity controlled compression ignition (RCCI). However, GCI and RCCI does not necessarily operate under PPCI concept entirely, as will be shown in some applications in the next section.

2.3 Gasoline Compression Ignition Overview

This work focuses on the gasoline compression ignition concept. In this section, progresses on recent GCI research and development will be summarized.

2.3.1 Early GCI Concept Demonstrations

In one of the early GCI works (Hashizume et al. 1998), a concept of MULtiple stage DIesel Combustion (MULDIC) was developed on a single cylinder engine. The concept employs two separate combustion events, in which the first combustion is a lean premixed combustion, and the second combustion proceeds as a diffusion combustion under high temperature but low O_2 level ambient gas condition. Although diesel fuel was used, the influence of fuel cetane number (CN) was investigated by using a CN 62 diesel and a CN 19 diesel, in which CN 19 was in the range of gasoline ratings, although the other properties remained in the diesel range. The CN 19 diesel was used specifically for the first stage combustion. Nonetheless, use of CN 19 diesel was found to reduce UHC, NO_x, and soot emissions, without increasing the fuel consumption.

Gasoline (CN ~15) was used as one of the four test fuels in another early GCI work (Kalghatgi, Risberg, and Ångström 2006), with the other three including a Swedish MK1 diesel fuel (CN 54), and diesel 1 (CN 39) and diesel 2 (CN 30), which are blends of diesel kerosene component with an aromatic solvent. On a single cylinder engine, PPCI operations were achieved by using gasoline, which results in much higher indicated mean effective pressure (IMEP) and low NO_x, low soot relative to diesel operations under the same intake pressure and EGR level. It was suggested that high noise levels, CO and UHC emissions need better control methods as well as cold starts and low load operations.

2.3.2 Low Load GCI Operating Challenges and Load Expansion

Thanks to the low reactivity of gasoline, GCI operations can achieve higher levels of mixing relative to diesel under the same operating conditions. Due to the very same reason, operations at low load and advanced injection timings are unstable (Kalghatgi, Risberg, and Ångström 2006). Thus unlike PPCI operations that high load operations are restrained by excessive MPRR, GCI operations are challenging at low load conditions.

In a GCI concept design work (Rose et al. 2013), several design recommendations were made for successful GCI operations using European market gasoline:

- Fuel injection pressures should increase from SI engine ranges around 200 bar to CI engine ranges of 1000 bar and above.
- Enhanced fuel lubricity to adapt to a diesel type injection system.
- A need for evaporative emissions control systems due to the high volatility of gasoline.
- After-treatment systems are needed, including a NO_x catalyst, oxidation catalyst for UHC and CO, and a gasoline particulate filter.
- Two stage boosting and high EGR levels to maintain high charge pressure and temperature, while reducing combustion temperatures.
- Combustion assistance (spark plug or glow plug), in regards to starting and mild ambient conditions.

On a single cylinder bench engine, GCI was demonstrated to achieve full load power at a compression ratio (CR) of 19 comparable to diesel operations with an IMEP over 20 bar at an engine speed of 2000 revolutions per minute (rpm), and an IMEP slightly shy of 19 bar at 4000 rpm. At 1500 rpm with single injection, the lower limit for stable operation was 7 bar IMEP. A glow plug was installed and oriented for the lowest CO/HC emissions and combustion durations, but did not prove to extend the operating range under low load conditions. Recommendations for extending low load operations include the use of (1) a spark plug, (2) more flexible variable valve timing (VVT), (3) increased boost pressure at low loads, and (4) variable compression ratio.

Load expansion utilizing negative valve overlap (NVO) was demonstrated on a single cylinder diesel engine running on RON 91 gasoline at an idle speed of 800 rpm without boosting the intake pressure (Vallinayagam et al. 2018). Both HCCI and PPCI mode were ran with start of injections at -180 CAD and -30 CAD after TDC (aTDC), respectively. The exhaust valve closed early, to retain hot residual gas and increase the in-cylinder gas temperature. Default exhaust valve closes (EVC) at 10 CAD aTDC, and default intake valve opens (IVO) at -10 CAD aTDC. Advancing the EVC by 30 CAD and 50 CAD, NVOs of 10 CAD and 30 CAD were achieved. This strategy reduced the intake temperature requirement by 15-20˚C, while achieving a minimum load of net IMEP at 1 bar, however, at the expense of thermal efficiency because of reduced volumetric efficiency and heat losses. HCCI operations reduced soot and NO_x emissions while the CO and UHC emission increased. An increase in the NVO was effective in decreasing the CO and UHC emissions.

GCI operations are not only limited to market gasoline with high resistance to auto-ignition, as shown in previous works. Relaxing the fuel reactivity to achieve easier auto-ignition during low loads is another pathway to expanding the GCI operating range. Researches pertaining to the use of other fuels are demonstrated in the next section.

2.3.3 GCI Operations with Lower Octane Fuels

As demonstrated by (Kalghatgi, Hildingsson, and Johansson 2010), through the use of RON 84 (CN 21) gasoline, RON 95 (CN 16) gasoline, and CN 56 diesel on a single cylinder diesel engine, it was discovered that RON 84 gasoline ran more robust and stable under high speeds (2000 rpm and 3000 rpm) and low loads (IMEP 4 – 5 bar).

Dieseline, a mixture of diesel and gasoline, was used on a single cylinder diesel engine to extend the low load limit of GCI operations without employing methods including intake heating, rebreathing, and NVO (Wang, Wang, et al. 2015). Two dieseline blends were used, including 90% and 80% gasoline by volume. Their respective estimated RONs were 84.1 and 74.3. With high intake pressure (0.14 MPa) and low injection pressure (20 MPa), 0.07 MPa IMPE was achieved.

As demonstrated, a diverse fuel reactivity, with RON ranging from 50 to 80, is well suited for GCI operations. This range of fuel reactivity lies in between conventional diesel and gasoline, and has been shown by a great number of studies to benefit GCI operations. While a blend of gasoline and diesel is the most viable option to achieve the reactivity target, the overall cost of producing these GCI fuels would be at disadvantages compared to blending multiple refinery streams with RON ranges from 50 to 80. As shown in a life cycle analysis on the fuel consumption and greenhouse gas emissions of conventional gasoline SI and low octane GCI pathways, 24.6% less energy consumption and 22.8% less GHG emissions were achieved by the low octane GCI pathway (Hao et al. 2016). Production of low octane GCI fuels allows removal of isomerization and catalytic reforming units in the fuel production process, which alone led to 46.1% and 42.6% reductions in energy consumption and GHG emissions, respectively.

To enable better control of fuel properties for research purposes, a standardized GCI fuel matrix was proposed by (Badra et al. 2018). Important fuel properties considered to vary within the matrix include density, T90, and RON. Considerations for choosing these properties are: (1) density, for its relevance in fuel consumption (2) T90, for its relevance in fuel vaporization, and (3) RON, for its relevance to the auto-ignition quality of the fuel. Eleven GCI fuels were recommended, with a density range from 650 to 750 kg/m^3, a T90 range from 70 to 200 ˚C, and a RON range from 40 to 85.

2.3.4 GCI Operations on Multi-Cylinder Engines

Many successful demonstrations on single cylinder engines are provided in previous sections. Successful adoption of the GCI technology on multi-cylinder engines is the key

to mass production and commercialization. A series of research activities relevant to GCI operations with multi-cylinder engines is reviewed in this section.

A series of GCI operations on a six-cylinder Cummins ISX15 heavy-duty engine (model year 2013) was performed by (Zhang et al. 2016, Zhang et al. 2017, Zhang, Kumar, et al. 2018). A wide range of fuels were tested, including RON 59 gasoline and RON 69 gasoline (Zhang et al. 2016, Zhang, Kumar, et al. 2018), RON 80 gasoline and non-ethanol RON 91 market gasoline (Zhang et al. 2017, Zhang, Kumar, et al. 2018). Compression ratios used was 17.3 (Zhang et al. 2016), 18.9 as used in the stock engine (Zhang et al. 2017), and 15.7 in an effort to reduce NO_x emissions (Zhang, Kumar, et al. 2018). An engine speed of 1375 rpm, and engine loads of 5/10/15 bar brake mean effective pressure (BMEP) were swept for these investigations.

Single injection was used in (Zhang et al. 2016). Under mixing controlled combustion mode, (1) reactivity benefits of gasoline on mixing was suppressed under 15 bar BMEP condition, where gasolines and ULSD exhibit similar ignition delays, (2) lower soot emission benefit of gasoline was maintained throughout all load conditions. Under PPCI mode, late injections with high injection pressure (2400 bar) led the successful LTC operations up to 10 bar and 11 bar BMEP, for RON 59 and RON 69 gasoline, respectively, however, at the expense of reduced brake thermal efficiency. The authors suggested improved air systems hardware that enable higher EGR and boost be potential methods to improve PPCI operations. UHC and CO emissions was low under both mixing controlled combustion and PPCI.

A split injection strategy was employed to reduce the maximum MPRR (Zhang et al. 2017). Both gasolines exhibited lower brake specific fuel consumption (BSFC) but lower brake thermal efficiency (BTE) than ULSD, when the NO_x emissions were maintained similar. The lower BSFC was related to the higher energy content, and the lower BTE was hypothesized as a result of higher fuel pump parasitic losses from gasoline's low viscosity relative to ULSD. Soot reduction potentials of both gasolines relative to ULSD were more effective at 5 bar BMEP, while engine performance and emissions were similar at 15 bar BMEP. The two gasolines produced higher UHC and CO levels than ULSD at 25% load conditions in the non-idle, 12 mode, steady state supplemental emissions test (SET 12) test modes.

Evaluations of the four fuels (Zhang, Kumar, et al. 2018) showed improved soot emissions at the expense of reduced fuel efficiency and combustion loss, more sound at low loads. Gasolines generally exhibited similar or higher efficiency than ULSD. Three dimensional computational fluid dynamics (3D CFD) studies suggested engine design optimizations to improve RON 80 gasoline GCI low NO_x operations, which includes: piston bowl design, spray patterns, higher compression ratios, and thermal boundary conditions.

Combustion system optimizations by 3D CFD studies was performed by (Pei, Zhang, et al. 2017). The optimization was performed for a RON 59 gasoline with targets of reduced fuel consumptions at emission levels equivalent to production engines. Six piston bowl

geometries, injector nozzle holes, spray included angles, and start of injections were design parameters. Two thousand simulations were performed on a supercomputer MIRA at Argonne National Laboratory, and located two designs with ISFC improvements of 1.9% at B50 condition and up to 2.8% at A75 condition compared to engine experiment result running on RON 59 gasoline. Through CFD simulations, it was also found that ULSD favors smaller nozzle sizes but higher swirl, which was the opposite for gasoline.

GCI studies on a four-cylinder Delphi Gen 2 GDCI (gasoline direct injection compression ignition) engine was performed to understand the UHC emissions from operations on low octane fuels (Storey et al. 2017). Comparisons were made between 10% ethanol US market gasoline RON 92, and a RON 80 gasoline under three operating points, ranging from low load of 800 rpm and 2 bar gross IMEP, to medium load of 1500 rpm and 6 bar gross IMEP, and 2000 rpm and 10 bar gross IMEP. RON 80 fuel produced lower levels of UHC and CO compared to RON 92 E10 gasoline. RON 92 E10 gasoline exhibited ethanol in the UHC emission, and higher fractions of formaldehyde emissions, while RON 80 gasoline exhibited higher fractions of benzaldehyde emissions, and increased partial oxidation products of pentene and heptene.

2.3.5 Air System for Multi-Cylinder GCI Operations

Air system design requirements for the six-cylinder Cummins ISX heavy duty engine was investigated using a one dimensional (1D) GT-Power model coupled with 3D CFD simulations by (Kumar et al. 2017). Investigations were based on PPCI operations with RON 70 gasoline. 3D CFD simulation assisted in identifying the boundary conditions and heat release profiles corresponding to an optimal operation from the SET 12 cycles. The boundary conditions and heat release profiles were coupled into a 1D GT-Power model to evaluate the air system performance. Both a one-stage and a two-stage turbocharge with high pressure EGR loop were investigated by incorporating existing high efficiency turbocharger maps. Results showed the capability of both systems in meeting the desired EGR and boost pressure requirement and while meeting the engine out NO_x emission target of 1 g/hp-hr.

2.3.6 GCI Fuel Lubricity

GCI fuels, including market gasoline and other low octane fuels, generally share lower lubricity and viscosity than diesel. This is a concern for successful deployment of GCI technology in medium to heavy duty applications, where the fuel systems are optimized for diesel fuels. A study by (Voice, Tzanetakis, and Traver 2017) investigated the lubricity of a range of light-end fuels and ULSD. High-frequency reciprocating rig (HFRR) tests showed that light-end fuels without lubricity additives resulted in wear scar diameters (WSD) twice the size of ULSD. With additive dosage of 200 mg/kg, several lubricity additives provide substantial improvements over the neat light-end fuels, with WSDs even smaller than ULSD.

The fuel system durability is another critical factor to ensure stable operation of GCI engines with light-end fuels. Investigations by (Tzanetakis, Voice, and Traver 2018) employed a 400-hour NATO (North Atlantic Treaty Organization) durability test, aimed at accelerating wear. Experiments were conducted with RON 60 gasoline dosed with 200 ppm of lubricity improver, on a Cummins XPI common rail injection system. The lubricity improver dosage was designed to match the wear scar diameter (WSD) of diesel. Performance degradations were minimal in terms of driving torque, fuel return rates, fuel flow rates during injection, rail pressure, fuel temperature, and system pressures. Break-in periods for iron in the fuel and fuel-in-oil dilution followed a similar period of 200-250 hours. Due to the low fuel viscosity and high volatility, (1) under 2500 bar injection pressure, fuel metering could not keep up with injection durations due to the very high return flow, (2) the 400 hour pump head was unable to control rail pressure at very low injection durations. The primary failure mode of the fuel system was identified to be cavitation damage.

2.4 Gasoline Spray Combustion Relevant to CI Engine Conditions

Detailed processes that occur in a gasoline spray injection are widely investigated using hollow-cone type injectors by numerous studies, like the standardized spray G in the Engine Combustion Network (SNL 2018), and the recommended parametric variations for SI engine conditions include ambient gas temperatures up to 800 K, ambient gas densities up to 10 kg/m^3, and injection pressures up to 20 MPa. The interest of the current work focuses on spray injection and combustion events that occur under typical CI engine conditions, with injection pressures usually over 100 MPa, and charge gas densities over 20 kg/m^3. Relevant researches are limited and summarized in this section.

Payri et al. (Payri, Garcia, et al. 2012, Payri, García, et al. 2012) compared the injection rate, momentum flux and spray characteristics of gasoline and diesel under 25 ˚C temperature, which was a non-vaporizing condition. The charge gas pressures were 2.5 and 5 MPa. Nozzle-hole diameters of 0.097 mm and 0.136 mm were tested. Injection pressures were 60, 90, 120, and 150 MPa. Injection rates were higher for diesel than gasoline for the same energizing time. No clear differences were observed between gasoline and diesel in terms of the spray penetration, spray dispersion angle, and momentum flux under the experimental conditions.

In another set of studies, Han et al. (Han et al. 2014) and Feng et al. (Feng et al. 2016) independently reported the effects of different blending ratios of gasoline into diesel on spray characteristics. In their investigations, diesel mixtures with 0%, 20% and 40% blended gasoline by volume were tested in both studies, while the effect of ethanol substitution of gasoline was specifically investigated by (Feng et al. 2016). The nozzle diameters were 0.157 mm in (Han et al. 2014), and 0.18 mm in (Feng et al. 2016). The experiments from were conducted at ambient conditions of 298 K and 0.1 MPa, with injection pressures of 40 and 100 MPa (Han et al. 2014), and ambient conditions of 293 K

with 0.2/0.4 MPa, and injection pressures of 60, 90, and 120 MPa (Feng et al. 2016). Higher volumetric injection rates and similar mass injection rates were found for gasoline and diesel blends. Shorter injection delays and longer hydraulic injection durations were observed for the blend. Both works reported decreased spray tip penetrations distances, increased spray cone angles, and decreased local sauter mean diameters of fuel blends compared to ULSD were observed. In addition, ethanol substitution of gasoline led to increased spray tip penetration, subtly smaller spray cone angles, and increased droplet size.

One important difference between (Payri, Garcia, et al. 2012, Payri, García, et al. 2012) and (Feng et al. 2016, Han et al. 2014) was their field of view. Maximum observable spray penetrations were less than 40 mm in (Payri, Garcia, et al. 2012, Payri, García, et al. 2012) and over 90 mm in (Feng et al. 2016, Han et al. 2014). The smaller field of view may prevented observations of spray behaviors further downstream that lead to different observations between the two set of works.

Medina et al. investigated gasoline sprays using a 0.110 mm nozzle diameter injector, under charge gas conditions of 5, 10, and 20 bar, with 298 K (Medina, Fatouraie, and Wooldridge 2018). Injection pressures include 300, 600, 900, 1200, and 1500 bar, which are typical of CI engine ranges. In comparing gasoline spray characteristics to spray correlations developed for diesel, the authors found that the good agreement at some times and conditions and the overall trends. Correlations under predicted the penetration distances at longer times after the spray break-up.

Non-reacting and reacting diesel and gasoline sprays under CI engine like conditions were investigated by (Kim, Bae, and Johansson 2013). A single-hole injector nozzle with a diameter of 0.356 mm was used. Injection pressures of 50, 100, and 150 MPa were employed. Ambient charge gas conditions simulating HCCI, PPCI, and conventional CI engine operations were performed for the experimental studies. Ambient gas temperatures for the HCCI, PPCI, and CI conditions were 474, 723, and 925 K, respectively. Charge gas densities for the HCCI, PPCI, and CI conditions were 3.74, 11.38, and 23.39 kg/m^3, respectively. Non-reacting spray experiments were performed for HCCI and PPCI, whereas CI conditions were performed with a sweep of O_2 levels, including 15%, 18%, and 21%. Important observations include: (1) shorter gasoline liquid lengths than diesel, (2) similar vapor and penetration and spray cone angle between the two fuels, (3) longer ignition delay, lift-off lengths, and lower combustion luminosity.

Reacting gasoline and n-heptane mixture (80/20 percent by volume) sprays in a constant volume vessel was investigated by (Zheng et al. 2012). A single-hole nozzle with a diameter of 0.168 mm was used, two injection pressures, 20 and 50 MPa, were used. Ambient charge gas conditions were 4 MPa pressure, and 870 K and 910 K temperature. O_2 level sweeps were 11.1%, 14.2%, 16.3%, and 21%. Shorter liquid lengths of gasoline/heptane mixture were observed in comparison to diesel. Ignition delays were longer for gasoline/heptane mixture than diesel. Significantly lower flame luminosity was observed for gasoline/heptane mixture when the O_2 concentration decreased from 21% to

16.3%, while for ULSD, 11.1% was required for such significant decrease. EGR was more effective compared to ambient temperature in affecting the flame luminosity and ignition delays. An increase in the injection pressure led to decreased flame luminosity, longer ignition delay and longer flame distance to the injector tip.

Reacting sprays of gasoline and diesel blend was investigated regarding the liquid length, lift-off, and soot volume fractions (Zheng et al. 2015). Blends of gasoline into diesel were at 0%, 20%, 40%, and 60% volume fractions. Injections were performed using a single-hole injector with a nozzle size of 0.168 mm, and 80 MPa injection pressure. Test conditions include an ambient charge gas of 830 K and 4 MPa. With an increase in the fraction of gasoline in the fuel mixture blend, (1) liquid lengths decreased, (2) lift-off lengths increased, (3) peak soot volume fractions significantly reduced, (4) peak soot formation shifted from the spray periphery to the spray center, (5) first soot location shifted further downstream, (6) soot inception time delayed.

Previous studies addressed fundamental gasoline spray combustion characteristics in comparison to diesel under controlled environments, including constant volume vessels and constant flow rigs. In another study, the influence of fuel reactivity on lift-off lengths were experimentally observed in an optical engine, which was modified based on a six-cylinder Volve MD13 engine (Lundgren et al. 2018). A primary reference fuel (PRF) 87 was used to represent gasoline, which was comprised of iso-octane and n-heptane by 87%, and 13% by volume. Pure n-heptane was used to represent diesel. A six-hole nozzle injector with nozzle diameters of 0.212 mm was used, and injection pressures varied among 1500 bar, 2000 bar, and 2300 bar. The engine was running at a high load of 1200 rpm and 22 bar gross IMEP. CA 50 were kept constant. Longer lift-off lengths of PRF 87 fuel than pure n-heptane were observed, however, they converged to the same lift-off lengths at CA 50 regardless of fuel, injection pressure, and inlet temperature.

2.5 Summary of Literature

This section provided a review of the literature studies on the current progress of the GCI technology. Current research efforts focus on successful deployment of the GCI technology on multi-cylinder engines, through the development of the combustion system, fuel system, and optimizations using numerical simulations.

This study focuses on the fundamental aspects of gasoline spray and combustion in comparison to ULSD. The test conditions from section 2.4 are summarized in Figure 2.4 in colored markers. Some key observations of the effect of gasoline on injection characteristics relative to ULSD is summarized in Table 2.1.

The literature experimental conditions scattered at low temperatures (around 300 K). Experiments under elevated pressures and temperatures were scarce. Comparisons are made to a polytropic compression curve, assuming the polytropic coefficient as 1.4, with an initial pressure and temperature of 0.3 MPa and 100 ˚C, a compression ratio of 20, and

a displacement volume of 1 liter. This work propose to expand the coverage of pressures and temperatures as illustrated by the black markers.

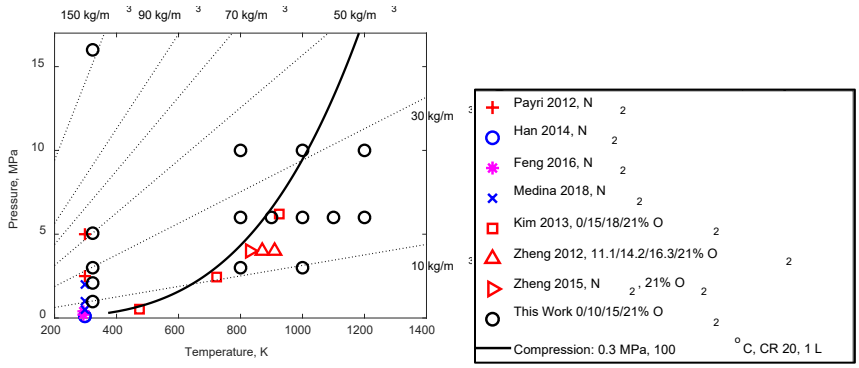

Figure 2.4. Summary of experimental conditions (pressure-temperature, and O_2 level), in comparison to the proposed experimental conditions in this work. A polytropic compression curve is shown for comparison to the test conditions, with an initial condition of 0.3 MPa and100 ˚C, compression ratio of 20, and a displacement volume of 1 liter.

Table 2.1. Influence of gasoline relative to ULSD on injection characteristics (↑ increase, ↓ decrease, → unchanged).

↑ (Payri, Garcia, et al. 2012, Payri, García, et al. 2012)	Injection rate
↑ (Han et al. 2014, Feng et al. 2016)	Volumetric injection rate
→ (Han et al. 2014, Feng et al. 2016)	Mass injection rate
→ (Payri, García, et al. 2012, Payri, Garcia, et al. 2012, Kim, Bae, and Johansson 2013), ↑ (Han et al. 2014, Feng et al. 2016)	Spray dispersion
→ (Payri, García, et al. 2012, Payri, Garcia, et al. 2012, Kim, Bae, and Johansson 2013) ↓ (Han et al. 2014, Feng et al. 2016)	Spray penetration
↓ (Han et al. 2014, Feng et al. 2016)	Sauter mean diameter
↓ (Zheng et al. 2012, Kim, Bae, and Johansson 2013, Zheng et al. 2015)	Liquid length
↑ (Zheng et al. 2012, Kim, Bae, and Johansson 2013, Zheng et al. 2015)	Ignition delay
↑ (Zheng et al. 2012)	Lift-off length
↓ (Zheng et al. 2012, Kim, Bae, and Johansson 2013)	Combustion luminosity
↓ (Zheng et al. 2015)	Peak soot volume fractions
↑ (Zheng et al. 2015)	Soot inception time

3 Experimental Setup

3.1 Optically Accessible Constant Volume Combustion Vessel Overview

Spray combustion experiments in this work were performed in an optically accessible constant volume combustion vessel, shown below in Figure 3.1. The combustion vessel was developed based on a proven design at Sandia National Laboratories, and was funded by National Science Foundation through the Major Research Instrument Development program, grant number 0619585.

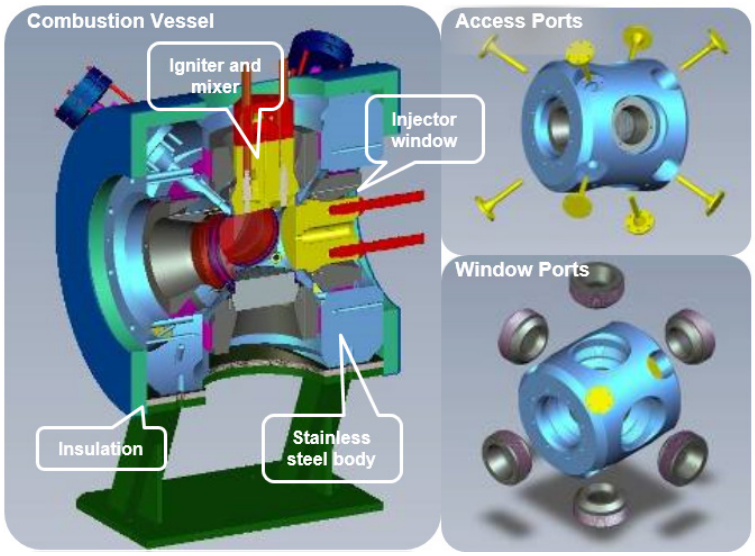

Figure 3.1. Overview of the constant volume combustion vessel, including a cross-sectional view, eight access ports, and six window ports.

The combustion vessel features a 1.1 liter cubical design in stainless steel body with a size of 108 mm × 108 mm × 108 mm in each direction. Outside the stainless steel body, there is a layer of thermal insulation. The combustion vessel assembly is fixed on to an optical table through a stand. This facilitates optical setups around the vessel for measurements. The combustion vessel is rated for pressures up to 345 bar, and temperatures on the order of 2000 K during a combustion event. This enables investigations into premixed and diffusion combustion events that exceed the operating ranges of current light and heavy duty internal combustion engines.

The vessel is equipped with eight corner access ports and six window ports. As shown in Figure 3.1, a top window is used to hold the igniter and mixer, and a side window is used as a holder for the injector. All other windows could provide optical accesses. The window ports provide flexibility in adapting to customized or production automotive spark plugs, mixing fans, and injectors, including but not limited to gaseous injectors, GDI (gasoline

direct injection) injectors, heavy duty diesel injectors, and other customized injectors. The mixer is a metal fan driven by a motor that typically runs between 1000 rpm to 7000 rpm. Mixing is promoted with higher fan speeds.

Three out of the eight corner ports are used in this work, which include one intake port, one exhaust port, and one port to hold a pressure transducer (Kistler 6001 quartz dynamic transducer). The pressure transducer is connected to a Kistler 5010B charge amplifier to measure the vessel pressure. Seals (o-rings, c-rings, and dynamic seals) are installed on all window ports, corner ports, and on the injector assembly, igniter and mixing fan assembly.

The combustion vessel temperature is controlled by a closed-loop system, which is comprised of heaters and thermocouples. Sixteen cartridge heaters are installed into the stainless steel body from two opposite sides. Thermocouples are integrated near the cartridge heaters. The cartridge heaters can increase the combustion vessel to 200 ˚C. This temperature range is usually used for diesel spray experiments for minimum vaporization, also known as non-vaporizing sprays. The cartridge heaters are programmed to control the temperature increase at a rate of 1 ˚C per minute. This is to allow homogeneous increase in temperatures within the bulk stainless steel body, and avoid temperature gradients that may result in internal stresses.

Various subsystems of the combustion vessel are controlled through a process control software, called iTest, and a data acquisition system, called ADX. These two systems are developed in collaboration with A&D Technology. The iTest integrates a number of control actions that occur during a test routine into automatic procedures for repeatable and reliable operations. Example procedures include combustible mixture preparation, combustion vessel purging, and spray test execution. Important trigger signals are sent by iTest (for example, the injection trigger signal). iTest also monitors signals including the vessel body temperature, the vessel pressure, the injection system pressure, and the mixing vessel pressure. The ADX system provides channels to record a series of signals during the test, such as the vessel pressure history, ignition signals, injection signals, and etc. The ADX sampling rate is 100 kHz, which is enough for recording the aforementioned signals. Other signals that require higher sampling rates, such as primary and secondary current and voltage from an ignition coil, can be recorded using oscilloscopes.

To conduct a spray combustion test, the combustion vessel is checked for leak rates to ensure proper sealing and safety. Usually, higher vessel body temperatures help the seals expand for better sealing. Leak rate checking procedures are as follows:

1. Fill the combustion vessel with nitrogen at 100 psi, monitor the leak rate to achieve a leak rate no more than 6 psi/minute, with intake valve open and closed.
2. Fill the combustion vessel with nitrogen at 500 psi, monitor the leak rate to achieve a leak rate no more than 30 psi/minute, with intake valve open and closed.
3. Repeat step 1.
4. Fill the combustion vessel with nitrogen to 2000 psi, or the maximum pressure achievable by the nitrogen tank, monitor and record the leak rate.

3.2 Premixed Combustion for Thermodynamic State Generation

To achieve vessel temperatures higher than 200 ˚C, a premixed combustion is needed while the vessel temperature is maintained at temperatures above the room temperature for best sealing performance. The premixed combustion is called preburn, to distinguish it from the spray combustion event from spray injections. In the preburn, a gaseous mixture of acetylene (C_2H_2), hydrogen (H_2), nitrogen (O_2), and oxygen (O_2) is ignited. Turbulent combustion is assisted by the rotating mixing fan to improve the homogeneity of the temperature field in the vessel.

After the preburn, acetylene and hydrogen are consumed entirely and the mixture is left with carbon dioxide, water vapor, nitrogen, and oxygen if the preburn gas mixture has excessive oxygen. The preburn mixture can be customized to obtain an oxygen level ranging from 0% to 21% mole fraction after the preburn. By specifying the mole fraction of oxygen as P_{O_2}, the fractions of the four gases for the preburn are calculated by equations (1) through (4). The range of oxygen concentrations in the mixture can simulate different EGR levels in an engine.

$$C_2H_2 = 0.03 + \frac{0.02 \times (21 - P_{O_2})}{21} \quad (1)$$

$$H_2 = 0.0005 \quad (2)$$

$$O_2 = 0.0825 + 0.0096P_{O_2} + \frac{0.001}{2100}(P_{O_2})^2 \quad (3)$$

$$N_2 = 0.883 - 0.0095P_{O_2} - \frac{0.001}{2100}(P_{O_2})^2 \quad (4)$$

The preburn mixture is prepared in a ten-liter mixing vessel. The iTest system is used to track the partial pressures of constituent gases and control the pneumatic valves. The filling order of the constituent gases is acetylene, hydrogen, nitrogen, and oxygen (in the form of 40% oxygen in a nitrogen-oxygen mixture). The mixture partial pressures are checked for five minutes at the end of filling for each gas to allow the temperature of the mixture and the mixing vessel body to balance, thus avoiding inaccurate mixture composition caused by heat release through pressurizing.

A typical pressure curve recorded during the preburn and the cool down process is provided in Figure 3.2. To begin with, the combustion vessel is filled with a combustible mixture to a designated charge gas density, which remains virtually unchanged during the test except for limited leak rates. Five ignition signals are sent to the ignition coil and spark plug to ensure successful ignition. Preburn occurs in a fraction of a second. The vessel body temperature is maintained by the cartridge heaters and is lower than the flame temperature, thus heat transfer occurs between the high temperature gas and the vessel body, as shown by the drop down in vessel pressure. Both the vessel pressure and temperature drops down during the heat transfer process, which occur on the order of seconds. Along the drop down

of the vessel pressure, injection is triggered and a diffusion flame occurs that increases the vessel pressure again, which is on the orders of milliseconds. The duration of injection and combustion is three orders of magnitude smaller than the cool down process, thus the vessel pressure and temperature are considered stable for a spray combustion event.

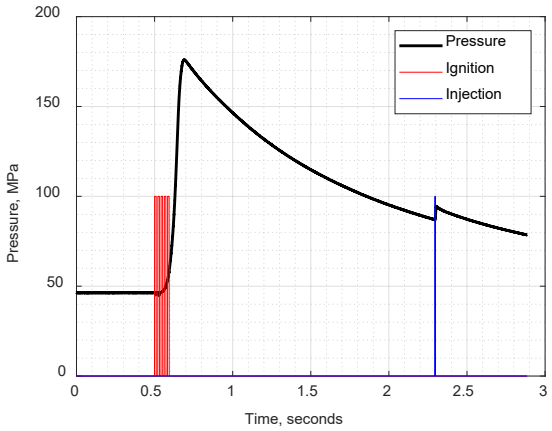

Figure 3.2. A typical pressure curve during the preburn and the cool down process, shown with ignition and injection signals.

The heat transfer that occurs between the preburn gas mixture after ignition and the vessel body creates a boundary layer about 1-2 mm, where a large temperature gradient exist. Inside the boundary layer, a uniform ($\pm$2%) temperature core region exist. The temperature gradient in the boundary layer creates a density gradient. The gas density of the core region is lower than that as calculated for the bulk of the gas mixture. A correction method provided by (Naber and Siebers 1996) is employed, shown as equation (5). In the equation, T_{core} is the core temperature in Kelvin, T_{bulk} is the bulk temperature in Kelvin, T_{wall} is the vessel body temperature in Kelvin, and ρ_{bulk} is the bulk gas density in kg/m^3. The charge gas densities and temperatures reported in this dissertation are all based on the core values.

$$\frac{T_{core}}{T_{bulk}} = 1 + \left(0.0406 \times \frac{\rho_{bulk}}{20.28}\right) \cdot \left(1 - \frac{T_{wall}}{T_{bulk}}\right) + 0.026 \cdot \left(\frac{T_{bulk}}{T_{wall}} - 1\right) \qquad (5)$$

3.3 High Pressure Fuel Injection System

A high pressure fuel injection system, shown in Figure 3.3, is utilized in this study. This system was initially designed and manufactured by Hydraulics International Inc. (Johnson 2009) and later customized at Michigan Technological University (Hughes and Schmidt 2016). Shown in the figure are its front operating panel, with a visible waste tank, fuel tank, two accumulators, regulators, valves, switches, and pressure gauges. On the side figure, a low pressure fuel outlet, a high pressure fuel outlet, and a return to the fuel tank port are shown.

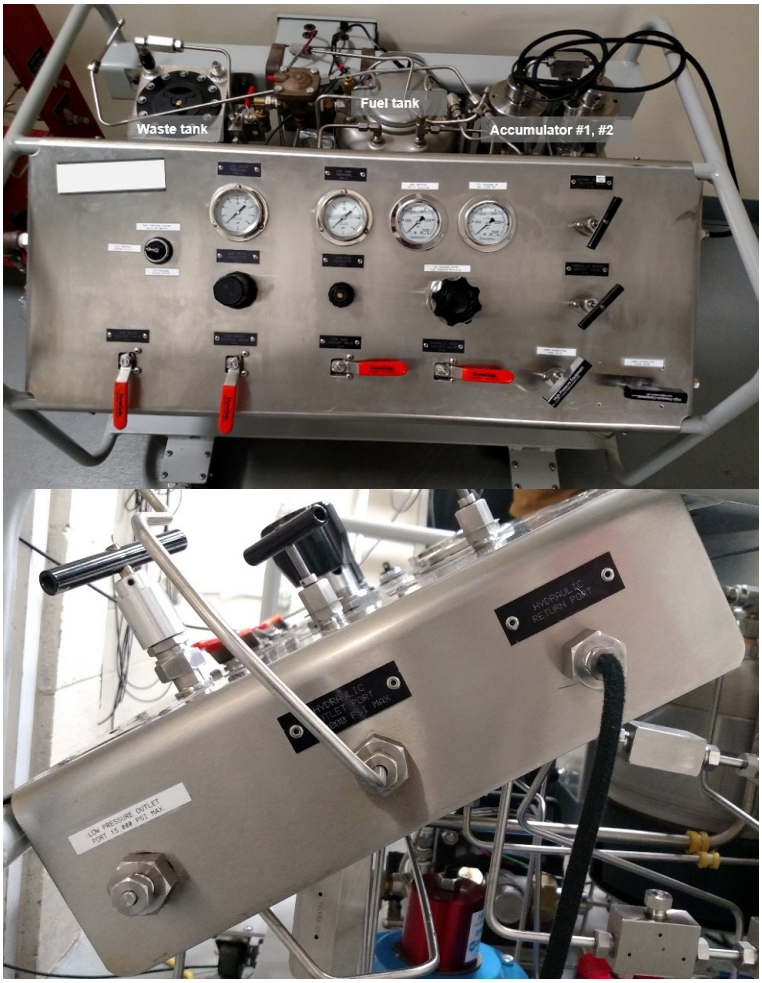

Figure 3.3. High pressure fuel injection system.

The fuel system utilizes a pump (Hydraulics International 5L-SD-600N) that operates on compressed air for pressure boosting. Compressed air pressure is regulated to achieve desired fuel outlet pressures. The pressurized fuel is stored in two 100-milliliter fuel accumulators that is filled from the bottom to the top. Two pressure transducers are mounted in the fuel system to monitor the fuel pressure and the signals are sent to iTest. The fuel system was designed for pressurizing liquid fuels to a pressure range of 6,000 psi to 60,000 psi. The operating range was extended to as low as 400 psi through addition of a fuel pressure regulator, a fuel pressure range selector, and tubing.

The fuel system is compatible with a multitude of liquid fuels. In this research, both a high reactivity gasoline and ULSD is used. A complete fuel switch is critical to the success of experimental investigations. Fuel switch is performed in the following general order and details procedures are found in (Hughes and Schmidt 2016):

1. Evacuate the remaining old fuel in the fuel tank to the waste tank, by pressurizing the fuel tank with compressed air. Wipe out the fuel residual in the fuel tank.
2. Fill new fuel into the fuel tank.
3. Flush new fuel through fuel lines up to the waste tank, by pressurizing the fuel tank with compressed air.
4. Flush new fuel through fuel lines up to the two accumulators.
5. Evacuate the remaining old fuel in the accumulators to the waste tank with compressed air, after which the accumulators are filled with air.
6. Flush new fuel through the accumulators through the low pressure system.
7. Flush new fuel through the low pressure system pressure relief valve.
8. Flush new fuel through the high pressure system.
9. Flush new fuel through the high pressure tubing up to the adapter to the fuel injector.
10. Flush the injector by performing repeated injections (recommended over hundreds of injections).

3.4 Injector and Injector Assembly

The injector used in the current study is a Cummins ISX injector (PN 2897320NX) as shown in Figure 3.4. The injector is a central axis, single-hole, solenoid driven, and hydraulic lifted injector. The injector specifications are shown in Table 3.1. The injector has a side feed, which is connected to the fuel system through a side feed fixture. Fuel return is through a hole on the side of the injector upstream of the side feed, although not explicitly shown. The return hole is covered by a ring fixture. The injector is fixed on to a metal window during the testing through an injector hold-down fixture. The side feed fixture, the fuel return ring, and the injector hold-down fixture are shown in Figure 3.5.

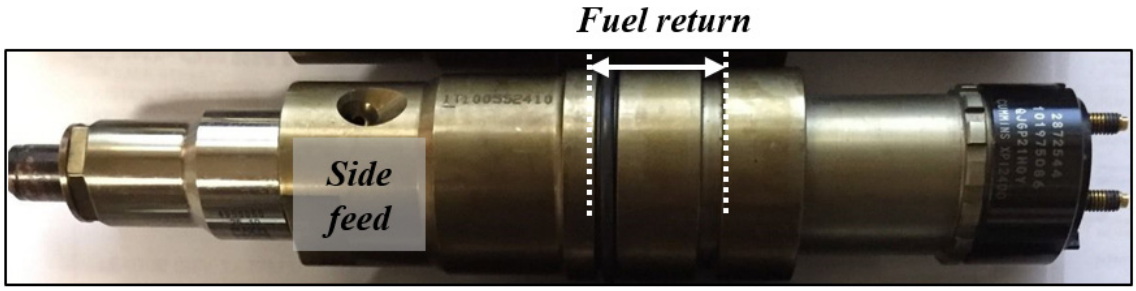

Figure 3.4. Cummins ISX injector, PN 2897320NX.

Table 3.1. Injector specifications.

Outlet Diameter (μm)	176
K-factor	1.8
Cd (Re = 12,000)	0.94

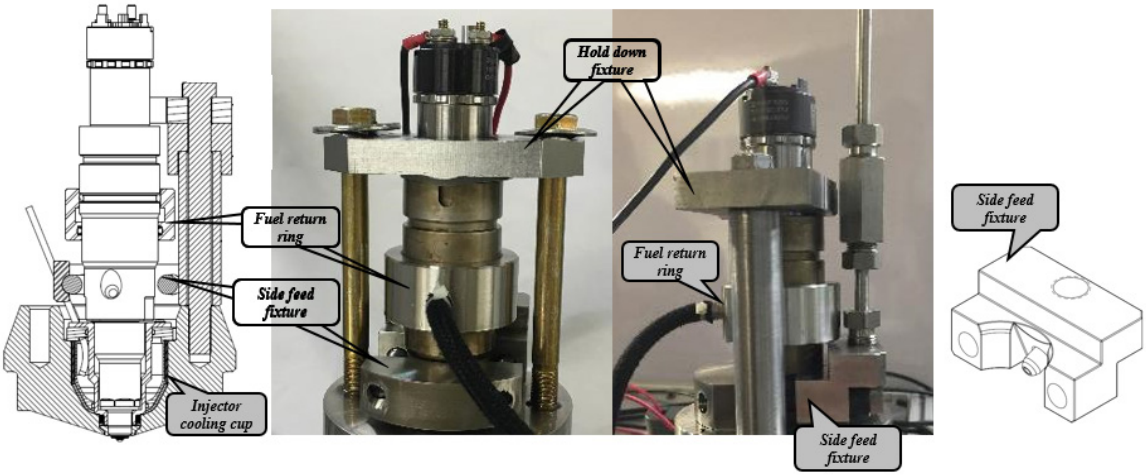

Figure 3.5. Illustration of the injector fixture assembly.

In Figure 3.5, the injector hold-down fixture is shown as single-sided. This design was susceptible to creating an uneven load on the copper seal and thus was difficult in sealing the combustion vessel. The hold-down fixture was later updated to double-sided shown on the photos of Figure 3.5. The torque for the hold-down fixture is 14-17 ft·lb. The side feed fixture is bolted with a torque of 15 N·m. A cooling cup is shown on the cross sectional view of the injector fixture assembly to maintain the injector body temperature close to normal operations on engines. Working fluids are recirculated through the cup by a Fisher Scientific IsoTemp3016D unit. When the combustion vessel is set at 180 ˚C for preburn tests, 1:1 by volume of distilled water and ethylene glycol is used as a coolant. When the combustion vessel is set at 50 ˚C for non-preburn tests, a XIA PMX 200 silicon fluid of 50 cSt is used to heat up the injector.

The injector driving current is shown in Figure 3.6. The boost voltage is 50 V. A MOSFET (metal-oxide-semiconductor field-effect transistor) driver driven by a pulse generator controls the injector driving current. The driving current is a replicate of the one used on production engines.

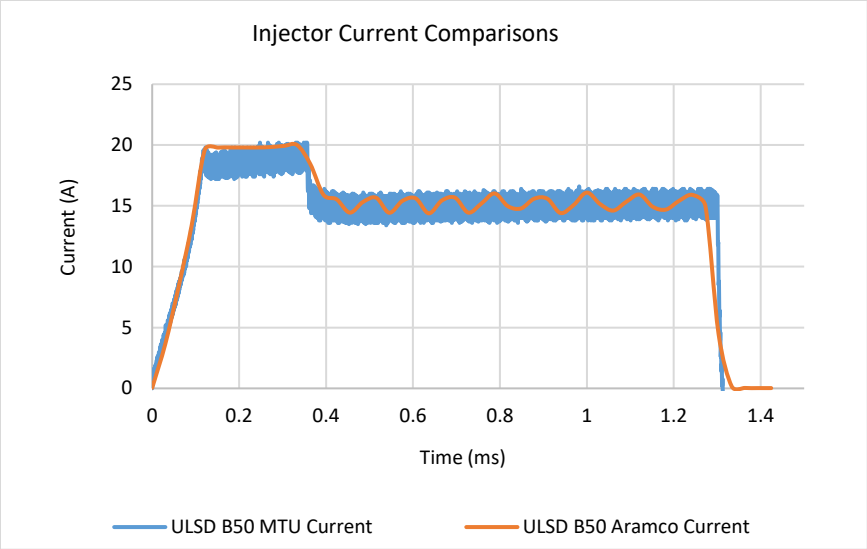

Figure 3.6. Injector driver current.

3.5 Diagnostics and Signal Processing Methods

Optical diagnostics and combustion vessel pressure are two main types of diagnostics in the experiment. Different optical diagnostics are used to visualize non-reacting and reacting sprays. For non-reacting sprays in low ambient temperatures, a shadowgraph imaging technique is used. For non-reacting, vaporizing sprays, a near-simultaneous shadowgraph/Mie scattering technique is used. For reacting sprays, both OH* chemiluminescence and flame natural luminosity diagnostics is used. These optical diagnostics are shown and discussed in this section.

3.5.1 Shadowgraph

Sprays in a gaseous environment create local density gradients, which affects the local refractive index. Refractive index is the ratio of the speed of light traveling in the medium to the speed of light traveling in vacuum. Upon entering a medium with higher refractive of index, an oblique light beam will bend toward the medium with a higher refractive index. Shadowgraph and Schlieren are two similar techniques that detect local density gradients. The Schlieren technique share almost the same optical setup as the shadowgraph technique, except that a sharp edge stop is place in front of the imaging camera lens at the focal point of the focusing optics. In theory, the shadowgraph technique detects the second derivative of density, while the Schlieren technique detects the first derivative of density (Settles 2001). The advantage of Schlieren technique is that the detection sensitivity is easily changed by the level of cut-off by the sharp edge stop, while the shadowgraph sensitivity is mostly dependent on the optical path length. The sharp edge stop, however, affects the directional sensitivity of the Schlieren system, whereas the shadowgraph system is uniform

in the directional sensitivity. In addition, a trade-off exist in the Schlieren system between the overall image brightness and the detection sensitivity.

For non-reacting spray tests under low ambient temperatures, a modified Z-type shadowgraph imaging technique is used and shown in Figure 3.7. All components in the optical setup placed on the same height at the center of the combustion vessel. The light path between the parabolic concave mirror and the plane mirror is parallel to the combustion vessel axis, while covering the entire optical window. The reflected light beam from the plane mirror should be orthogonal to the incident light beam.

An LED (light emitting diode) light source is focused onto a mechanical iris diaphragm, which serves as a point light source. The iris diaphragm is placed near the focal point of the concave mirror to create a collimated bean of light, although it should not interfere with the light beam and affect the imaging object. Thus a small acute angle is formed between the light path from and to the parabolic concave mirror. The collimated light beam passes then through the combustion vessel and gets reflected by the plane mirror onto another parabolic concave mirror, which is then reflected onto the high speed camera sensor through a bi-concave lens and a camera lens. The bi-concave lens is used to assist the camera lens in focusing. The bi-concave lens is placed concentric with the camera lens.

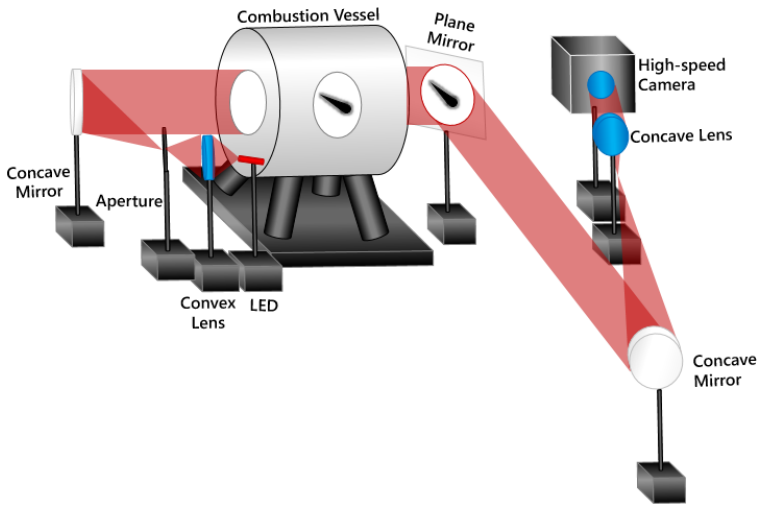

Figure 3.7. Optical setup for the shadowgraph imaging technique.

A high speed camera Photron Fastcam SA 1.1 is used to capture the spray image. A Nikon 85 mm f/1.4 camera lens is used. Two frame rates are used in the non-reacting sprays under low ambient temperatures, including a lower frame rate at 25,000 frames per second (fps) to cover the entire field of view and a higher frame rate at 100,000 fps to cover a limited portion near the injector tip, in which early portions of the spray development and the injector hydraulic delay can be captured more effectively. The injector hydraulic delay is defined as the duration from the onset of electronic injection signal to the onset of fuel spray in the high speed video.

Sample shadowgraph images are provided in Figure 3.8. The shadowgraph under a non-preburn condition exhibit clear backgrounds that is characteristic of a quiescent gaseous environment.

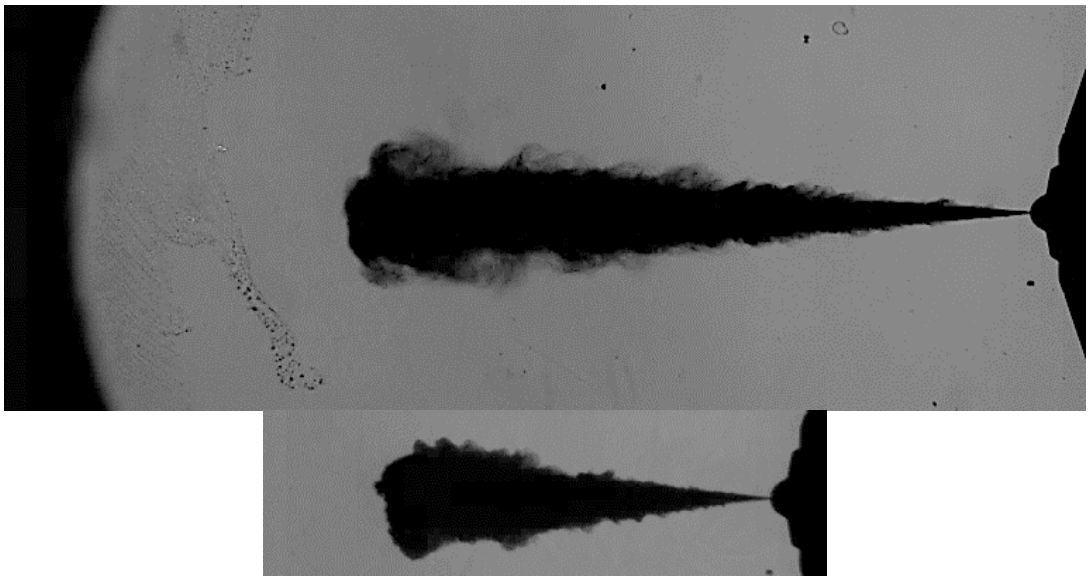

Figure 3.8. Sample shadowgraph images from the spray test (upper: 25,000 fps, lower: 100,000 fps).

3.5.2 Near-simultaneous Shadowgraph/Mie Scattering

In non-reacting, vaporizing spray tests, sprays are injected into a high temperature environment and then vaporize. A liquid core still exist in the upstream of the spray jet. The vapor phase of the spray jet is visualized through the shadowgraph technique, while the liquid phase of the spray jet is visualized through the Mie scattering technique. Fundamentals of the shadowgraph technique was shown in section 3.5.1. Mie scattering is the elastic scattering of light by particles that are larger in size compared to the wavelength of the incident light. Similarly, Rayleigh scattering is also the elastic scattering of light, only by particles that are smaller than about one-tenth of the wavelength of the incident light (Lockwood 2014). Two common natural phenomena are associated with these two scattering mechanisms, with the blue color of the sky explained by Rayleigh scattering, and the white color of the cloud explained by Mie scattering.

Mie scattering can be achieved by light sources from different directions relative to the observing direction. In this study, the Mie scattering optical setup is shown in Figure 3.9, which is orthogonal to the observing direction. A convex lens is placed in front of the LED light source to increase the light intensity. The rest of the shadowgraph optical setup is based on the shadowgraph optical setup in section 3.5.1, only with an additional shadowgraph sharp edge stop at the focal point of the parabolic concave mirror.

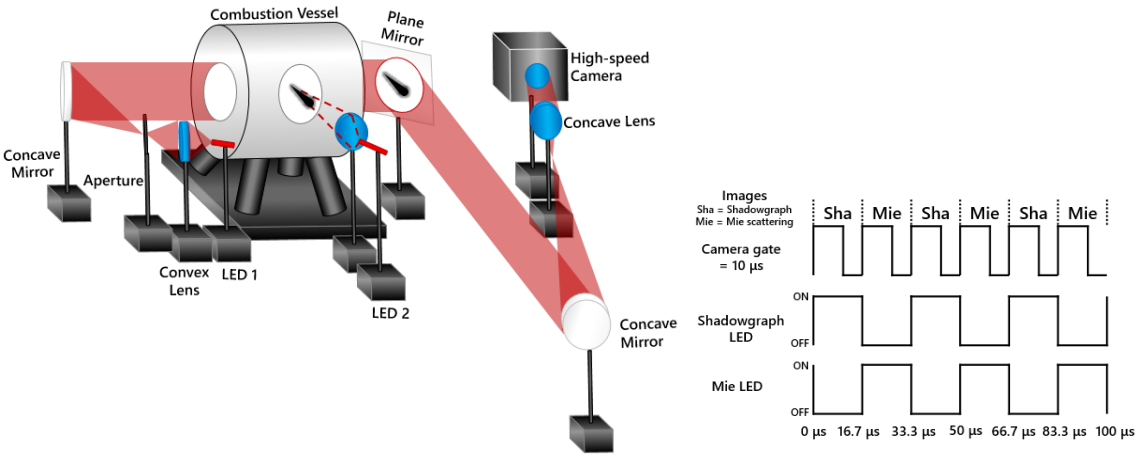

Figure 3.9. Optical setup for the near-simultaneous shadowgraph/Mie scattering technique.

The near-simultaneous shadowgraph/Mie scattering technique was seen in previous investigations (Parrish and Zink 2012, Zhang et al. 2014). The two LED light for shadowgraph and Mie scattering are programmable by using pulse generators. Their burst sequence are shown in Figure 3.9. The burst waves for the shadowgraph LED and the Mie LED are the same, only phase shifted by half a cycle. The high speed camera captures the video with double the frequency of the LED light. In this study, 60,000 fps is used, which is equivalent to a 30,000 fps for either optical diagnostics. Although a 16.7 µs phase shift exist between the two diagnostics, it is two orders of magnitude smaller than injection durations, which is effectively near-simultaneous. This enables investigating the vapor and liquid phases from the same spray injection and thus avoid the complication of shot-to-shot differences that is common in spray experiments.

Sample shadowgraph and Mie scattering images are shown in Figure 3.10. The shadowgraph image in preburn tests exhibit noisy backgrounds filled with wrinkles, and it is different than the clear background exhibited by the shadowgraph image as shown in Figure 3.8. This is due to the turbulence generated by the mixing fan, which assists premixed combustion to achieve homogeneous temperature distributions. Although the noisy background makes it challenging to directly visualize the spray plume, it can be visualized by image processing techniques, which will be discussed in the next chapter.

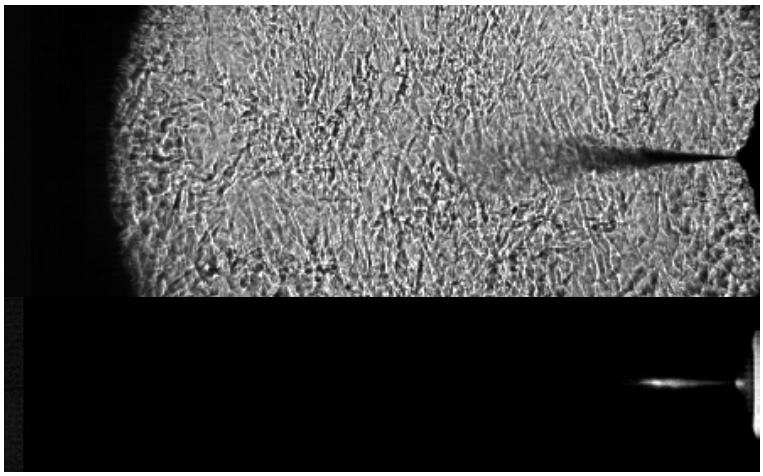

Figure 3.10. Sample shadowgraph (upper) and Mie scattering (lower) images.

3.5.3 OH* Chemiluminescence, Natural Luminosity, Photodiode, and Vessel Pressure

In reacting sprays, a greater multitude of the spray characteristics associated with the ignition, heat release, flame lift-off, and sooting intensity are captured by both optical diagnostics and pressure-based diagnostics. The diagnostics setups are shown in Figure 3.11. Optical diagnostics include the OH* chemiluminescence, natural luminosity, and a broadband photodiode. The combustion vessel pressure is also recorded by the pressure transducer (Kistler 6001).

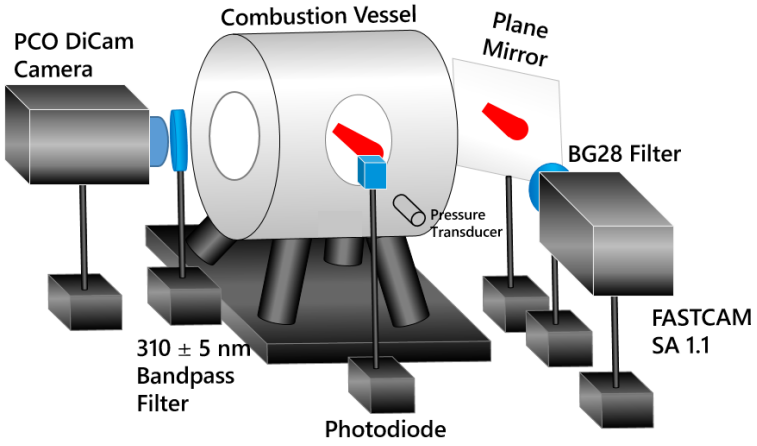

Figure 3.11. Diagnostics setups in for reacting spray tests.

The OH* radical is generated primarily through a kinetic pathway of $CH+O_2 \rightarrow CO+OH^*$, which is an indicator of high temperature stoichiometric combustion reaction. Chemiluminescence emission and collisional quenching occurs when the excited state OH*

radical returns to the ground state. The OH* chemiluminescence has been utilized to study the lift-off behavior of a reacting spray flame (Higgins and Siebers 2001, Siebers and Higgins 2001). The OH* chemiluminescence spans through a range of wavelengths, and the strongest intensity occurs near 310 nm, which is in the ultraviolet range (Ikeda, Kojima, and Hashimoto 2002).

In the experiment, the OH* chemiluminescence is captured using an intensified CCD (charge-coupled device) camera, whose CCD captures wavelengths in the ultraviolet range. A Jenoptik 105 mm f/4 UV camera lens is used. A bandpass filter of 310 ± 5 nm is placed in front of the camera lens. The ICCD (intensified CCD) camera takes a single image from the start of injection to the end of combustion, which effectively takes a time-integrated chemiluminescence image. Lift-off length of a flame remains steady during the combustion, as shown by investigations of high speed OH* chemiluminescence (Maes et al. 2016). The intensifier is turned on to enhance the signal intensity level while preventing saturation.

Natural luminosity is comprised of chemiluminescence from combustion reactions and soot incandescence. The contribution from the chemiluminescence is 4-5 orders of magnitude smaller compared to soot incandescence, thus natural luminosity is a strong indicator of the occurrence of soot, and has been qualitatively linked to soot concentrations (Mueller and Martin 2002). Natural luminosity is broadband in wavelength. In this work, the high speed camera is used to capture the natural luminosity at a frame rate of 30,000 fps, using a Nikon 85 mm lens. A BG28 filter is used in front of the camera lens to suppress the high luminosity content. A baseline f/5.6 and 5.59 μs is used for the experiment, however, the f-stop numbers and shutter durations were adjusted according to different luminosity levels to prevent major pixel saturation.

Sample OH* chemiluminescence and natural luminosity images are shown in Figure 3.12.

A broadband (350-1100 nm) photodiode Thorlabs DET36A is used to record the total luminosity in the test as another optical-based ignition delay measurement. The photodiode is used with a Thorlabs PDA 200 benchtop photodiode amplifier. The photodiode amplifier setup was adjusted to ensure saturation of the signal during soot oxidation (Pickett and Hoogterp 2008). A pressure-based ignition delay measurement is performed by recording the pressure in the combustion vessel.

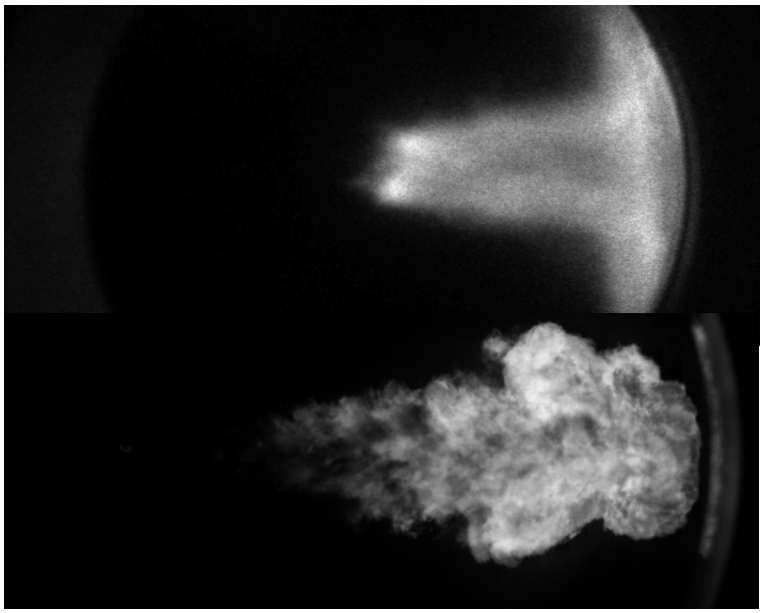

Figure 3.12. Sample OH* chemiluminescence image (upper), and natural luminosity image (lower).

4 Experimental Studies

4.1 Low Temperature Non-reacting Sprays [1]

4.1.1 Experimental Conditions

Low temperature non-reacting sprays are performed to understand the spray characteristics as a function of fuel properties, without influence from vaporization. The test conditions are shown in Table 4.1. The charge gas temperature is set at 323 K to prevent major extensive vaporization of the high reactivity gasoline during spray injection. A comparison of the ambient charge gas temperature to the distillation curves of the two fuels is shown in Figure 4.1. The spray injections are triggered under five charge gas densities, covering a range from mid-load CI engine operations to beyond typically expected conditions. Three injection pressures are used, including 100, 150, and 250 MPa. Three repeats are performed under each experimental condition.

Table 4.1. Low temperature non-reacting sprays experimental condition.

Injection Pressure (MPa)	100		150		250
Charge Gas Temperature (K)	323				
Charge Gas Density (kg/m^3)	10.3	22.8	31.3	52.5	166.5
Charge Gas	Nitrogen				
Fuels	ULSD		High Reactivity Gasoline		

[1] The material contained in section 4.1 was previously published as the following conference paper and presented at the 29th Annual Conference on Liquid Atomization and Sprays - ILASS Americas 2017. The authors own the copyright of the following paper, according to the copyright statement from the Institute for Liquid Atomization and Spray Systems, as attached in the Appendix A.1.

- Tang, M., Zhang, J., Menucci, T., Schmidt, H., Lee, S-Y., Naber, J., Tzanetakis, T., "Experimental Investigation of Spray Characteristics of High Reactivity Gasoline and Diesel Fuel Using a Heavy-Duty Single-Hole Injector, Part I: Non-Reacting, Non-Vaporizing Spray", 29th Annual Conference on Liquid Atomization and Sprays - ILASS Americas 2017, Atlanta, Georgia, May 15-18, 2017.

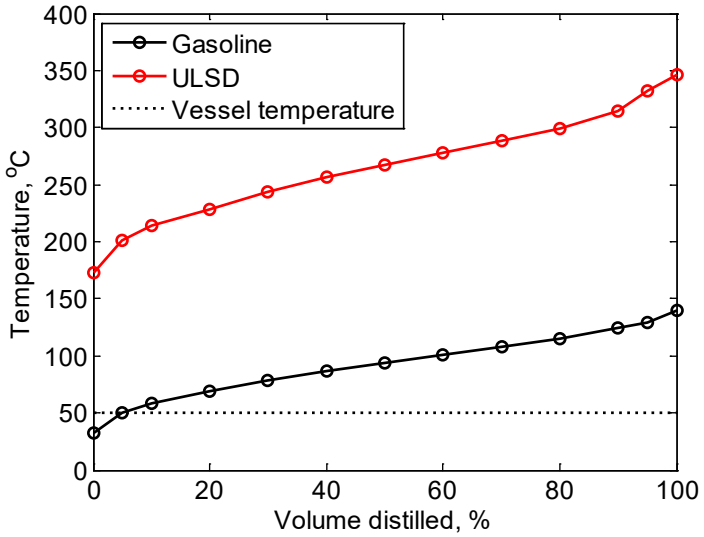

Figure 4.1. Distillation temperatures of high reactivity gasoline and ULSD compared to the vessel temperature during the test.

4.1.2 Data Processing Methods

Experimentally obtained images are analyzed to obtain the spray characteristics that include spray penetration and spray dispersion angle. The processing methods are shown in Figure 4.2, which includes the following procedures:

1. Read in image data from an 8 bit gray scale uncompressed file.
2. Perform background subtractions.
3. Apply thresholds to grayscale images to obtain binary images. The threshold is selected as 5% of the upper limit of pixel intensity (255).
4. Perform boundary tracking and identifying the spray penetration. The spray penetration corresponds to a distance downstream of the injector tip where the area between accounts for 99% of the total spray envelope area.
5. Identify the spray dispersion angle by performing a linear fit on either side of the spray plume boundary from the injector tip to 60% of the spray penetration distance. The spray dispersion angle is defined by the angle enclosed by the two linear fits.

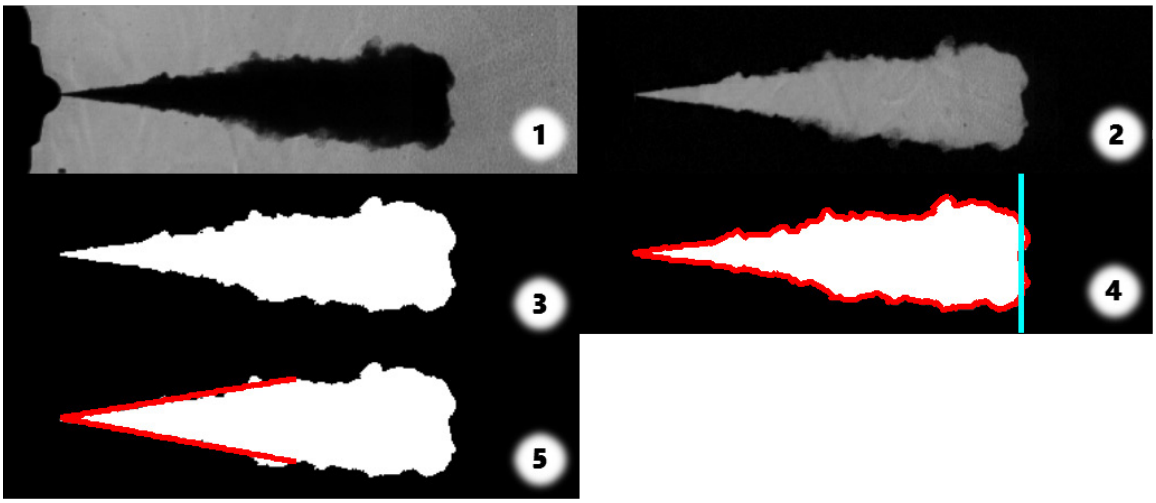

Figure 4.2. Illustration of the shadowgraph image processing workflow.

These procedures are implemented in a MathWorks® MATLAB® program. Spray penetrations and dispersion angles are obtained for each frame and are plotted against time after start of injection. Sensitivity of the spray penetration and dispersion angle to the thresholds used are tested by increasing and decreasing the threshold value by 20%, the results of which are shown in Figure 4.3. The sensitivity analyses show that the processing methods used are threshold-insensitive.

During testing, three repeats are performed under each test condition and ensemble averaged results are acquired. Note that when the spray penetration is plotted against the time after start of injection, as shown in Figure 4.4 (a), the data acquired from the two distinct frame rates used is not aligned because of the finite time difference between the first captured images in each case. In addition, the high speed camera cannot capture the exact start of injection which occurs between frames. Thus, alignment is required not only to match the results from the two frame rates used, but also to enable comparison between different conditions. The alignment is done via the following two procedures as shown in Figure 4.4 (b) and (c):

1. Fit the original penetration curves in Figure 4.4 (a) to equation $y = a\sqrt{b \cdot (t - c)}$. The 25,000 fps curve is shifted to the left by the fitted $\boldsymbol{c}$ term.
2. Fit the linear portion of the 100,000 fps curve to equation $y = d \cdot (t - e)$. Both penetration curves are shifted to the left by the fitted $\boldsymbol{e}$ term. A zero point is added to both penetration curves.

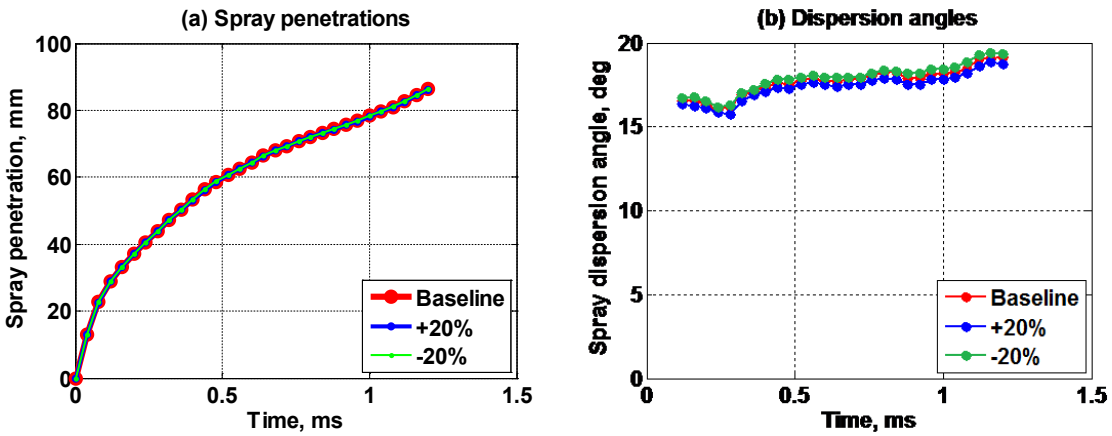

Figure 4.3. Sensitivity of the spray penetration and dispersion angle to the thresholds used in image processing.

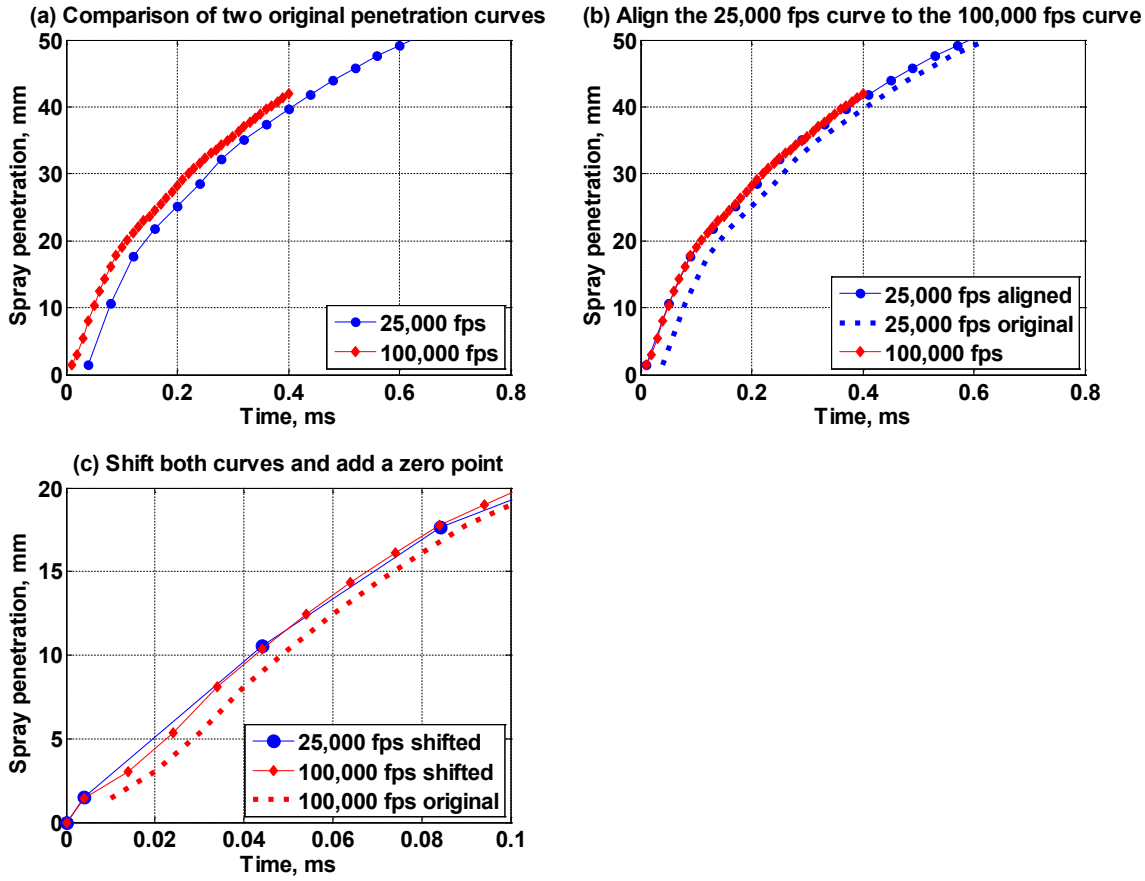

Figure 4.4. Methods for shifting the two penetration curves.

The two equations in steps 1 and 2 above are based on the square root and linear dependence of spray penetration at different times after start of injection as shown by Naber and Siebers (Naber and Siebers 1996). The shifted penetration curves in Figure 4.4 (c) are compared in the results and discussion.

4.1.3 Results and Discussions

4.1.3.1 Spray Dispersion

Fuel effects on spray dispersion angles are compared in Figure 4.5 using ensemble-averaged data. The average values and error bars are calculated as the mean and standard deviation of the spray dispersion angles from 0.4 ms after start of injection (ASOI) to 0.2 ms before end of injection for the three repeat tests, respectively. The error bars therefore indicate overall test repeatability.

The main observation from Figure 4.5 with respect to fuel effects is that the high reactivity gasoline exhibits an equal or larger mean spray dispersion angle under most of the test conditions. All gasoline cases with 250 MPa injection pressure show larger dispersion angle than ULSD, three points of which have error bars smaller than the differences observed. Under 100 and 150 MPa injection pressures, the general trend of equal or larger gasoline dispersion angle versus ULSD is maintained except for the highest charge gas density cases under both injection pressures, where there is significant overlap in the error bars.

Spray dispersion angle is related to ambient gas entrainment during injection, as well as possible fuel vaporization. Dimensional analysis on spray dispersion angles often relates the data to charge gas densities, injection pressures, hydraulic diameters and times after start of injection (Klein-Douwel et al. 2009). Non-dimensional analysis of spray dispersion angles relates the half-angle tangent to the ratio of densities between ambient charge gas and fuel as expressed in equation (6) (Naber and Siebers 1996).

$$tan\left(\frac{\theta}{2}\right) = a \cdot \left(\frac{\rho_a}{\rho_f}\right)^b \qquad (6)$$

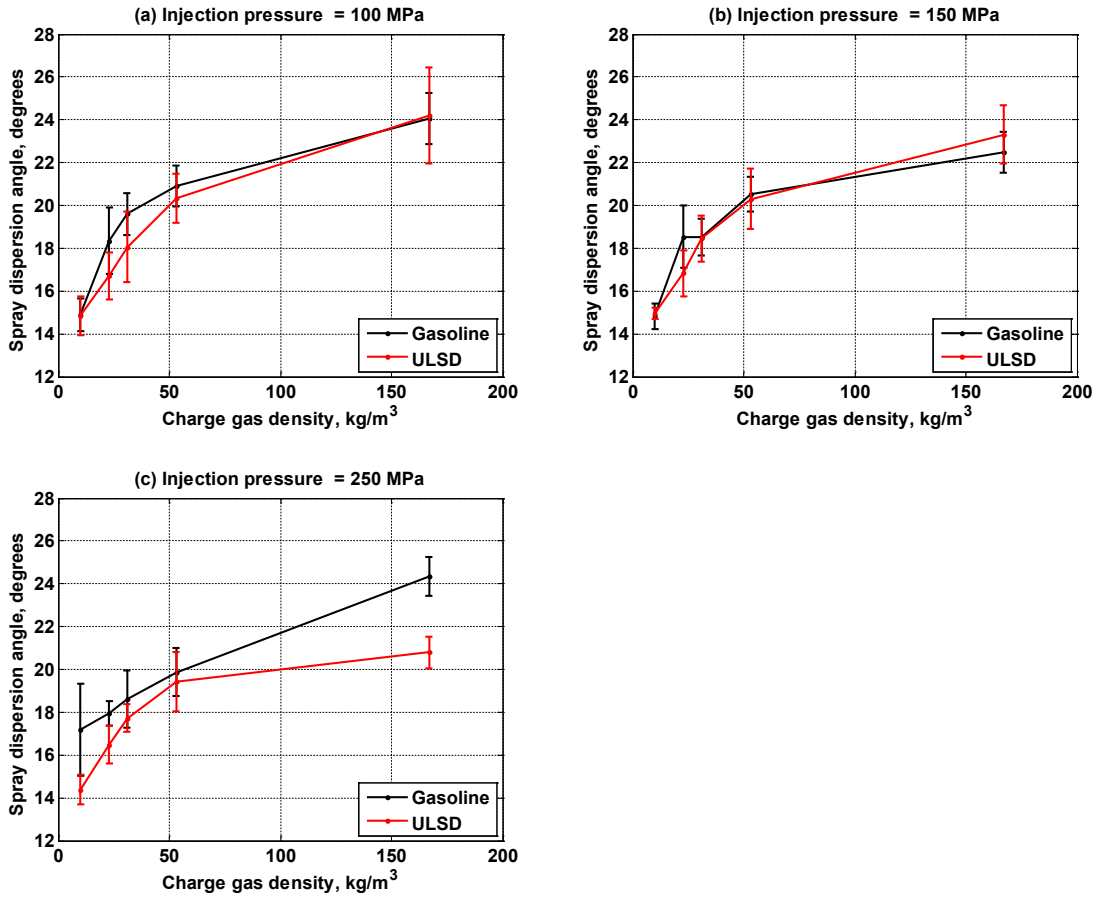

Figure 4.5. Spray dispersion angle vs. charge gas density at injection pressures of (a) 100 MPa, (b) 150 MPa, and (c) 250 MPa.

Non-dimensional analysis of the spray dispersion angles for gasoline and ULSD are shown in Figure 4.6. Data from all three injection pressures are plotted on a log-log scale. It is observed that gasoline and ULSD follow a similar trend. Upon fitting all data to equation (6), a = 0.26 and b = 0.15. Attempts to fit gasoline and ULSD separately to equation (6) resulted in $a_{gasoline} = 0.26$, $a_{ULSD} = 0.26$, $b_{gasoline} = 0.14$, $b_{ULSD} = 0.16$. The three fitted lines are plotted in Figure 4.6. These results confirm that the trends in the two data sets are very close and can thus be effectively collapsed onto a single correlation. The difference in dispersion angle between gasoline and ULSD is therefore mainly explained by the difference in fuel density. There may also likely be some vaporization for the gasoline. The results also suggest that some other minor factors might be responsible for the difference in fitted power used between the fuels. Relevant physical properties that could affect dispersion angle include boiling point and viscosity. Also plotted in Figure 4.6 is a dispersion angle band of +1˚ based on the gasoline fit and -1˚ based on ULSD fit. The majority of data is scattered between the upper and lower bands.

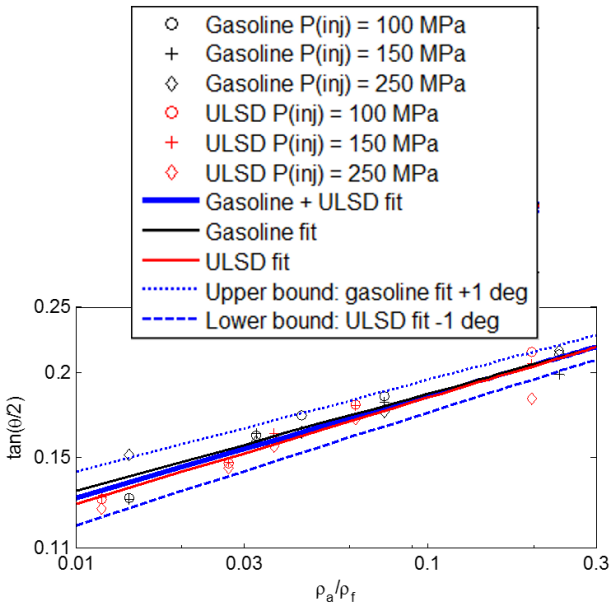

Figure 4.6. Spray dispersion angle vs. charge gas density at injection pressures of (a) 100 MPa, (b) 150 MPa, and (c) 250 MPa.

Other observations with respect to spray dispersion angles is the effect of injection pressures. Figure 4.7 shows a plot of the spray dispersion angles versus injection pressures. In general, injection pressures have little effects on spray dispersion angles, although in some special cases a slight decreasing trend with respect to injection pressures is observed. This observation is in line with a number of researches (Naber and Siebers 1996, Payri, Desantes, and Arrégle 1996, Arrègle, Pastor, and Ruiz 1999, Klein-Douwel et al. 2009).

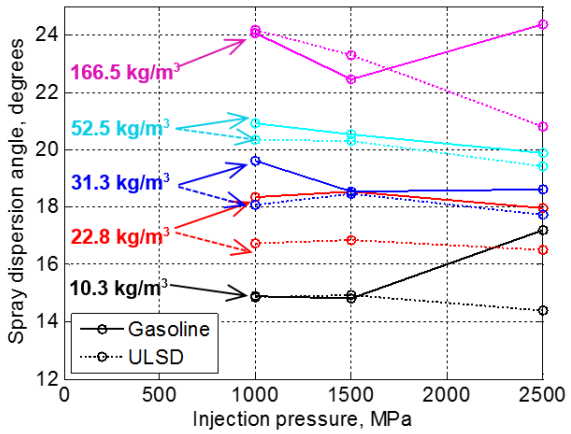

Figure 4.7. Spray dispersion angle vs. injection pressures for all five charge gas densities.

4.1.3.2 Spray Penetration

Fuel effects on the spray penetration are shown in Figure 4.8 for all charge gas densities and injection pressures. The main observation from Figure 4.8 is that ULSD has faster penetration compared to gasoline under the same injection pressure and charge gas conditions. A correlation for spray penetration by Naber and Siebers (Naber and Siebers 1996) is given by equation (7) in its dimensional form. In this equation S is the spray penetration, C_v is the velocity coefficient, C_a is the area contraction coefficient, a is a term set to 0.66 (Naber and Siebers 1996), P_f is the fuel pressure, P_a is the ambient charge gas pressure, ρ_a is the ambient charge gas density, d_o is the orifice diameter, and t is the time.

$$S = \sqrt{\frac{C_v \cdot \sqrt{2 \cdot C_a}}{a \cdot tan(\theta/2)}} \cdot \sqrt{\sqrt{\frac{(P_f - P_a)}{\rho_a}} \cdot d_o \cdot t} \qquad (7)$$

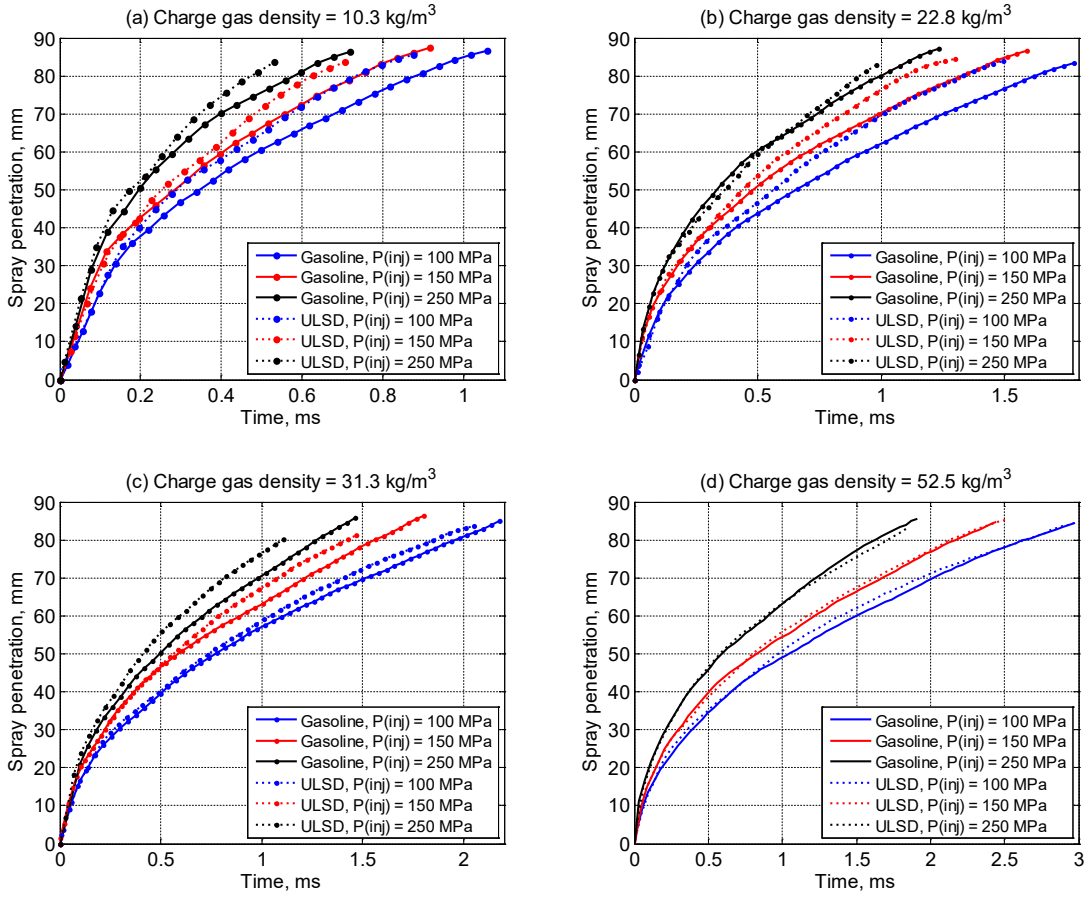

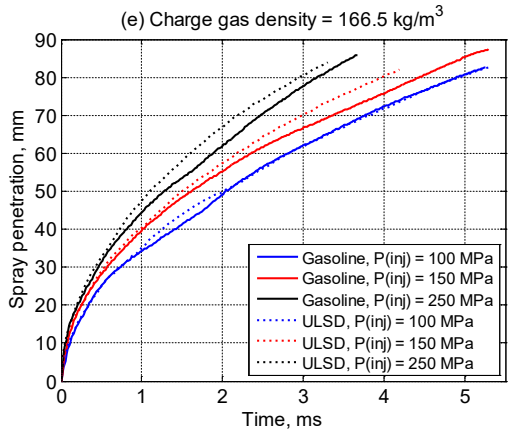

Figure 4.8. Spray penetration vs. time ASOI under charge gas densities of (a) 10.3 kg/m^3, (b) 22.8 kg/m^3, (c) 31.3 kg/m^3, (d) 52.5 kg/m^3, and (e) 166.5 kg/m^3.

From this correlation, it is evident that fuel properties have no direct influence on the spray penetration. The second term remains the same regardless of the fuel, thus any differences in spray penetration due to fuel properties are attributed to the first term. A larger first term is expected for ULSD compared to gasoline. As previously discussed, gasoline exhibits a larger dispersion angle than ULSD under most conditions. This leads to a smaller first term, assuming that the flow coefficients are independent of the fuel. Therefore, the spray penetration rate for gasoline is expected to be slower than ULSD.

Evidence from non-dimensional spray penetration analyses also supports this observation. Spray penetrations can be non-dimensionalized by using a length scale as given by equation (8) and a time scale as given by equation (9). The non-dimensional form of the Naber and Sieber's spray penetration correlation (Naber and Siebers 1996) is therefore given by equation (10). In this equation, x^+ is the length scale to normalize the spray penetration, t^+ is the time scale to normalize the time vector, $\tilde{t}$ is the non-dimensional time, $\bar{S}$ is the non-dimensional spray penetration, ρ_f is the fuel density.

$$x^+ = \frac{\sqrt{C_a} \cdot d_0 \cdot \sqrt{\rho_f/\rho_a}}{a \cdot tan(\theta/2)} \tag{8}$$

$$t^+ = \frac{\sqrt{C_a} \cdot d_0 \cdot \sqrt{\rho_f/\rho_a}}{a \cdot tan(\theta/2) \cdot C_v \sqrt{2 \cdot (P_f - P_a)/\rho_f}} \tag{9}$$

$$\tilde{t} = \frac{\tilde{S}}{2} + \frac{\tilde{S}\sqrt{1+16\tilde{S}^2}}{4} + \frac{ln\left(4\tilde{S} + \sqrt{1+16\tilde{S}^2}\right)}{16} \tag{10}$$

Comparison of the non-dimensional spray penetration of ULSD and gasoline for a charge gas density of 22.8 kg/m^3 and an injection pressure of 100 MPa is shown in Figure 4.9. The non-dimensional spray penetration of ULSD and gasoline collapse onto the same line representing the correlation. Data below a normalized time of 1 is limited by the charge gas densities considered in this work which do not go below 10 kg/m^3. Since the length

and time scales used to non-dimensionalize the spray penetration both include fuel density, any differences caused by this property are cancelled out. Note that the analysis is performed assuming the same area contraction and velocity coefficients between the two fuels.

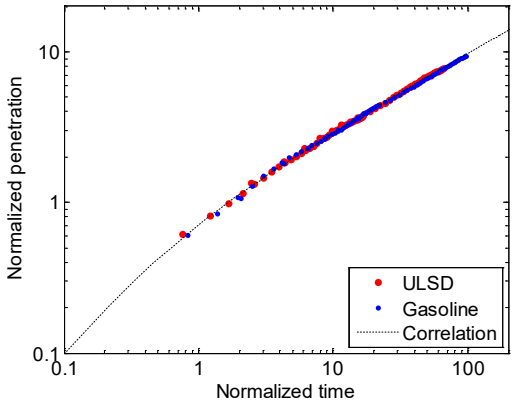

Figure 4.9. Comparison of normalized penetration versus normalized time between ULSD and gasoline for a charge gas density of 22.8 kg/m^3 and an injection pressure of 100 MPa.

When examining individual test sets in Figure 4.5, some cases show a deviation from the general trend of larger ULSD penetration rate, including the following cases exhibiting equal or faster penetration for gasoline compared to ULSD:

1. Penetrations prior to 0.1 ms, under a charge gas density of 10.3 kg/m^3 and an injection pressure of 150 MPa.
2. Penetrations prior to 0.6 ms, under a charge gas density of 22.8 kg/m^3 and an injection pressure of 250 MPa.
3. Penetrations prior to 0.8 ms, under a charge gas density of 52.5 kg/m^3 and an injection pressure of 150 MPa.
4. Penetrations after 1.0 ms, under a charge gas density of 52.5 kg/m^3 and an injection pressure of 250 MPa.
5. Penetrations after 2.0 ms, under a charge gas density of 166.5 kg/m^3 and an injection pressure of 100 MPa.

A direct comparison of spray dispersion angles at all these cases is shown in Table 4.2. For the cases where gasoline has equal or faster penetration than ULSD, the spray dispersion angles are very close to each other, except for case 2.

Table 4.2. Spray dispersion angle comparisons for equal or larger gasoline spray penetrations than ULSD.

Case No.	1	2	3	4	5
Dispersion: Gasoline (˚)	14.8	18.0	20.5	19.9	24.1
Dispersion: ULSD (˚)	15.0	16.5	20.3	19.4	24.2

The above analysis shows that fuel effects impact spray penetration mainly through the difference in spray dispersion angle. This is based on both the general trends of faster ULSD spray penetration compared to gasoline and results from the special cases of equal or slower ULSD spray penetration.

4.1.4 Summary

As a general trend, it was observed that high reactivity gasoline exhibits larger spray dispersion angles and slower spray penetration than ULSD, although several cases exist that do deviate from this behavior. It was found that fuel effects on spray dispersion and spray penetration are mainly reflected in the difference in fuel density. Vaporization might also play a role for high reactivity gasoline injections under these conditions because of its high volatility. It is also believed that other fuel parameters, including viscosity, likely play a minor role compared to fuel density in influencing spray injection characteristics under these conditions. However, further analyses considering the effect of fuel properties on the velocity and area contraction coefficients will be needed to understand these influences in greater detail.

4.2 Non-reacting, Vaporizing Sprays [2]

4.2.1 Experimental Conditions

The experimental conditions are listed in Table 4.3. Charge gas conditions are based on the conditions found in a HD diesel engine for a wide range of injection timings. Variables include charge gas temperature, charge pressure, injection pressure, and fuel type. In Table 4.3, the change in charge density is achieved by changing the charge temperature at a constant charge pressure. Two repeats are performed under each test condition. Ensemble

[2] The material contained in section 4.2 was previously published as the following conference paper and presented at the 29th Annual Conference on Liquid Atomization and Sprays - ILASS Americas 2017. The authors own the copyright of the following paper, according to the copyright statement from the Institute for Liquid Atomization and Spray Systems, as attached in the Appendix A.1.

- Zhang, J., Tang, M., Menucci, T., Schmidt, H., Lee, S-Y., Naber, J., Tzanetakis, T., "Experimental Investigation of Spray Characteristics of High Reactivity Gasoline and Diesel Fuel Using a Heavy-Duty Single-Hole Injector, Part II: Non-Reacting, Vaporizing Spray", 29th Annual Conference on Liquid Atomization and Sprays - ILASS Americas 2017, Atlanta, Georgia, May 15-18, 2017.

averaged results are based on the two repeat measurements and represent the data discussed herein.

Table 4.3. Non-reacting, vaporizing sprays experimental conditions.

Fuels	ULSD, High Reactivity Gasoline			
Charge Temperature (K)	900	800, 1000	800, 900, 1000, 1100, 1200	800, 1000, 1200
Charge Pressure (MPa)	6	3	6	10
Charge Density (kg/m^3)	22.5	12.8, 10.3	25.4, 22.5, 20.3, 18.5, 17.0	41.7, 33.4, 28.0
Injection Pressure (MPa)	100	150, 250		

4.2.2 Data Processing Methods

Shadowgraph and Mie scattering images captured by the high-speed camera require post processing to obtain quantitative penetration, dispersion angle, and liquid length data. Figure 4.10 shows an example of the processing steps for the shadowgraph image. These steps are also applied to the Mie scattering images, however, the dispersion angle of the liquid spray is not acquired during Mie scattering image processing.

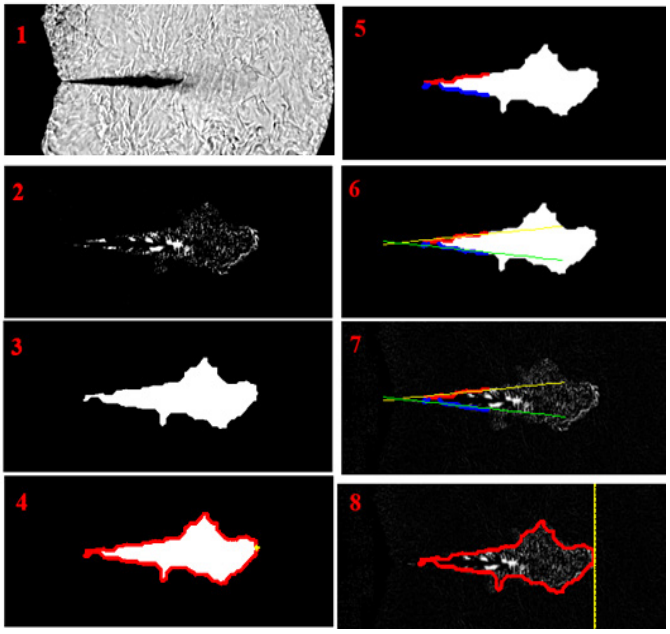

Figure 4.10. Illustration of shadowgraph image processing methods.

The steps are as follows:

1. Read in raw image data from 8 bit gray scale uncompressed files.
2. Perform image background subtraction. For shadowgraph, subtract the previous frame from the current frame (I_n- I_{n-1}) to obtain a vapor boundary. For Mie scattering, subtract the background only.
3. Apply a threshold using the MATLAB® "graythresh" function to obtain binary images. This process uses Ostu's method to find the global image threshold (Otsu 1979).
4. Implement boundary tracking and define the vapor penetration that is the distance from the injector tip to a point in the downstream vapor envelope covering 99% of the total envelope. This compensates for fluctuations in the leading edge of the vapor envelope caused by test-to-test variations in the spray structure.
5. Find the region of the spray where 60% of the spray penetration occurs.
6. Define the vapor dispersion angle as the angle enclosed by the two linearly fitted lines from the boundary identified in Step 5.
7. Dispersion angle linear fits overlaid on shadowgraph vapor envelope.
8. Vapor penetration tracking line as 99% of the shadowgraph vapor envelope.

Since boundary tracking of the images depends on the pixel light intensity threshold value, a sweep of threshold values is conducted to determine the sensitivity of vapor penetration, liquid penetration, and vapor dispersion angles to this parameter. Figure 4.11 shows results from a sweep completed between ± 50% of the original threshold value and indicates the small differences observed in vapor penetration. Results show that vapor penetrations are not sensitive to a change of ± 50% thresholds, while the liquid penetration exhibited more fluctuations but still achieved reasonable agreement with results using the original threshold. The vapor dispersion angle had the largest sensitivity to the threshold, with a deviation on the order of 10%. This is related to the challenges associated with background removal from the developing jet, especially near the liquid core region where the pixel intensities are low. Nevertheless, this level of sensitivity is still considered reasonable.

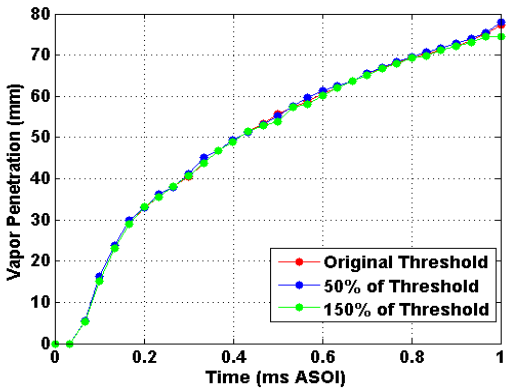

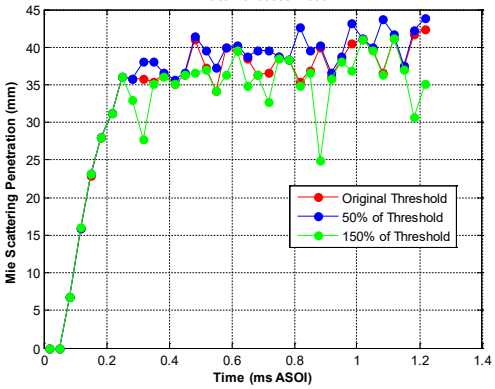

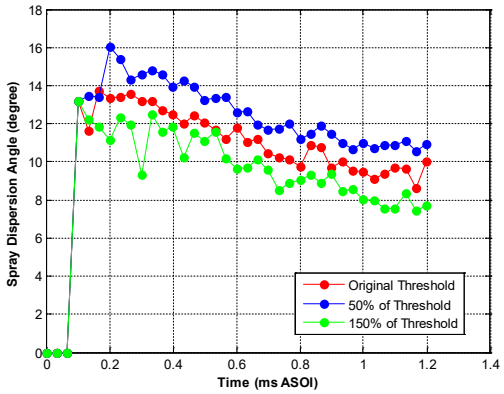

Figure 4.11. Threshold sensitivity of the vapor penetration, liquid penetration, and vapor dispersion angles.

The actual start of liquid injection (SOI) from the orifice needs to be calculated via post-processing techniques because it occurs before the first frame in which Mie scattering data is captured given the temporal resolution of the optical setup. A linear fit is applied to the first five points of the spray penetration versus time curve and extrapolated to zero-penetration in order to determine the true SOI. A time shift is then applied to the ensemble-averaged vapor penetration curves accounting for the real SOI. Details are provided in descriptions from section 4.1.2.

4.2.3 Results and Discussions

The results for both fuels are presented in three separate sections: vapor dispersion angle, vapor penetration, and liquid length. The influence of charge gas conditions and injection pressure are also discussed in each section. Figure 4.12 shows an example of the post-processed shadowgraph (top four rows) and Mie scattering (bottom row) images of ULSD and high reactivity gasoline at various times between 0.1 to 0.8 ms after the start of injection (ASOI). The shadowgraph images in Figure 4.12 demonstrate the boundary tracking and dispersion angle fitting to the vapor envelope identified. The Mie scattering images displayed in the last row represent the steady-state liquid length of the sprays. The major differences between ULSD and gasoline are apparent from the figures and include the following observations: (1) the dispersion angle of gasoline is larger than ULSD; (2) the vapor penetration of the two fuels is similar; (3) the liquid length of gasoline is significantly lower than ULSD.

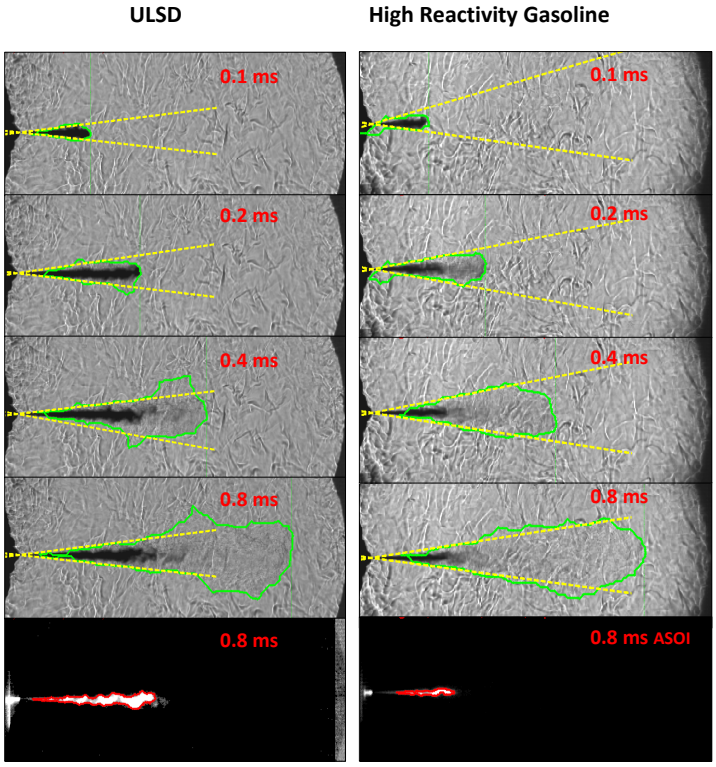

Figure 4.12. Sample of processed vapor (top four rows) and liquid (bottom row) spray images comparing ULSD and high reactivity gasoline.

4.2.3.1 Vapor Spray Dispersion

Vapor dispersion angle indicates the extent of fuel-air mixing in diesel sprays and is an important macroscopic characteristic. A large dispersion angle denotes higher rates of ambient air entrainment that promotes the liquid fuel vaporization process. There are two realizations for each test condition and only the ensemble-average dispersion angles are plotted in the following figures. Within each individual test realization, a single mean value for the dispersion angle is calculated from the steady state portion of the spray injection event.

Figure 4.13 provides the dispersion angle over the entire range of charge gas densities from 10.3 to 41.7 kg/m^3. For both fuels, the dispersion angle becomes larger as charge gas density is increased. This result agrees with prior studies; it is attributed to the higher rates of air mass entrainment due to higher density air (Naber and Siebers 1996). In addition, the dispersion angle of high reactivity gasoline is notably larger than the ULSD under most of the operating conditions. At 10.3 kg/m^3 charge density and 150 MPa of injection pressure, the high reactivity gasoline has 20% larger dispersion angle. At a higher injection pressure of 250 MPa, the difference in dispersion angle between fuels falls to within 5%. The overall trends in dispersion angle for both fuels with respect to charge gas density and injection pressure are quite consistent.

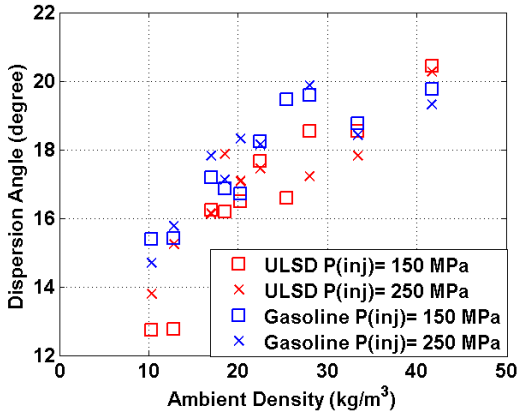

Figure 4.13. Steady-state dispersion angle vs. charge gas density at different injection pressures.

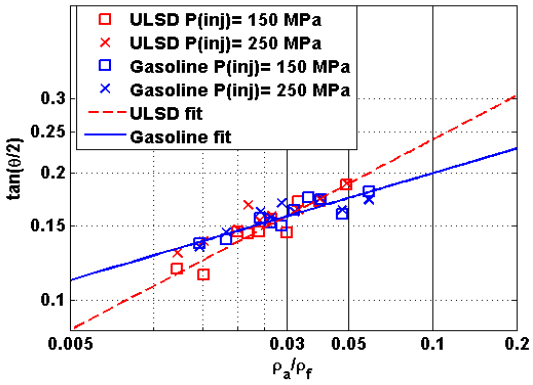

Figure 4.14. Vapor dispersion angle versus charge gas to fuel density ratio.

The dispersion half angle tangent versus the ratio of charge gas to fuel density is fitted to equation (6), repeated below:

$$tan\left(\frac{\theta}{2}\right) = a \cdot \left(\frac{\rho_a}{\rho_f}\right)^b$$

The data for both fuels fitted using equation (6) and plotted on a log-log scale are shown in Figure 4.14. The coefficients of the fitted curves for ULSD and high reactivity gasoline are also provided in Table 4.4. The observations from non-vaporizing tests in section 4.1 indicate that ULSD and high reactivity gasoline exhibit similar trends in spray dispersion and could be represented by a single fit to equation (1). Based on that work, it was concluded that the differences in spray dispersion angles were primarily due to differences in the fuel density. However, the fitted lines in Figure 4.14 clearly show distinctive slopes for the ULSD and high reactivity gasoline. In addition to the influence that viscosity and orifice flow coefficients may have on the minor differences observed in dispersion angle

between fuels under non-vaporizing conditions, it is quite likely that the overall higher volatility of gasoline plays a significant role in the differences observed under vaporizing conditions.

Table 4.4. Dispersion angle fit coefficients for non-reacting, vaporizing spray dispersion angles.

	a	b
Gasoline	0.30	0.18
ULSD	0.34	0.22

4.2.3.2 Vapor Penetration

Vapor penetration represents the axial momentum of the spray after the start of injection and is related to the dispersion angle because of the ambient air continually being entrained within the plume (Naber and Siebers 1996).

In Figure 4.15, the vapor penetration of high reactivity gasoline is plotted for charge gas densities between 17 to 25.4 kg/m^3 at 6 MPa ambient pressure and for an injection pressure of 150 MPa. It is observed that the penetration exhibits a linear dependence during the initial stage of the spray (< 0.3 ms). During this period, there is no apparent impact of charge gas density on penetration rate because the spray is dominated by liquid injection. After 0.3 ms, the penetration slows down and follows a square root dependence that is consistent with prior work and due to the influence of ambient air entrainment into the spray envelope. As charge gas density is increased, the vapor dispersion angle becomes larger. This is caused by more air entrainment that results in reduced fuel momentum and vapor penetration. From charge gas densities of 17 to 25.4 kg/m^3, the maximum difference between the penetrations for gasoline is 14%.

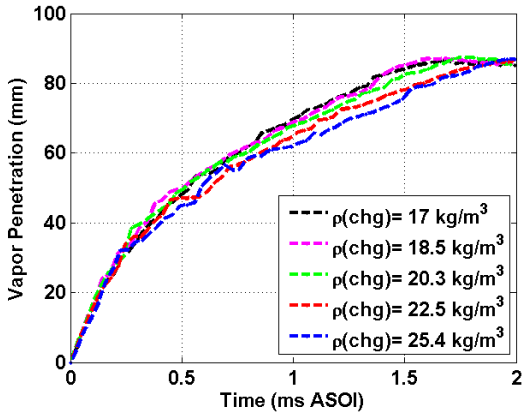

Figure 4.15. Vapor penetration vs. time for high reactivity gasoline at various charge gas densities under 6 MPa ambient pressure and 150 MPa injection pressure.

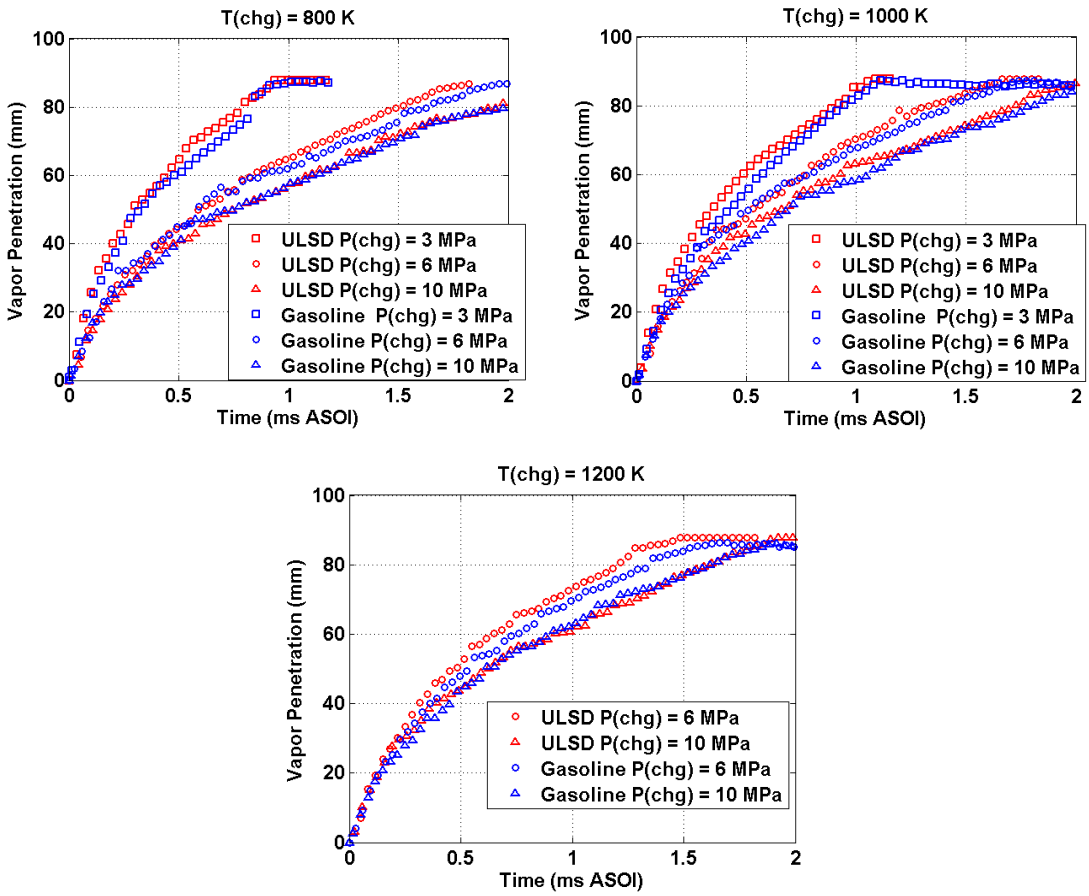

Figure 4.16. Vapor penetration vs. time for ULSD and high reactivity gasoline at an injection pressure of 150 MPa for a range of ambient pressures and temperatures.

The vapor penetration of ULSD and high reactivity gasoline at charge gas pressures of 3, 6 and 10 MPa, charge gas temperatures of 800, 1000 and 1200 K, and an injection pressure of 150 MPa are shown in Figure 4.16. The differences between fuels at all conditions are relatively small (within 5%).

The influence of injection pressure between 100 to 250 MPa on vapor penetration for gasoline is shown in Figure 4.17. Penetration rate increases with higher injection pressure due to the higher velocity and momentum of the fuel spray. Vapor penetration increases by a maximum of 40% when the injection pressure is increased from 100 to 250 MPa. In general, the trends of vapor penetration vs. charge gas density, temperature, and injection pressure for the high reactivity gasoline are consistent with expectations based on prior work with diesel (Naber and Siebers 1996). It was also found that for the conditions discussed herein, there was no significant difference in vapor penetration between ULSD and high reactivity gasoline.

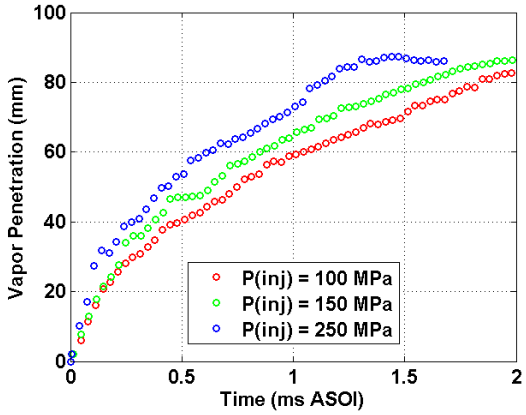

Figure 4.17. Vapor penetrations versus time for high reactivity gasoline with 6 MPa charge gas pressure and 900K charge gas temperature.

4.2.3.3 Liquid Penetration

The liquid lengths of ULSD and high reactivity gasoline between charge gas temperatures of 800-1200 K and for injection pressures of 100-150 MPa are plotted in Figure 4.18 and Figure 4.19, respectively. Similar to the vapor penetration, the liquid length values are obtained from the Mie scattering image boundaries that contain 99% of the total liquid envelope area from the injector tip. The charge gas density in these experiments is controlled by changing the charge gas temperature while keeping the charge gas pressure constant per Table 4.3. Therefore, at a specific charge gas temperature, increasing the charge gas pressure corresponds to a higher charge gas density.

Figure 4.18 displays that the liquid length of high reactivity gasoline is more than 50% shorter than the ULSD under the corresponding conditions. This is due to the higher volatility of high reactivity gasoline (T50 of ULSD is 267 ˚C and of the high reactivity gasoline is 94.4 ˚C). Further it is seen that the liquid length decreases with an increasing back pressure. From Figure 4.19, the injection pressure is seen to have no significant impact on liquid length. These observations are consistent with those observed in Siebers' and others work on liquid penetrations (Siebers 1998, 1999).

Interestingly, the liquid length of ULSD in Figure 4.18 decreases by 33% from 36 to 24 mm at a constant charge pressure of 6 MPa and across a charge temperature range from 800 to 1200 K. The liquid length of ULSD under 3 and 10 MPa have the same trends, which is consistent with prior observations. However, the liquid length of high reactivity gasoline is insensitive (less than 5% reduction from 13.9 to 13.3 mm at 6 MPa) to changes in ambient temperature over the same range which does not follow the expected trend in Siebers' studies (Siebers 1999, 1998).

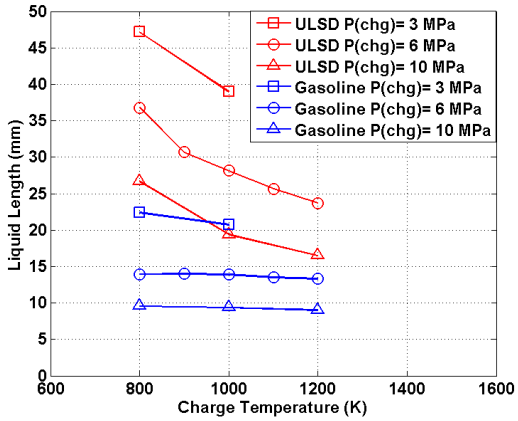

Figure 4.18. Liquid length vs. charge temperature at an injection pressure of 150 MPa.

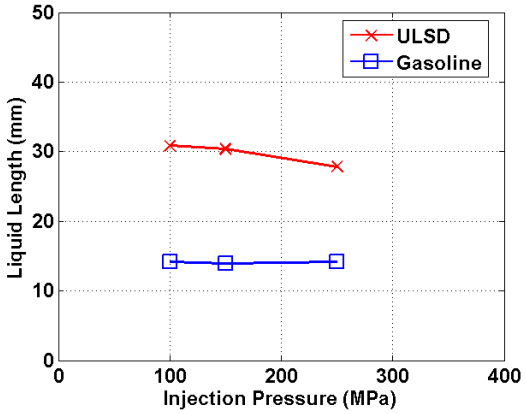

Figure 4.19. Liquid length vs. injection pressure at a charge gas pressure and temperature of 6 MPa and 900 K, respectively.

According to the correlations of Naber and Siebers (Naber and Siebers 1996) and Siebers (Siebers 1999, 1998), there are two regimes of these types of sprays where the spray transitions from one dominated by the initial velocity and the other dominated by gas entrainment. In the velocity dominated regime, primary atomization, momentum, mass, and energy transport processes control the spray evolution. This corresponds to a regime in the normalized spray penetration $\tilde{S}$ defined in equation (10) and normalized times $\tilde{t} = t/t^{+}$ in equation (9) less than 1 as shown in Figure 4.19. The transition in transport versus entrainment controlled is shown with the short and long time limits with linear and square root dependence on time. At normalized times $\tilde{t}$ greater than 1, the momentum, mass and energy exchange between the fuel (liquid or gas) can be considered to be in equilibrium, and the fuel reaches its saturation temperature. This is the regime in which the liquid length is predicted by the Siebers' scaling law (Siebers 1999).

$$x^+ = \frac{\sqrt{C_a} \cdot d_0 \cdot \sqrt{\rho_f/\rho_a}}{a \cdot tan(\theta/2)} \quad (8)$$

$$t^+ = \frac{\sqrt{C_a} \cdot d_0 \cdot \sqrt{\rho_f/\rho_a}}{a \cdot tan(\theta/2) \cdot C_v \sqrt{2 \cdot (P_f - P_a)/\rho_f}} \quad (9)$$

$$\tilde{t} = \frac{\tilde{S}}{2} + \frac{\tilde{S}\sqrt{1+16\tilde{S}^2}}{4} + \frac{ln\left(4\tilde{S} + \sqrt{1+16\tilde{S}^2}\right)}{16} \quad (10)$$

Note that the location in the spray where mass, momentum and energy equilibrium may not occur at the same location $\tilde{S}$; however, this transition still occurs near $\tilde{t} = 1$. Also shown in Figure 4.20 are the normalized liquid lengths of ULSD and high reactivity gasoline, marked as the red and the blue dots for the test cases shown in Figure 4.18, respectively. These are obtained by normalizing the liquid length using the length scale shown in equation (8), in which x^+ is the length scale to normalize the spray penetration, C_a is the area contraction coefficient, assuming to be 1 in this study, d_o is the orifice diameter, ρ_f is the fuel density, ρ_a is the ambient charge gas density, a is a term set to 0.66, θ is the spray dispersion angle.

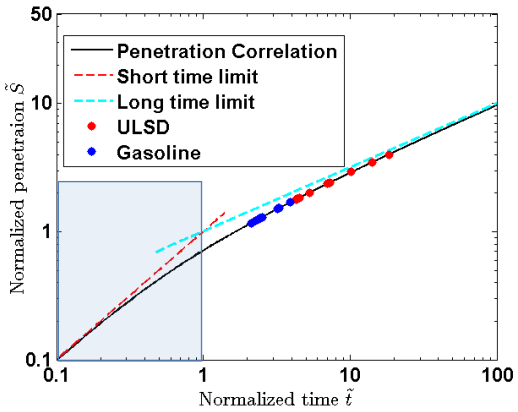

Figure 4.20. The normalized penetration correlation with short and long time limits of correlation.

In Figure 4.20, it is observed that the ULSD normalized liquid lengths are larger than those of the high reactivity gasoline. It is also observed that gasoline data approaches the transition regime from entrainment limited to rate limited. This is hypothesized to be the reason for the unexpected trend of gasoline liquid lengths with respect to charge gas temperature.

To further illustrate this, shown in Figure 4.21, are the normalized liquid lengths of ULSD and gasoline compared to the normalized penetration at a normalized time of 1 for the three charge gas pressures. The trends here further highlight the observation and hypothesis for rate limited conditions for the high reactivity gasoline with respect to vaporization. As the

temperature increases the normalized liquid lengths of the three charge gas pressures are approaching the transition between the regimes and trend to the same value.

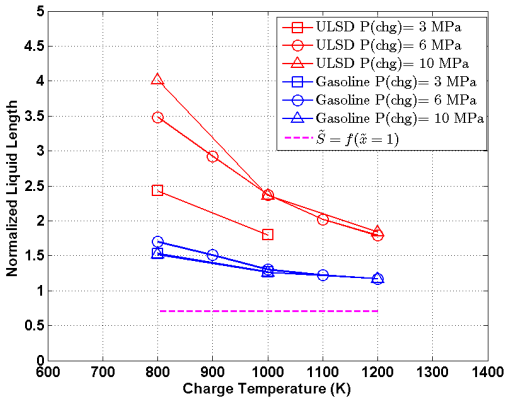

Figure 4.21. The normalized liquid length versus charge gas temperature.

4.2.4 Summary

In general, the characteristics of high reactivity gasoline sprays are in good agreement with previous literature. The vapor dispersion angle increases with higher charge gas density (30% increase from 10.3 to 41.7 kg/m^3) but exhibits only minor differences with increasing injection pressures (less than 5%). The vapor penetration increases (by a maximum of 40%) with increasing injection pressure (100 to 250 MPa) and a 14% increase in penetration is observed when lowering the charge gas density (from 25.4 to 17 kg/m^3). The liquid length decreases with higher charge gas density while changing the injection pressure has only a minor impact on this parameter (2% reduction from 100 to 250 MPa).

High reactivity gasoline has a vapor dispersion angle up to 20% larger than ULSD at a charge density of 10kg/m^3 and injection pressure of 150 MPa, although both fuels exhibit very similar vapor penetration (within 5%). The gasoline also has significantly shorter liquid length (by 50%) compared to ULSD. Although high reactivity gasoline and ULSD liquid length share a similar insensitivity to injection pressure, there is an interesting difference observed with respect to charge gas temperature. ULSD shows decreasing liquid length with increasing charge gas temperature, which is the expected trend based on previous work. However, gasoline liquid length remains insensitive to charge gas temperature between 800-1200 K for the injection pressures investigated in this work. This may be due to the influence of local transport of mass, momentum and energy. More analysis is needed to understand this behavior with specific attention to the large differences in fuel properties between ULSD and high reactivity gasoline.

4.3 Reacting Sprays[3]

4.3.1 Experimental Conditions

Experimental conditions for the reacting sprays are shown in Table 4.5. A sweep of injection pressures at 100, 150, and 250 MPa, and a sweep of charge gas oxygen levels at 10%, 15%, and 21% are used, which are conducted under a charge gas temperature of 900 K. A charge gas temperature sweep from 800 to 1200 K is conducted with an injection pressure of 150 MPa and an oxygen level of 15%. Tests are repeated three times for each test condition.

Table 4.5. Reacting sprays experimental conditions.

Injection Pressure (MPa)	100, 150, 250 (900 K)				
Temperature (K)	800	900	1000	1100	1200
Density (kg/m^3)	25.9	23.1	20.7	18.9	17.3
Gas Pressure (MPa)	6				
Charge Gas	10%, 15%, 21% O_2, (900 K)				
Fuels	ULSD		High Reactivity Gasoline		

4.3.2 Data Processing Methods

Experimental data were post-processed to quantify the ignition and soot oxidation characteristics from the spray combustion tests. Ignition delays were quantified by three methods: (1) cumulative heat release, (2) photodiode signal output, (3) and high-speed videos of natural spray luminosity.

Heat release rate analyses were based on pressure measurements during spray combustion events. An example is shown in Figure 4.22. The pressure rise due to spray combustion is isolated from the pressure decay curve by subtracting an exponentially fitted pressure curve from the original signal. Data smoothing is done by an improved method based on Higgins et al. (Higgins, Siebers, and Aradi 2000). The pressure curve is separated along half of the rising edge from the first pressure oscillation due to spray combustion. The portion prior to spray combustion is smoothed by a 5th order low-pass Butterworth filter with a cutoff frequency of 1.5 kHz. The portion corresponding to spray combustion is smoothed by a

---

[3] Part of the material contained in section 4.3 was previously published as the following conference paper and presented at the 10th US National Combustion Meeting. The authors own the copyright of the following paper, according to the program co-chair, as attached in the Appendix A.2.

- Tang, M., Zhang, J , Menucci, T., Schmidt, H., Lee, S-Y., Naber, J., Tzanetakis, T., "Spray Ignition and Soot Forming Characteristics of High Reactivity Gasoline and Diesel Fuel Using a Heavy-Duty Single-Hole Injector", 10th US National Combustion Meeting, College Park, Maryland, April 23-26, 2017.

The section 4.3 is prepared as a journal publication, due to the significant expansion of the scope of work from the conference paper.

50th order low-pass finite impulse response (FIR) filter with a cutoff frequency of 5 kHz. After assembling the two smoothed portions, a spline interpolation is performed on the entire pressure curve with a sampling rate of 1 MHz. Heat-release rate analyses are based upon the smoothed pressure curves using equation (11), where γ represents the ratio of specific heats. Cumulative heat release is obtained by numerical integration of the heat release rate, and in this work, the ignition delay by pressure measurement is defined as the time until 1% of the cumulative heat release has occurred. The time delays associated with hydraulic injector response and pressure wave propagation have been accounted for using methods similar to those in Higgins et al.(Higgins, Siebers, and Aradi 2000).

$$\frac{dQ}{dT} = \frac{1}{\gamma - 1} V \frac{dP}{dt} \tag{11}$$

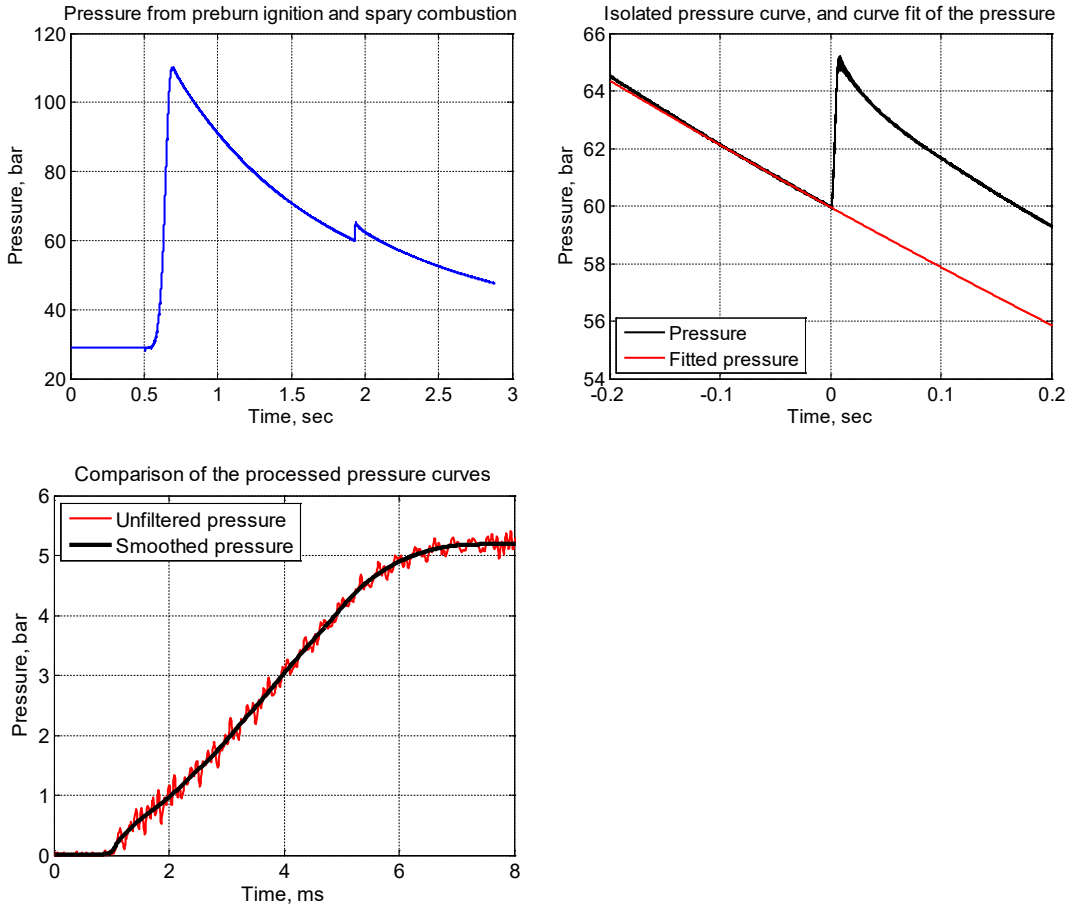

Figure 4.22. Demonstration of vessel pressure processing methods.

Photodiode outputs were also used to define ignition delays. Three photodiode amplifier setups were used, including 10/100/1000 μA. At the baseline case of 100 μA, ignition delay is defined as the time until the output reaches 0.2/8V (max output). This threshold is adjusted according to amplifier settings.

Luminosity from high-speed videos was also used to determine ignition delay. Combinations of different aperture size and shutter duration were employed. The baseline case of f-stop and shutter duration were f/2 and 5.59 μs, respectively. The ignition delay at this baseline case is defined as the time until the maximum luminosity reaches 20 out of 255 counts. This threshold luminosity level was adjusted as the f-stop values and shutter durations were adjusted. Processing of the OH* chemiluminescence images followed the method by Higgins et al (Higgins, Siebers, and Aradi 2000) to obtain the lift-off length. An example is shown in Figure 4.23.

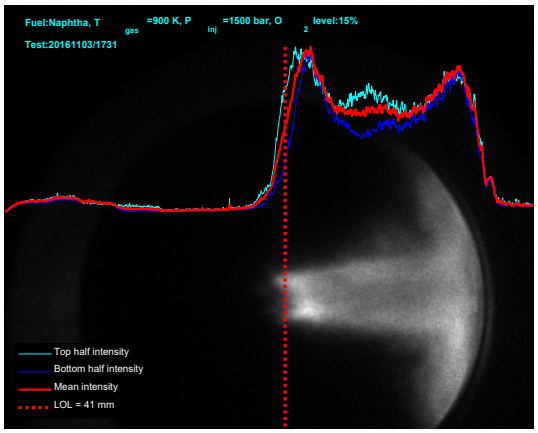

Figure 4.23. Demonstration of lift-off length processed from the OH* chemiluminescence image.

4.3.3 Results and Discussions

4.3.3.1 Ignition Delay and Lift-off Length

4.3.3.1.1 Effect of Charge Gas Temperature

Among the three ignition delay measurements, photodiode signals and luminosity are optical techniques and their results are subject to optical settings, while cumulative heat-release does not suffer from these factors. Comparisons of the results from the three diagnostic techniques are shown in Figure 4.24. Note that the cumulative heat-release is represented by the pressure curve, although they share similar characteristics. Ignition delays from the 1% cumulative heat release method are shorter than those from the photodiode and the luminosity. Overall, three measurements are within 0.3 ms to one other, with maximum differences on the order of 20% when considering all of the test conditions.

The trends of ignition delay (1% cumulative heat release) with charge gas temperature are provided in Figure 4.25. Mean ignition delays from at least three test repeats are plotted with one standard deviation to represent the experimental repeatability. Ignition delays decreased with increasing temperatures, as expected. Ignition delays from gasoline are

longer than ULSD and the differences decrease with an increase in the temperature. One of the main reasons for the differences in ignition delays between the two fuels is simply the difference in reactivity, which is related to the Cetane number. However, spray combustion is a complex phenomenon that includes both physical and chemical processes (denoted as physical delay and chemical delay in this study), and both contribute to the overall ignition delay.

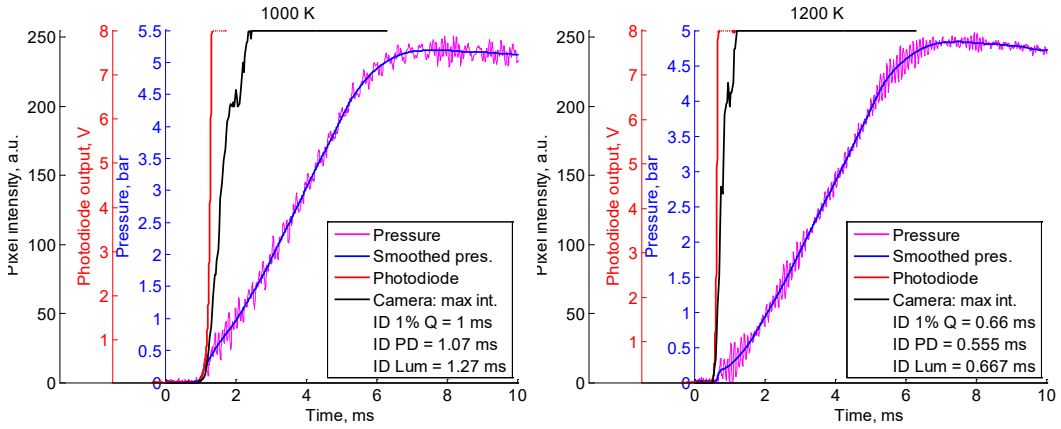

Figure 4.24. Comparison of high reactivity gasoline ignition delay measurements using three diagnostic techniques at different charge gas temperature conditions.

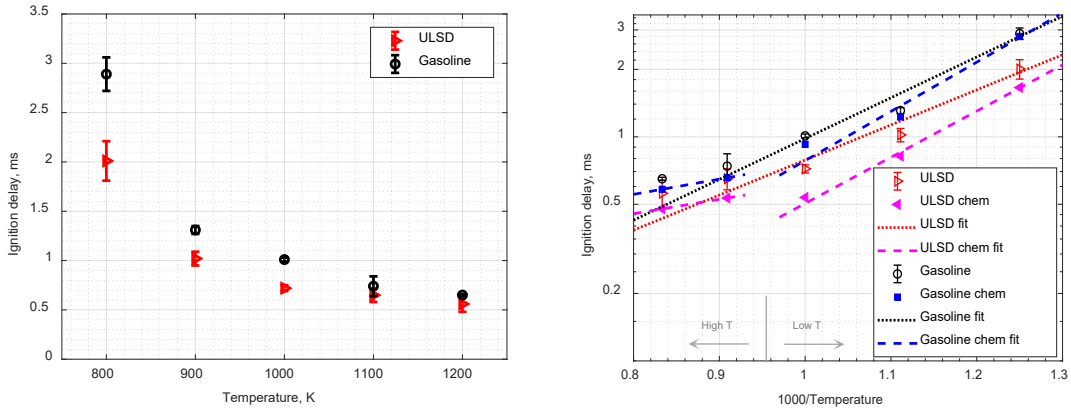

Figure 4.25. Ignition delays of ULSD and gasoline as a function of charge gas temperatures (left), fittings of ignition delays (right).

Compared to previous studies (Henein and Bolt 1967, Ryan and Stapper 1987, Sánchez et al. 2014), the physical and chemical delays in this work are defined somewhat differently. For example, physical delays can refer to the duration that includes fuel injection, atomization, and vaporization (Ryan and Stapper 1987), or the duration for the fuel-air mixture to reach its self-ignition temperature (Sánchez et al. 2014), or the initiation time of

pre-flame reactions (Henein and Bolt 1967). Experimentally, the physical delay period can be determined by the separation of pressure traces from fuel injection into air versus into nitrogen under the same charge gas conditions (Zheng et al. 2013). While the pressure rise from the first-stage ignition is detectable for volumes used in an ignition quality tester (0.2 L) (Zheng et al. 2013) or a combustion bomb (0.05 L) (Ryan and Stapper 1987), the same measurement for the 1 L vessel used in this study is difficult (Pickett, Siebers, and Idicheria 2005). Thus, the physical delays are obtained from non-reacting, vaporizing test data presented in section 4.2 and defined by the time of separation between the liquid and the vapor penetration curves, as shown in Figure 4.26. At the separation location, fuel vapor, liquid, and entrained gas are considered to be in phase equilibrium as evidenced by liquid length measurements in (Siebers 1999), thus this definition is a reasonable estimate of the physical processes that lead up to vaporization.

Physical delay and its fraction of the total ignition delay are shown in Figure 4.26. Physical delays are nearly the same for all gasoline sprays, which is consistent with previous non-reacting, vaporizing test data that showed temperature-insensitive liquid lengths due to gasoline's higher volatility compared to ULSD. Physical delays for ULSD have a negative correlation with temperatures. Generally, the physical delay is a small fraction (<30%) of the total ignition delay, suggesting that chemical processes dominate the ignition behavior.

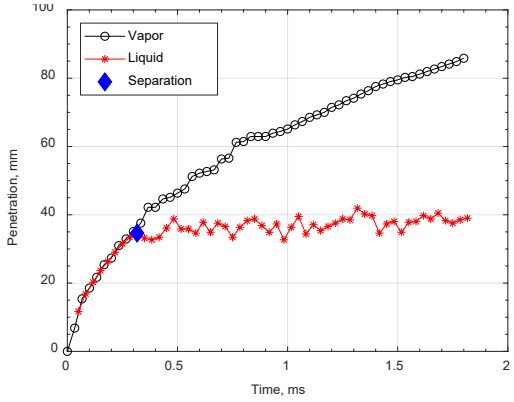

Figure 4.26. Physical delay as derived from the separation of vapor and liquid penetration length for a non-reacting, vaporizing spray test.

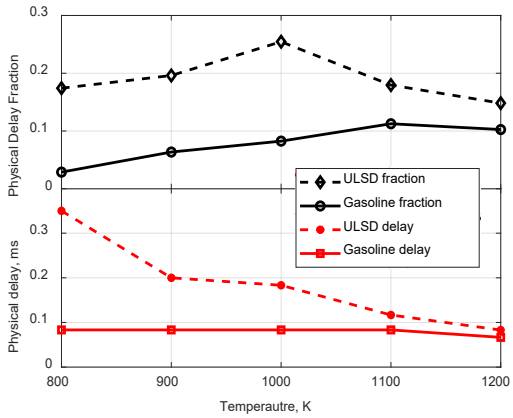

Figure 4.27. Effect of charge gas temperature on physical delay (lower) and fraction (upper).

Physical delays are deducted from total ignition delays to get chemical delays, which are shown in Figure 4.25. Note that in reality, physical and chemical processes occur at the same time in a spray and are not easily separated. Also, the fuel air mixture stoichiometry and temperature are changing continuously in a spray environment. Therefore, the chemical delays shown in this study are not the same as those from shock tubes or rapid compression machines. Comparing the trend of chemical delay against total ignition delay, while gasoline exhibited similar behavior, ULSD chemical delay exhibited a trend that resembles negative-temperature coefficient (NTC) behavior from 1000 K to 1100 K. This temperature range characterizes the charge gas, while the mixture temperature will be lower by 200-300 K, as calculated using n-dodecane as a surrogate and the mass of gas from the equivalence ratio at the lift-off lengths (shown in the next section). The calculation is substantiated by temperature measurements using Rayleigh scattering (Idicheria and Pickett 2007). The mixture temperature is likely in the NTC regime. The slopes of the total ignition delays were different between the two fuels, whereas the slopes of the chemical delays of the two fuels were similar when separately comparing the two temperature regimes. The slopes in Figure 4.25 represent the temperature dependence of ignition delay and can be described by an Arrhenius expression (12).

$$\tau_{ID} = A \cdot exp(E_a/RT) Z_{st}^{m} \tag{12}$$

A is a pre-exponential factor, E_a is the apparent activation energy, R is the universal gas constant, T is the charge gas temperature, Z_{st} is the stoichiometric mixture fraction. Results of the fitted curves are shown in Figure 4.25 and the fitted powers are shown in Table 4. From Table 4, it is clear that the temperature dependence is closer for chemical delay than it is for total ignition delay, excluding the NTC regime.

Table 4.6. Dependence of ignition delay on charge gas temperature.

	Ea/R (K)	R^2
ULSD	3597	0.9597
ULSD chem low T	4747	0.9966
ULSD chem high T	1473	1.000
Gasoline	4192	0.9688
Gasoline chem low T	5059	0.9787
Gasoline chem high T	1563	1.000

The effect of charge gas temperature on lift-off length is shown in Figure 4.28. The results are shown as averages from a minimum of three test repeats with one standard deviation as the test repeatability. With an increase in the temperature, the lift-off length decreases. In general, ULSD exhibits shorter lift-off lengths than gasoline. Lift-off lengths can be represented by a power law expression (Siebers, Higgins, and Pickett 2002, Pickett, Siebers, and Idicheria 2005, Benajes et al. 2013)

$$H = C \cdot T_a^m \cdot P_a^n \cdot d_o^x \cdot U^y \cdot Z_{st}^z. \tag{13}$$

H is the lift-off length, C is a constant, T_a is the ambient charge gas temperature, P_a is the ambient charge gas pressure, d_o is the orifice diameter, U is the injection velocity, and Z_{st} is the stoichiometric mixture fraction, which is defined as the mass of fuel over the total mass of fuel and air in a stoichiometric mixture. The results from data fitting are shown as dashed lines in Figure 4.28 and the fitted powers are provided in Table 4.7. Gasoline exhibits a higher sensitivity to charge gas temperature than ULSD.

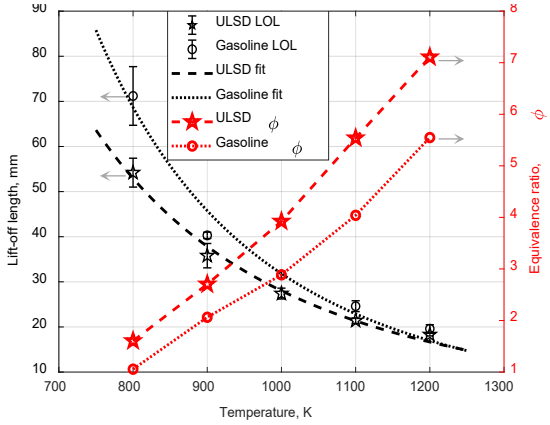

Figure 4.28. Effect of charge gas temperature on lift-off length and equivalence ratio (ϕ) at the lift-off length.

Table 4.7. Dependence of lift-off length on charge gas temperature

	m	R^2
ULSD	-2.870	0.9894
Gasoline	-3.453	0.9724

Due to the higher liquid density of ULSD, the spray velocity of ULSD is expected to be lower than that of gasoline when the injection pressure and nozzle diameter are kept constant, according to Bernoulli's principle shown in (14). Also, ULSD exhibits smaller spray cone angles in non-reacting, vaporizing experiments. These two combined effects result in slower mixing rates for ULSD than gasoline, which means that ULSD will reach the same equivalence ratio as gasoline further downstream in the spray. If the two fuels had similar reactivity, ULSD would exhibit longer lift-off lengths than gasoline. However, the reverse trend from test results suggests that differences in the reactivity characteristics are responsible for the lower lift-off length of ULSD.

$$V_{spray} = \sqrt{\frac{2\cdot(P_{inj}-P_{charge})}{\rho_f}}. \tag{14}$$

To understand the effect of mixing quality on the lift-off behavior, the equivalence ratio at each lift-off length is calculated by equation (15) (Siebers, Higgins, and Pickett 2002). AFR_{stoic} is the mass-based stoichiometric air-fuel ratio (14.5 for ULSD and 14.6 for gasoline (Heywood 1988)), H is the lift-off length, ρ_f is the fuel density, ρ_a is the ambient charge gas density, C_a is the area contraction coefficient (assumed as 0.94 in this study), d_o is the orifice diameter, a is a constant that equals 0.75 (Siebers, Higgins, and Pickett 2002), and θ is the spray cone angle. The calculated equivalence ratios are plotted as a function of charge gas temperature in Figure 4.28. At 800 K, combustion occurs near stoichiometric conditions for gasoline at the lift-off length. As the temperature increases, combustion for both fuels occurs under fuel rich conditions at the lift-off length. The mixture at the lift-off length is always richer for ULSD than gasoline, and the trends in Figure 4.28 suggest that combustion for ULSD is achievable at a temperature of up to 100 K lower than gasoline at the same level of mixing.

$$\phi = \frac{2\cdot AFR_{stoic}}{\left[1+16\cdot\left(H/\left[\left(\frac{\rho_f}{\rho_a}\right)^{0.5}\cdot\frac{C_a^{0.5}\cdot d_o}{a\cdot tan(\theta/2)}\right]\right)^2\right]^{0.5}-1} \tag{15}$$

From the previous analysis, lift-off lengths are closely related to ignition delays in this study. The relationship between the two variables is shown in Figure 4.29. The scatter plot includes all of the test cases. Dashed lines indicate power-law fits through the ULSD and gasoline datasets, respectively. The close proximity of the two fits suggests that despite the differences in physical and chemical properties, the lift-off length and the ignition delay correlate well. Dumitrescu et al. (Dumitrescu et al. 2014) showed similar observations, and it was also found that a change in injection pressures leads to a shift in the lift-off length versus ignition delay relationship. In that work, the fuel physical property differences

(density and volatility) are smaller than the current study, while the differences in Cetane number or fuel reactivity are similar. Both studies suggest that Cetane number dominates the lift-off versus ignition correlation rather than thermophysical properties.

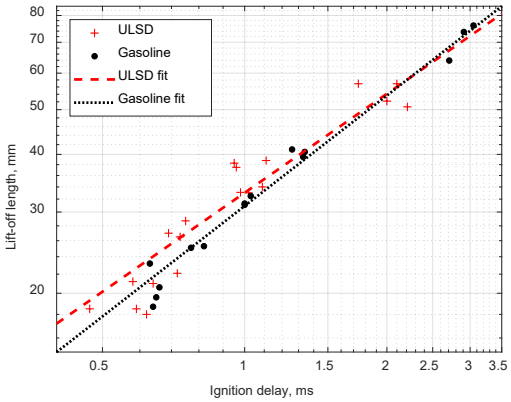

Figure 4.29. Relationship between lift-off length and ignition delay, with a sweep of charge gas temperatures.

4.3.3.1.2 Effect of Injection Pressure

The effect of injection pressure on ignition delay is plotted in Figure 4.30. The effect of injection pressure on lift-off length is plotted in Figure 4.31. Results show that gasoline exhibit longer ignition delays than ULSD. With an increase in the injection pressures, both fuels experienced a slight increase in the ignition delay, followed by a decrease. The percent change in ignition delay times with respect to injection pressures are less than 10%, suggesting a weak correlation between ignition delays and injection pressures. With the same charge gas temperature, and the same oxygen concentration, the mixture preparation process is critical in affecting the ignition delay. The observation that ignition delays are weakly correlated to injection pressures suggest that the rate of entrainment generally scales with injection pressures. Pickett et al. (Pickett, Siebers, and Idicheria 2005) observed a slight decreasing trend of ignition delays with an increase in the injection pressures. However, the decrease was by no means close to the magnitude imposed by changing ambient charge gas temperatures. Comparing results from this work to those reported by Pickett et al., the small change (<10%) in the ignition delays across the injection velocity ranges agree well, although deviations in the general trends of the two datasets exist. It is possible that the trend in this work could be established more clearly with more test repeats and more injection pressure sweeps.

The lift-off lengths are plotted against the injection velocity as calculated using Bernoulli's equation (14) for the three injection pressures. The injection velocity increases with injection pressures. The lift-off length data are fitted using equation (13), and the results are shown in Table 4.8. Except for gasoline under 150 MPa injection pressure, the two fuels fall very closely onto the same fitted curve. The calculated equivalence ratios at the lift-off lengths are plotted on Figure 4.31. Results show that the mixture equivalence ratios

at the lift-off lengths are lower for gasoline than ULSD. A decreasing trend of equivalence ratios with increases in the injection velocity is also observed, which is also weaker compared to the trend imposed by sweeps of charge gas temperatures.

With almost unchanged ignition delays and increasing lift-off length with increased injection pressures, the two characteristics are weakly correlated. This is opposed to the correlations of the two characteristics with a sweep in charge gas temperatures, as shown in Figure 4.29.

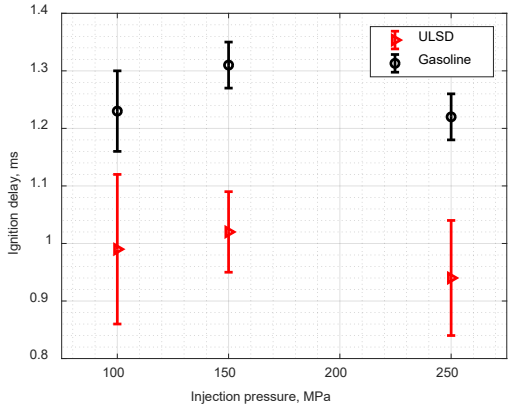

Figure 4.30. Ignition delays of ULSD and gasoline as a function of injection pressure.

Table 4.8. Dependence of lift-off length on injection pressure

	y	R^2
ULSD	0.5819	0.9964
Gasoline	0.4626	0.9087

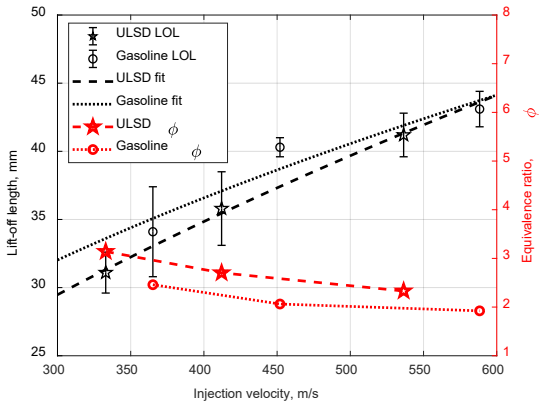

Figure 4.31. Effect of injection velocity (injection pressure) on lift-off length and equivalence ratio (ϕ) at the lift-off length.

4.3.3.1.3 Effect of Oxygen Concentration

The effect of oxygen concentration on ignition delays are shown in Figure 4.32. The oxygen concentrations are represented as the stoichiometric mixture ratio, defined as the mass of fuel over the total mass of fuel and air in a stoichiometric mixture. The stoichiometric mixture ratio increases with the ambient gas oxygen concentration. Comparing the two fuels, gasoline exhibit longer ignition delays than ULSD, as expected. The trend of longer ignition delay becomes weaker as the oxygen concentration increases, however, the effect of oxygen concentration is weaker relative to the effect of gas temperature as discussed previously. Ignition delays are fitted as a function of stoichiometric mixture fraction through equation (12) and plotted on Figure 4.32, with the power of the stoichiometric mixture fraction given in Table 4.9.

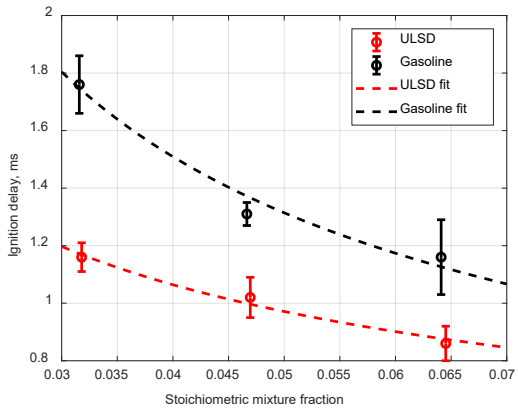

Figure 4.32. Ignition delays of ULSD and gasoline as a function of stoichiometric mixture fraction (oxygen concentration).

Table 4.9. Dependence of ignition delay on stoichiometric mixture fraction (oxygen concentration).

	z	R^2
ULSD	-0.4098	0.9811
Gasoline	-0.8935	0.9903

The effect of oxygen concentration on lift-off length is shown in Figure 4.33. The oxygen concentrations are again represented by the stoichiometric mixture fraction. An increase in the oxygen concentration leads to a decrease in the lift-off length. The lift-off length results are fitted with equation (13). Results of the fitting are shown in Figure 4.33 and Table 4.10. The mixture equivalence ratios at the flame lift-off lengths are calculated using equation (15) and shown in Figure 4.33. Interestingly, the equivalence ratios at the lift-off lengths across three oxygen levels are very similar. Flame stabilization is believed to be controlled by both ignition and flame propagation (Pickett, Siebers, and Idicheria 2005). From the standpoint of ignition, the same injection pressure and charge gas temperature results in the same rate of ambient gas entrainment, thus the oxygen entrainment rate scales only

with the oxygen concentration. Longer durations are required for lower oxygen concentration conditions to achieve the same level of gas stoichiometry, and this results in longer ignition delays and longer lift-off lengths. This is exactly reflected by the ignition delay and lift-off length results.

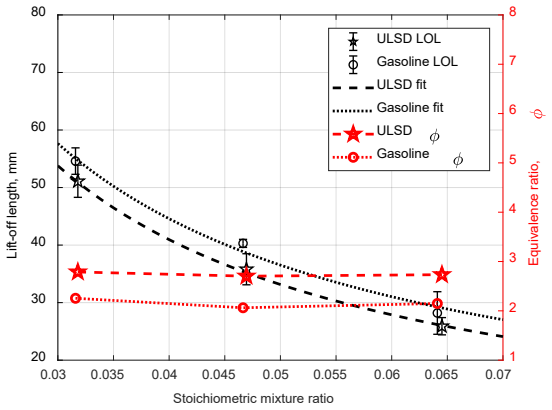

Figure 4.33. Effect of stoichiometric mixture fraction (oxygen concentration) on lift-off length and equivalence ratio (ϕ) at the lift-off length.

Table 4.10. Dependence of lift-off length on stoichiometric mixture fraction (oxygen concentration).

	z	R^2
ULSD	-0.9478	0.9992
Gasoline	-0.8935	0.9903

The simultaneous reduction in ignition delays and lift-off lengths with a sweep of ambient charge gas oxygen concentration suggest that the two characteristics exhibit positive correlations, which are plotted in Figure 4.34. Unlike the LOL-ID correlation under a sweep of charge gas temperatures in Figure 4.29, where they fall almost under the same correlation, the two fuels follow different paths under a sweep of charge gas oxygen concentrations. This suggest the different sensitivity of LOL-ID relationship to the charge gas oxygen concentrations.

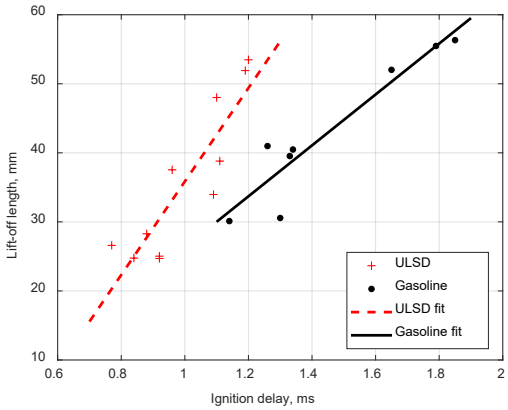

Figure 4.34. Relationship between lift-off length and ignition delay, with a sweep of charge gas oxygen concentrations.

4.3.3.2 Natural Luminosity

Natural luminosity is comprised of chemiluminescence from combustion reactions and soot incandescence. The contribution from the chemiluminescence is 4-5 orders of magnitude smaller compared to soot incandescence, thus natural luminosity is a strong indicator of the occurrence of soot, and has been qualitatively linked to soot concentrations (Mueller and Martin 2002).

Natural luminosity images of the reacting spray diffusion flames are provided in Figure 4.35 for gasoline and ULSD, with sweeps of charge gas temperatures, injection pressures, and oxygen concentrations. Some images are enhanced for the ease of visualization. In general, the natural luminosity level increases with an increase in the charge gas temperature and the oxygen concentration. In some cases, natural luminosity occur almost only near the boundary of the combustion vessel. Examples include, both fuels under 800 K, both fuels under 10% oxygen concentration, and gasoline under 250 MPa injection pressure. These suggest that a quasi-steady state soot cloud cannot be formed within the boundary of the vessel, which may become possible when given extended axial distances. Also, the combustion vessel has a boundary layer with a thickness on the order of 2-3 mm (Naber and Siebers 1996), within which the temperature drops from the a nearly homogeneous core temperature to the vessel wall temperature. This change in thermodynamic condition may exert additional effect on the soot natural luminosity, thus it is a challenge when directly comparing the luminosity from the boundary layer to those from the core region of the combustion vessel.

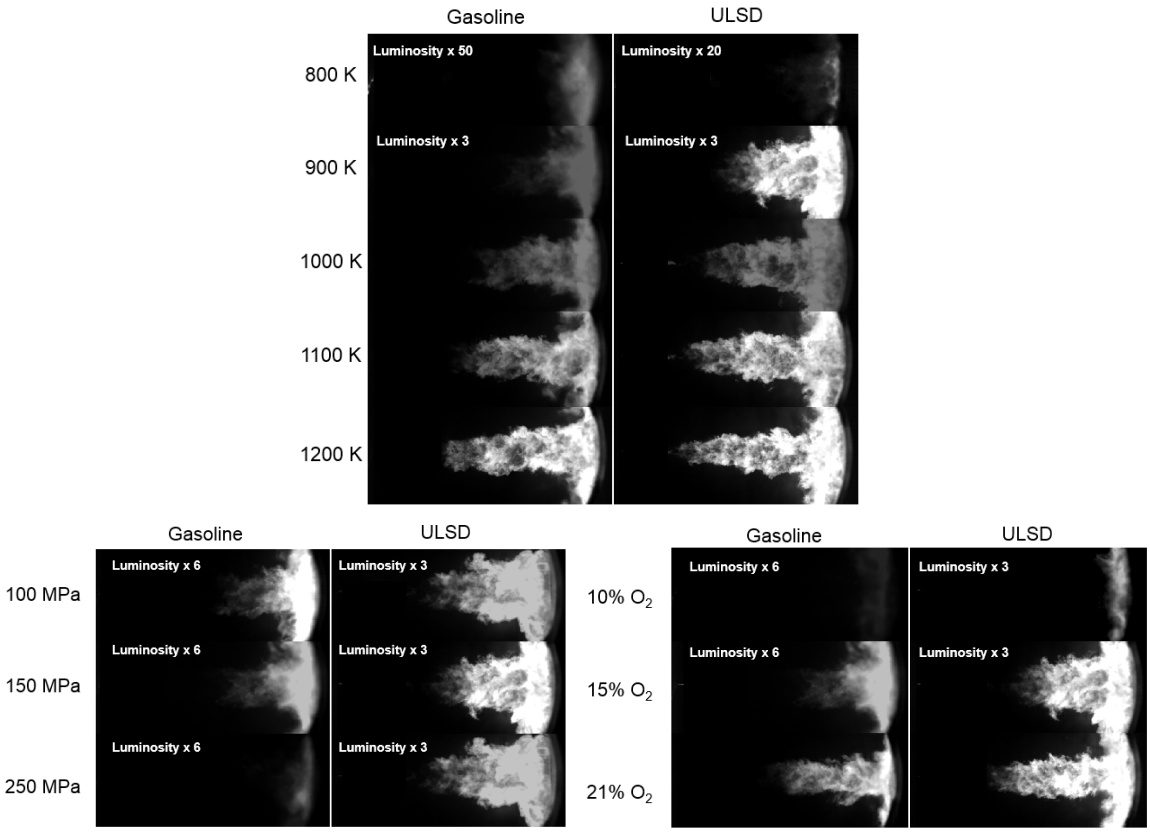

Figure 4.35. Comparison of the natural luminosity images of the diffusion flame between gasoline and ULSD.

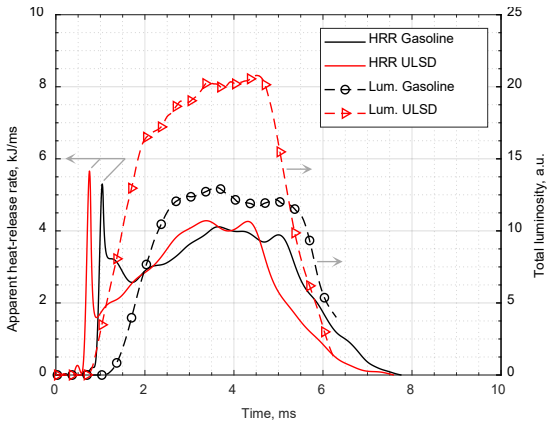

Figure 4.36. Comparison of the gasoline and ULSD on heat-release rate and natural luminosity at 1000 K, 15% oxygen charge gas, and 150 MPa injection pressure.

Temporally, the luminosity data are plotted in Figure 4.36 for the two fuels. The luminosity data are ensemble averages from three repeats of integrated pixel intensities during combustion. The fast rise in luminosity coincides with the beginning of mixing-controlled

combustion, whereas premixed combustion does not produce as much luminosity. A quasi-steady state of the total luminosity exist during the mixing-controlled combustion.

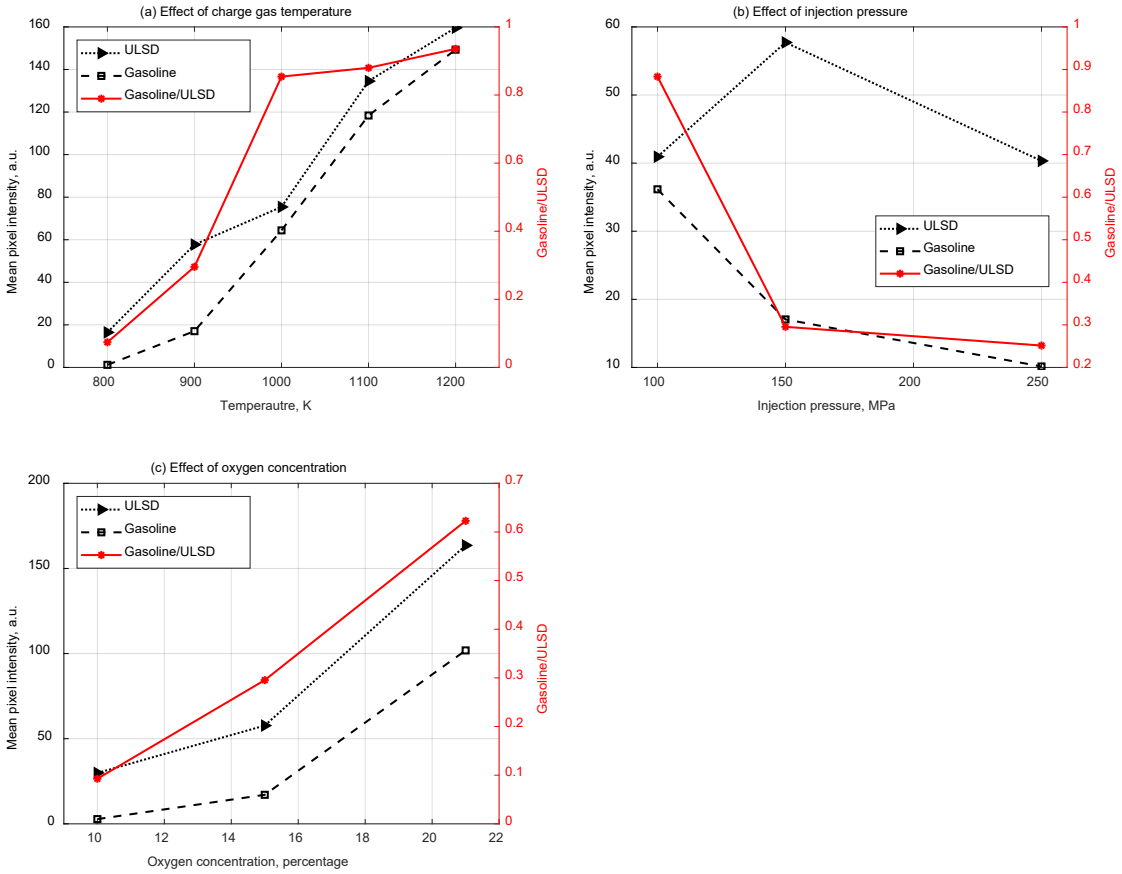

Figure 4.37. Spatially-integrated natural luminosity (SINL) of gasoline and ULSD, under the influence of (a) charge gas temperatures, (b) injection pressures, (c) oxygen concentrations.

Using natural luminosity as a measure of the soot levels in the spray flames, the mean pixel intensities within spray flames are plotted against charge gas temperatures, injection pressures, and oxygen concentrations, as shown in Figure 4.37. The mean pixel intensity signal is a representation of the average soot concentration under a specific test condition. The mean pixel intensity signal for one condition is an average of three test repeats, at three time instants during the quasi-steady state for each repeat as shown in Figure 4.36. The relative mean pixel intensity ratio between gasoline and ULSD is also shown. Overall, natural luminosity levels are low under low charge gas temperatures and low oxygen concentrations. These two conditions favor slower reaction rates, including soot formation rates that leads to lower levels of soot. Effects of injection pressures on the natural luminosity signal level is greatly affected by the long soot cloud lift-off for gasoline under 250 MPa injection pressure. From a mixing standpoint, the decreasing mixture equivalence ratios with an increase in the injection pressure suggests that better mixing prior to ignition

is achieved at higher injection pressures. This may translate to lower overall levels of soot in the spray flame, which is reflected by the gasoline fuel. Partial saturation of the natural luminosity signals are also responsible for the trends of the mean pixel intensities with injection pressures.

Natural luminosity is quantitatively linked to the soot volume fraction through a number of factors, including the detection system spectral characteristics, adiabatic flame temperature, optical thickness, soot particle size, soot refractive index, soot particle spectral emittance, and soot particle spatial distribution (Mueller and Martin 2002). These factors are examined and discussed next for a semi-quantitative interpretation of the natural luminosity signals.

The detection system consists of a BG28 filter, a camera lens, and a high speed camera, all of which exhibit different spectral characteristics as shown in Figure 4.38. The overall spectral efficiency of the detection system shows that 400-600 nm has the highest transmittance, while wavelengths over 600 nm has a transmittance below 1%.

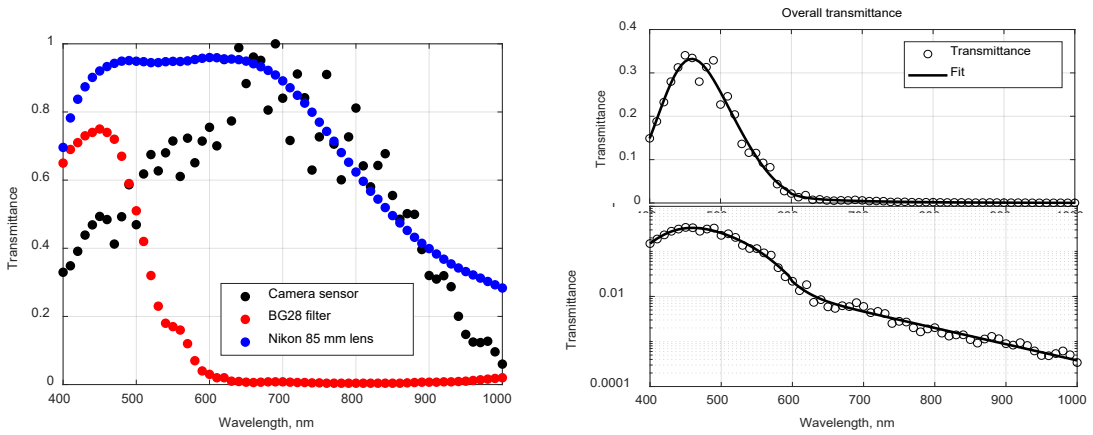

Figure 4.38. Spectral transmittance of the camera sensor, BG28 filter, and Nikon 85 mm lens (left), and the overall spectral efficiency of the detection system (right).

The adiabatic flame temperatures of the two fuels under the test conditions and assuming stoichiometric combustion, are calculated for the sweep of charge gas temperature, and oxygen concentrations. Results are shown in Table 4.11. According to the fuel properties as shown in Table 1.1, gasoline has a lower carbon mass fraction (84.9%) than ULSD (86.8%), this leads to higher stoichiometric air-to-fuel ratio for gasoline (15.2) than ULSD (14.8). Despite the higher net heat value of gasoline, the calculated adiabatic flame temperatures are lower than ULSD.

Table 4.11. Adiabatic flame temperatures of gasoline and ULSD, with a sweep of charge gas temperature and oxygen concentrations.

	Charge gas temperature					O_2 concentration	
	800 K	**900 K (15%)**	**1000 K**	**1100 K**	**1200 K**	**10%**	**21%**
ULSD (K)	2117	2194	2273	2352	2432	1814	2602
Gasoline (K)	2064	2140	2217	2296	2375	1782	2528

ULSD spray flames are expected to be optically thicker than gasoline, based on the soot emission benefits of gasoline in engine tests. It is not known whether gasoline spray flames are optically thick. The thickness of the soot cloud affects the spatial transmission of the luminosity because natural luminosity signals are two-dimensional line-of-sight projections of the three-dimensional distribution of soot information.

The effect of soot particle characteristics has been discussed by (Mueller and Martin 2002) and it was concluded that the natural luminosity signal is a proportional to soot volume fraction, with the proportionality as a function of soot refractive index with spectrum and the detection system's efficiency. In another work (Hessel et al. 2017), the radiation intensity is expressed by equation (16), which is the rate of emitted energy from unit surface area through unit solid angle, assuming blackbody radiation. I is the spectral blackbody radiation (in W/sr·m^2·nm). T is the temperature (in Kelvin) of the aerosol (assumed to represent soot particles), which is in thermal equilibrium with the soot particles. n is the refractive index of the medium, and assumed to be 1. λ is the wavelength (in nm) and C_1 is Planck's first constant, 3.7419e-16 (W·m^2). C_2 is Planck's second constant, 14388 (µm·K). Equation (17) calculates the soot emissivity, equation (18) calculates the soot transmissivity, while equation (19) calculates the signal received by the camera sensor from a line-of-sight, which is a spectral integration of the product of the radiation intensity, the soot emissivity, the transmissivity, and the spectral response of the detection system. Soot emissivity is the degree of departure from the blackbody radiation assumption.

$$I_{bb,\lambda,\Omega}(T,\lambda) = C_1/\left(\pi n^2 \lambda^5 (exp(C_2/n\lambda T) - 1)\right) \tag{16}$$

$$\varepsilon_{soot} = 1 - exp\left(-\left(g f_v L_{cfd\_cell}\right)/\lambda^{\alpha}\right) \tag{17}$$

$$\tau_{soot} = 1 - \varepsilon_{soot} \tag{18}$$

$$S_\lambda = \int_{400\,nm}^{1000\,nm} \left\{ f\left[< \left(I_{bb,\lambda_\Omega(\lambda)} \cdot \varepsilon_{\mathrm{soot}}(\lambda) \right) \cdot \tau_{\mathrm{soot}}(\lambda) > A \cdot C_\lambda \right] \right\} d\lambda \tag{19}$$

A semi-quantitative interpretation of the natural luminosity is possible with the above information, and the following assumptions/simplifications: (1) soot properties, including soot particle characteristics, soot spectral emissions, and soot refractive indices, from spray flames of the two fuels are the same under the same ambient charge gas and injection pressure conditions, (2) spray flames of both fuels are optically thick.

The first simplification avoids the complexities associated with soot particle properties, which is beyond the scope of this work. By assuming the same soot related properties, the

radiation intensity per unit surface area through unit solid angle can be simplified as the radiation intensity per soot particle.

The second simplification ensures that the natural luminosity received by the camera is dominated by the radiation emission from the thin diffusion flame on the camera side of the flame. The soot transmissivity in equation (19) is reduced to a minimum, thus preventing the transmission of major luminosity from the far side of the flame.

The above two simplifications reduces the integral term in the equation (19) to only the blackbody radiation term, which is the spectral integration of radiation intensity for one soot particle. The total luminosity is then the cumulative radiation intensity from the total number of soot particles, as summarized in equation (20). Mean pixel intensity is thus related to the soot concentrations.

$$\frac{NL_G}{NL_D} = \frac{I_{bb_G}}{I_{bb_D}} \cdot \frac{f_{v_G}}{f_{v_D}} \tag{20}$$

Using the calculated adiabatic flame temperature in Table 4.11, and the spectral transmission from Figure 4.38, equation (16) predicts the spectral blackbody radiation emission that is received by the detection system from a unit of soot volume fraction. An example is shown in Figure 4.39 for radiation intensities through the detection system calculated using the ULSD adiabatic flame temperatures. Integrations of radiation emission intensities under all wavelengths results in the total received radiation emissions as a function of adiabatic flame temperatures, as represented by ULSD and gasoline, shown in Figure 4.40. Normalizations are performed with respect to the radiation of gasoline at 800 K and 10% oxygen concentration, respectively.

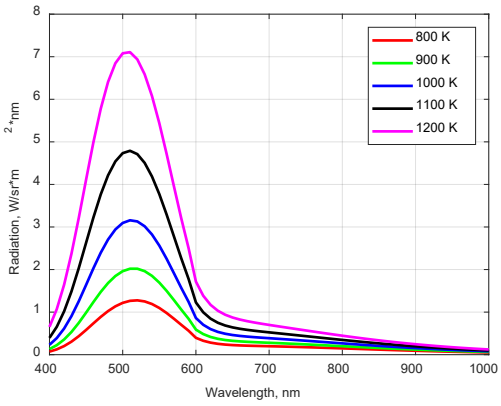

Figure 4.39. Spectral blackbody radiation emission received by the detection system, using adiabatic flame temperatures calculated for ULSD, under a sweep of charge gas temperatures (shown in the legend).

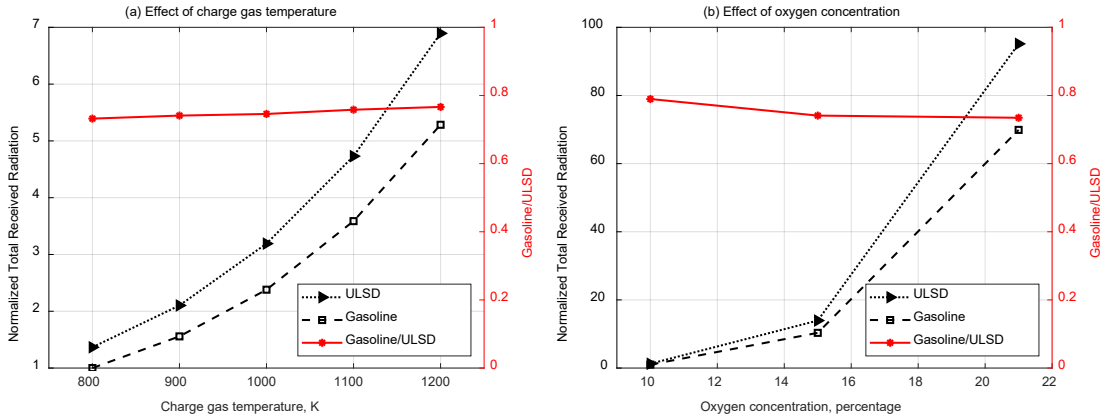

Figure 4.40. Total received radiation emissions by the detection system, calculated based on the adiabatic flame temperatures of gasoline and ULSD, and normalized by gasoline luminosity at 800 K and 10% oxygen concentration, respectively.

As shown in Figure 4.40, the total radiation intensity that transmits through the optical system in this work increases with adiabatic flame temperatures, and much higher sensitivity is shown from the oxygen concentration sweep. The relative ratio between gasoline and ULSD are between 70% and 80%, and exhibit a slight increasing trend and a decreasing trend. This means that a soot particle in a gasoline spray flame will emit 70% to 80% of the total radiation intensity relative to its emission in a ULSD spray flame, under the same ambient charge gas and injection condition. As the charge gas temperature increases, the relative radiation emission from a gasoline spray flame approaches that from a ULSD spray flame.

Comparison of the relative ratio of mean pixel intensity in Figure 4.37 to the relative ratio of total received radiation emissions in Figure 4.40 sheds some light on the relative soot concentrations between gasoline and ULSD. Equation (21) is a direct derivation from equation (20), and quantitatively describe the relationship of relative soot concentration on the relative total received natural luminosity and the relative mean pixel intensities. The two relative ratios are plotted again in Figure 4.41. As equation (21) shows, when the relative total received natural luminosity (NL) signal is lower than the relative mean pixel intensities (I), gasoline spray flame exhibit a lower soot concentration than ULSD, and vice versa.

$$\frac{f_{v_G}}{f_{v_D}} = \frac{NL_G}{NL_U} \cdot \frac{1}{\frac{I_{bb_G}}{I_{bb_U}}} \tag{21}$$

With a sweep of charge gas temperatures, the increase of the relative ratio of mean pixel intensities significantly outpaced the slow increase of relative ratio of received radiation intensities. This suggests that at lower temperatures (800 K, 900 K), much lower soot concentrations occur for gasoline than ULSD. At higher temperatures, the soot

concentrations in the gasoline spray flame exceeds that from ULSD. With a sweep of charge gas oxygen concentrations, the lower relative ratio of mean pixel intensities than the relative ratio of received radiation intensities suggest that lower concentrations of soot exist in gasoline spray flame than ULSD.

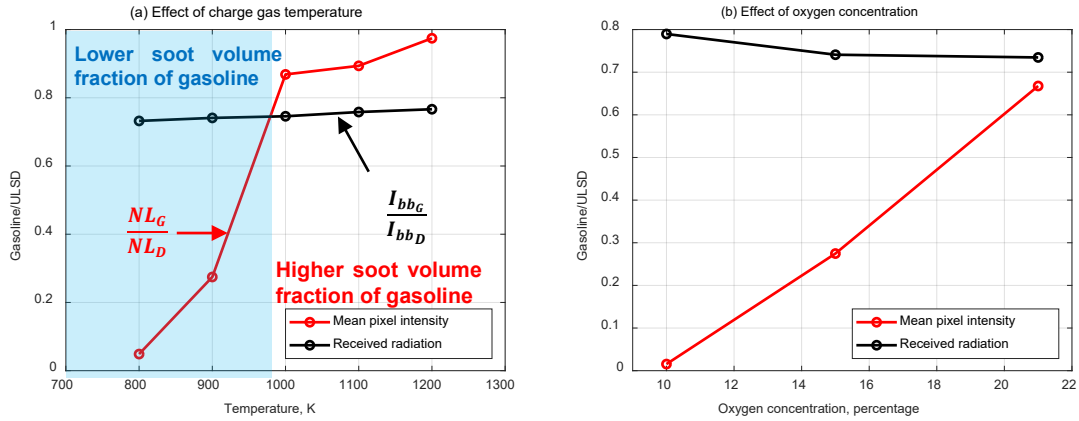

Figure 4.41. Relative ratio of mean pixel intensities and received blackbody radiation intensities.

In general, analyses show that gasoline exhibit lower levels of soot concentration in a spray flame, which is consistent with other experimental investigations. The observation of gasoline's higher than ULSD soot concentrations for temperatures above 1000 K may be affected by the optically thick spray flame assumption. By assuming overall lower soot concentrations of gasoline, the transmission of radiation intensity through the soot cloud is enhanced relative to ULSD. The natural luminosity of the gasoline spray flame therefore consists of contributions not only from the near side of the diffusion flame, but also from the flame core region and even the far side of the diffusion flame. By neglecting the additional contributions, the relative mean pixel intensity ratios may decrease to levels equivalent to the relative received radiation intensity ratio, although quantifying the reduction is challenging.

Through the above analyses, it can be concluded that overall lower levels of soot concentration occur in a gasoline spray flame than ULSD. The soot emission benefits quickly diminishes with an increase in the charge gas temperature and the oxygen concentration.

4.3.4 Summary

High reactivity gasoline and ULSD sprays were tested in a constant-volume vessel under typical diesel engine conditions. The sprays were generated using a single-hole injector indicative of heavy-duty engine applications. A sweep of charge gas temperatures, injection pressures, and oxygen concentrations was conducted. Both optical and pressure-

based diagnostic techniques were employed to investigate the ignition delay, lift-off, and sooting characteristics of the two fuels.

It was found that there is good agreement (on the order of 20%) among the different ignition delay diagnostics used. The deviation, though, originates from the different definitions of ignition events.

Comparing gasoline to ULSD, longer ignition delays and longer lift-off lengths are observed. The ignition delays dominated by chemical processes for both fuels. While ULSD exhibits NTC behavior in the chemical processes, gasoline does not exhibit this behavior. The longer lift-offs are closely related to the longer ignition delays of gasoline, which lead to leaner mixture formed around the ignition location for gasoline.

Ignition of the spray injections is largely kinetically controlled and less influenced by mixing. Higher ambient charge gas temperatures allowed ignition of richer mixtures. Fuel air mixing improvements by higher injection pressures and oxygen concentrations have much smaller influence on the fuel air stoichiometry at the ignition location.

Gasoline exhibits lower levels of soot luminosity than ULSD under all test conditions. It is inferred that soot concentrations in the gasoline spray flame are lower than that in the ULSD spray flame, in general. The benefit of lower soot concentrations is reduced with an increase in the charge gas temperatures and oxygen levels. These two conditions correspond to low temperature combustion and high EGR levels.

4.4 Chapter Summary

This chapter presented the experimental work on the spray and combustion of gasoline in comparison to ULSD. Both non-reacting sprays and reacting sprays are conducted to understand the spray injection, mixing, ignition, combustion, and soot emission characteristics, by using a variety of optical and pressure-based diagnostics. Key observations and conclusions are summarized below:

1. In non-reacting sprays under low ambient temperatures:
   a) Gasoline exhibits larger spray dispersion angles and slower spray penetration than ULSD.
   b) Fuel effects on spray dispersion and spray penetration are mainly reflected in the difference in fuel density. Vaporization might also play a role for high reactivity gasoline injections under these conditions because of its high volatility. It is also believed that other fuel parameters, including viscosity, likely play a minor role compared to fuel density in influencing spray injection characteristics under these conditions.
2. In non-reacting, vaporizing sprays:
   a) Gasoline has a vapor dispersion angle up to 20% larger than ULSD at a charge density of 10kg/m^3 and injection pressure of 150 MPa, although both fuels exhibit very similar vapor penetration (within 5%).

b) Gasoline also has significantly shorter liquid length (by 50%) compared to ULSD.
c) Although high reactivity gasoline and ULSD liquid length share a similar insensitivity to injection pressure, there is an interesting difference observed with respect to charge gas temperature. ULSD shows decreasing liquid length with increasing charge gas temperature, which is the expected trend based on previous work. However, gasoline liquid length remains insensitive to charge gas temperature between 800-1200 K for the injection pressures investigated in this work.
d) This may be due to the influence of local transport of mass, momentum and energy. More analysis is needed to understand this behavior with specific attention to the large differences in fuel properties between ULSD and high reactivity gasoline.

3. In reacting sprays:
   a) Gasoline has longer ignition delays than ULSD under all tested conditions, which is dominated by chemical processes for both fuels. While ULSD exhibits NTC behavior in the chemical processes, gasoline does not exhibit this behavior.
   b) Gasoline has longer lift-off lengths than ULSD, which is closely related to the slower ignition process. The longer lift-off and longer mixing time allows gasoline to form leaner mixtures than ULSD.
   c) The lift-off lengths exhibit different relationships with ignition delays. Under the charge gas temperature sweep, the lift-off length vs ignition delay of the two fuels collapse onto very close curve fit. Under an injection pressure sweep, the ignition delays of both fuels are insensitive while the lift-off lengths increase with injection pressures, and thus lift-off lengths are not correlated. Under an oxygen concentration sweep, lift-off lengths are positively related to ignition delays, however, the two fuels fall on different curve fits.
   d) Ignition of the spray injections is largely kinetically controlled and less influenced by mixing. Higher ambient charge gas temperatures allowed ignition of richer mixtures. Fuel air mixing improvements by higher injection pressures and oxygen concentrations have much smaller influence on the fuel air stoichiometry at the ignition location.
   e) Gasoline exhibits lower levels of soot luminosity than ULSD under all test conditions. It is inferred that soot concentrations in the gasoline spray flame are lower than that in the ULSD spray flame, in general. The benefit of lower soot concentrations is reduced with an increase in the charge gas temperatures and oxygen levels. These two conditions correspond to low temperature combustion and high EGR levels.

5 Development of a Transient Spray Cone Angle Correlation for CFD Simulations at Diesel Engine Conditions [4]

5.1 Background

The spray cone angle of fuel entering the combustion chamber in a diesel engine plays an important role in overall air entrainment and the fuel-air mixing process which in turn leads to flame lift-off length and soot formation. It has been observed in many experimental studies (Raul Payri 2004, Jaclyn Johnson 2011, Payri et al. 2008, Payri et al. 2015) that the spray plume experiences a large cone angle at the beginning of the injection event and then decreases until reaching a quasi-steady state. An increase in the spray cone angle towards the end of injection has also been observed in some studies (Blessing et al. 2003, Jung et al. 2015b, Jung et al. 2015a). The dynamic behavior of the spray dispersion has been observed to affect liquid and vapor phase penetrations (Jung et al. 2015b), as well as ignition locations and lift-off lengths (Jung et al. 2015a) in experiments.

A number of correlations have previously been developed that describe the quasi-steady state spray cone angles with respect to injection and charge gas parameters, and these are summarized in Table 5.1. These correlations share some similarities. For example, the effect of ambient charge gas density has frequently been accounted for with a term of normalized ambient charge gas density by the liquid fuel density. A number of differences remain among the correlations in several aspects:

1. Some of the earlier correlations were developed with water/glycerol (Reitz and Bracco 1979) and water (Arai et al. 1984) which exhibit different liquid properties than the actual fuels the injectors were designed to work with. The range of injection pressures in (Reitz and Bracco 1979, Arai et al. 1984) were also lower than typical injection pressure ranges (over 100 MPa) used on modern diesel engines.
2. The definition of the spray cone angle varies significantly among the correlations in Table 5.1 and also in other references. This has resulted in difficulties directly comparing results from different institutions. Some common methods to quantify the spray cone angles are listed as follows:
   a) An angle formed between the injector tip and two intersection points of half the penetration (Zhang et al. 2014) with the spray boundary
   b) An angle formed between two linear fits on the spray boundary between 1.5 mm and 9 mm (Payri et al. 2015), between 2 mm and 7 mm (Tang, Zhang, Zhu, et al. 2017), from the nozzle tip to 60% of the penetration (Pastor, Arrègle, and

[4]

• Tang, M., Pei, Y., Zhang, Y., Tzanetakis, T., Traver, M., Cleary, D., Quan, S., Naber, J,. Lee, S-Y., "Development of a Transient Spray Cone Angle Correlation for CFD Simulations at Diesel Engine Conditions," SAE Technical Paper 2018-01-0304, 2018, https://doi.org/10.4271/2018-01-0304.

Palomares 2001), or to 10, 20, 30 (Jung et al. 2015b), 45 (Johnson, Naber, and Lee 2012) times the orifice diameter.

c) An angle formed by an isosceles triangle with its height equal to 50% of the penetration and its area equal to that of the spray plume prior to 50% of the penetration (Naber and Siebers 1996), or formed by two lateral sides of an isosceles trapezoid with the two bases 2.5 mm and 20% over the liquid length from the injector tip (Siebers 1999) and the area equal to that of the spray plume between the two bases.

In computational fluid dynamics (CFD) simulations, the spray cone angles are used as inputs to initialize the simulations. As a common practice in CFD simulations, it is the quasi-steady state spray cone angle that is most frequently used rather than the full transient profile. With increasing demands for improved simulation accuracy to meet the design targets, more accurate descriptions of the spray injection process are needed, which includes spray cone angle profiles. The associated challenges are derived from two aspects:

1. For spray simulations under constant charge gas density conditions with high temperatures targeting reacting and non-reacting but vaporizing conditions, the spray cone angle profiles are either not easily measured (reacting condition) or involves effects of vaporization that increases the spray cone angle relative to a non-vaporizing condition (Naber and Siebers 1996). It is the spray cone angle profile under a non-reacting and non-vaporizing condition that is a direct reflection of the hydraulics and liquid-gas momentum transfer associated with fuel injection, which should be used as CFD model inputs.
2. For spray simulations in engine applications, the moving piston induces a change in the charge gas density, which is a parameter known to affect the spray cone angle. This was largely ignored in past studies.

Therefore, the objective of the current work was to develop a correlation that characterizes the spray cone angles from the start of injection to the end of injection and also reflects the change in charge gas density in CFD simulations. Both ultra-low sulfur diesel (ULSD) fuel and a gasoline range fuel (RON = 60) were used, since the application of GCI in a heavy duty engine has shown promise (Pei, Zhang, et al. 2017, Zhang et al. 2017, Zhang et al. 2016), particularly under mixing-controlled combustion conditions

Table 5.1. Summary of literature on spray cone angle correlations.

Reference	Correlation	Angle Definition	Liquid	Gas	Injection pressure (MPa)	Nozzle diameter (mm)	Gas temperature (K)	Gas pressure or density
Reitz, 1979 (Reitz and Bracco 1979)	$\tan\left(\frac{\theta}{2}\right) = \frac{4\pi}{A}\sqrt{\frac{\rho_g}{\rho_L}} f\left(\frac{\rho_L}{\rho_g}\frac{Re_L}{We_L}\right)^2$	N/A	Water + glycerol	Air/N_2/ He/Xe	3.3-16.8	0.34	300	Up to 4 MPa
Arai, 1984 (Arai et al. 1984)	$\theta = 0.025 \cdot \left(\frac{\rho_a \cdot \Delta P \cdot d_o^2}{\mu_a^2}\right)^{0.25}$	Nozzle tip & two intersections @ 60 d_o downstream	Water	N/A	11/19	0.3	N/A	3 MPa
Hiroyasu, 1990 (Hiroyasu and Arai 1990)	$\theta = 83.5\left(\frac{L}{D}\right)^{-0.22}\left(\frac{d_o}{d_{sac}}\right)^{0.15}\left(\frac{\rho_a}{\rho_l}\right)^{0.26}$	N/A	Diesel	N_2	Up to 80	0.3	N/A	3 MPa
Arrègle, 1999 (Arrègle, Pastor, and Ruiz 1999)	$\tan\left(\frac{\theta}{2}\right) = d_0^{0.508} \cdot P_{inj}^{0.00943} \cdot \rho_a^{0.335}$	N/A	Diesel	SF_6 (Coghe 1994)	30/50/70/ 90/110	0.11/0.19/ 0.27	Room temp	10/20/30 kg/m^3
Siebers, 1999 (Siebers 1999)	$\tan\left(\frac{\theta}{2}\right) = c \cdot \left[\left(\frac{\rho_a}{\rho_f}\right)^{0.19} - 0.0043\sqrt{\frac{\rho_f}{\rho_a}}\right]$	$\frac{\theta}{2} = tan^{-1}\left(\frac{A_x}{x_2^2 - x_1^2}\right)$, x_1, x_2: 2.5 mm - 20% + liquid length	Diesel	N_2+CO_2+ H_2O	40-190	100/180/ 251/246/ 267/363/ 498	700-1300	3.3-60 kg/m^3
Delacourt, 2005 (Delacourt, Desmet, and Besson 2005)	$\theta = \frac{360}{\pi} arctan\left[0.31 \cdot \left(\frac{\rho_a}{\rho_f}\right)^{0.2}\right]$	Average of all angles from 1.5d_o to 70% penetration	Diesel	CO_2	80-250	0.15	303	15-45 kg/m^3

5.2 Experiments and Data Processing Methods

The same experiments in the non-reacting sprays under low charge gas temperatures are used in this chapter to develop the spray cone angle correlation.

Experimentally generated images were analyzed to obtain the spray cone angle. The image processing methods are shown in Figure 5.1, which includes the following procedure:

1. Reading in image data from an 8 bit gray scale uncompressed file.
2. Performing background subtractions of irrelevant information.
3. Applying thresholds to grayscale images to obtain binary images. The threshold is selected as 5% of the upper limit of pixel intensity (255).
4. Performing boundary tracking.
5. Identifying the spray cone angle by performing a linear fit on either side of the spray plume boundary from the injector tip to 45 times the orifice diameter (Johnson, Naber, and Lee 2012). The spray cone angle is defined by the angle enclosed by the two linear fits. Exceptions occur at very short times after the start of injection, when the spray penetrations do not reach 45 times the orifice diameter. Thus 60% of spray penetration is used until 45 times the orifice diameter is reached by 60% of the spray penetration.

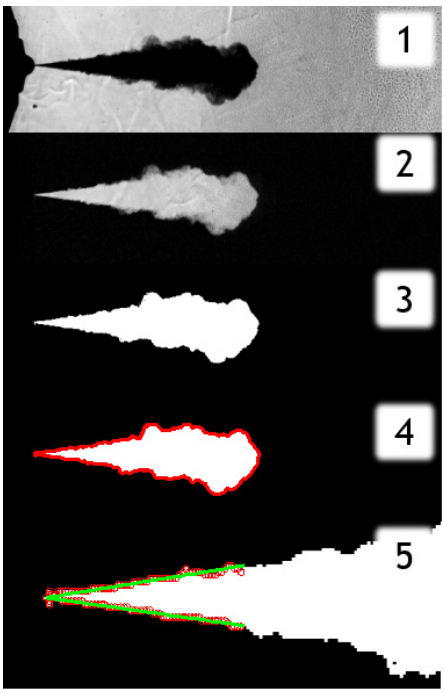

Figure 5.1. Illustration of the image processing methods. The liquid fuel is shown as a dark spray plume in the bright background.

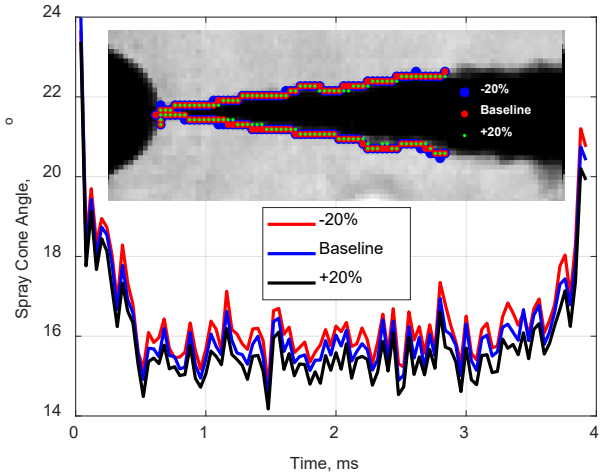

Figure 5.2. Sensitivity of spray cone angles to thresholds. Spray boundaries from different thresholds overlaid on the test image taken at 2 ms. Test condition: 31.3 kg/m^3 charge gas density, 100 MPa injection pressure, gasoline.

This procedure was implemented in the MathWorks® MATLAB® programming environment. Sensitivity of the spray cone angle to the threshold used was tested by increasing and decreasing the threshold value by 20%, the results of which are shown in Figure 5.2. Only a minor influence of the threshold value was detected using the sensitivity study. In terms of the distance downstream of the injector tip for definition of the spray cone angle, it was shown in the introduction that many distances have been used by different studies without a clear consensus. A sensitivity study of the spray cone angles using definitions of 30 times, 45 times and 60 times the orifice diameters (corresponding to 5.3 mm, 7.9 mm and 10.6 mm) downstream of the injector tip is shown in Figure 5.3. Results indicate that the range of distances selected has minimal influence on the result, and so 45 times the orifice diameter was chosen for this study.

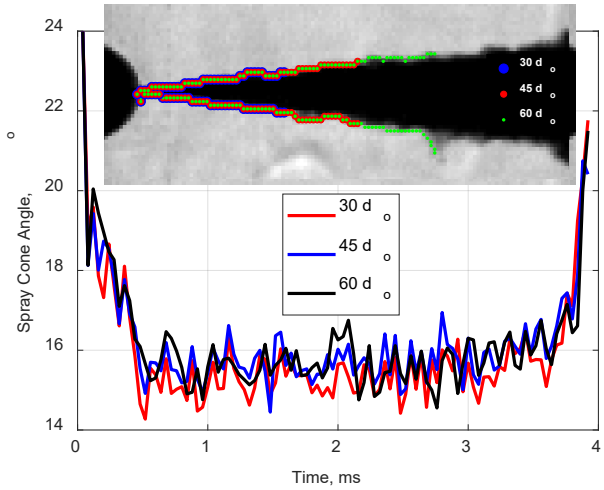

Figure 5.3. Spray cone angles resulting from definitions using different distances downstream. Spray boundaries defined using different distances overlaid on the test image taken at 2 ms. Test condition: 31.3 kg/m^3 charge gas density, 100 MPa injection pressure, gasoline.

5.3 Development of the Correlation

The characteristics of the spray cone angle profile from one sample test is shown in Figure 5.4. As shown, three realizations were averaged to obtain the mean spray cone angle profile. The trend of the profile shows a decay after the start of injection (SOI) until it reaches a quasi-steady state, and then transitions to a rise towards the end of injection (EOI). To model the spray cone angle profile from SOI to EOI, several important features were characterized as shown in Figure 5.4:

1. Max angle @ SOI: the maximum angle at the start of injection.
2. Initial decay: the period from the SOI to the transition @ SOI.
3. Transition @ SOI: the time when the decreasing average profile (black line) intersects the mean spray cone angle plus one standard deviation from the quasi-steady state (red dashed line).
4. Quasi-steady state: the mean spray cone angle is defined as the mean of the spray angle profile between 20% and 80% of the injection duration.
5. Transition @ EOI: the time when the increasing average profile (black line) intersects the mean spray cone angle plus one standard deviation from the quasi-steady state (red dashed line).
6. Rise @ EOI: the period from the transition @ EOI to the EOI.
7. Max angle @ EOI: the maximum angle at the end of injection.

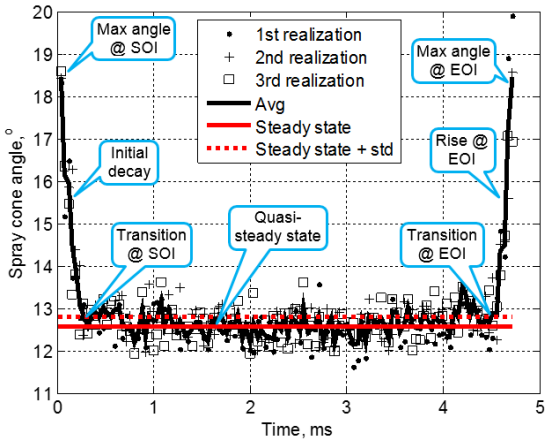

Figure 5.4. A sample spray cone angle profile resulting from three test repeats. Gasoline, 10.3 kg/m^3 charge gas density, 150 MPa injection pressure.

Development of the correlation relied on the seven characteristics listed above except for the 2nd and the 6th, since the initial decay and the rise towards the end of injection can be represented by fitting through the connecting characteristics. An overview of the influence of injection pressure and charge gas densities on the spray cone angle profile is shown in Figure 5.5. An increase in the quasi-steady state spray cone angle with respect to increased injection pressures and charge gas densities was observed. In addition, the hydraulic injection duration increased with injection pressures. The rest of this section quantifies the key characteristics discussed above.

5.3.1 Maximum Angles at SOI

The spray cone angle profile begins with a larger angle compared to the quasi-steady state. The angle at SOI is usually the largest, although there are observations from Figure 5.5(b) and another study (Jung et al. 2015b) that the maximum angle occurs sometime after the SOI. A simplification was made that assumed that the maximum angle occurs right at the SOI. Another artifact observed from Figure 5.5(a) for the 100 MPa injection pressure case is that a nearly 40% drop in the spray cone angle occurs between the first and the second time instances. There are uncertainties in characterizing the very initial spray angle which is dependent upon nozzle and sac conditions (liquid / vapor / gas) that are not the same in the spray chamber as compared to an engine. Given that it occurs for a relatively short time, it can be ignored with respect to the impact of the overall spray and development. The maximum angles under these circumstances consider the first data point as an outlier. The maximum angles at the SOI are plotted against the charge gas density and the injection pressure in Figure 5.6. The maximum angles at SOI have relatively weak correlations with respect to both charge gas densities and injection pressures. Consequently, these angles have been simplified as ensemble averages for both gasoline and ULSD, as shown in Table 5.2. The errors are quantified as the mean differences between all data points and model results are also shown in Table 5.2, which are normalized by the model results to obtain the percent difference.

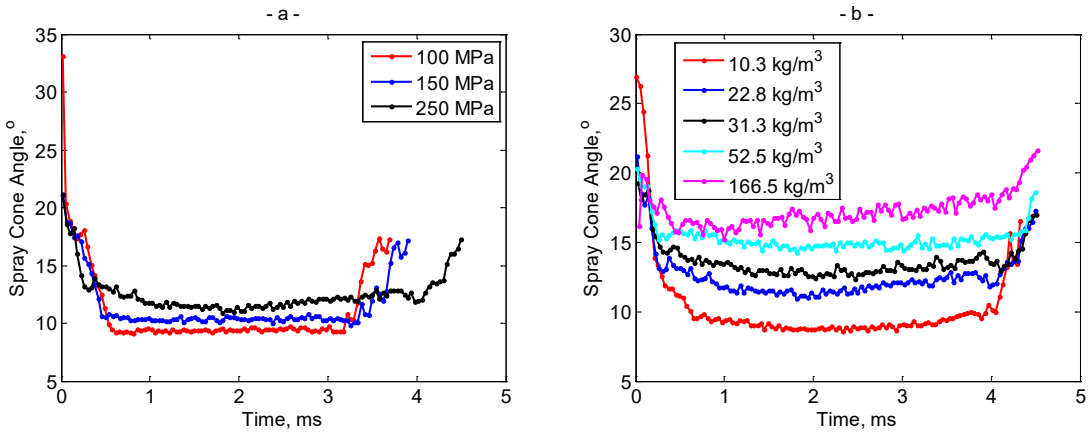

Figure 5.5. Spray cone angle profile versus (a) injection pressures and (b) charge gas densities. The injection pressure sweep was performed with gasoline fuel, under a charge gas density of 10.3 kg/m^3. The charge gas density sweep was done at an injection pressure of 250 MPa.

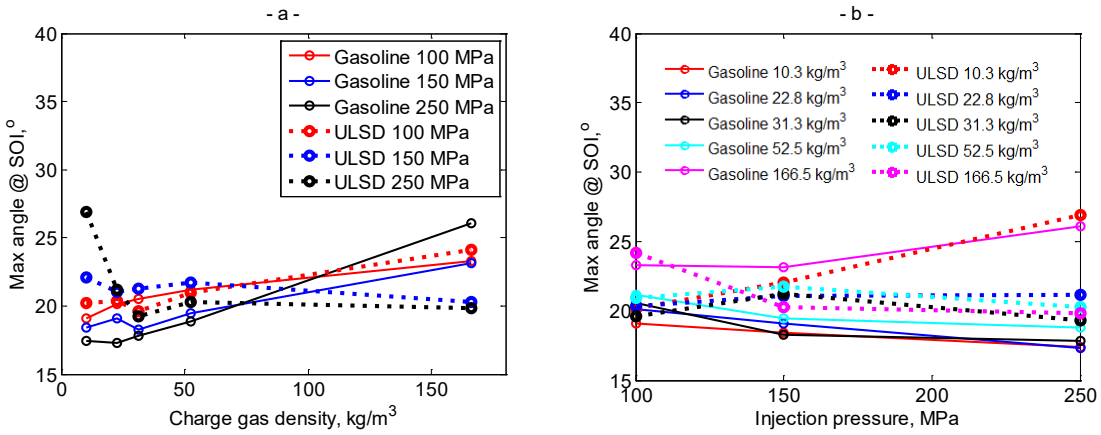

Figure 5.6. Max angle @ SOI versus (a) charge gas densities and (b) injection pressures

Table 5.2. Maximum angle @ SOI for ULSD and gasoline.

Fuel	Max angle @ SOI, °	Mean difference, °	% difference
ULSD	20.8	1.24	5.96%
Gasoline	20.6	2.10	10.2%

5.3.2 Transition Times at SOI

The transition time between the initial decay and the quasi-steady state were characterized at the spray cone angle that corresponds to the mean angle plus one standard deviation at the quasi-steady state condition. Results are shown in Figure 5.7. The durations are influenced more by injection pressures than charge gas densities. This is related to the movement of the needle in the nozzle. With higher injection pressures, the needle

accelerates faster and reduces the time needed to fully open the nozzle holes, which agrees with the needle lift measurements performed for the production injector at Argonne National Laboratory's Advanced Photon Source facilities (Torelli et al. 2017). However, (Jung et al. 2015b) concluded that the transition period in the spray cone angles lasts longer than the rise in the rate of injection profile. Since this is also related to the needle lift profile, there may be other processes that control the stabilization of spray cone angles.

The transition time is modeled against the injection pressure to reflect the trend observed in Figure 5.7(b). The transition times are averaged for all charge gas densities for each of the fuels under each injection pressure. This leads to results shown in Figure 5.8. The transition times are lower for gasoline than ULSD, which is hypothesized to be related to gasoline's lower viscosity (see Table 1.1). The decreases in time with respect to injection pressure are modeled by power functions given in Table 5.3. The errors are quantified as the mean differences between all data points and the modeled results, as well as the percent difference.

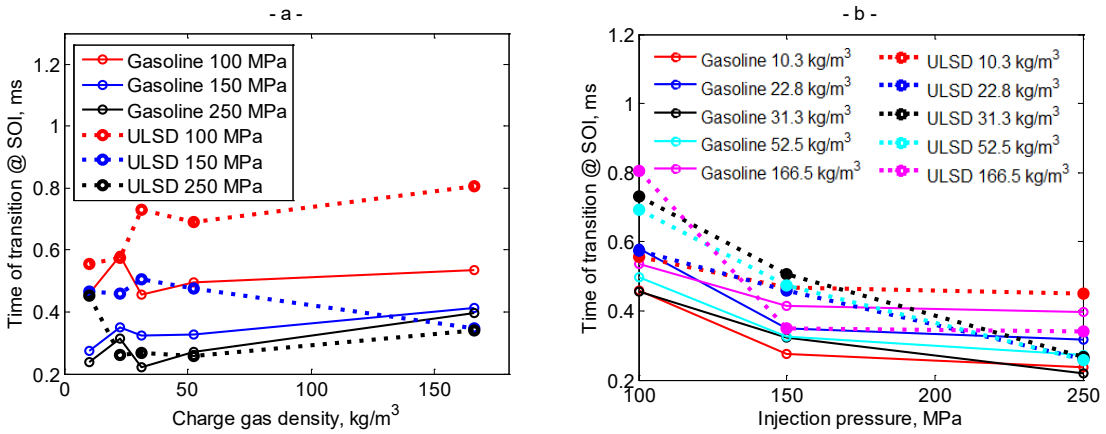

Figure 5.7. Transition time @ SOI versus (a) charge gas densities and (b) injection pressures.

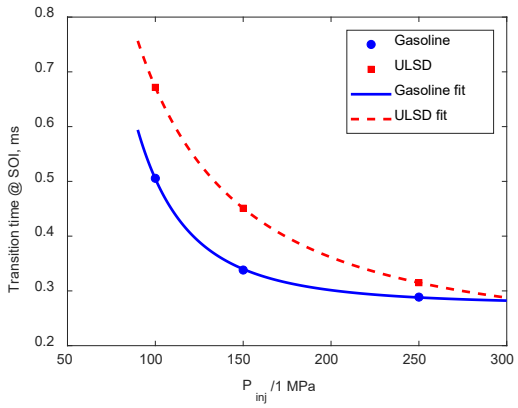

Figure 5.8. Transition time @ SOI versus normalized injection pressures.

Table 5.3. Correlations for transition time @ SOI for ULSD and gasoline.

Fuel	Transition time @ SOI, ms	Mean diff., ms	% diff.
ULSD	$t_{\text{ULSD trans SOI}} = (6.850e2) \cdot \left(\frac{P_{inj}}{1\ MPa}\right)^{-1.584} + 0.2058$	0.063	13.2%
Gasoline	$t_{\text{Gasoline trans SOI}} = (3.846e5) \cdot \left(\frac{P_{inj}}{1\ MPa}\right)^{-3.112} + 0.2747$	0.044	11.6%

5.3.3 Quasi-Steady State Spray Cone Angles

Quasi-steady state spray cone angles were defined as the mean of the spray cone angle profile between 20% and 80% of the injection duration. The angles are plotted against charge gas densities for gasoline and ULSD under each injection pressure with their standard deviations in Figure 5.11. It is observed that gasoline sprays exhibit larger angles than ULSD under the same injection pressure during the quasi-steady state period across all the test conditions investigated. Also, gasoline angles are relatively insensitive to injection pressures, while ULSD angles show otherwise. This leads to difficulties in direct application of the correlations for quasi-steady state spray cone angles shown in Table 5.1, since no single correlation accounts for sensitivities of spray cone angles to injection pressures according to different fuels. Thus the modeling practice in (Naber and Siebers 1996) is followed in order to correlate the tangent of half the spray cone angle with the normalized charge gas density through power functions.

For gasoline, the spray cone angles under three injection pressures are modeled as a single correlation, while for ULSD, the spray cone angles under three injection pressures are modeled separately. The results of the curve fitting are shown in Figure 5.10 with the details in Table 5.4. For ULSD, the coefficients in the three correlations are plotted against normalized injection pressures as shown in Figure 5.11, and are modeled with power functions shown in Table 5.4. The r-squared value for each fitting is listed in the table as well, and are all above 90%, indicating that the fits are good representations of the data points. Mean differences and percent differences between all data points and the modeled results are also shown that suggest a good representation of the data point.

From the formulation of the correlations, it is observed that the charge gas density normalized by fuel liquid density could affect the spray cone angle. With larger liquid fuel densities, the spray cone angles tend to become smaller. One of the prior studies using the same experiments (Tang et al. May 2017) concluded that the liquid fuel density was the main cause of the difference in the quasi-steady state spray cone angles, with other potential contributing factors including boiling points and viscosity. In that study the spray cone angle was defined using the linear fits from the injector tip to 60% of the spray penetration. The different conclusions drawn from two spray cone angle definitions suggest that the fuel effects are likely more complex.

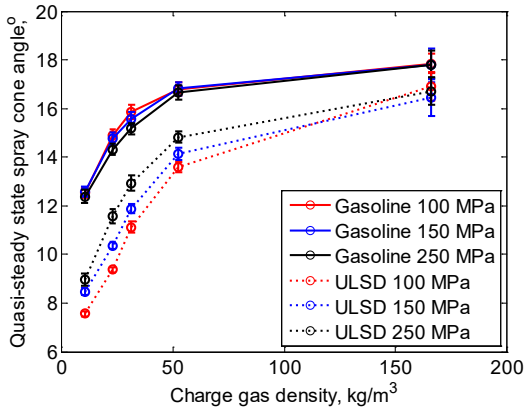

Figure 5.9. Quasi-steady state spray cone angles versus charge gas densities for ULSD and gasoline.

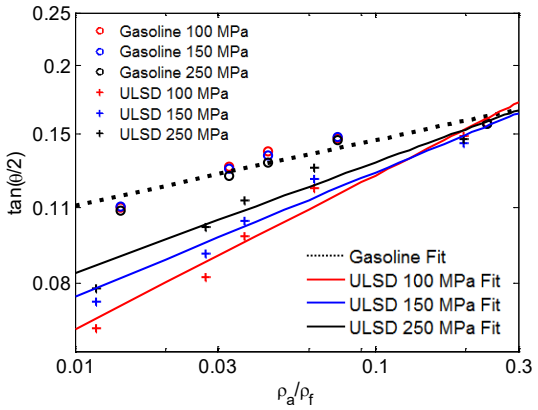

Figure 5.10. Quasi-steady state spray cone angles vs. charge gas to fuel density ratio for ULSD and gasoline.

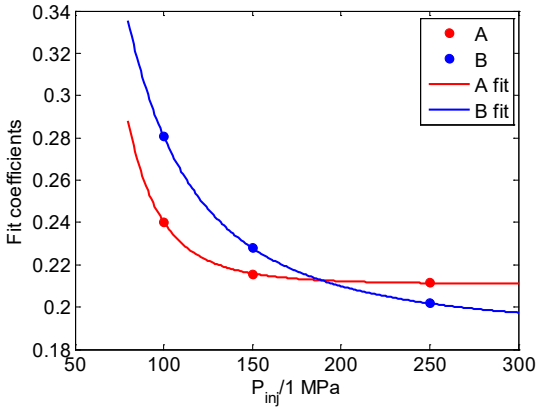

Figure 5.11. A, B coefficient for ULSD spray cone angle correlations.

Table 5.4. Correlations for quasi-steady state spray cone angles for ULSD and gasoline.

Fuel	Quasi-steady state spray cone angle	R^2	Mean diff, °	% diff
ULSD	P_{inj} = 100 MPa, $\tan\left(\frac{\theta_{ULSD}}{2}\right) = 0.2403 \cdot \left(\frac{\rho_a}{\rho_f}\right)^{0.2808}$	96.8%	0.52	4.44%
	P_{inj} = 150 MPa, $\tan\left(\frac{\theta_{ULSD}}{2}\right) = 0.2156 \cdot \left(\frac{\rho_a}{\rho_f}\right)^{0.2280}$	95.1%	0.56	4.57%
	P_{inj} = 250 MPa, $\tan\left(\frac{\theta_{ULSD}}{2}\right) = 0.2116 \cdot \left(\frac{\rho_a}{\rho_f}\right)^{0.2018}$	93.3%	0.64	4.92%
	$\Rightarrow$ $\tan\left(\frac{\theta_{ULSD}}{2}\right) = A \cdot \left(\frac{\rho_a}{\rho_f}\right)^{B}$ $A = (1.314e7) \cdot \left(\frac{P}{1\ MPa}\right)^{-4.325} + 0.2108$ $B = (1283) \cdot \left(\frac{P}{1\ MPa}\right)^{-2.070} + 0.1878$			
Gasoline	$\tan\left(\frac{\theta_{Gasoline}}{2}\right) = 0.1922 \cdot \left(\frac{\rho_a}{\rho_f}\right)^{0.1192}$	90.2%	0.53	3.43%

5.3.4 Transition Times at EOI

In characterizing the transition of spray cone angles from the quasi-steady state towards the end of injection, two methods can be used:

1. Characterizing the time when the transitions occur.
2. Characterizing the duration from the transition until the end of injection.

Since only one electronic injector drive signal duration was used in this study, characterizing the time when transitions occur was not considered useful. However, the duration from the transition until the end of injection is expected to be similar across injection durations, since the spray has fully developed. Therefore the second method is used in this study to represent the transition times towards the EOI.

The transition times towards the EOI are plotted with respect to charge gas densities and injection pressures in Figure 5.12. It is observed that transition times are weakly correlated with charge gas densities. There are some general trends of the transition time with respect to injection pressures with a drop from 100 MPa to 150 MPa and a rise from 150 MPa to 250 MPa. This becomes more evident by taking averages of the transition times at the same injection pressure for each fuel, shown in Figure 5.13. This trend is modeled with a second-order polynomial function with respect to normalized injection pressures as shown in Table 5.5.

The time when the transition from the quasi-steady state to the end of injection increases with the injection pressure as shown in Figure 5.5(a), which is related to the movement of

the needle as also found during the initial transient period. The factors affecting the transition times toward the EOI are as complex as those for the transition times at the SOI.

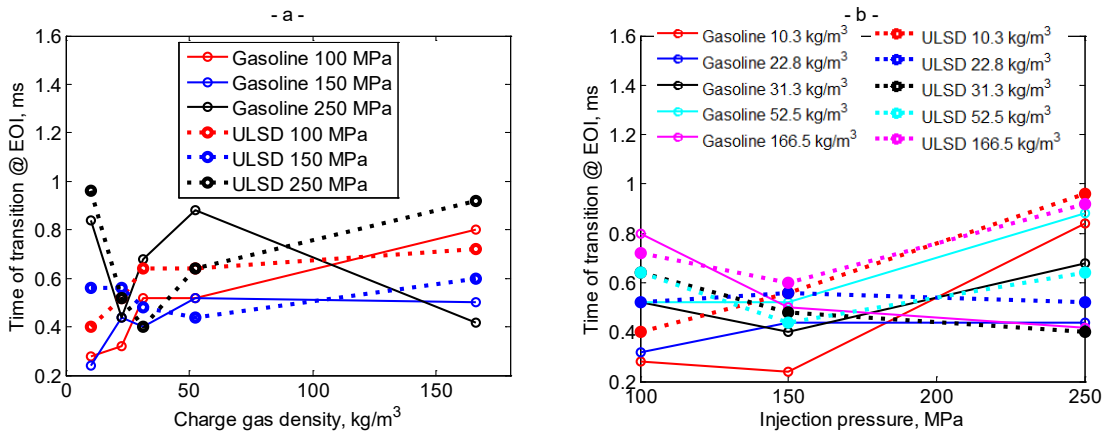

Figure 5.12. Transition time @ EOI versus (a) charge gas densities and (b) injection pressures.

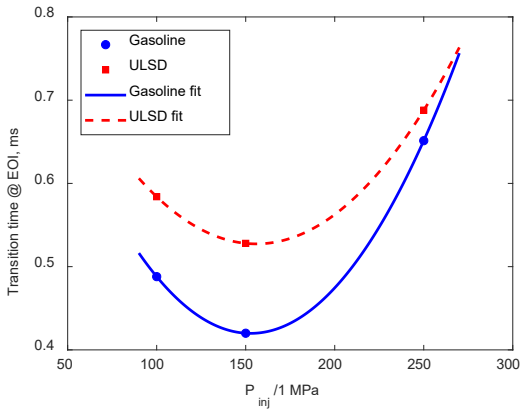

Figure 5.13. Transition time @ EOI versus normalized injection pressures.

Table 5.5. Correlations for transition time @ EOI for ULSD and gasoline.

Fuel	Transition time @ EOI, ms	Mean diff, ms	% diff
ULSD	$t_{ULSD\ trans\ EOI} = (1.813e-5)\cdot\left(\frac{P_{inj}}{1MPa}\right)^2 - (5.653e-3)\cdot\left(\frac{P_{inj}}{1MPa}\right) + 0.9680$	0.12	19.7%
Gasoline	$t_{Gasoline\ trans\ EOI} = (2.449e-5)\cdot\left(\frac{P_{inj}}{1MPa}\right)^2 - (7.482e-3)\cdot\left(\frac{P_{inj}}{1MPa}\right) + 0.9913$	0.14	26.2%

5.3.5 Maximum Angles at EOI

The maximum angles at the EOI are processed the same way as those at the SOI. Results are plotted against charge gas densities and injection pressures in Figure 5.14. With respect to charge gas densities, the maximum angles for ULSD exhibit an increasing trend whereas those for gasoline exhibit a weak correlation. With respect to injection pressures, no obvious trends are established for either ULSD or gasoline. Except for the highest charge gas density condition, the maximum angles at the EOI are generally larger for gasoline than ULSD, despite gasoline's shorter periods for the increase in spray cone angles towards the EOI, shown in Figure 5.13.

Modeling of the ULSD maximum angles at the EOI were done to capture the trend in Figure 5.14 by averaging the angles under the same charge gas density for each fuel. Results are plotted in Figure 5.15, and a second-order polynomial is used to model the trend. For gasoline, an average value was used and these correlations are shown in Table 5.6.

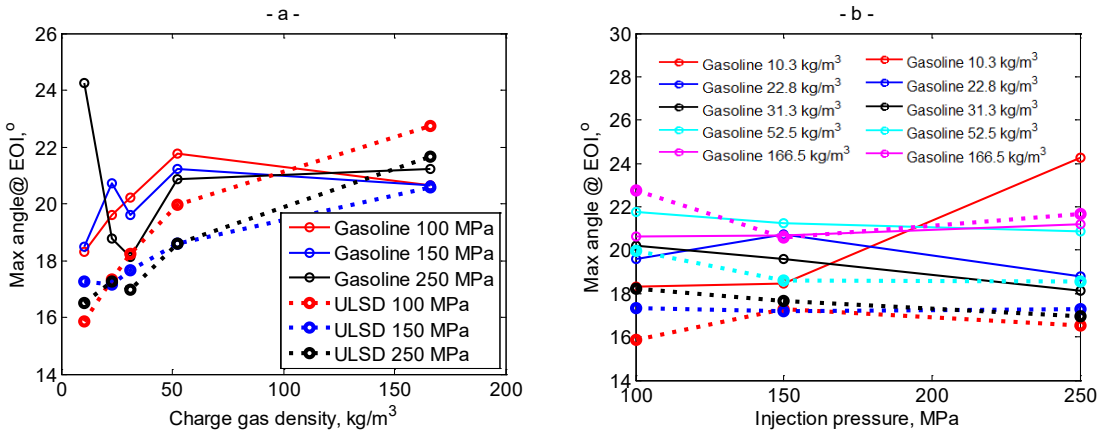

Figure 5.14. Max angle @ EOI versus (a) charge gas densities and (b) injection pressures.

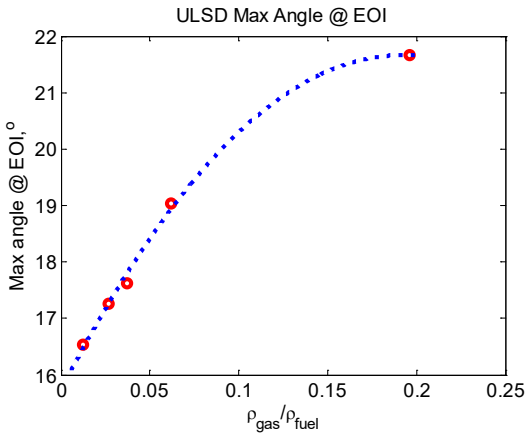

Figure 5.15. Mean max angles @ EOI versus normalized charge gas densities.

Table 5.6. Correlations for maximum angles @ EOI for ULSD and gasoline.

Fuel	Max angle @ EOI, °	Mean diff., °	% diff.
ULSD	$\theta_{ULSD\ max\ EOI} = -160.2 \cdot \left(\frac{\rho_{gas}}{\rho_{fuel}}\right)^2 + 61.67 \cdot \left(\frac{\rho_{gas}}{\rho_{fuel}}\right) + 15.73$	0.46	2.50%
Gasoline	20.3	1.20	5.91%

5.3.6 Formulation of the Spray Cone Angle Correlation

With the correlations for five of the seven characteristics already developed, the final step before formulation of the spray cone angle correlation was to model the initial decay and rise towards the EOI. These two processes were modeled with exponential functions in the form of equation (22), in which the positive and negative signs represent the rise and the decay, respectively. With two unknowns a and b, and the coordinates for the beginning and ending points known from the exponential functions, the a and b terms were solved to represent the two transient processes in the correlation.

$$\theta = a \cdot e^{\frac{\pm t}{t_{trans}}} + b \qquad (22)$$

The objective of the spray cone angle correlation was to enable spray and combustion simulations with a more realistic spray cone angle profile that not only scales with injection pressures but dynamically changes with respect to the in-cylinder or ambient charge gas conditions. The model works with the following independent variables:

1. Fuel type: ULSD or gasoline.
2. Injection pressure P_{inj}.
3. Charge gas density ρ_{inj}.
4. Hydraulic injection duration t_{EOI}.

The first three inputs were used in the development of the correlation while the last input, the hydraulic injection duration, is an important parameter that affects the shape of the spray cone angle profile. For a pilot injection with a very short injection duration (shorter than the transient periods at the SOI and EOI combined), the quasi-steady state of the spray cone angle does not exist in the profile. The injection duration is then divided into two periods corresponding to a decay and a rise, which are proportional to the transient periods at the SOI and the EOI. In formulating the decay and the rise, the quasi-steady state spray cone angle is still used as an input, but is not reached during the injection. For injection durations of sufficient length (greater than the transient periods at the SOI and EOI combined), the profile consists of a decay, a quasi-steady state and a rise. The detailed correlation is shown in Table 5.7. Correlation for the ULSD and gasoline spray cone angle profile. Note that the gasoline in this study was a high-reactivity gasoline and caution

should be exercised when applying the correlations to market gasoline despite their similarities in physical properties.

Table 5.7. Correlation for the ULSD and gasoline spray cone angle profile.

ULSD	If $t_{EOI}<t_{ULSD\ trans\ SOI}+t_{ULSD\ trans\ EOI}=\left[(6.850\cdot10^{2})\cdot\left(\frac{P}{1MPa}\right)^{-1.584}+0.2058\right]+\left[(1.813\cdot10^{-5})\cdot\left(\frac{P}{1MPa}\right)^{2}-(5.653\cdot10^{-3})\left(\frac{P}{1MPa}\right)+0.9680\right]$, ms
	If $t_{CFD}<\frac{t_{ULSD\ trans\ SOI}}{t_{ULSD\ trans\ SOI}+t_{ULSD\ trans\ EOI}}\cdot t_{EOI}$
	$\theta=1.5820\cdot(\theta_{ULSD\ max\ SOI}-\theta_{ULSD\ ss})\cdot e^{\frac{-t_{CFD}}{t_{ULSD\ trans\ SOI}}}+(1.5820\cdot\theta_{ULSD\ ss}-0.5820\cdot\theta_{ULSD\ max\ SOI})$, degrees $\theta_{ULSD\ max\ SOI}=20.8$, degrees
	Else
	$\theta=0.5820\cdot(\theta_{ULSD\ max\ EOI}-\theta_{ULSD\ ss})\cdot e^{\frac{t_{CFD}\cdot(t_{EOI}-t_{ULSD\ trans\ EOI})}{t_{ULSD\ trans\ EOI}}}+(1.5820\cdot\theta_{ULSD\ ss}-0.5820\cdot\theta_{ULSD\ max\ EOI})$, degrees $\theta_{ULSD\ max\ EOI}=-160.2\cdot\left(\frac{\rho_{amb}}{\rho_{ULSD}}\right)^{2}+61.67\cdot\left(\frac{\rho_{amb}}{\rho_{ULSD}}\right)+15.73$, degrees
	Else
	If $t_{CFD}\le t_{ULSD\ trans\ SOI}=(6.850\cdot10^{2})\cdot\left(\frac{P}{1MPa}\right)^{-1.584}+0.2058$ ms
	$\theta=1.5820\cdot(\theta_{ULSD\ max\ SOI}-\theta_{ULSD\ ss})\cdot e^{\frac{-t_{CFD}}{t_{ULSD\ trans\ SOI}}}+(1.5820\cdot\theta_{ULSD\ ss}-0.5820\cdot\theta_{ULSD\ max\ SOI})$, degrees
	Elseif $t_{CFD}\le t_{EOI}-t_{ULSD\ trans\ EOI}=t_{EOI}-\left[(1.813\cdot10^{-5})\cdot\left(\frac{P}{1MPa}\right)^{2}-(5.653\cdot10^{-3})\cdot\left(\frac{P}{1MPa}\right)+0.9680\right]$, ms
	$\theta=\theta_{ULSD\ ss}=2\cdot\arctan(A\cdot(\rho_{amb}/\rho_{ULSD})^{B})\cdot\frac{180}{\pi}$, degrees $A=(1.314\cdot10^{7})\left(\frac{P}{1MPa}\right)^{-4.325}+0.2108$, $B=(1283)\left(\frac{P}{1MPa}\right)^{-2.07}+0.1878$
	Else
	$\theta=0.5820\cdot(\theta_{ULSD\ max\ EOI}-\theta_{ULSD\ ss})\cdot e^{\frac{t_{CFD}\cdot(t_{EOI}-t_{ULSD\ trans\ EOI})}{t_{ULSD\ trans\ EOI}}}+(1.5820\cdot\theta_{ULSD\ ss}-0.5820\cdot\theta_{ULSD\ max\ EOI})$, degrees
Gasoline	If $t_{EOI}<t_{Gasoline\ trans\ SOI}+t_{Gasoline\ trans\ EOI}=\left[(3.846\cdot10^{5})\left(\frac{P_{inj}}{1MPa}\right)^{-3.112}+0.2747\right]+\left[(2.449\cdot10^{-5})\cdot\left(\frac{P_{inj}}{1MPa}\right)^{2}-(7.482\cdot10^{-3})\left(\frac{P_{inj}}{1MPa}\right)+0.9913\right]$, ms
	If $t_{CFD}<\frac{t_{Gasoline\ trans\ SOI}}{t_{Gasoline\ trans\ SOI}+t_{Gasoline\ trans\ EOI}}\cdot t_{EOI}$
	$\theta=1.5820\cdot(\theta_{Gasoline\ max\ SOI}-\theta_{Gasoline\ ss})\cdot e^{\frac{-t_{CFD}}{t_{Gasoline\ trans\ SOI}}}+(1.5820\cdot\theta_{Gasoline\ ss}-0.5820\cdot\theta_{Gasoline\ max\ SOI})$, degrees $\theta_{Gasoline\ max\ SOI}=20.6$, degrees
	Else
	$\theta=0.5820\cdot(\theta_{Gasoline\ max\ EOI}-\theta_{Gasoline\ ss})\cdot e^{\frac{t_{CFD}\cdot(t_{EOI}-t_{Gasoline\ trans\ EOI})}{t_{Gasoline\ trans\ EOI}}}+(1.5820\cdot\theta_{Gasoline\ ss}-0.5820\cdot\theta_{Gasoline\ max\ EOI})$, degrees $\theta_{Gasoline\ max\ EOI}=20.3°$, degrees
	Else
	If $t_{CFD}\le t_{Gasoline\ trans\ SOI}=(3.846\cdot10^{5})\cdot\left(\frac{P}{1MPa}\right)^{-3.112}+0.2747$ ms
	$\theta=1.5820\cdot(\theta_{Gasoline\ max\ SOI}-\theta_{Gasoline\ ss})\cdot e^{\frac{-t_{CFD}}{t_{Gasoline\ trans\ SOI}}}+(1.5820\cdot\theta_{Gasoline\ ss}-0.5820\cdot\theta_{Gasoline\ max\ SOI})$, degrees
	Elseif $t_{CFD}\le t_{EOI}-t_{Gasoline\ trans\ EOI}=t_{EOI}-\left[(2.449\cdot10^{-5})\cdot\left(\frac{P}{1MPa}\right)^{2}-(7.482\cdot10^{-3})\cdot\left(\frac{P}{1MPa}\right)+0.9913\right]$, ms
	$\theta=\theta_{Gasoline\ ss}=2\cdot\arctan\left(0.1922\cdot(\rho_{amb}/\rho_{Naphtha})^{0.1192}\right)\cdot\frac{180}{\pi}$, degrees
	Else
	$\theta=0.5820\cdot(\theta_{Gasoline\ max\ EOI}-\theta_{Gasoline\ ss})\cdot e^{\frac{t_{CFD}\cdot(t_{EOI}-t_{Gasoline\ trans\ EOI})}{t_{Gasoline\ trans\ EOI}}}+(1.5820\cdot\theta_{Gasoline\ ss}-0.5820\cdot\theta_{Gasoline\ max\ EOI})$, degrees

5.4 Comparison of Correlation Outputs against Experimental Measurements

Due to the limited variation of injection pressures (three) and charge gas densities (five), all data points from the experiments were used in developing the correlation, thus

validation on an independent dataset is not available. In this study comparisons of correlation outputs against experimental measurements are provided instead. Four sample comparisons are shown in Figure 5.16, in which the three realizations, the derived mean profile and the modeled spray cone angle profile are shown and compared for both gasoline and ULSD. The trend of spray cone angle profile is captured with reasonable agreement. To quantify the difference between the experimental and modeled results, the normalized root mean square difference (NRMSD) was calculated and is presented in Figure 5.17 for both fuels under all test conditions. Among the 30 cases for correlation development, 23 cases could be modeled with a NRMSD below 10%. Note that when calculating the NRMSDs, the outliers in the spray cone angle were neglected. The case with the largest NRMSD is shown in Figure 5.16(d). The main reason for the large deviation is the underestimation of the maximum angle at the SOI, which is due to the simplification in developing the model.

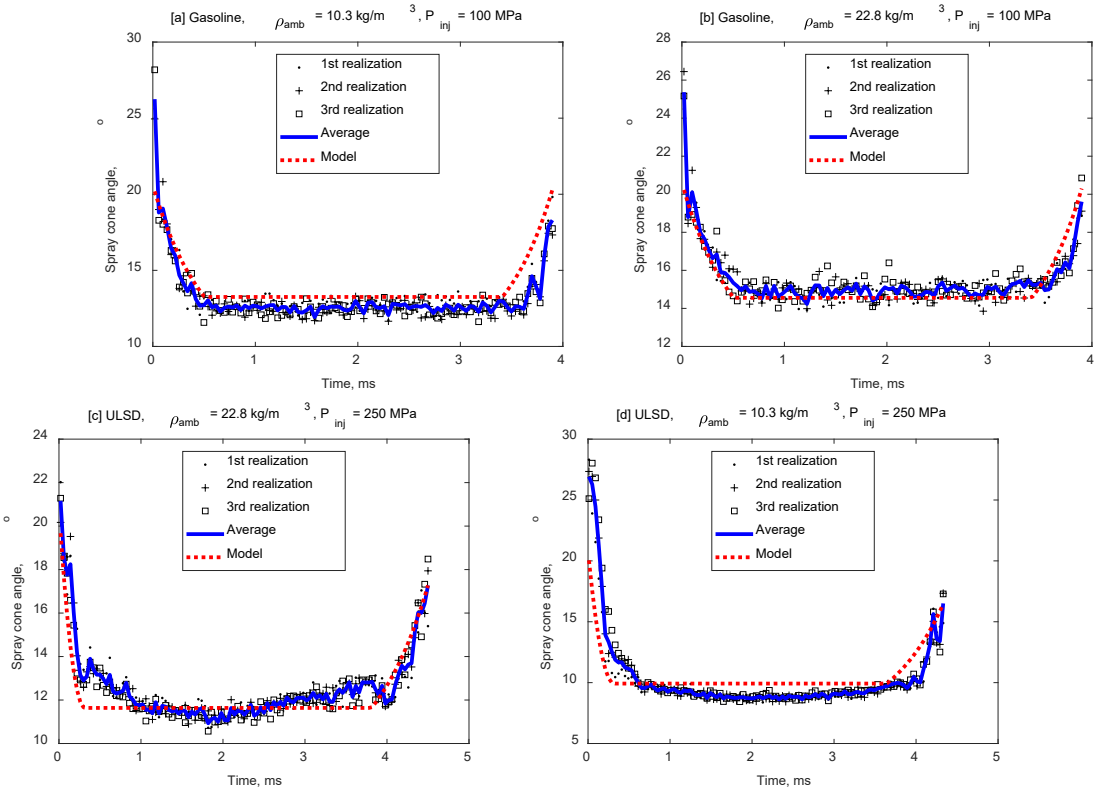

Figure 5.16. Comparisons of model outputs against experimental measurements for selected fuels and test conditions.

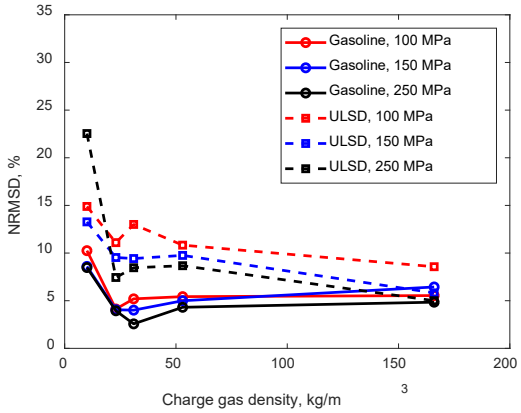

Figure 5.17. Normalized root mean square difference between the experimental and the modeled spray cone angle results.

5.5 Application of the Correlation in CFD Simulations

The effect of transient spray cone angles have been experimentally investigated in (Jung et al. 2015b, Jung et al. 2015a) with respect to vapor and liquid penetrations, ignition delay and lift-off length. A larger spray cone angle at the SOI was demonstrated to lead to a better agreement of the vapor penetrations shortly after SOI through 1D spray modeling, as shown in (Jung et al. 2015b). With the development of the transient spray cone angle correlation and its integration with 3D CFD simulations, it is expected that more accurate transient spray and mixing predictions can be obtained.

The commercial CFD software CONVERGE 2.3 (Manente et al. 2010) was used to simulate gasoline and ULSD sprays under a non-reacting, vaporizing condition with a charge gas density of 20.3 kg/m^3, a charge gas temperature of 1000 K, and an injection pressure of 150 MPa. The injected fuel temperature was 358 K. A traditional Lagrangian spray model was used and its parameters are summarized in Table 5.8. The computational domain was initialized with 89.7% of N_2, 6.5% of CO_2 and 3.8% of H_2O as the ambient gas composition, 0.06 m^2/s^2 as the kinetic energy $\boldsymbol{k}$, and 0.092 m^2/s^3 as the dissipation rate $\boldsymbol{\varepsilon}$. More details of the model description can be found in (Pei, Torelli, et al. 2017b). Integration of the transient spray cone angle correlation was accomplished through the user-defined function, which was updated at each computational time step during the spray injection process.

For comparative purposes, simulations for each fuel were conducted with both a constant and a transient spray cone angle profile as shown in Figure 5.18. The transient profiles for both fuels have similar cone angles at SOI, but ULSD exhibited lower quasi-steady state values, longer transient durations, and smaller spray cone angles at the EOI compared to gasoline.

Table 5.8. Spray model and numerical setups.

Spray models	Liquid phase	Discrete droplet modeling (Dukowicz 1980)
	Injection	Blob (Reitz 1987b)
	Break-up	Kelvin Helmholtz – Rayleigh Taylor (KH-RT) (Patterson and Reitz 1998)
	Droplet collision	No-time-counter (NTC) (Schmidt and Rutland
	Droplet evaporation	Frossling (Frossling 1956)
	Momentum exchange	Dynamic drag model (Liu, Mather, and Reitz
Turbulence Model		Re-normalization group (RNG) k-ε (Yakhot et al.
Grid		Cartesian grid, 4 mm (base), 0.25 mm (smallest) with adaptive mesh refinement (AMR) and fixed embedding near the nozzle

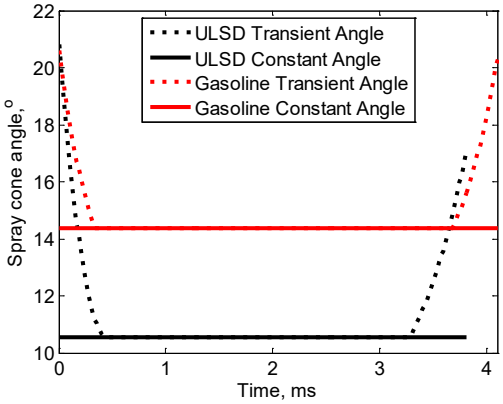

Figure 5.18. Constant and transient spray cone angle profiles for ULSD and gasoline in CFD simulations.

Macroscopic spray characteristics including the vapor and liquid penetrations were extracted from the simulations as shown in Figure 5.19 and Figure 5.20. The liquid length in the simulation was defined as the distance from the nozzle tip to the furthest axial location containing 97% of the liquid fuel mass, and the vapor penetration was defined similarly with 99.9% of the fuel vapor mass. The close agreement with experimental results suggests that the CFD model was capable of capturing the macroscopic spray features of both fuels.

In terms of the vapor penetration length, the result with a transient spray cone angle profile shows a slower ramp-up, which is due to the larger spray cone angle at the beginning of the spray injection process. The slower ramp-up at the beginning trends towards a better agreement with the experimental results compared to using a constant spray cone angle. However, the two penetration curves cross at nearly 0.5 ms for ULSD and 0.3 ms for gasoline. These times occur after the spray cone angle transitions to the quasi-steady state.

The acceleration in penetration is not expected to surpass the spray growth that resulted from using a constant angle and more analysis will be presented later. Comparisons of vapor penetrations were only made up to approximately 2 ms, after which the vapor phase has reached the boundary of the vessel. For mean liquid penetrations, minor effects are observed by using a transient spray cone angle profile.

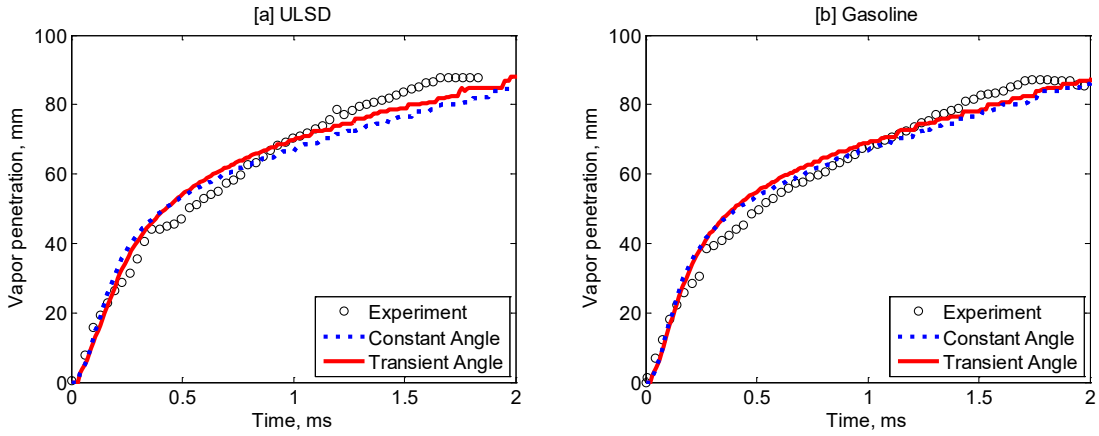

Figure 5.19. Experimental versus simulated vapor penetration lengths using a constant and a transient spray cone angle profiles for (a) ULSD and (b) gasoline.

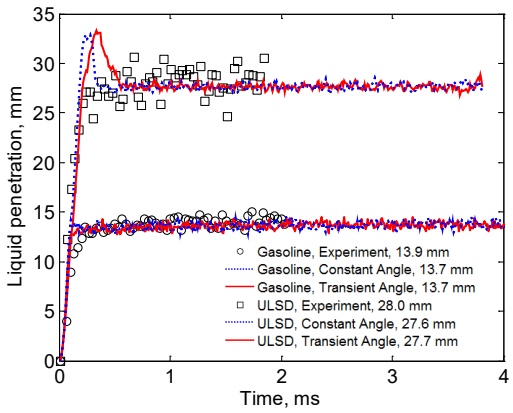

Figure 5.20. Experimental versus simulated liquid penetrations using a constant (quasi-steady state) and a transient spray cone angle profiles for ULSD and gasoline.

The crossing of vapor penetration curves for both fuels is unexpected. To gain more insight, simulations using two more constant cone angles were performed with ULSD. Results using different cone angle profiles are compared, including (1) the transient spray cone angle profile, (2) the constant angle using the quasi-steady state (denoted as 10˚ later), (3) the maximum cone angle at SOI (denoted as 20˚ later), and (4) 30˚.

When comparing the vapor penetrations with a sweep of the spray cone angles as shown in Figure 5.21, it is observed that with an increase in the spray cone angle, the initial ramp-

up slows down, and the penetration curve with a transient spray cone angle profile matches the rising trend with a constant angle at 20˚. Penetration curves with 20˚ and 30˚ spray cone angles converge while the one with 10˚ crosses the other two curves. Illustrations showing the overall fuel mass fraction contours are provided in Figure 5.22. For the simulation with the smallest cone angle, it is very clear that at 0.2 ms, a longer but narrower spray plume is formed, resulting in higher fuel mass fractions than other conditions. This is a result of less entrainment of ambient gases compared to larger cone angles. Penetrations are similar at 0.6 ms but the spray plume grows wider, and continues to 1.2 ms, at which time the penetration shortens and the spray plume becomes visually wider than other conditions. The spray plume at this time also exhibits a diverging shape that is narrower near the nozzle and is wider towards the jet head. This helps explain the reason for the shorter penetrations with the 10˚ spray cone angle. It is hypothesized that two factors, entrained air momentum and droplet collision and coalescence, are in competition. At the beginning phase, the momentum of the spray is so high that the spray dominates the penetration, as observed in Figure 23b. However, in the later phase, with wider spray cone angles leading to more entrained air, the higher entrained air momentum accelerates the spray momentum further, similar to multiple-injection spray behavior, where the momentum created by the pilot injection accelerates the main injection and makes it penetrate further (Moiz, Cung, and Lee , Skeen, Manin, and Pickett 2015, Moiz et al. 2015). Narrower spray cone angles condense the liquid parcels into a smaller region and increase the probability of collision, which may reduce the spray momentum and subsequent vapor penetration.

In addition, comparisons of gasoline spray fuel mass fractions also suggest a similar trend as that observed for ULSD. The differences become smaller as the drop from the maximum angle at SOI towards the quasi-steady state becomes smaller.

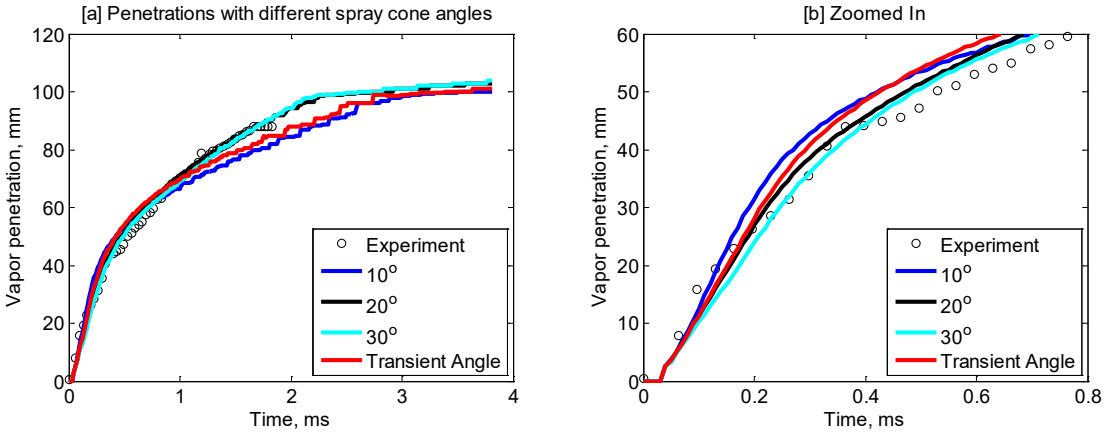

Figure 5.21. [a] ULSD penetrations with different spray cone angles [b] zoomed in view.

Differences in spray cone angle profiles and their resulting vapor penetrations are associated with the mixing process. This is examined by plotting the fuel mass fraction distributions along the spray centerline (injector axis), and along radial directions at different distances downstream of the injector tips as shown in Figure 5.23. The axial and

radial distances are relative to the injector tip and the centerline in these figures. Figure 5.23[a] and [b] show the fuel mass distribution for ULSD while [c] and [d] are results for gasoline. The fuel mass fraction distributions along the axial direction are plotted at two points after SOI while those along the radial directions are plotted at 20 and 75 mm downstream for ULSD and 15 and 75 mm for gasoline. For both fuels, the larger spray cone angle at the SOI leads to lower fuel concentrations, which corresponds to a wider but shorter jet. As the spray progresses, the transient spray cone angle profile results in a penetrating spray with more mass at the jet head than that from a constant angle. With larger differences in spray cone angle profiles and the resulting vapor penetrations for ULSD, the differences in fuel mass distributions are also more evident for ULSD than gasoline.

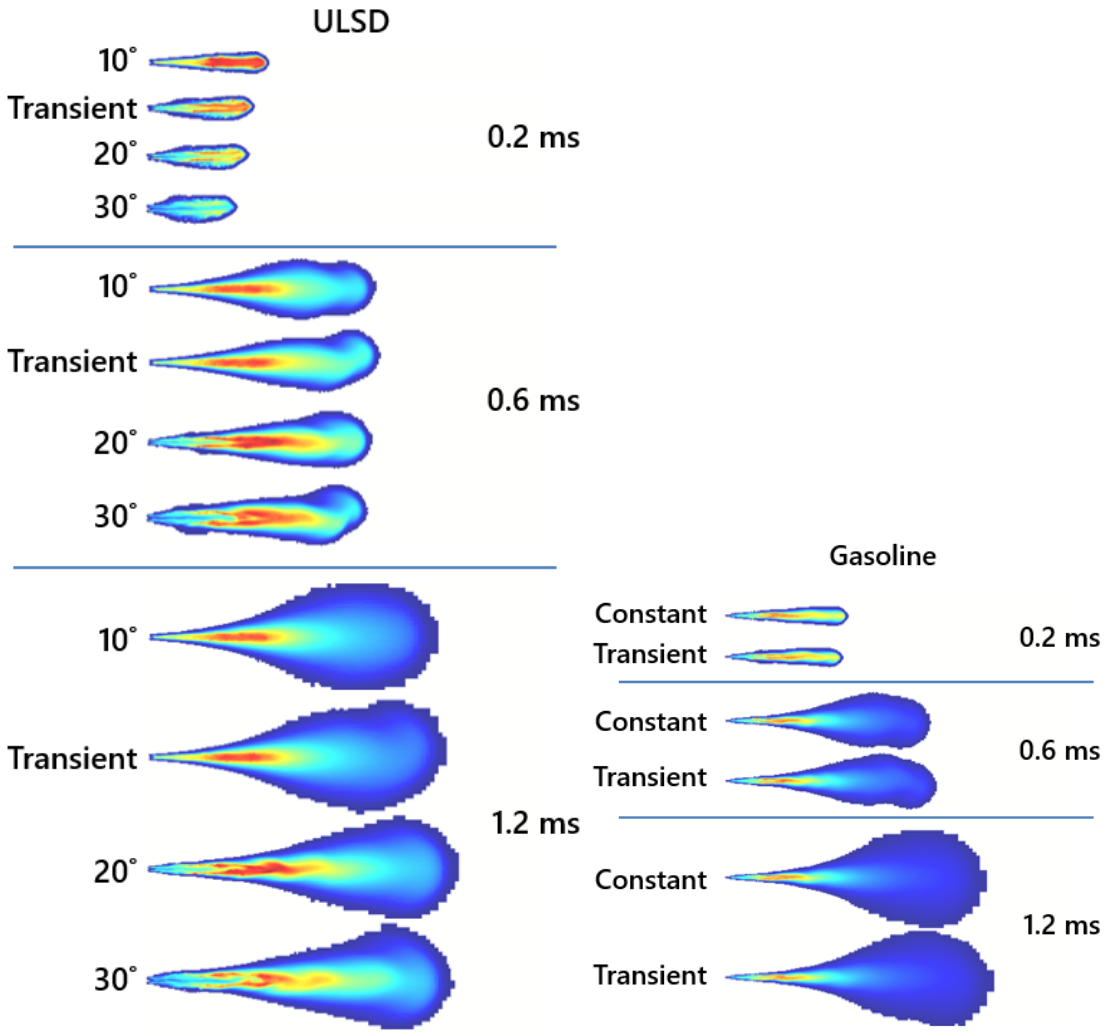

Figure 5.22. Fuel mass fraction contour plots for simulations with 10˚, 20˚, 30˚, and transient spray cone angle for ULSD, a constant angle (quasi-steady state) and transient spray cone angles for gasoline.

To further quantify the mixing process, air utilization is plotted with respect to time after SOI, which is represented by the mass fraction of the cells within the spray region where fuel concentration falls within a certain band. In this study, the two fuel concentration bands are fuel mass fractions over 0.1 and below 0.05, essentially representing rich and lean mixtures, respectively. It is observed that with a transient spray cone angle profile, more lean mixture is formed at the beginning of the injection, after which the mixture gets richer compared to results using a constant angle. The differences are more evident at the start of injection than towards the end of injection.

Results from both Figure 5.23 and Figure 5.24 suggest that the transient spray cone angle affects the mixing field, which may affect the subsequent processes including ignition timings and locations etc.

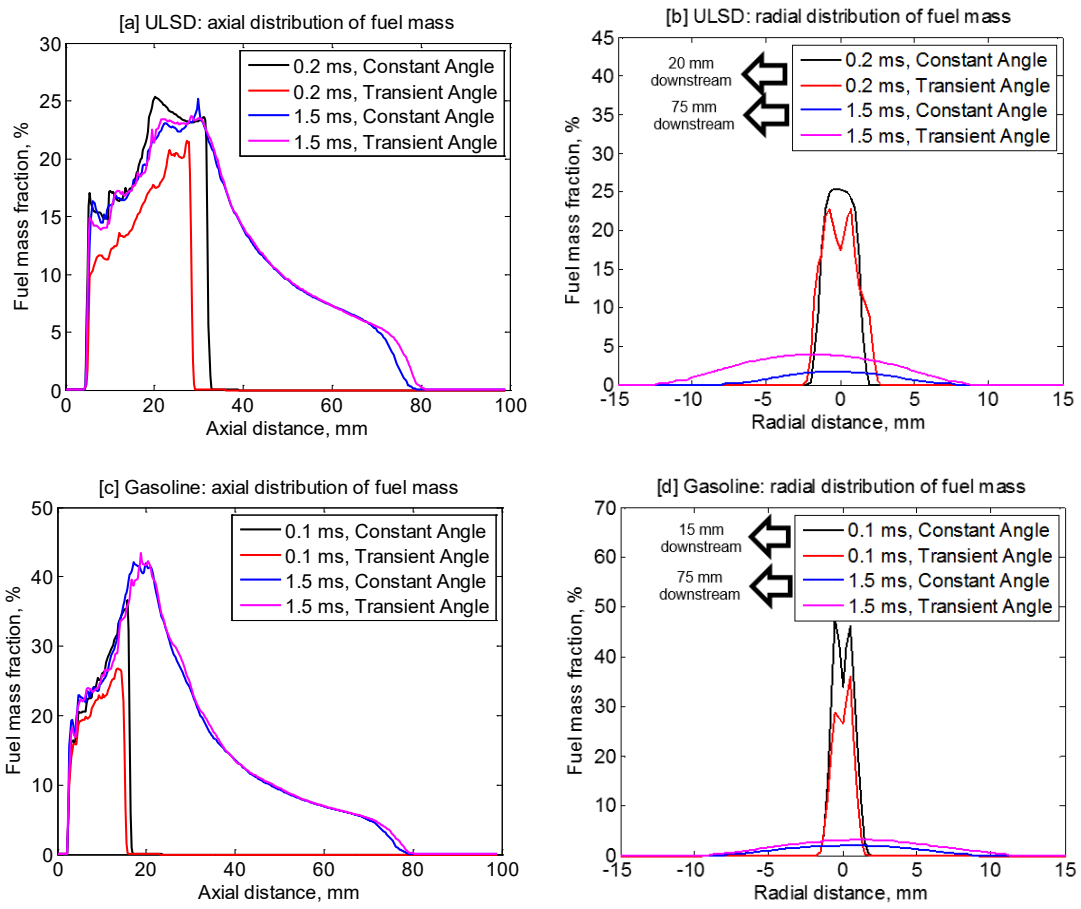

Figure 5.23. Fuel mass distributions along the spray axial and radial directions for both fuels. Constant angle refers to the angle during the quasi-steady state of the spray cone angle profile.

It is noted that there are also other aspects that can improve the CFD model prediction of spray formation and mixing processes, e.g., a large eddy simulation (LES) turbulence model with refined mesh resolution could improve the predictions of vapor penetration and

ignition delay as investigated in (Pei, Som, et al. 2015). The development of a transient spray cone angle correlation in this study is one of the efforts towards more predictive engine combustion simulations.

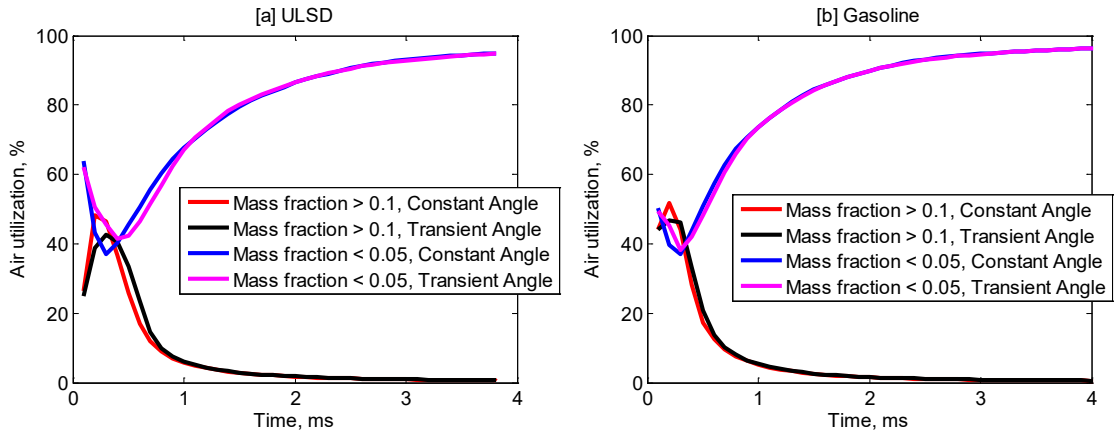

Figure 5.24. Air utilization comparisons between simulations using a constant (quasi-steady state) angle profile and a transient spray cone angle profile for (a) ULSD and (b) gasoline.

5.6 Summary and Conclusions

The spray cone angle is an important macroscopic spray characteristic that exhibits dynamic behavior during the spray injection process which in turn affects the macroscopic spray structure and local mixing fields. The spray cone angle is also an important input for spray simulations with 1D or 3D CFD models, in which a constant value from the quasi-steady state region was commonly used. As the need for improved accuracy in models increases, existing correlations developed for quasi-steady state spray cone angles will not be sufficient. The moving piston in the cylinder of an engine induces changes in the charge gas density and affects the spray cone angle. This effect has been largely ignored in previous studies. Also, the characteristics of short injection times where the quasi-steady portion does not occur will be largely different than the quasi-steady state behavior, given longer durations. The objective of this study was thus to develop a correlation capable of working with CFD simulations and providing dynamic spray cone angles as the simulation progresses in time.

Non-reacting and non-vaporizing spray experiments were carried out to measure the spray cone angle profiles as a result of the hydrodynamics of the fuel flow. Modeling of key characteristics of the spray cone angle profile was performed for each fuel and the resulting correlation was validated with normalized root mean square differences that were mostly below 10%. Limitations are from predictions in the transient durations at the SOI and the EOI, which is to be improved by further work. The correlation was built into a user-defined function and incorporated into the Converge CFD software. Simulations of non-reacting and vaporizing sprays were performed to examine the effect of a transient spray cone angle

profile on the spray development and mixing process. It was found that by utilizing a transient spray cone angle profile:

1. A slower ramp-up in the vapor penetration was observed, resulting in a wider and shorter jet initially, which was followed by an accelerating jet that led to a narrower but longer jet.
2. A minimal difference in the liquid penetrations was observed.
3. Leaner mixtures were formed at the beginning of the spray, and then entered a transition to richer mixtures after the initial transient period.
4. Larger effects on macroscopic spray characteristics and spray mixing processes were seen with a larger drop from the initial maximum to the quasi-steady state spray cone angle

6 Numerical Investigation of Fuel Effects on Soot Emissions at Heavy-duty Diesel Engine Conditions[5]

The content in this chapter has been submitted to the ASME 2018 Internal Combustion Engine Fall Technical Meeting, and is currently under peer-review.

6.1 Experimental Conditions

The experimental conditions in this chapter is a subset of the reacting spray tests in section 4.3, and given below in Table 6.1.

Table 6.1. Experimental conditions.

Gas Pressure (MPa)	Gas Density (kg/m^3)	Gas Temperature (K)	O_2 level (%)	Injection Pressure (MPa)
6.0	23.1	900	15	150
	20.7	1000		
	18.9	1100		
	23.1	900	10	
			21	

6.2 CFD Simulation Setup

Reacting spray simulations were performed using the CFD software Converge 2.3 (Richards, Senecal, and Pomraning 2017). Liquid droplets were modeled as Lagrangian parcels while the gas phase was modeled using the Eulerian method. Mass, momentum, and energy transport equations were established to describe the compressible, reacting, and viscous flow. They were solved using the finite volume method to obtain pressure, temperature, density, flow velocity, and species concentrations in the flow field.

Strong turbulence occurs in spray injections, which span a wide range of length and time scales. Turbulence was solved using both turbulence models for the Reynolds-averaged Navier-Stokes (RANS) equations and the Large Eddy Simulation (LES) method. The RANS method decomposes the flow field properties into the sum of an ensemble average and a fluctuation term, based on ensemble averaging of the conservation and transport equations. This results in additional terms (Reynolds stresses) in the equation sets, which are solved using the renormalization group k-ε turbulence model. The LES method

[5] The material contained in this chapter has been submitted to and accepted by the ASME 2018 Internal Combustion Engine Fall Technical Conference. The paper is going to be published by the American Society of Mechanical Engineers, after presentation at the ASME 2018 Internal Combustion Engine Fall Technical Conference in San Diego, California, November 4-7, 2018.

decomposes the flow field properties into the sum of a resolved field and a sub-grid field, based on spatial filtering of the conservation and transport equations. The flow fields with sizes beyond the grid resolution are solved while the sub-grid field is modeled. The dynamic structure model was used for the LES method, which was a one-equation model. Success using the RANS method have been seen in previous work (Pei, Torelli, et al. 2017a) where non-reacting vaporizing sprays were simulated. Improvements with the use of the LES method in simulating both non-reacting and reacting sprays are also seen in the literature (Xue et al. 2013, Pei, Hu, and Som 2016).

The CFD domain in this work was a 100×100×100 mm cube. Cartesian grids were used with minimum grid sizes of 0.25 mm and 0.125 mm for the RANS and LES simulations, respectively. Fixed embedding around the nozzle orifice and adaptive mesh refinement (AMR) based on velocity, temperature, and species gradients were adopted. This resulted in peak cell counts at 1.7 million and 10 million for the RANS and LES simulations, respectively. The grid resolution was shown to be sufficient for the RANS approach (Xue et al. 2013, Pei, Torelli, et al. 2017a), but for the LES approach, grid convergence was found at 0.0625 mm based on reacting spray simulations of the Engine Combustion Network (ECN) Spray A (Pei, Som, et al. 2015). It was also found that a grid size of 0.125 mm in the LES simulations of non-reacting sprays was able to capture the temperature and mixture fraction contours (Xue et al. May 2013). This study used a grid size of 0.125 mm to balance efficiency and accuracy. A variable time-step was used with a maximum time step of 0.5 μs and a minimum time step of 0.05 μs.

Spray simulations were performed using the blob injection method (Reitz 1987a), and parcels were injected at sizes equal to the effective nozzle diameter. Each parcel represented a group of drops with identical properties. Droplet drag was modeled using the dynamic drag model (Liu, Mather, and Reitz 1993) which accounted for the deformation of droplets in calculating the droplet drag coefficient. Secondary drop breakup was modeled using the Kelvin Helmholtz - Rayleigh Taylor (KH-RT) model (Patterson and Reitz 1998) without specifying a breakup length that defines the regime for the RT mechanism to apply. The no-time-counter (NTC) numerical scheme (Schmidt and Rutland 2000) and the post collision outcomes scheme were used to model the collision and coalescence of the droplets. The Frossling correlation (Amsden, O'Rourke, and Butler 1989) was used to determine the droplet radius change associated with vaporization. Fuel liquid properties used were different between the two fuels, with the properties of ULSD used as is in the fuel library, and the property of gasoline determined from a fuel physical surrogate using ASPEN HYSYS (Pei, Torelli, et al. 2017a, Zhang, Voice, et al. 2018).

Combustion simulations were performed using the SAGE detailed chemical kinetics solver (Senecal et al. 2003). A reduced toluene reference fuel (TRF) mechanism with 109 species and 543 reactions was used along with a polycyclic-aromatic hydrocarbon (PAH) sub-mechanism from Wang et al (Wang, Yao, et al. 2015). This has been well validated for soot emissions and was used for both ULSD and gasoline combustion. ULSD was represented by n-heptane while gasoline was represented by a mixture of 39% n-heptane and 61% iso-octane.

Soot emissions were modeled using two models: (1) the two-step Hiroyasu Nagel and Strickland-Constable (Hiroyasu-NSC) model (Nagle and Strickland-Constable 1962, Hiroyasu and Kadota 1976), and (2) the Particulate Mimic (PM) model (Richards, Senecal, and Pomraning 2017). The two steps in the Hiroyasu-NSC model include soot formation and soot oxidation which are formulated by Arrhenius equations. The PM model is a more detailed model and has six processes, including soot inception, coagulation, fragmentation, oxidation, surface growth, and condensation. The PAH sub-mechanism was required by the PM model for soot prediction with pyrene as a soot pre-cursor, whereas C_2H_2 was used by the Hiroyasu-NSC model as a soot pre-cursor.

6.3 Line-of-sight Integration of Soot Field

A method to visualize the soot field from a spray flame in CFD simulations was developed by Hessel et al. (Hessel et al. 2017) and utilized in this study. This method enables direct comparisons between natural luminosity images and CFD simulation results. The method was based on projecting blackbody radiation from the soot cloud along line-of-sights onto a two-dimensional plane, while accounting for both the emission and transmission from the soot cloud. A summary of the model is provided below in equation (16) through (19), repeated below.

$$I_{bb,\lambda,\Omega}(T,\lambda) = C_1/\left(\pi n^2 \lambda^5 (exp(C_2/n\lambda T) - 1)\right) \tag{16}$$

$$\varepsilon_{soot} = 1 - exp\left(-\left(g f_v L_{cfd\_cell}\right)/\lambda^{\alpha}\right) \tag{17}$$

$$\tau_{soot} = 1 - \varepsilon_{soot} \tag{18}$$

$$S_\lambda = \int_{400\ nm}^{1000\ nm} \left\{ f\left[< \left(I_{bb,\lambda_\Omega(\lambda)} \cdot \varepsilon_{\text{soot}}(\lambda) \right) \cdot \tau_{\text{soot}}(\lambda) > A \cdot C_\lambda \right] \right\} d\lambda \tag{19}$$

Equation (16) calculates the radiant intensity of a soot particle assuming blackbody radiation. I is the spectral blackbody radiation (in W/sr·m^2·nm). T is the temperature (in Kelvin) of the aerosol (assumed to represent soot particles), which is in thermal equilibrium with the soot particles. n is the refractive index of the medium, and assumed to be 1. λ is the wavelength (in nm) and C_1 is Planck's first constant, 3.7419e-16 (W·m^2). C_2 is Planck's second constant, 14388 (µm·K). Equation (17) calculates the soot emissivity with g representing a constant of 6.3 (µm^{-1}). f_v is the soot volume fraction (ppm), L_{cfd_cell} is the distance along the line-of-sight within a CFD cell and $\alpha = 1.22 - 0.245\ln(\lambda[\mu m])$, is an empirical function. Equation (18) calculates the soot transmissivity while equation (19) calculates the signal received by the camera sensor from a line-of-sight. A is the area of the CFD cell onto which the radiation is projected. C_λ is the spectral response of the detection system, which consists of a BG28 filter, a camera lens, and a high-speed camera. The spectral responses of the individual system and the overall transmittance are shown in Figure 6.1. Further details and assumptions in the model are provided in Hessel et al. (Hessel et al. 2017).

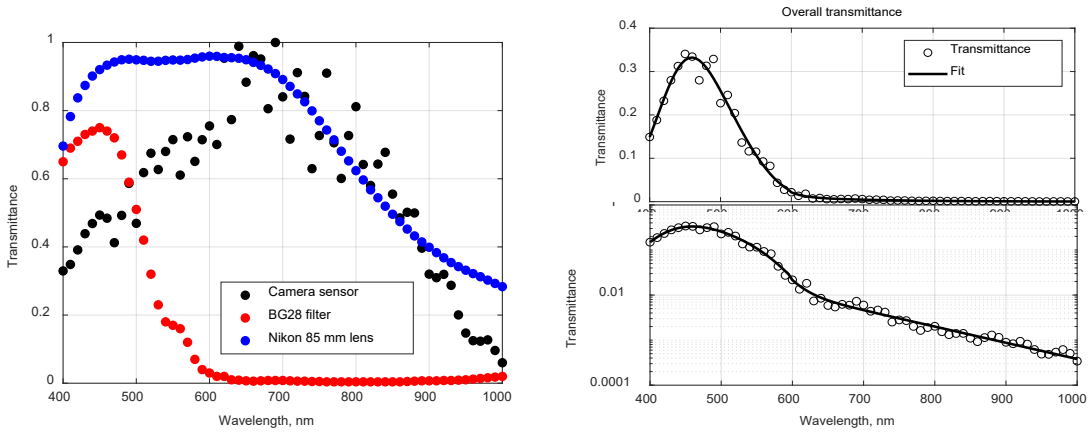

Figure 6.1. Spectral transmittance of the camera sensor, BG28 filter, and Nikon 85 mm lens (left), and the overall spectral efficiency of the detection system (right).

6.4 Results and Discussions

6.4.1 Model Validations

Validations of CFD simulations on non-reacting, vaporizing sprays were performed in a previous work by Pei et al (Pei, Torelli, et al. 2017a). Vapor and liquid penetrations matched experimental measurements well. The numerical setup and spray models are adopted for the reacting spray simulations performed in this work.

In CFD simulations, ignition delays were defined according to suggestions from the Engine Combustion Network, which was the time from the start of injection to the time when the maximum Favre-averaged temperature gradient occurs (Hawkes 2014). In general, ignition delay predictions by both turbulence models were close to the experimental measurements (Figure 6.2(a-b)), and the LES simulations predicted shorter (overall better) ignition delays than those from the RANS simulations at most conditions. At some more reactive conditions, e.g., ULSD from 1000 to 1100 K and gasoline at 1100 K, very similar ignition delays were obtained for both models. While at low-reactive 10% O_2 level, RANS over-predicted the ULSD ignition delay by 50%. The shorter ignition delay predictions by the LES simulations are likely due to the enhanced mixing predictions. The instantaneous nature of the LES model, despite the spatial average, can better capture turbulent fluctuations and this is critical for predicting ignition and combustion in less reactive conditions, e.g., low temperature or low O_2. This is consistent with previous findings in diesel spray combustion (Pei, Som, et al. 2015, Pei, Hu, and Som 2016). For the RANS model, the ensemble time-averaged nature dampens the turbulence fluctuation and makes the prediction challenging without a proper turbulence-chemistry-interaction (TCI) closure (Pei et al. 2016, Kundu, Ameen, and Som 2017). The TCI investigation is currently a work in progress and will be reported in future studies. As the temperature and O_2 level increases,

the turbulence model effects become smaller. The faster ignition of ULSD relative to gasoline was correctly predicted by both turbulence models.

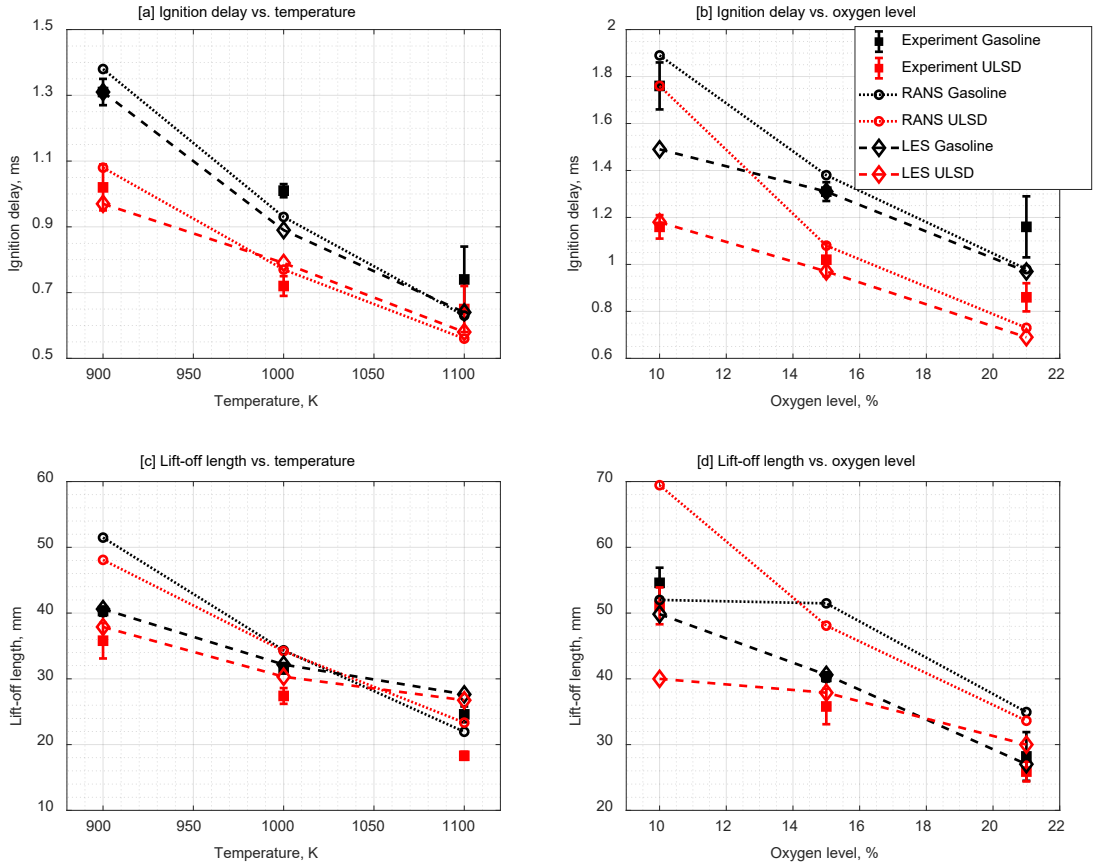

Figure 6.2. Ignition delays with respect to charge gas (a) temperatures, (b) oxygen levels, and lift-off lengths with respect to charge gas (c) temperatures, (d) oxygen levels. The legend from (b) applies to all figures.

Lift-off lengths (LOL) are shown in Figure 6.2(c-d). In the CFD simulations, LOLs were defined as the distance from the nozzle tip to the axial location with a mass fraction of OH reaching 14% of the maximum OH mass fraction (Pei, Hawkes, et al. 2015). Overall, LOL predictions by the RANS simulations deviated more relative to experimental measurements compared to the LES simulations. With respect to temperatures, steeper trends of RANS LOLs were observed relative to experimental results, while flatter trends of LES LOLs were observed that matched better from 900 to 1000 K but were even flatter from 1000 to 1100 K. With respect to O_2 levels, over-predictions were common for the RANS lift-off lengths except at 10% O_2, while LES LOLs exhibited a closer match to experimental results. It is noted that the LOL transition from 10% to 15% O2 was not captured by the RANS simulations, where the trend remained flat compared to both experimental and LES results. It is noted that multiple realizations of LES simulations might be necessary to obtain a more representative ensemble-averaged LOL (Pei, Som, et al. 2015). For this study, only

one realization was performed for each investigated condition for the sake of computational efficiency. Although the LOL accuracy could be improved, the general trend is expected to remain compared to RANS.

High-speed natural luminosity images provide information on the sooting characteristics of the spray flame. Direct comparisons between natural luminosity images and simulation results are difficult, because natural luminosity is a function of local soot volume fraction, temperature, and soot optical density along a line-of-sight. A reasonable comparison to natural luminosity images is performed through the line-of-sight integration of the soot field from CFD simulations (Hessel et al. 2017). Using the line-of-sight integration method mentioned earlier, results from CFD simulations are compared to experimental results and examples are shown in Figure 6.3.

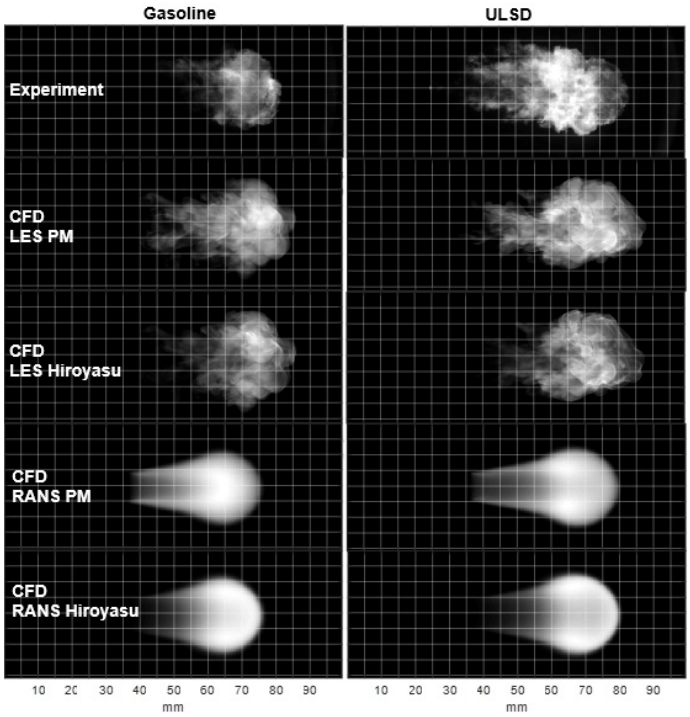

Figure 6.3. Comparisons of experimental natural luminosity image and line-of-sight integrated soot field from CFD simulations. Simulations were conducted using both LES and RANS turbulence models. Soot was modeled using both Hiroyasu-NSC model and PM model. Comparisons are made for both fuels under 1000 K and 15% O_2 charge gas, with 150 MPa injection pressure, at 1.5 ms ASOI. Grayscale intensities only applies to the individual image and not to be compared among images.

It should be noted that the inputs for the line-of-sight integration method from the CFD simulations include both the three-dimensional temperature and soot volume fraction distributions. While these results are readily available for simulations using the PM soot model, the soot volume fraction distributions from the Hiroyasu-NSC soot model were calculated. Using the readily available soot mass output from the Hiroyasu-NSC model,

the soot volume fractions were calculated as the soot mass divided by the soot particle density, which was assumed to be 1800 kg/m^3 (Attili et al. 2014).

It is observed from Figure 6.3 that the soot images from the CFD simulations generally agreed with the experimental natural luminosity image. The LES simulation results better resolved the local flow fields and were closer to the experimental image than the RANS simulation results, which were ensemble-averaged. In terms of the location of soot lift-off, the LES results were visually closer to the experiment than the RANS results for gasoline, whereas both LES and RANS results performed similarly when using the PM model for ULSD. Between the PM and Hiroyasu soot models, the Hiroyasu soot model resulted in higher lift-off lengths than the PM model. A closer examination of the luminosity distributions in the RANS results using two soot models reveals that luminosity was higher on the flame front towards the head of the combusting jet for the Hiroyasu model, whereas the luminosity was higher in the center of the flame for the PM model. With respect to the jet head location, LES results over-predicted by about 5 mm, whereas RANS results under-predicted by about 5 mm. Observing the simulated luminosity distributions using two soot models with the same turbulence model, the differences were due to different soot distributions as a result of the soot model, because the same temperature field was shared by the two soot models. This set of comparisons provides a qualitative understanding of the performance of CFD simulations on soot modeling, as demonstrated by the line-of-sight integration method. The above observations may not be extended to other test conditions and fuels, however.

Similar to the lift-off length of a reacting spray flame, natural luminosity images also define a lift-off length for the soot cloud, which is referred to as soot lift-off length (SLOL) in this work. The definition of SLOL is shown in Figure 6.4, in which soot luminosity images are integrations of one single injection and combustion event from the start of injection to the end of injection. Mean pixel intensity curves are overlaid on the figures, which represent mean flame pixel intensities (excluding the background) versus distances downstream of the injector tip. A threshold of 10% of the maximum pixel intensity along the curve is selected to define the location of the soot lift-off. Examining the mean pixel intensity curves from the experimental and CFD results, the rising edges of these curves do not exhibit similar “knees” compared to those in the mean OH* chemiluminescence intensity curves (Higgins and Siebers 2001) that define spray flame lift-off lengths. This suggests that the SLOL definition is sensitive to the threshold to some extent. Direct comparisons of the SLOLs and the soot cloud locations from Figure 6.4 showed that the SLOLs were reasonable descriptions of the lifting behavior of the soot cloud relative to the injector tip. Selection of 10% maximum pixel intensity as the threshold for SLOL was on a similar order of magnitude as the 14% of the maximum OH mass fraction in defining the lift-off lengths.

The SLOLs from the experiments and simulations are shown in Figure 6.4, and these are the same sets of experiments and simulations shown in Figure 6.3. The LOLs are also shown for comparison. In terms of the SLOL predictions, for gasoline, the LES Hiroyasu simulation was closest to the experiment with an under-prediction of about 3 mm, whereas

for ULSD, the RANS PM simulation best matched the experiment, although the LES PM simulation was close with an over-prediction of about 3 mm. Comparing the SLOL and the LOL from each figure, larger SLOLs than the LOLs were observed in both the experiment and the simulations. The larger SLOLs are often observed in experimental studies by the natural luminosity technique shown in this work, and also by planar-laser induced incandescence (Pickett and Siebers 2006) and extinction-based diagnostics (Skeen et al. 2013). Generally, the gap between SLOL and LOL was minimal in the RANS PM simulations regardless of the fuels, and this indicated that the axial locations of soot formation and flame stabilization were very close. The LES Hiroyasu simulation presented overall similar characteristics of the flame lift-off and soot cloud interaction compared to the experiment for the particular experimental condition under investigation.

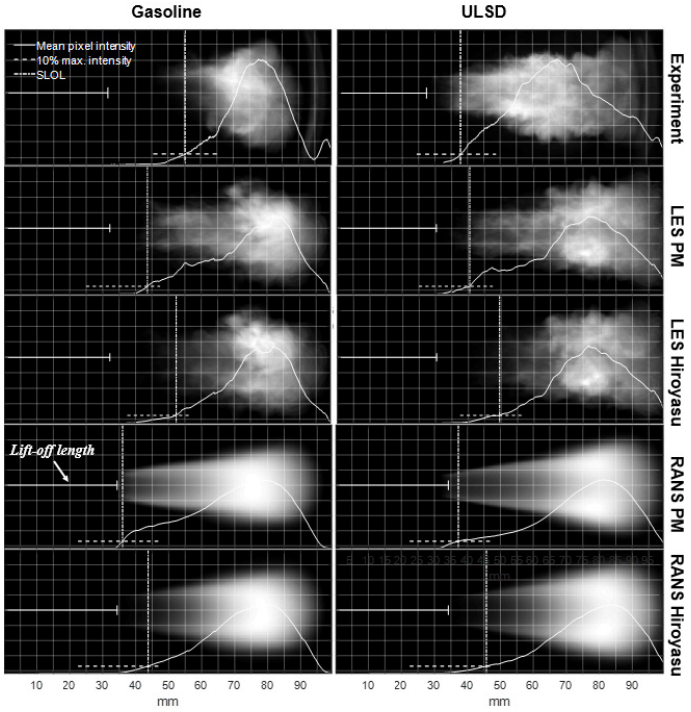

Figure 6.4. Comparisons of experimental natural luminosity image and line-of-sight integrated soot field from CFD simulations. Simulations were conducted using both LES and RANS turbulence models. Soot was modeled using both Hiroyasu-NSC model and PM model. Comparisons are made for both fuels under 1000 K and 15% O_2 charge gas, with 150 MPa injection pressure, at 1.5 ms ASOI. Grayscale intensities only applies to the individual image and not to be compared among images.

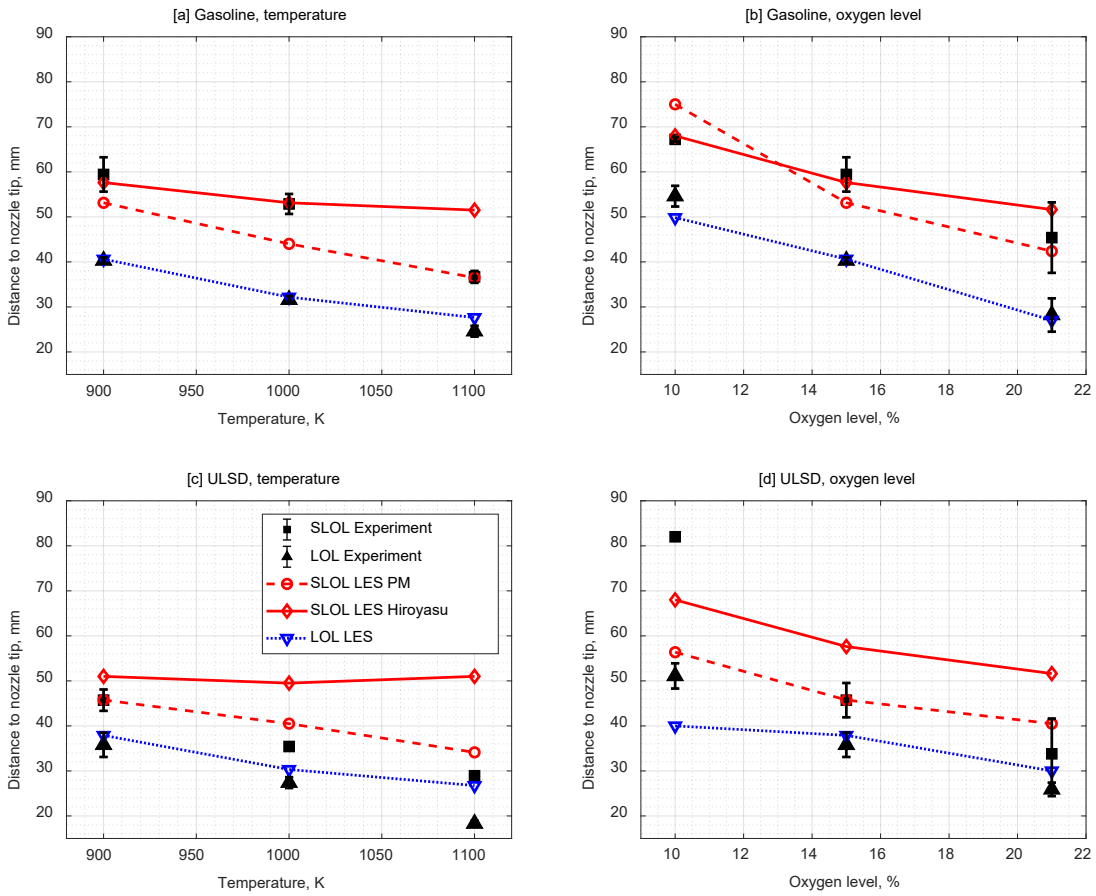

Figure 6.5. Soot lift-off lengths and lift-off lengths of gasoline with respect to charge gas (a) temperatures, and (b) oxygen levels with ULSD results shown in (c) and (d). The legend in figure (c) applies to all figures.

SLOLs and LOLs under the same test conditions for all the experiments and simulations are presented in Figure 6.5. Previous discussions have shown the superior performance of the LES simulations in predicting both the ignition delay and the lift-off length, which are critical for the subsequent soot processes. The following discussions in terms of the SLOLs and LOLs will focus on the LES simulations.

Comparisons are firstly made with respect to the SLOLs. For gasoline, the Hiroyasu model and the PM model had comparable performance. For ULSD, the PM model had consistently better predictions than the Hiroyasu model, where the Hiroyasu model exhibited over-predictions in all but the 10% O_2 case for ULSD. The other important characteristics are the gaps between the SLOLs and the LOLs. For gasoline, both the Hiroyasu model and the PM model exhibited reasonable SLOL – LOL gaps over different ranges of the temperature and O_2 level charge gas conditions. For ULSD, due to the over-predictions of SLOLs by the Hiroyasu model, the SLOL – LOL gaps were better matched by the PM model.

To understand the temporal evolution of the spray flames, the natural luminosity images are axially integrated and plotted against time, which is named an IXT (Intensity-aXial-Time) plot (Cung et al. 2015). The IXT plots for both fuels under all test conditions are shown in Figure 6.6. Note that for the 10% O_2 level for both fuels, due to the extended ignition delay, experimental and simulation results are shown up to 3 ms, whereas the rest of the cases are shown up to 2.4 ms. Natural luminosities among different charge gas conditions can vary by orders of magnitudes (shown later in Figure 6.7), and so to ease visualizing the luminosity evolution within one case, the color map scales within each IXT plot only. Ignition, flame front, soot lift-off, and axial distribution of natural luminosities can be observed directly from these IXT plots. The trends of ignition delays and soot lift-off lengths previously discussed are generally replicated in the IXT plots. Experimental IXT plots showed that the high luminosity flame region exhibited a relatively stable lift-off from the injector tip. The LES simulations better replicated this feature than the RANS simulations. A majority of RANS simulations exhibited a high luminosity flame region moving downstream versus time.

Comparisons among different test conditions are made in Figure 6.7. A time integration of the IXT plot, which is the sum of all pixel intensities from the spray flame natural luminosity images, is calculated for all experiments and CFD simulations using the same model setups. This is essentially the time-integration of the spatially-integrated natural luminosities (TISINL) signal. Similar methods are seen in literature, where the peak SINL during a combustion event is used to represent the average in-cylinder soot volume fractions (Mueller and Martin 2002), and the time-averaged SINL is used during the quasi-steady portion of the injection event to represent the average soot concentrations (Mueller et al. 2003). The TISINL signal is normalized by the indicated mean effective pressure (IMEP) for a relative measure of soot with different injection timings and injection pressures (Fang and Lee 2011). These interpretations are semi-quantitative with respect to the soot emission because natural luminosities are functions of, but not limited to, soot volume fractions, soot temperature, soot refractive index and the quantum efficiency of the detection system, and many are not directly related to the mass of emissions.

Normalizations of the TISINL signals were performed with respect to 1000 K and 15% O_2 for the temperature and O_2 level sweep, respectively. Also, as observed in Figure 6.6, long ignition delays at the 10% O_2 condition resulted in long flame lift-offs and soot lift-offs and that most of the flame luminosities occurred near the wall of the combustion vessel. This leads to uncertainties in quantifying the luminosity levels, primarily due to the temperature boundary layer in these preburn-type vessels where a steep temperature gradient exists (Naber and Siebers 1996). For this reason, comparisons did not include results from the 10% O_2 condition.

Observing Figure 6.7, among the four combinations of turbulence and soot models, it is evident that RANS PM simulations deviated the most from the experimental trend of TISINL evolution. The LES simulations with both soot models and the RANS Hiroyasu simulations had comparable performance under all the investigated conditions.

To understand fuel effects through natural luminosities, the TISINL signals of gasoline and ULSD are compared. Figure 6.8 presents relative TISINL of gasoline over ULSD for different charge gas temperatures and O_2 levels. It is observed that LES PM simulations best replicated the trends of relative TISINL signals. All other simulations exhibited significant deviations compared to the experimental trends.

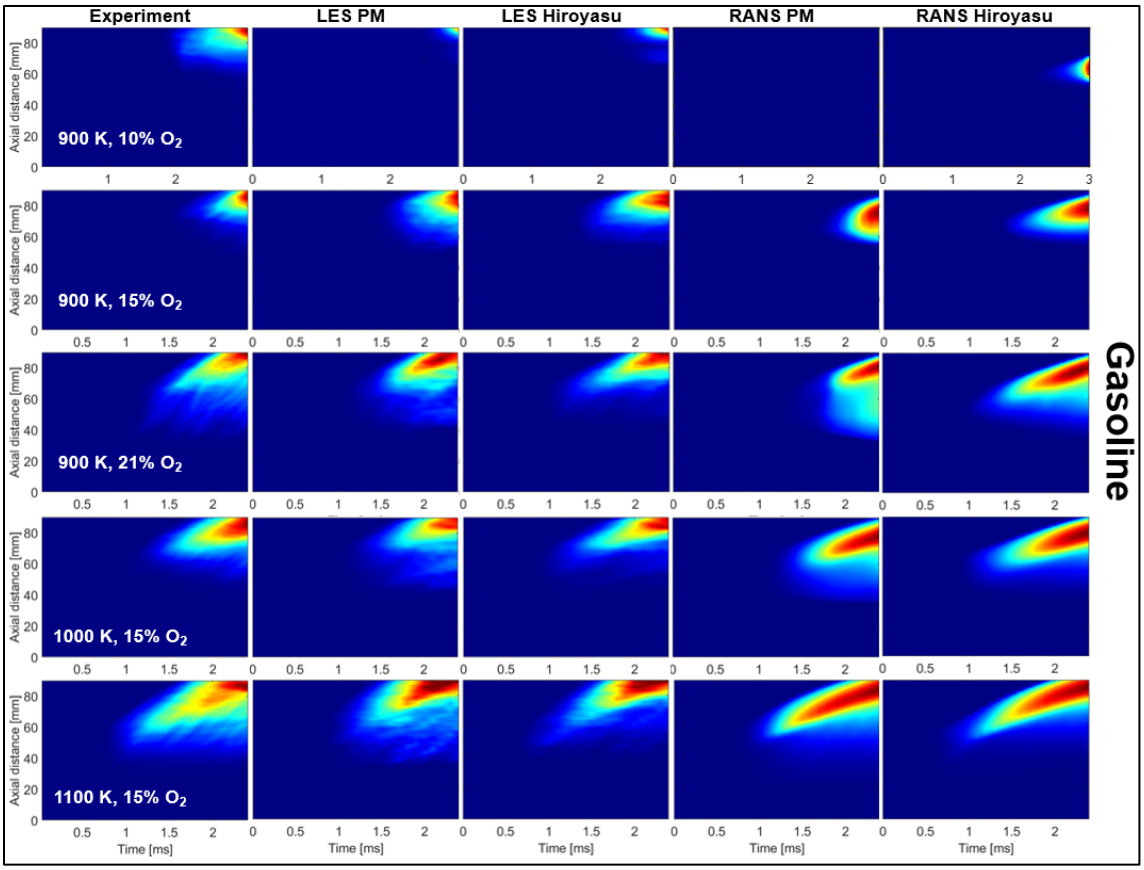

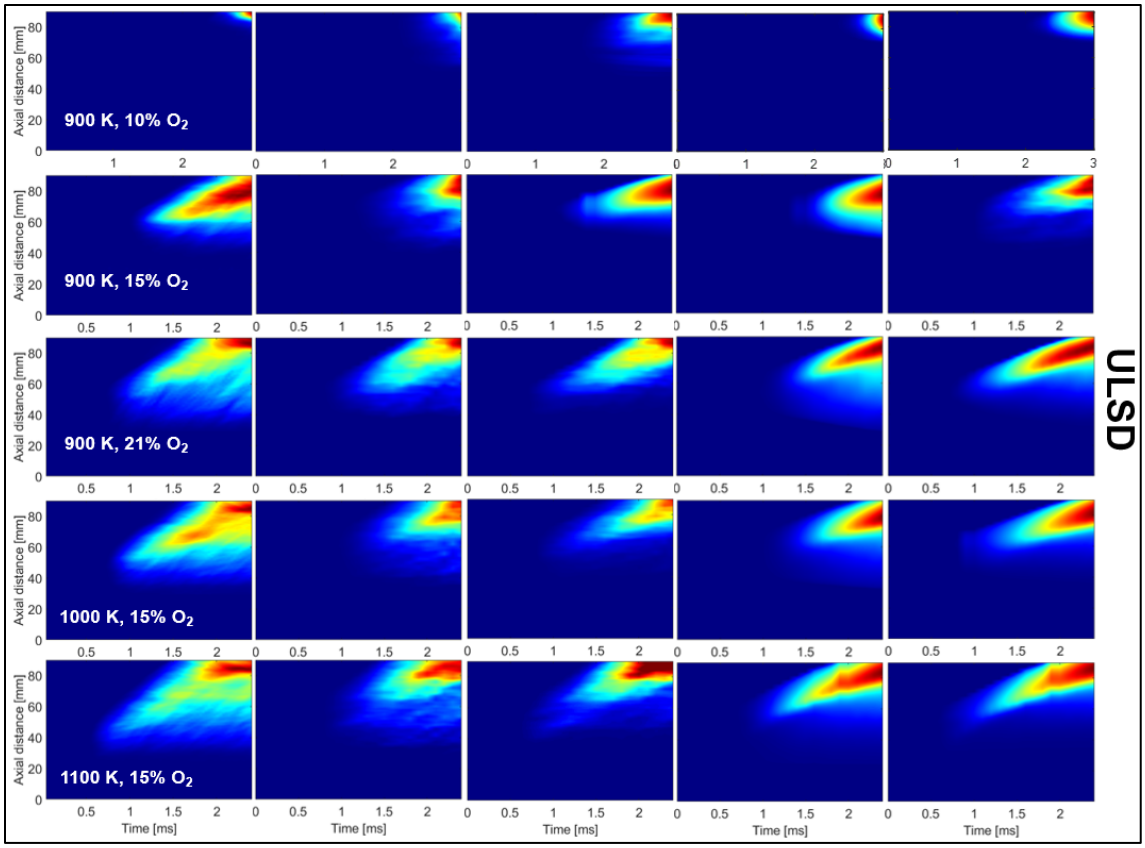

Figure 6.6. Intensity-aXial-Time (IXT) plots of the spray flames for gasoline and ULSD, with a sweep of O_2 level and charge gas temperatures. Color map only scales to the individual plot and not to be compared among other plots.

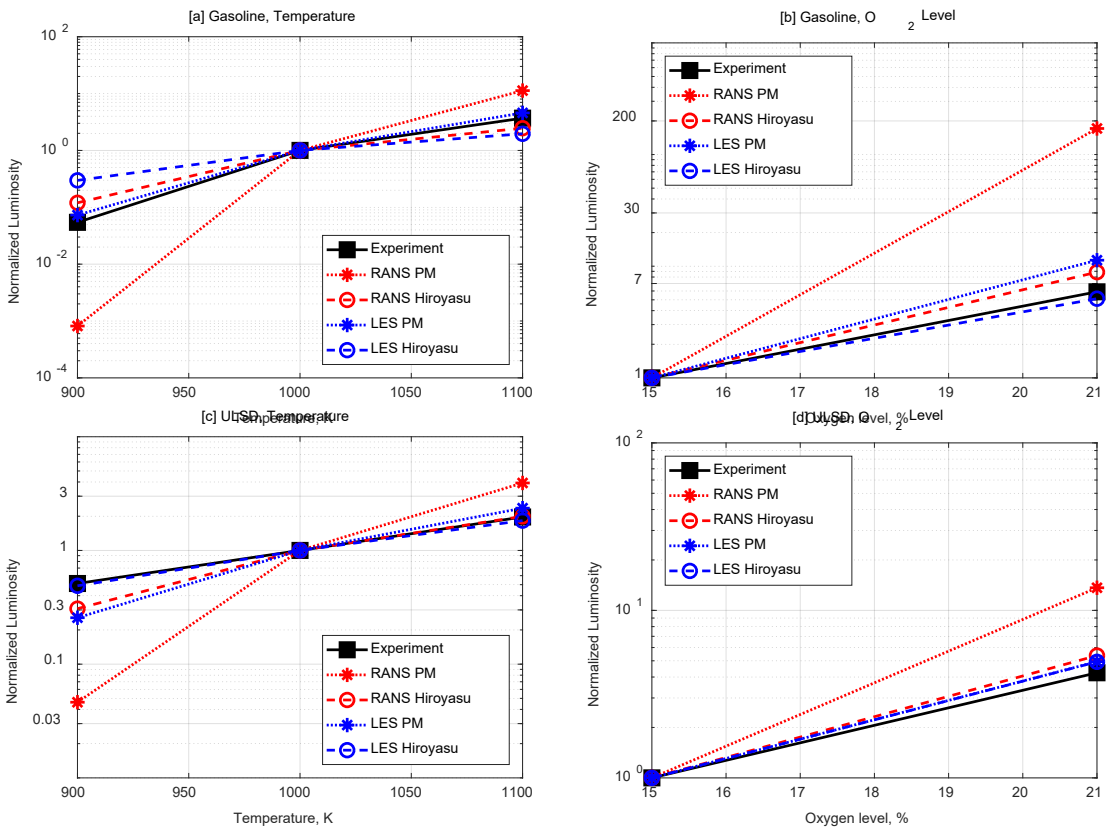

Figure 6.7. Normalized time-integrated of spatially-integrated natural luminosity (TISINL) for gasoline and ULSD.

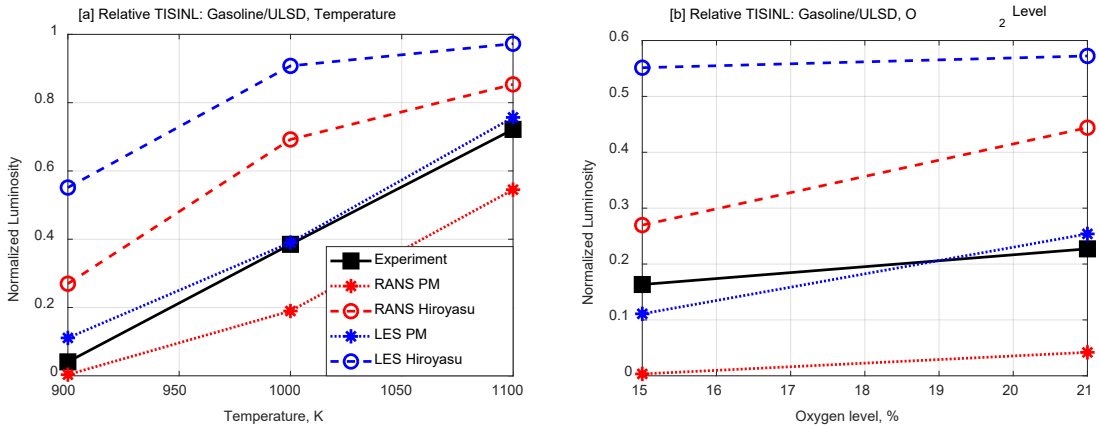

Figure 6.8. Relative TISINL signal of gasoline/ULSD with respect to charge gas (a) temperatures, (b) oxygen levels. Legend from figure (a) applies to (b) as well.

6.4.2 Fuel Effects on the Soot Emission Processes

Previous discussions of the CFD model validations showed that several aspects of CFD models are critical in characterizing spray flames. The LES PM simulations showed improved predictions of the ignition delay, the flame lift-off, and the soot lift-off. Improvements in the predicted TISINL signal profiles versus variations in charge gas temperatures, oxygen levels, within one fuel and between two fuels were also observed. These validations warrant further useful investigations on the detailed soot emission process with the LES PM simulations.

Of particular interest in this work is the fuel effect on soot emissions. Quantitative understanding of the soot emissions formation process is important, but analyses would not be reliable unless the model is quantitatively validated on soot emissions data. Although this work did not provide quantitative measurement of the soot emissions, comparisons can be made to results from existing literature. Idicheria and Pickett (Idicheria and Pickett 2005) quantitatively investigated soot emissions from a diesel spray using laser extinction and planar laser-induced incandescence with a charge gas of 1000 K, 14.8 kg/m^3 and 15% O_2. This is close to the ULSD tests of 1000 K, 20.7 kg/m^3 and 15% O_2 in this study and thus comparisons are made between the two datasets as shown in Figure 6.9. Differences between the experimental and simulation conditions include the charge gas density, 14.8 kg/m^3 for the experiments and 20.7 kg/m^3 for the simulations, and nozzle sizes, 180 μm in Figure 6.9[a], and 100 μm in Figure 6.9[b] for the experiments and 176 μm for the simulations.

The reported experimental optical thickness (KL) measurements and soot volume fractions in (Idicheria and Pickett 2005) are compared to simulated cumulative soot mass and averaged soot volume fractions in Figure 6.9[a] and [b], respectively. Simulation data are taken as averages of results on a plane through the spray axis between 2 ms and 3 ms, as shown in Figure 6.9[c] in order to make fair comparisons to laser extinction measurements, which were made during the quasi-steady state of the spray flame in the experiment.

Simulation results exhibited similarities compared to experimental results. With respect to the axial soot profile, results were normalized to 70 mm. A similar rising trend is observed for both experimental and simulation results, although it is difficult to interpret the differences in the normalized results. With almost similar nozzle diameter, the charge gas density was the largest difference. The rising trends may suggest the location of the soot lift-off, and Figure 6.9[a] indicates a higher soot lift-off with a lower charge gas density. Higgins and Siebers (Higgins and Siebers 2001) showed a similar trend in the flame lift-off lengths (by OH* chemiluminescence).

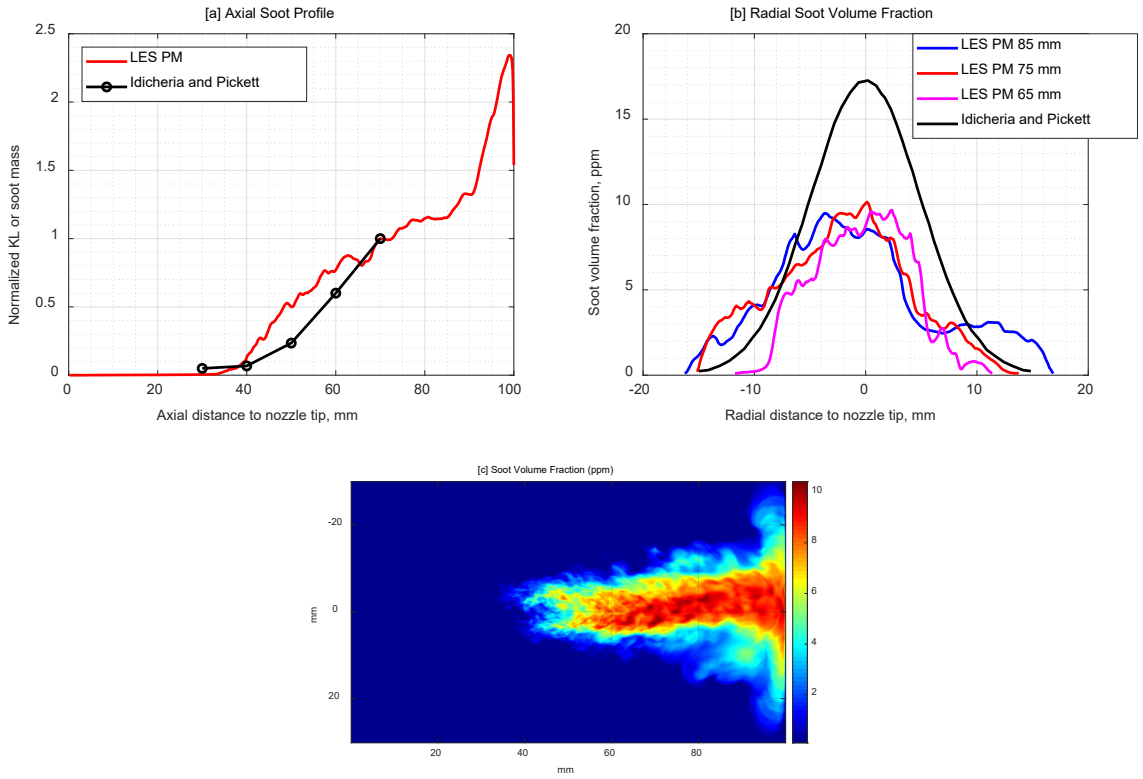

Figure 6.9. Axial and radial soot profiles. Comparisons are made to Idicheria and Pickett (Idicheria and Pickett 2005). Experimental results are KL in [a] and converted soot volume fraction in [b], respectively. (LES PM) Simulation results are cumulative soot mass in [a] and averaged soot volume fractions in [b], and both of which are obtained from a cut plane averaged from 2.0 to 3.0 ms as illustrated in [c]. Experimental conditions: 1000 K, 14.8 kg/m^3 and 15% O_2 charge gas, 140 MPa pressure drop across the nozzle, nozzle size of 180 µm in[a] and 100 µm in [b].

With respect to the radial soot volume fraction profile, experimental results were taken at 65 mm from the nozzle, and simulation results were taken at three distances (65/75/85 mm) from the nozzle. The 65 mm in the experimental measurement corresponds to the peak KL along the axial direction. Simulation results exhibited peak values at distances above 65 mm, and radial soot volume fraction profiles shown at three distances had similar peak values. The axisymmetric experimentally measured soot volume fraction profile was an axisymmetric spline fit of the KL measurement at different radial locations. The ratio of experimental peak soot volume fractions to those from the simulation is about 1.7 when the radial soot volume fraction was taken at 65 mm. The main differences between the experimental and simulation conditions include charge gas density (14.8 kg/^{3} in experiment vs. 20.7 kg/m^3 in simulation), and nozzle diameter (100 µm in experiment vs. 176 µm in simulation). With respect to the effect of charge gas density, Pickett and Siebers (Pickett and Siebers 2004b) identified a sensitivity of axial peak soot volume fraction to charge gas densities of $\rho_a^{2.2} - \rho_a^{2.5}$. The density ratio of the simulation over the experiments would result in a peak soot volume fraction of 2.0 to 2.3 times the experimental result in Figure

6.9[b]. With respect to the effect of nozzle diameter, Idicheria and Pickett (Idicheria and Pickett 2005) showed that about twice the peak soot volume fraction was measured with a 180 µm relative to a 100 µm nozzle. Additionally, conversion of experimental KL measurements to soot volume fractions was based on the small particle Mie theory, which required a term accounting for the scattering-to-absorption ratio, and the soot refractive index. A value of 0.26 was used by Idicheria and Pickett (Idicheria and Pickett 2005) and the Engine Combustion Network later recommended this value to be 0.46 (Payri, García, et al. 2012). This would reduce the experimental result to 56% of the original reported value. Accounting for all the above factors, the experimental to simulation ratio of the peak soot volume fractions is about 3.8 to 4.3. This ratio is still subject to a variety of uncertainties, including but not limited to injector nozzle geometry differences beyond the nozzle sizes and the estimation of the soot refractive index. Also, the soot model was not explicitly calibrated against quantitative soot emission measurements. These comparisons of the axial and radial soot profile suggest that the soot model could produce reasonable trends of soot emissions with similar orders of magnitude.

The spatial distribution of soot volume fractions are shown in Figure 6.10, which are similar to Figure 6.9[c] but expanded to include gasoline and ULSD with a sweep of charge gas O_2 levels and temperatures. These are time-averaged results between 2 ms and 3 ms from the LES PM simulations, and taken through the spray axis. The color scales are different for each plot and they represent the soot volume fractions in ppm. These comparisons exhibit the previous trends in soot lift-off lengths with respect to different charge gas temperatures and O_2 levels. In terms of the soot volume fractions, by comparing the color scales, gasoline consistently exhibits lower levels of soot volume fraction than ULSD by up to one order of magnitude. The soot benefit of gasoline reduces as the charge gas temperature and O_2 level increases. These are in-line with the trends of the TISINL signals in Figure 6.8.

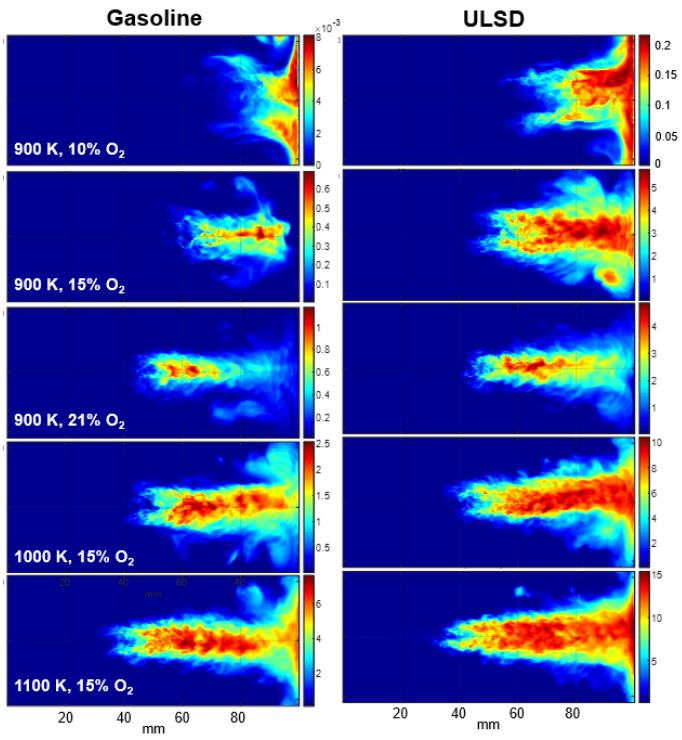

Figure 6.10. Time-averaged soot volume fraction contours from LES PM simulations for ULSD and gasoline (between 2 ms and 3 ms) through the spray axis. Each plot is provided a color scale, representing the soot volume fraction in ppm.

Very interesting observations were made with respect to a change of O_2 level: (1) with higher levels of O_2, peak soot volume fractions were more upstream for both fuels and (2) peak soot volume fractions at 21% O_2 were lower than 15% for ULSD. The second observation, in particular, was in contrast to the trend for gasoline, and was not the same trend as represented by the TISINL signals that an increasing O_2 level also led to a higher luminosity for ULSD. These two observations are indications of stronger soot oxidation processes, because (1) TISINL signals or natural luminosity signals are indications of strong soot oxidation, and (2) higher O_2 levels facilitate soot oxidation further downstream where more O_2 becomes available from the entrained ambient gas. This effect could alter the soot volume fraction distributions. The axial location shifts of peak soot volume fractions with respect to charge gas O_2 levels are not observed in the charge gas temperature sweep, where charge gas O_2 levels remained similar, leading to similar levels of charge gas and fuel mixing at the same axial distances.

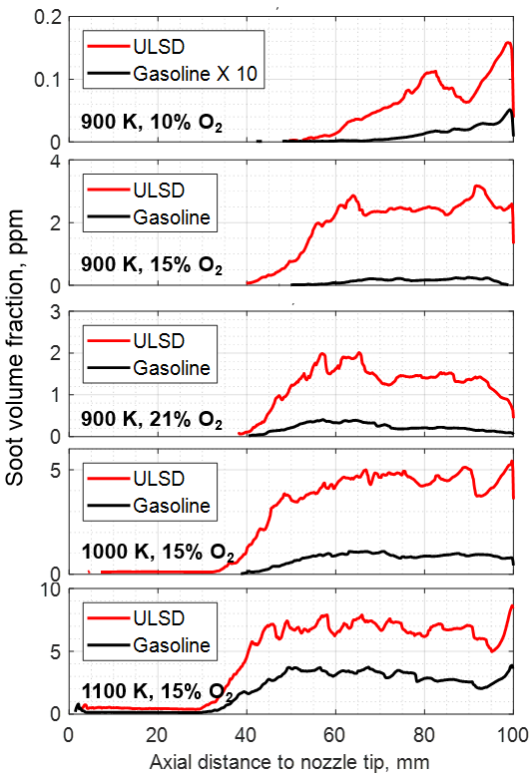

Figure 6.11. Axial distribution of soot volume fractions based on Figure 6.10.

Quantitative comparisons of the soot volume fractions along the axial direction are shown in Figure 6.11, which are averages of the soot volume fractions versus axial distances within the spray flame. Spray flames are from Figure 6.10 and defined using 1% of the peak soot volume fraction in each plot to isolate the soot cloud from the background. Results for the gasoline case at 900 K and 10% O_2 charge gas were scaled ten times for ease of visualization. The previously discussed trends are more obviously presented. As shown by the results at 900 K and 21% O_2, the time-averaged soot volume fraction distributions indicate that soot formation and oxidation has reached a balance around 60 mm, beyond which soot oxidation starts to dominate relative to soot formation. The same balance appeared farther downstream for the 10% and 15% O_2 charge gas conditions at 900 K. Under the 1000 K and 1100 K conditions, soot formation and oxidation were balanced over a range of distances downstream and reached a plateau. Recall that the contour plots in Figure 6.10 were time-averaged, so this does not indicate that such a transition occurs for each spray flame at an instance in time. Also, it does not suggest the time at which the soot formation-oxidation dominance transition occurs.

Soot mass histories from LES PM simulations are shown in Figure 6.12 with a sweep of charge gas [a] temperatures and [b] O_2. The soot formation – oxidation dominance transition is explicitly shown as a soot mass increase – decrease transition. The soot formation rate and oxidation rate respectively dominate prior to and after the observed transitions. The following observations are made:

a) Gasoline had lower soot mass under all conditions at the end of the simulations compared to ULSD. The soot benefit decreases with an increase in charge gas temperatures and O_2 levels. The percentages of gasoline soot mass at 3 ms compared to ULSD are 7%, 17%, and 39% at 900 K, 1000 K, and 1100 K, and are 3%, 7%, and 10% at 10%, 15%, and 21% O_2 levels.
b) Soot formation – oxidation transitions are observed for gasoline at 1000 K and 1100 K with 15% O_2, and for both fuels at 900 K and 21% O_2. Comparing gasoline at 1000 K and 1100 K, the transition occurred later at 1000 K (2.9 ms). Higher charge gas temperature results in higher flame temperature, and increases both the soot formation and oxidation rates. The later transition at 1000 K compared to 1100 K indicates that a larger sensitivity of soot oxidation rates to charge gas temperatures exists.
c) The transition occurred later in time for ULSD than gasoline at 900 K and 21% O_2. This is partly due to faster soot oxidation rates as a result of higher O_2 entrainment rates of gasoline, given the larger spray cone angles of gasoline compared to ULSD (Tang et al. 2018, Tang et al. May 2017, Zhang et al. May 2017). Also, after the onset of soot, soot formation rates were higher for ULSD than gasoline under all conditions. These indicate that gasoline has a lower sooting tendency compared to ULSD.
d) After the onset of soot, formation rates increase with both charge gas temperatures and O_2 levels, which are both due to increases in the combustion temperature (further discussed in Figure 6.14). The change of charge gas temperatures affected both soot formation and oxidation, whereas the change of charge gas O_2 levels had an additional effect on soot oxidation. With an increase in the O_2 levels, both the combustion temperature and the O_2 entrainment rate increases, which lead to increased soot formation and oxidations rates. The two competing processes performed differently with a change of O_2 levels. A soot mass increase from 10% to 15% O_2, and a soot mass decrease from 15% to 21% O_2 were observed for both fuels. This trend is consistent with observations from Idicheria and Pickett (Idicheria and Pickett 2005) using n-heptane and diesel.

Charge gas temperatures and mixture fractions are very important conditions that affect soot formation and oxidation. The temperatures, mixture fractions, and soot volume fractions through the spray axes for the two fuels are shown in Figure 6.13. It is observed that:

a) The liquid core from the spray formed rich mixtures just downstream of the nozzle tip, and exhibited the lowest gas temperatures. As the spray proceeds downstream, more ambient gas entrainment leads to lower mixture fractions that lead to higher gas temperatures and fuel ignition.
b) The gasoline flame exhibited a smaller lower-temperature inner region compared to ULSD. This cooler inner region corresponded to lower mixture fractions from gasoline, i.e. better mixing, as seen between 40 – 60 mm. This is closely related to gasoline's shorter liquid length compared to ULSD, which are 16 mm and 30 mm in the LES simulations, and 14 mm and 28 mm in the experimental measurements (Zhang et al. May 2017).

c) For both fuels, fuel rich and lower-temperature (compared to the peak combustion temperature) conditions are closely related to the high soot volume fraction regions. Comparisons are made between the flame around 60 mm and 80 mm downstream. Around 60 mm, temperature was higher and mixture fractions were lower on both sides of the flame compared to the flame around 80 mm. This is more conveniently visualized through the soot volume fraction distributions on the mixture fraction – temperature (Z – T) space in Figure 6.13.

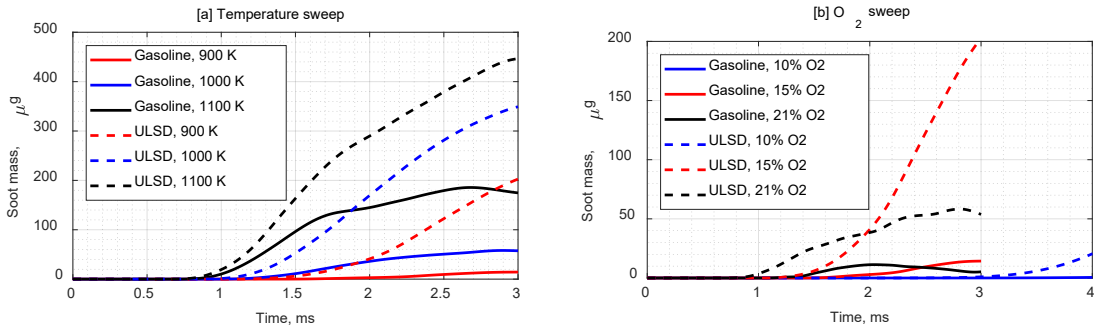

Figure 6.12. History of soot mass in LES PM simulations with a sweep of charge gas [a] temperatures and [b] O_2 levels.

To interpret the Z – T plot in Figure 6.13, fuel sprays and mixing occur along the leftmost boundary that encompass lower than ambient gas temperatures and high fuel concentrations. As the spray proceeds downstream, the mixture becomes diluted with more charge gas entrainment, and the gas temperature increases. On the Z – T space, data points move from the left boundary towards the right until auto-ignition occurs. Combustion further increases the gas temperature and dilutes the spray jet, and the peak temperature forms at the stoichiometric mixture. Comparing gasoline and ULSD, the following observations are made:

a) Gasoline was able to achieve much richer mixtures with the ambient gas compared to ULSD, and this is due to gasoline's shorter liquid lengths (Zhang et al. May 2017).
b) The peak combustion temperatures were similar between the two fuels, which were 2358 K for gasoline and 2361 K for ULSD. This is in-line with less than a 1% difference in the calculated adiabatic flame temperatures (Tang, Zhang, Menucci, et al. 2017).
c) Gasoline exhibits less scatter of points between mixture fractions of 0.15 and 0.3 in the Z – T plot of Figure 6.13 compared to ULSD.
d) Soot concentrations were higher along the boundaries on the Z – T space on the fuel rich side.
e) ULSD has a stronger soot tendency and produced higher soot concentrations over a wider range of mixture fractions and temperatures.

Soot volume fraction distributions on the Z – T space are shown for gasoline and ULSD under all test conditions in Figure 6.14. Comparisons are during the steady state of the spray flame at 3.0 ms ASOI. Higher peak temperatures were achieved with both higher

levels of O_2 and higher charge gas temperatures, but through different mechanisms. Combustion stoichiometry changes with O_2 levels, leading to a different heat of combustion that in turn resulted in peak temperature changes of over 300 K. Charge gas temperature changes the specific heat of the gas, while the heat of combustion remained almost the same. Thus the increase of peak temperatures was less than the changes in charge gas temperatures (100 K). It is observed that at 900 K, high soot concentrations occurred in richer and hotter mixtures for higher charge O_2 conditions for both fuels. From the comparison under all test conditions, the previous observation of the stronger soot tendency of ULSD than gasoline is still true.

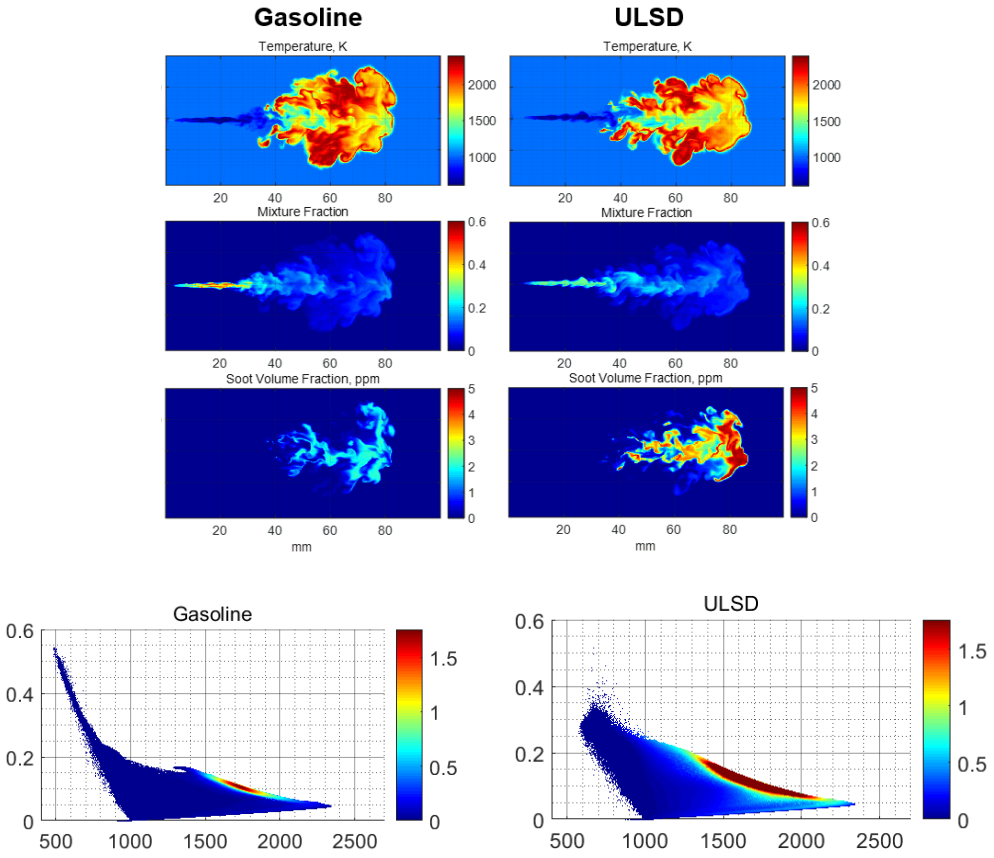

Figure 6.13. Temperature, mixture fraction, and soot volume fraction distributions for gasoline and ULSD through the spray axes. Examples shown under 1000 K and 15% O2 charge gas, at 1.5 ms ASOI.

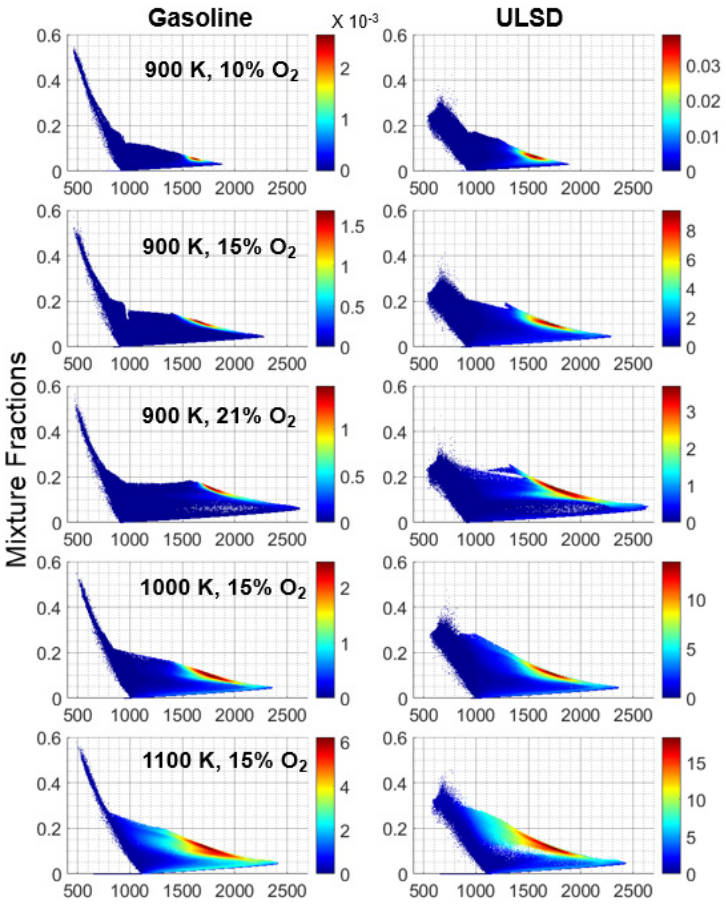

Figure 6.14. Distribution of soot volume fractions on the mixture fraction – temperature space from LES PM simulations. Shown for gasoline and ULSD. Comparisons are made during the steady state at 3.0 ms ASOI for all charge gas conditions.

6.5 Summary and Conclusions

This study numerically examined the soot emission processes from ULSD and a high-reactivity gasoline with sweeps of charge gas temperatures (900 – 1100 K) and O_2 levels (10%-21%). Experimental studies (Tang, Zhang, Menucci, et al. 2017) were performed using a heavy-duty single axial hole nozzle 176 µm in diameter in a constant volume combustion vessel. Measurements of ignition delays, flame lift-off lengths, and soot natural luminosity signals provided understanding of the fuel effects on combustion. Numerical investigations enabled further insights into the combustion and soot emission processes. Two turbulence models (RNG k-ε RANS, dynamic structure LES), and two soot models (Hiroyasu-NSC, Particulate Mimic) were used in the CFD simulations for validation.

Quantitative validations, including the measured ignition delays, lift-off lengths, and soot lift-off lengths, and semi-quantitative validations against soot luminosities were performed with variations in charge gas temperatures and O_2 levels. A line-of-sight integration of the

soot field method was utilized to interpret CFD simulation results for direct comparisons against experimental soot natural luminosity measurements.

It was found from the validation studies that LES PM simulations best represented the overall performance in predicting the ignition delays, lift-off lengths, soot lift-off lengths, and relative luminosity signals. In general, the LES simulations exhibited improvements in ignition delay and flame lift-off length predictions relative to the RANS predictions. Of the two soot models, the PM soot model performed better with the LES turbulence model, and the LES PM simulations replicated reasonable separation distances between the flame lift-off location and the soot lift-off location.

Qualitative comparisons between experimental studies in the literature and the LES PM simulation results confirmed that the predicted results were reasonable in the trend of axial soot concentrations, and were on similar orders of magnitudes on radial soot concentrations.

The LES PM simulations showed that higher soot natural luminosity signals may correspond to higher levels of soot oxidation, which suggests that soot natural luminosity signals can only be used semi-quantitatively to correlate to soot emissions. The soot emission processes exhibited temporal and spatial transitions between soot formations and oxidations. The faster soot formation rate after the onset of soot, and the temporally delayed soot formation – oxidation transition for ULSD compared to gasoline, suggest that ULSD has a higher sooting tendency than gasoline. Distributions of soot volume fractions on the mixture fraction – temperature space from CFD simulations showed the fuel effects on spray mixing, which are linked to the volatility difference between the two fuels. Fuel effects on soot emissions are also shown to exhibit a smaller range of higher soot concentration over the mixture fraction - temperature space for gasoline.

7 Summary and Conclusions

The better fuel economy and reduced emission benefits of gasoline compression ignition technology has been demonstrated by many researches. Application of the gasoline compression ignition technology requires extensive system level development, including the combustion system. Design of combustion system components, fuel injection strategy, EGR strategy, and etc. would benefit greatly from a deeper understanding of gasoline spray combustion phenomena and the differences with diesel spray combustion. In addition, development of more accurate numerical tools are also critical in the development, optimization, and application of the GCI technology.

The two objectives of this dissertation cater to the aforementioned needs for GCI technological development and application, which are:

1. Experimentally understand the fundamental characteristics of the spray combustion of a high reactivity gasoline with a research octane number (RON) of 60, in comparison to ULSD.
2. Enable accurate computational fluid dynamics (CFD) simulations for the high-reactivity gasoline under conditions typical of medium to heavy duty CI engine operations.

With respect to the first goal, extensive experimental work were performed with two fuels (gasoline, ULSD), a variety of ambient charge gas conditions (charge gas temperature, oxygen concentration), and a variety of injection pressures. Observations were made with respect to the spray dispersion, spray penetration, ignition, flame lift-off, and soot concentrations. Key observations and conclusions are summarized below:

1. Non-reacting sprays:
   a) Gasoline exhibited larger spray dispersion angles (up to 20%) and shorter spray penetrations (on the order of 10%) than ULSD under both low and high ambient charge gas temperature conditions. However, different mechanisms were behind the observed differences. Under low ambient temperature where vaporization was minimum, the fuel liquid density was the dominating factor. Under high ambient temperature, extensive vaporization exerted additional influence.
   b) Gasoline exhibited significantly shorter liquid length (by 50%) compared to ULSD. This is dominated by fuel volatility differences.
   c) The liquid lengths of the two fuels exhibited different sensitivity to ambient temperatures: the liquid lengths of gasoline were in-sensitive to a change of ambient temperatures, while the liquid lengths of ULSD decreased with increasing ambient temperatures. The saturation effect of the liquid length with respect to the ambient temperature was closely linked to the influence of local transport of mass, momentum and energy.
2. Reacting sprays:
   a) Gasoline exhibited longer ignition delays than ULSD under the influence of charge gas temperatures, oxygen concentrations, and injection pressures. The

ignition delay differences were dominated by the chemical kinetics differences of the two fuels. The chemical kinetics were dominated by the temperature condition and were less influenced by the mixture quality. Higher ambient charge gas temperatures allowed ignition of richer mixtures. Fuel air mixing improvements by higher injection pressures and higher oxygen concentrations had much smaller influence on the fuel air stoichiometry at the ignition location.

b) Gasoline exhibited longer lift-off lengths than ULSD, which was closely related to the slower ignition process. The lift-off – ignition delay relationship was affected differently by charge gas and injection conditions. Under the charge gas temperature sweep, the lift-off length vs ignition delay of the two fuels collapsed onto very close curve fit. Under an injection pressure sweep, the ignition delays of both fuels were insensitive while the lift-off lengths increased with injection pressures, and thus lift-off lengths were not correlated to ignition delays. Under an oxygen concentration sweep, lift-off lengths were positively related to ignition delays, however, the two fuels fell on different curve fits.

c) Gasoline exhibited lower levels of soot luminosity than ULSD under the influence of charge gas temperatures, oxygen concentrations, and injection pressures. It is inferred that soot concentrations in the gasoline spray flame were lower than that in the ULSD spray flame, in general. The benefit of lower soot concentrations was reduced with an increase in the charge gas temperatures and oxygen concentrations. These two conditions correspond to low temperature combustion and high EGR levels.

With respect to the second goal, two attempts were performed. The first attempt involved the development of a transient spray cone angle correlation, which was aimed at (1) better describing the transient spray cone angle behavior in a spray plume, (2) providing a customized correlation for a gasoline-range fuel other than ULSD, and (3) integrating the correlation into an existing numerical tool to improve simulation accuracy. The second attempt was aimed at a quantitative understand the soot emission characteristics through 3D CFD reacting spray simulations.

Development of the transient spray cone angle correlation was based on experimental data from non-reacting sprays under low ambient charge gas temperatures that prevented major vaporization. The spray cone angle definition was also adjusted for better alignment with the practices in CFD simulations. The developed correlation was implemented into the CFD software Converge through a user-defined function and is now implemented as a hidden feature starting from Converge 2.4.19. Application of the transient spray cone angle correlation resulted in closer matches in the vapor penetration, which was critical for spray mixing.

Reacting spray 3D CFD simulations for the two fuels was attempted by the use of two turbulence models (RNG k-ε RANS, dynamic structure LES), and two soot models (Hiroyasu-NSC, Particulate Mimic). A combination of the dynamic structure LES turbulence model and a Particulate Mimic soot model proved to be successful in matching key spray combustion characteristics, including ignition delays, lift-off lengths, and trends

in soot natural luminosity signals. Qualitative comparisons between experimental studies in the literature and the LES PM simulation results confirmed that the predicted results were reasonable in the trend of axial soot concentrations, and were on similar orders of magnitudes on radial soot concentrations.

The soot emission processes exhibited temporal and spatial transitions between soot formations and oxidations. The faster soot formation rate after the onset of soot, and the temporally delayed soot formation – oxidation transition for ULSD compared to gasoline, suggesting that ULSD has a higher sooting tendency than gasoline. Distributions of soot volume fractions on the mixture fraction – temperature space from CFD simulations showed the fuel effects on spray mixing, which are linked to the volatility difference between the two fuels. Fuel effects on soot emissions are also shown to exhibit a smaller range of higher soot concentration over the mixture fraction - temperature space for gasoline.

8 Future Work

The experimental work provided quantitative understanding of key macroscopic spray combustion characteristics of a high reactivity (RON 60) gasoline type fuel. Further experimental investigations into the microscopic level of the spray combustion characteristics will greatly complement the observations in this work. The interested microscopic spray combustion characteristics includes, but are not limited to: local air fuel mixture quality, local flame temperature distributions, soot cloud optical thickness distributions, instantaneous soot particle distributions, distribution of important intermediate combustion radicals.

Further numerical investigations should direct toward the application of the transient spray cone angle correlation in reacting sprays, and on engine applications. Preliminary validations on non-reacting sprays demonstrated the potential of the correlation for spray simulations. Applications in reacting spray simulations enables understanding the effect of mixing on ignition and lift-off. Applications on engine combustion simulations enables the realization of the one of the key features of the spray cone angle correlation, which was a dynamic spray cone angle profile induced by piston movements.

Future experimental efforts on the microscopic spray combustion characteristics will also enable better calibrations of the spray model, the combustion model, the soot model, and selections of more accurate chemical reaction mechanisms for simulating ignition and combustion.

9 Reference List

Abdul Malik, Muhammad, Ashrul Shaiful, Mohd Mohd. Ismail, Mohammad Mohd Jaafar, and Amirah Mohamad Sahar. 2017. "Combustion and Emission Characteristics of Coconut-Based Biodiesel in a Liquid Fuel Burner." *Energies* 10 (4):458.

Amsden, A.A., P.J. O'Rourke, and T.D. Butler. 1989. KIVA-II: A computer program for chemically reactive flows with sprays. ; Los Alamos National Lab., NM (USA).

Ansari, Ehsan, Kamran Poorghasemi, Behrouz Khoshbakht Irdmousa, Mahdi Shahbakhti, and Jeffrey Naber. 2016. "Efficiency and Emissions Mapping of a Light Duty Diesel - Natural Gas Engine Operating in Conventional Diesel and RCCI Modes." SAE International. https://doi.org/10.4271/2016-01-2309.

Arai, M., M. Tabata, H. Hiroyasu, and M. Shimizu. 1984. "Disintegrating Process and Spray Characterization of Fuel Jet Injected by a Diesel Nozzle." SAE International. 10.4271/840275.

Arrègle, Jean, José V. Pastor, and Santiago Ruiz. 1999. "The Influence of Injection Parameters on Diesel Spray Characteristics." SAE International. https://doi.org/10.4271/1999-01-0200.

Attili, Antonio, Fabrizio Bisetti, Michael E. Mueller, and Heinz Pitsch. 2014. "Formation, growth, and transport of soot in a three-dimensional turbulent non-premixed jet flame." *Combustion and Flame* 161 (7):1849-1865. doi: https://doi.org/10.1016/j.combustflame.2014.01.008.

Badra, Jihad, Radwan Bakor, Abdullah AlRamadan, Mohammed Almansour, Jaeheon Sim, Ahfaz Ahmed, Yoann Viollet, and Junseok Chang. 2018. "Standardized Gasoline Compression Ignition Fuels Matrix." SAE International. https://doi.org/10.4271/2018-01-0925.

Benajes, Jesús, Raúl Payri, Michele Bardi, and Pedro Martí-Aldaraví. 2013. "Experimental characterization of diesel ignition and lift-off length using a single-hole ECN injector." *Applied Thermal Engineering* 58 (1):554-563. doi: https://doi.org/10.1016/j.applthermaleng.2013.04.044.

Bessonette, Paul W., Charles H. Schleyer, Kevin P. Duffy, William L. Hardy, and Michael P. Liechty. 2007. "Effects of Fuel Property Changes on Heavy-Duty HCCI Combustion." SAE International. https://doi.org/10.4271/2007-01-0191.

Blessing, M., G. König, C. Krüger, U. Michels, and V. Schwarz. 2003. "Analysis of Flow and Cavitation Phenomena in Diesel Injection Nozzles and Its Effects on Spray and Mixture Formation." SAE International. 10.4271/2003-01-1358.

Borgqvist, Patrick, Öivind Andersson, Per Tunestål, and Bengt Johansson. 2013. "The Low Load Limit of Gasoline Partially Premixed Combustion Using Negative Valve Overlap." *Journal of Engineering for Gas Turbines and Power* 135 (6):062002-062002-7. doi: 10.1115/1.4023613.

BP. 2018. BP Energy Outlook 2018 Edition.

Cho, Kukwon, Manbae Han, C. Scott Sluder, Robert M. Wagner, and Gregory K. Lilik. 2009. "Experimental Investigation of the Effects of Fuel Characteristics on High Efficiency Clean Combustion in a Light-Duty Diesel Engine." SAE International. https://doi.org/10.4271/2009-01-2669.

Chong, Cheng Tung, and Simone Hochgreb. 2015. "Fundamental Spray Combustion Characteristics of Rapeseed Biodiesel, Diesel and Blend." *Energy Procedia* 75:2394-2399. doi: https://doi.org/10.1016/j.egypro.2015.07.186.

Coghe, A., Cossali, G.E. 1994. "Phase Doppler characterization of a Diesel spray injected into a high density gas under vaporization regimes." VII Int. Symposium of Application of Laser Technology to Fluid Mechanics, Lisbon, 1994.

Cung, Khanh, Abdul Moiz, Jaclyn Johnson, Seong-Young Lee, Chol-Bum Kweon, and Alessandro Montanaro. 2015. "Spray–combustion interaction mechanism of multiple-injection under diesel engine conditions." *Proceedings of the Combustion Institute* 35 (3):3061-3068. doi: https://doi.org/10.1016/j.proci.2014.07.054.

Dec, John E. 1997. "A Conceptual Model of DI Diesel Combustion Based on Laser-Sheet Imaging*." SAE International. https://doi.org/10.4271/970873.

Delacourt, E., B. Desmet, and B. Besson. 2005. "Characterisation of very high pressure diesel sprays using digital imaging techniques." *Fuel* 84 (7):859-867. doi: https://doi.org/10.1016/j.fuel.2004.12.003.

Dronniou, Nicolas, Marc Lejeune, Iyad Balloul, and Pascal Higelin. 2005. "Combination of High EGR Rates and Multiple Injection Strategies to Reduce Pollutant Emissions." SAE International. https://doi.org/10.4271/2005-01-3726.

Dukowicz, John K. 1980. "A particle-fluid numerical model for liquid sprays." *Journal of Computational Physics* 35 (2):229-253. doi: https://doi.org/10.1016/0021-9991(80)90087-X.

Dumitrescu, Cosmin Emil, Christopher Polonowski, Brian T. Fisher, A. S. Cheng, Gregory K. Lilik, and Charles J. Mueller. 2014. "An Experimental Study of Diesel-Fuel Property Effects on Mixing-Controlled Combustion in a Heavy-Duty Optical CI Engine." *SAE International Journal of Fuels and Lubricants* 7 (1):65-81. doi: 10.4271/2014-01-1260.

EPA. 2012. "Regulations for Greenhouse Gas Emissions from Passenger Cars and Trucks."

ExxonMobil. 2016. The Outlook for Energy: A View to 2040.

Fang, Tiegang, and Chia-fon F. Lee. 2011. "Low sooting combustion of narrow-angle wall-guided sprays in an HSDI diesel engine with retarded injection timings." *Fuel* 90 (4):1449-1456. doi: https://doi.org/10.1016/j.fuel.2010.12.031.

Feng, Zehao, Cheng Zhan, Chenglong Tang, Ke Yang, and Zuohua Huang. 2016. "Experimental investigation on spray and atomization characteristics of diesel/gasoline/ethanol blends in high pressure common rail injection system." *Energy* 112:549-561. doi: https://doi.org/10.1016/j.energy.2016.06.131.

Frossling, Nils. 1956. Evaporation, Heat Transfer, and Velocity Distribution in Two-Dimensional and Rotationally Symmetrical Laminar Boundary-Layer Flow. edited by National Advisory Committee for Aeronautics. Washington DC.

Han, Dong, Chunhai Wang, Yaozong Duan, Zhisong Tian, and Zhen Huang. 2014. "An experimental study of injection and spray characteristics of diesel and gasoline blends on a common rail injection system." *Energy* 75:513-519. doi: https://doi.org/10.1016/j.energy.2014.08.006.

Hanson, Reed, Scott Curran, Robert Wagner, Sage Kokjohn, Derek Splitter, and Rolf D. Reitz. 2012. "Piston Bowl Optimization for RCCI Combustion in a Light-Duty Multi-Cylinder Engine." *SAE International Journal of Engines* 5 (2):286-299. doi: https://doi.org/10.4271/2012-01-0380.

Hao, Han, Feiqi Liu, Zongwei Liu, and Fuquan Zhao. 2016. "Compression ignition of low-octane gasoline: Life cycle energy consumption and greenhouse gas emissions." *Applied Energy* 181:391-398. doi: https://doi.org/10.1016/j.apenergy.2016.08.100.

Hashizume, Takeshi, Takeshi Miyamoto, Akagawa Hisashi, and Kinji Tsujimura. 1998. "Combustion and Emission Characteristics of Multiple Stage Diesel Combustion." SAE International. https://doi.org/10.4271/980505.

Hawkes, E.R. 2014. "Model Comparisons: n-heptane Session." Engine Combustion Network Work Shop One. http://www.ca.sandia.gov/ecn/workshop/ECN1.php.

Henein, N. A., and Jay A. Bolt. 1967. "Ignition Delay in Diesel Engines." SAE International. https://doi.org/10.4271/670007.

Hessel, Randy, Zongyu Yue, Rolf Reitz, Mark Musculus, and Jacqueline O'Connor. 2017. "Guidelines for Interpreting Soot Luminosity Imaging." *SAE International Journal of Engines* 10 (3):1174-1192. doi: https://doi.org/10.4271/2017-01-0716.

Heywood, John B. 1988. *Internal combustion engine fundamentals*: New York : McGraw-Hill, [1988] ©1988.

Higgins, Brian, and Dennis L. Siebers. 2001. "Measurement of the Flame Lift-Off Location on DI Diesel Sprays Using OH Chemiluminescence." SAE International. https://doi.org/10.4271/2001-01-0918.

Higgins, Brian, Dennis L. Siebers, and Allen Aradi. 2000. "Diesel-Spray Ignition and Premixed-Burn Behavior." SAE International. https://doi.org/10.4271/2000-01-0940.

Hiroyasu, H., and T. Kadota. 1976. "Models for Combustion and Formation of Nitric Oxide and Soot in Direct Injection Diesel Engines." SAE International. https://doi.org/10.4271/760129.

Hiroyasu, Hiro, and Masataka Arai. 1990. "Structures of Fuel Sprays in Diesel Engines." SAE International. 10.4271/900475.

Huestis, Edwin, Paul A. Erickson, and Mark P. B. Musculus. 2007. "In-Cylinder and Exhaust Soot in Low-Temperature Combustion Using a Wide-Range of EGR in a Heavy-Duty Diesel Engine." SAE International. https://doi.org/10.4271/2007-01-4017.

Hughes, William, and Henry Schmidt. 2016. "Fuel Cart Low Pressure System Detailed User Guide. APS LABS Report. Michigan Technological University."

Idicheria, Cherian A., and Lyle M. Pickett. 2005. "Soot Formation in Diesel Combustion under High-EGR Conditions." SAE International. https://doi.org/10.4271/2005-01-3834.

Idicheria, Cherian A., and Lyle M. Pickett. 2007. "Quantitative Mixing Measurements in a Vaporizing Diesel Spray by Rayleigh Imaging." SAE International. https://doi.org/10.4271/2007-01-0647.

Ikeda, Yuji, Jun Kojima, and Hideki Hashimoto. 2002. "Local chemiluminescence spectra measurements in a high-pressure laminar methane/air premixed flame." *Proceedings of the Combustion Institute* 29 (2):1495-1501. doi: https://doi.org/10.1016/S1540-7489(02)80183-3.

Inagaki, Kazuhisa, Takayuki Fuyuto, Kazuaki Nishikawa, Kiyomi Nakakita, and Ichiro Sakata. 2006. "Dual-Fuel PCI Combustion Controlled by In-Cylinder Stratification of Ignitability." SAE International. https://doi.org/10.4271/2006-01-0028.

Jaclyn Johnson, Jeffrey Naber, Seong-Young Lee. 2011. "Characterizing Diesel Fuel Spray Cone Angle From Back-Scattered Imaging by Fitting Gaussian Profiles to Radial

Spray Intensity Distributions." *Journal of Engineering for Gas Turbines and Power* 134 (6). doi: doi:10.1115/1.4005994.

Jing, Wei, William L. Roberts, and Tiegang Fang. 2015. "Spray combustion of Jet-A and diesel fuels in a constant volume combustion chamber." *Energy Conversion and Management* 89:525-540. doi: https://doi.org/10.1016/j.enconman.2014.10.010.

Johnson, Jaclyn E., Jeffrey D. Naber, and Seong-Young Lee. 2012. "Characterizing Diesel Fuel Spray Cone Angle From Back-Scattered Imaging by Fitting Gaussian Profiles to Radial Spray Intensity Distributions." *Journal of Engineering for Gas Turbines and Power* 134 (6):062802-062802-8. doi: 10.1115/1.4005994.

Johnson, Samuel. 2009. "Premixed Lean Gas Combustion and HPCR Rate of Injection used with a Constant Volume Combustion Vessel." Master of Science, Mechanical Engineering - Engineering Mechanics, Michigan Technological University.

Jung, Yongjin, Julien Manin, Scott A. Skeen, and Lyle M. Pickett. 2015a. "Assessment of the Ignition and Lift-off Characteristics of a Diesel Spray with a Transient Spreading Angle." SAE International. 10.4271/2015-01-1828.

Jung, Yongjin, Julien Manin, Scott Skeen, and Lyle M Pickett. 2015b. "Measurement of Liquid and Vapor Penetration of Diesel Sprays with a Variation in Spreading Angle." SAE International. 10.4271/2015-01-0946.

Kalghatgi, Gautam, Leif Hildingsson, and Bengt Johansson. 2010. "Low NOx and Low Smoke Operation of a Diesel Engine Using Gasolinelike Fuels." *Journal of Engineering for Gas Turbines and Power* 132 (9):092803-092803-9. doi: 10.1115/1.4000602.

Kalghatgi, Gautam T., Per Risberg, and Hans-Erik Ångström. 2006. "Advantages of Fuels with High Resistance to Auto-ignition in Late-injection, Low-temperature, Compression Ignition Combustion." SAE International. https://doi.org/10.4271/2006-01-3385.

Keeler, B., and P. J. Shayler. 2008. "Constraints on Fuel Injection and EGR Strategies for Diesel PCCI-Type Combustion." SAE International. https://doi.org/10.4271/2008-01-1327.

Kim, Kihyun, Choongsik Bae, and Bengt Johansson. 2013. "Spray and Combustion Visualization of Gasoline and Diesel under Different Ambient Conditions in a Constant Volume Chamber." SAE International. https://doi.org/10.4271/2013-01-2547.

Kimura, Shuji, Osamu Aoki, Hiroshi Ogawa, Shigeo Muranaka, and Yoshiteru Enomoto. 1999. "New Combustion Concept for Ultra-Clean and High-Efficiency Small DI Diesel Engines." SAE International. https://doi.org/10.4271/1999-01-3681.

Kitamura, T, T Ito, J Senda, and H Fujimoto. 2002. "Mechanism of smokeless diesel combustion with oxygenated fuels based on the dependence of the equivalence ration and temperature on soot particle formation." *International Journal of Engine Research* 3 (4):223-248. doi: 10.1243/146808702762230923.

Klein-Douwel, R. J. H., P. J. M. Frijters, X. L. J. Seykens, L. M. T. Somers, and R. S. G. Baert. 2009. "Gas Density and Rail Pressure Effects on Diesel Spray Growth from a Heavy-Duty Common Rail Injector." *Energy & Fuels* 23 (4):1832-1842. doi: 10.1021/ef8003569.

Kumar, Praveen, Yu Zhang, Michael Traver, and David Cleary. 2017. "Simulation-Guided Air System Design for a Low Reactivity Gasoline-Like Fuel under Partially-Premixed Combustion in a Heavy-Duty Diesel Engine." SAE International. https://doi.org/10.4271/2017-01-0751.

Kundu, Prithwish, Muhsin M. Ameen, and Sibendu Som. 2017. "Importance of turbulence-chemistry interactions at low temperature engine conditions." *Combustion and Flame* 183:283-298. doi: https://doi.org/10.1016/j.combustflame.2017.05.025.

Ladommatos, N., S. M. Abdelhalim, Hua Zhao, and Z. Hu. 1996. "The Dilution, Chemical, and Thermal Effects of Exhaust Gas Recirculation on Diesel Engine Emissions - Part 1: Effect of Reducing Inlet Charge Oxygen." SAE International. https://doi.org/10.4271/961165.

Liu, Alex B., Daniel Mather, and Rolf D. Reitz. 1993. "Modeling the Effects of Drop Drag and Breakup on Fuel Sprays." SAE International. https://doi.org/10.4271/930072.

Lockwood, David J. 2014. "Rayleigh and Mie Scattering." In *Encyclopedia of Color Science and Technology*, edited by Ronnier Luo, 1-12. Berlin, Heidelberg: Springer Berlin Heidelberg.

Lundgren, Marcus, Alexios Matamis, Zhenkan Wang, Pablo Garcia Valladolid, Mattias Richter, Oivind Andersson, and Arne Andersson. 2018. "Lift-Off Lengths in an Optical Heavy-Duty Engine Operated at High Load with Low and High Octane Number Fuels." SAE International. https://doi.org/10.4271/2018-01-0245.

Maes, Noud, Maarten Meijer, Nico Dam, Bart Somers, Hubert Baya Toda, Gilles Bruneaux, Scott A. Skeen, Lyle M. Pickett, and Julien Manin. 2016. "Characterization of Spray A flame structure for parametric variations in ECN constant-volume vessels using chemiluminescence and laser-induced fluorescence." *Combustion and Flame* 174:138-151. doi: https://doi.org/10.1016/j.combustflame.2016.09.005.

Manente, Vittorio, Bengt Johansson, Per Tunestal, and William J. Cannella. 2010. "Influence of Inlet Pressure, EGR, Combustion Phasing, Speed and Pilot Ratio on

High Load Gasoline Partially Premixed Combustion." SAE International. https://doi.org/10.4271/2010-01-1471.

Medina, Mario, Mohammad Fatouraie, and Margaret Wooldridge. 2018. "High-Speed Imaging Studies of Gasoline Fuel Sprays at Fuel Injection Pressures from 300 to 1500 bar." SAE International. https://doi.org/10.4271/2018-01-0294.

Moiz, Ahmed Abdul, Khanh D Cung, and Seong-Young Lee. "Ignition, lift-off, and soot formation studies in n-dodecane split injection spray-flames." *International Journal of Engine Research* 0 (0):1468087417700778. doi: 10.1177/1468087417700778.

Moiz, Ahmed Abdul, Sibendu Som, Luis Bravo, and Seong-Young Lee. 2015. "Experimental and Numerical Studies on Combustion Model Selection for Split Injection Spray Combustion." SAE International. 10.4271/2015-01-0374.

Mueller, Charles J., and Glen C. Martin. 2002. "Effects of Oxygenated Compounds on Combustion and Soot Evolution in a DI Diesel Engine:Broadband Natural Luminosity Imaging." SAE International. https://doi.org/10.4271/2002-01-1631.

Mueller, Charles J., William J. Pitz, Lyle M. Pickett, Glen C. Martin, Dennis L. Siebers, and Charles K. Westbrook. 2003. "Effects of Oxygenates on Soot Processes in DI Diesel Engines: Experiments and Numerical Simulations." SAE International. https://doi.org/10.4271/2003-01-1791.

Naber, Jeffrey D., and Dennis L. Siebers. 1996. "Effects of Gas Density and Vaporization on Penetration and Dispersion of Diesel Sprays." SAE International. https://doi.org/10.4271/960034.

Nagle, J., and R. F. Strickland-Constable. 1962. "Oxidation of Carbon Between 1000-2000°C." Proceedings of the Fifth Carbon Conference.

Najt, Paul M., and David E. Foster. 1983. "Compression-Ignited Homogeneous Charge Combustion." SAE International. https://doi.org/10.4271/830264.

NHTSA. 2012. "Corporate Average Fuel Economy."

Noehre, Christof, Magnus Andersson, Bengt Johansson, and Anders Hultqvist. 2006. "Characterization of Partially Premixed Combustion." SAE International. https://doi.org/10.4271/2006-01-3412.

Noguchi, Masaaki, Yukiyasu Tanaka, Taro Tanaka, and Yukihisa Takeuchi. 1979. "A Study on Gasoline Engine Combustion by Observation of Intermediate Reactive Products during Combustion." SAE International. https://doi.org/10.4271/790840.

Ochoterena, R., M. Larsson, S. Andersson, and Ingemar Denbratt. 2008. "Optical Studies of Spray Development and Combustion Characterization of Oxygenated and Fischer-Tropsch Fuels." SAE International. https://doi.org/10.4271/2008-01-1393.

Onishi, Shigeru, Souk Hong Jo, Katsuji Shoda, Pan Do Jo, and Satoshi Kato. 1979. "Active Thermo-Atmosphere Combustion (ATAC) - A New Combustion Process for Internal Combustion Engines." SAE International. https://doi.org/10.4271/790501.

Otsu, N. 1979. "A Threshold Selection Method from Gray-Level Histograms." *IEEE Transactions on Systems, Man, and Cybernetics* 9 (1):62-66. doi: 10.1109/TSMC.1979.4310076.

Parrish, Scott E., and R. J. Zink. 2012. "DEVELOPMENT AND APPLICATION OF IMAGING SYSTEM TO EVALUATE LIQUID AND VAPOR ENVELOPES OF MULTI-HOLE GASOLINE FUEL INJECTOR SPRAYS UNDER ENGINE-LIKE CONDITIONS." 22 (8):647-661. doi: 10.1615/AtomizSpr.2012006215.

Pastor, José V., Jean Arrègle, and Alberto Palomares. 2001. "Diesel spray image segmentation with a likelihood ratio test." *Applied Optics* 40 (17):2876-2885. doi: 10.1364/AO.40.002876.

Patterson, Mark A., and Rolf D. Reitz. 1998. "Modeling the Effects of Fuel Spray Characteristics on Diesel Engine Combustion and Emission." SAE International. 10.4271/980131.

Payri, F., J. M. Desantes, and J. Arrégle. 1996. "Characterization of D.I. Diesel Sprays in High Density Conditions." SAE International. https://doi.org/10.4271/960774.

Payri, R., F. J. Salvador, J. Gimeno, and J. de la Morena. 2008. "Macroscopic Behavior of Diesel Sprays in the Near-Nozzle Field." *SAE International Journal of Engines* 1 (1):528-536. doi: 10.4271/2008-01-0929.

Payri, Raul, Antonio García, Vicent Domenech, Russell Durrett, and Alejandro H. Plazas. 2012. "An experimental study of gasoline effects on injection rate, momentum flux and spray characteristics using a common rail diesel injection system." *Fuel* 97:390-399. doi: https://doi.org/10.1016/j.fuel.2011.11.065.

Payri, Raul, Antonio Garcia, Vicent Domenech, Russ Durrett, and Alejandro Plazas Torres. 2012. "Hydraulic Behavior and Spray Characteristics of a Common Rail Diesel Injection System Using Gasoline Fuel." SAE International. https://doi.org/10.4271/2012-01-0458.

Payri, Raul, Francisco Javier Salvador, Jaime Gimeno, and Juan P. Viera. 2015. "Experimental Analysis on the Influence of Nozzle Geometry Over the Dispersion of Liquid N-Dodecane Sprays." *Frontiers in Mechanical Engineering* 1 (13). doi: 10.3389/fmech.2015.00013.

Pei, Yiqiang, Jing Qin, Yuli Dai, and Kun Wang. 2017. "Investigation on the spray development, the combustion characteristics and the emissions of Fischer–Tropsch fuel and diesel fuel from direct coal liquefaction." *Proceedings of the Institution of Mechanical Engineers, Part D: Journal of Automobile Engineering* 231 (13):1829-1837. doi: 10.1177/0954407016687861.

Pei, Yuanjiang, Evatt R. Hawkes, Michele Bolla, Sanghoon Kook, Graham M. Goldin, Yue Yang, Stephen B. Pope, and Sibendu Som. 2016. "An analysis of the structure of an n-dodecane spray flame using TPDF modelling." *Combustion and Flame* 168:420-435. doi: https://doi.org/10.1016/j.combustflame.2015.11.034.

Pei, Yuanjiang, Evatt R. Hawkes, Sanghoon Kook, Graham M. Goldin, and Tianfeng Lu. 2015. "Modelling n-dodecane spray and combustion with the transported probability density function method." *Combustion and Flame* 162 (5):2006-2019. doi: https://doi.org/10.1016/j.combustflame.2014.12.019.

Pei, Yuanjiang, Bing Hu, and Sibendu Som. 2016. "Large-Eddy Simulation of an n-Dodecane Spray Flame Under Different Ambient Oxygen Conditions." *Journal of Energy Resources Technology* 138 (3):032205-032205-10. doi: 10.1115/1.4032771.

Pei, Yuanjiang, Sibendu Som, Eric Pomraning, Peter K. Senecal, Scott A. Skeen, Julien Manin, and Lyle M. Pickett. 2015. "Large eddy simulation of a reacting spray flame with multiple realizations under compression ignition engine conditions." *Combustion and Flame* 162 (12):4442-4455. doi: https://doi.org/10.1016/j.combustflame.2015.08.010.

Pei, Yuanjiang, Roberto Torelli, Tom Tzanetakis, Yu Zhang, Michael Traver, David Cleary, and Sibendu Som. 2017a. "Modeling the Fuel Spray of a High Reactivity Gasoline under Heavy-Duty Diesel Engine Conditions." ASME 2017 Internal Combustion Engine Division Fall Technical Conference. ICEF2017-3530, Seattle, WA.

Pei, Yuanjiang, Roberto Torelli, Tom Tzanetakis, Yu Zhang, Michael Traver, David Cleary, and Sibendu Som. 2017b. "Modeling the Fuel Spray of of a High Reactivity Gasoline under Heavy-Duty Diesel Engine Conditions." ASME 2017 Internal Combustion Engine Division Fall Technical Conference. ICEF2017-3530, Seattle, WA.

Pei, Yuanjiang, Yu Zhang, Praveen Kumar, Michael Traver, David Cleary, Muhsin Ameen, Sibendu Som, Daniel Probst, Tristan Burton, Eric Pomraning, and P. K. Senecal. 2017. "CFD-Guided Heavy Duty Mixing-Controlled Combustion System Optimization with a Gasoline-Like Fuel." *SAE International Journal of Commercial Vehicles* 10 (2):532-546. doi: https://doi.org/10.4271/2017-01-0550.

Pickett, L M, and D L Siebers. 2006. "Soot Formation in Diesel Fuel Jets Near the Lift-Off Length." *International Journal of Engine Research* 7 (2):103-130. doi: 10.1243/146808705x57793.

Pickett, Lyle M., and Laura Hoogterp. 2008. "Fundamental Spray and Combustion Measurements of JP-8 at Diesel Conditions." *SAE International Journal of Commercial Vehicles* 1 (1):108-118. doi: https://doi.org/10.4271/2008-01-1083.

Pickett, Lyle M., and Dennis L. Siebers. 2004a. "Non-Sooting, Low Flame Temperature Mixing-Controlled DI Diesel Combustion." SAE International. https://doi.org/10.4271/2004-01-1399.

Pickett, Lyle M., and Dennis L. Siebers. 2004b. "Soot in diesel fuel jets: effects of ambient temperature, ambient density, and injection pressure." *Combustion and Flame* 138 (1):114-135. doi: https://doi.org/10.1016/j.combustflame.2004.04.006.

Pickett, Lyle M., Dennis L. Siebers, and Cherian A. Idicheria. 2005. "Relationship Between Ignition Processes and the Lift-Off Length of Diesel Fuel Jets." SAE International. https://doi.org/10.4271/2005-01-3843.

Plee, S. L., T. Ahmad, J. P. Myers, and G. M. Faeth. 1982. "Diesel NOx emissions—A simple correlation technique forintake air effects." *Symposium (International) on Combustion* 19 (1):1495-1502. doi: https://doi.org/10.1016/S0082-0784(82)80326-3.

Raul Payri, S. Molina, F. J. Salvador, J. Gimeno. 2004. "A study of the relation between nozzle geometry, internal flow and sprays characteristics in diesel fuel injection systems." *KSME International Journal* 18 (7):1222-1235. doi: DOI: 10.1007/BF02983297.

Reitz, R. 1987a. "Mechanisms of Atomization Processes in High-Pressure Vaporizing Sprays." *Atomization and Spray Technology* 3 (4):309-337.

Reitz, Rolf. 1987b. "Modeling Atomization Processes in High-Pressure Vaporizing Sprays." *Atomization and Spray Technology* 3:309-337.

Reitz, Rolf D., and F. B. Bracco. 1979. "On the Dependence of Spray Angle and Other Spray Parameters on Nozzle Design and Operating Conditions." SAE International. 10.4271/790494.

Richards, K. J., P. K. Senecal, and E. Pomraning. 2017. "CONVERGE (v2.3)." *Convergent Sciences, Inc. Madison, WI.*

Rose, K.D., J. Ariztegui, R.F. Cracknell, T. Dubois, H.D.C. Hamje, L. Pellegrini, D.J. Rickeard, B. Heuser, T. Schnorbus, and A.F. Kolbeck. 2013. "Exploring a Gasoline

Compression Ignition (GCI) Engine Concept." SAE International. https://doi.org/10.4271/2013-01-0911.

Ryan, Thomas W., and Blake Stapper. 1987. "Diesel Fuel Ignition Quality as Determined in a Constant Volume Combustion Bomb." SAE International. https://doi.org/10.4271/870586.

Sánchez, Fernando Z., Carlos V. M. Braga, Leonardo C. Braga, Sergio L. Braga, Flávio G. Dias, Franck Y. Turkovics, and Renata N. C. De Souza. 2014. "Experimental Study of the Ignition Delay for Ethanol-Powered in a Rapid Compression Machine." SAE International. https://doi.org/10.4271/2014-36-0127.

Schmidt, David P., and C. J. Rutland. 2000. "A New Droplet Collision Algorithm." *Journal of Computational Physics* 164 (1):62-80. doi: https://doi.org/10.1006/jcph.2000.6568.

Senecal, P. K., E. Pomraning, K. J. Richards, T. E. Briggs, C. Y. Choi, R. M. McDavid, and M. A. Patterson. 2003. "Multi-Dimensional Modeling of Direct-Injection Diesel Spray Liquid Length and Flame Lift-off Length using CFD and Parallel Detailed Chemistry." SAE International. https://doi.org/10.4271/2003-01-1043.

Settles, G.S. 2001. *Schlieren and Shadowgraph Techniques*: Springer.

Siebers, Dennis L. 1998. "Liquid-Phase Fuel Penetration in Diesel Sprays." SAE International. https://doi.org/10.4271/980809.

Siebers, Dennis L. 1999. "Scaling Liquid-Phase Fuel Penetration in Diesel Sprays Based on Mixing-Limited Vaporization." SAE International. https://doi.org/10.4271/1999-01-0528.

Siebers, Dennis L., and Brian Higgins. 2001. "Flame Lift-Off on Direct-Injection Diesel Sprays Under Quiescent Conditions." SAE International. https://doi.org/10.4271/2001-01-0530.

Siebers, Dennis L., Brian Higgins, and Lyle Pickett. 2002. "Flame Lift-Off on Direct-Injection Diesel Fuel Jets: Oxygen Concentration Effects." SAE International. https://doi.org/10.4271/2002-01-0890.

Skeen, Scott A., Julien Manin, Kristine Dalen, and Lyle M Pickett. 2013. "Extinction-based Imaging of Soot Processes over a Range of Diesel Operating Conditions." 8th U.S. National Combustion Meeting, Salt Lake City, Utah.

Skeen, Scott, Julien Manin, and Lyle M Pickett. 2015. "Visualization of Ignition Processes in High-Pressure Sprays with Multiple Injections of n-Dodecane." *SAE International Journal of Engines* 8 (2):696-715. doi: 10.4271/2015-01-0799.

SNL. 2018. "Engine Combustion Network. https://ecn.sandia.gov."

Storey, John, Samuel Lewis, Melanie Moses-DeBusk, Raynella Connatser, Jong Lee, Tom Tzanetakis, Kukwon Cho, Matthew Lorey, and Mark Sellnau. 2017. "Characterization of Hydrocarbon Emissions from Gasoline Direct-Injection Compression Ignition Engine Operating on a Higher Reactivity Gasoline Fuel." *SAE International Journal of Engines* 10 (4):1454-1464. doi: https://doi.org/10.4271/2017-01-0747.

Tang, Meng, Yuanjiang Pei, Yu Zhang, Tom Tzanetakis, Michael Traver, David Cleary, Shaoping Quan, Jeffrey Naber, and Seong-Young Lee. 2018. "Development of a Transient Spray Cone Angle Correlation for CFD Simulations at Diesel Engine Conditions." SAE International.

Tang, Meng, Jiongxun Zhang, Tyler Menucci, Henry Schmidt, Seong-Young Lee, Jeffrey Naber, and Tom Tzanetakis. May 2017. "Experimental Investigation of Spray Characteristics of High Reactivity Gasoline and Diesel Fuel Using a Heavy-Duty Single-Hole Injector, Part I: Non-Reacting, Non-Vaporizing Sprays." ILASS-Americas 29th Annual Conference on Liquid Atomization and Spray Systems, Atlanta, GA, May 2017.

Tang, Meng, Jiongxun Zhang, Tyler Menucci, Henry Schmidt, Jeffrey Naber, Seong-Young Lee, and Tom Tzanetakis. 2017. "Experimental Spray Ignition and Soot Forming Characteristics of High Reactivity Gasoline and Diesel Fuel in a Heavy-Duty Single-Hole Injector." 10th U. S. National Combustion Meeting, College Park, Maryland. 2HC-0298.

Tang, Meng, Jiongxun Zhang, Xiucheng Zhu, Kyle Yeakle, Henry Schmidt, Seong-Young Lee, Jeffrey Naber, and Cody Squibb. 2017. "Comparison of Direct-Injection Spray Development of E10 Gasoline to a Single and Multi-Component E10 Gasoline Surrogate." *SAE Int. J. Fuels Lubr.* 10 (2):352-368. doi: 10.4271/2017-01-0833.

Torelli, Roberto, Katarzyna Matusik, Kyle Nelli, Christopher Powell, Sibendu Som, Yuanjiang Pei, Tom Tzanetakis, Yu Zhang, Michael Traver, and David Cleary. 2017. "Numerical Evaluation of Shot-to-Shot In-Nozzle Flow Variations in a Heavy-Duty Diesel Injector Using Real Nozzle Geometry." (in review) SAE 2018 World Congress, Detroit, MI.

Tzanetakis, Tom, Alexander K. Voice, and Michael L. Traver. 2018. "Durability Study of a High Pressure Common Rail Fuel Injection System Using Lubricity Additive Dosed Gasoline-Like Fuel." SAE International. https://doi.org/10.4271/2018-01-0270.

USEIA. 2016. International Energy Outlook 2016.

Vallinayagam, R., Abdullah S. AlRamadan, S Vedharaj, Yanzhao An, Jaeheon Sim, Junseok Chang, and Bengt Johansson. 2018. "Low Load Limit Extension for Gasoline Compression Ignition Using Negative Valve Overlap Strategy." SAE International. https://doi.org/10.4271/2018-01-0896.

Voice, Alexander K., Tom Tzanetakis, and Michael Traver. 2017. "Lubricity of Light-End Fuels with Commercial Diesel Lubricity Additives." SAE International. https://doi.org/10.4271/2017-01-0871.

Wang, Buyu, Zhi Wang, Shijin Shuai, Linjun Yu, and Jianxin Wang. 2015. "Extension of the Lower Load Limit in Dieseline Compression Ignition Mode." *Energy Procedia* 75:2363-2370. doi: https://doi.org/10.1016/j.egypro.2015.07.492.

Wang, Hu, Mingfa Yao, Zongyu Yue, Ming Jia, and Rolf D. Reitz. 2015. "A reduced toluene reference fuel chemical kinetic mechanism for combustion and polycyclic-aromatic hydrocarbon predictions." *Combustion and Flame* 162 (6):2390-2404. doi: https://doi.org/10.1016/j.combustflame.2015.02.005.

Xue, Qingluan, Sibendu Som, P. K. Senecal, and E. Pomraning. May 2013. "A Study of Grid Resolution and SGS Models for LES under Non-reacting Spray Conditions." ILASS Americas, 25th Annual Conference on Liquid Atomization and Spray Systems, Pittsburgh, PA.

Xue, Qingluan, Sibendu Som, Peter K. Senecal, and E. Pomraning. 2013. "LARGE EDDY SIMULATION OF FUEL-SPRAY UNDER NON-REACTING IC ENGINE CONDITIONS." 23 (10):925-955. doi: 10.1615/AtomizSpr.2013008320.

Yakhot, V., S. A. Orszag, S. Thangam, T. B. Gatski, and C. G. Speziale. 1992. "Development of turbulence models for shear flows by a double expansion technique." *Physics of Fluids A: Fluid Dynamics* 4 (7):1510-1520. doi: 10.1063/1.858424.

Yang, Hong-Qiang, Shi-Jin Shuai, Zhi Wang, and Jian-Xin Wang. 2012. "High Efficiency and Low Pollutants Combustion: Gasoline Multiple Premixed Compression Ignition (MPCI)." SAE International. https://doi.org/10.4271/2012-01-0382.

Yang, Yi, John E. Dec, Nicolas Dronniou, Magnus Sjöberg, and William Cannella. 2011. "Partial Fuel Stratification to Control HCCI Heat Release Rates: Fuel Composition and Other Factors Affecting Pre-Ignition Reactions of Two-Stage Ignition Fuels." *SAE International Journal of Engines* 4 (1):1903-1920. doi: https://doi.org/10.4271/2011-01-1359.

Zhang, Anqi, Alessandro Montanaro, Luigi Allocca, Jeffrey Naber, and Seong-Young Lee. 2014. "Measurement of Diesel Spray Formation and Combustion upon Different Nozzle Geometry using Hybrid Imaging Technique." *SAE International Journal of Engines* 7 (2):1034-1043. doi: https://doi.org/10.4271/2014-01-1410.

Zhang, Jiongxun, Meng Tang, Tyler Menucci, Henry Schmidt, Seong-Young Lee, Jeffrey Naber, and Tom Tzanetakis. May 2017. "Experimental Investigation of Spray Characteristics of High Reactivity Gasoline and Diesel Fuel Using a Heavy-Duty Single-Hole Injector, Part II: Non-Reacting, Vaporizing Sprays." ILASS-Americas 29th Annual Conference on Liquid Atomization and Spray Systems, Atlanta, GA, May 2017.

Zhang, Yu, Praveen Kumar, Yuanjiang Pei, Michael Traver, and David Cleary. 2018. "An Experimental and Computational Investigation of Gasoline Compression Ignition Using Conventional and Higher Reactivity Gasolines in a Multi-Cylinder Heavy-Duty Diesel Engine." SAE International. https://doi.org/10.4271/2018-01-0226.

Zhang, Yu, Praveen Kumar, Michael Traver, and David Cleary. 2016. "Conventional and Low Temperature Combustion Using Naphtha Fuels in a Multi-Cylinder Heavy-Duty Diesel Engine." *SAE International Journal of Engines* 9 (2):1021-1035. doi: https://doi.org/10.4271/2016-01-0764.

Zhang, Yu, Steven Sommers, Yuanjiang Pei, Praveen Kumar, Alexander Voice, Michael Traver, and David Cleary. 2017. "Mixing-Controlled Combustion of Conventional and Higher Reactivity Gasolines in a Multi-Cylinder Heavy-Duty Compression Ignition Engine." SAE International. https://doi.org/10.4271/2017-01-0696.

Zhang, Yu, Alexander Voice, Yuanjiang Pei, Michael Traver, and David Cleary. 2018. "A Computational Investigation of Fuel Chemical and Physical Properties Effects on Gasoline Compression Ignition in a Heavy-Duty Diesel Engine." *Journal of Energy Resources Technology* 140 (10):102202-102202-10. doi: 10.1115/1.4040010.

Zheng, Liang, Xiao Ma, Zhi Wang, and Jianxin Wang. 2015. "An optical study on liquid-phase penetration, flame lift-off location and soot volume fraction distribution of gasoline–diesel blends in a constant volume vessel." *Fuel* 139:365-373. doi: https://doi.org/10.1016/j.fuel.2014.09.009.

Zheng, Liang, Yunliang Qi, Xu He, and Zhi Wang. 2012. "Visualization of Partially Premixed Combustion of Gasoline-like Fuel Using High Speed Imaging in a Constant Volume Vessel." *SAE International Journal of Engines* 5 (3):1320-1329. doi: https://doi.org/10.4271/2012-01-1236.

Zheng, Ziliang, Tamer Badawy, Naeim Henein, and Eric Sattler. 2013. "Investigation of Physical and Chemical Delay Periods of Different Fuels in the Ignition Quality Tester." *Journal of Engineering for Gas Turbines and Power* 135 (6):061501-061501-11. doi: 10.1115/1.4023607.

A Copyright documentation

A.1 ILASS Americas Copyright Statement for Section 4.1

ILASS-Americas
Institute for Liquid Atomization and Spray Systems

Home | About | Technical Committees | Upcoming Events | Membership | Literature

ILASS-Americas Proceedings

As part of our mission to advance the science of liquid atomization and spraying systems, we make available to our membership certain research documents and presentations from our conferences.

Please bear in mind that all content is the copyright © of the authors of the respective works and we advocate that no content obtained from this website may be reproduced or distributed without permission. We also make no representation regarding the accuracy of the content or its suitability for any particular purpose.

If you were unable to join us in the past or are simply interested in specific topic areas, you may search the links here for those proceedings.

- Full papers available: ILASS-Americas Conferences 2006-2017
- ICLASS 2000 and 2009 (hosted by ILASS-Americas) available from ILASS-Europe (http://ilasseurope.org/publications/proceedings/)
- Full papers between 1987-1999 available in pdf by year only. To access enter the "year" in the textbox of the search form

LIST OF PAPERS PRESENTED AT CONFERENCES

- 22nd ILASS-AMERICAS 2010 in Cincinnati, OH
- 19th ILASS-Americas 2006 in Toronto, Canada
- 18th ILASS-Americas 2005 in Irvine, CA
- 17th ILASS-Americas 2004 in Arlington, VA
- 16th ILASS-Americas 2003 in Monterey, CA
- 15th ILASS-Americas 2002 in Madison, WI
- 13th/14th ILASS-Americas unavailable
- 12th ILASS-Americas 1999 in Indianapolis, IN
- 11th ILASS-Americas 1998 in Sacramento, CA
- 10th ILASS-Americas 1997 in Ottawa, ON
- 9th ILASS-Americas 1996 in San Francisco, CA
- 8th ILASS-Americas 1995 in Troy, MI
- 7th ILASS-Americas 1994 in Bellevue, WA
- 6th ILASS-Americas 1993 in Worchester, MA
- 5th ILASS-Americas 1992 in San Ramon, CA
- 4th ILASS-Americas 1990 in Hartford, CT
- 3rd ILASS-Americas 1989 in Irvine, CA
- 2nd ILASS-Americas 1988 in Pittsburgh, PA
- 1st ILASS-Americas 1987 in Madison, WI

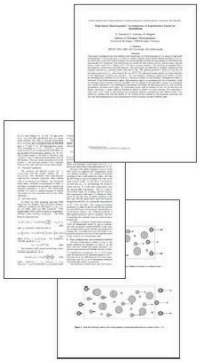

HOME | ABOUT | TECHNICAL COMMITTEES | UPCOMING EVENTS | MEMBERSHIP | LITERATURE

1 NEWS & EVENTS
2 MEET THE BOARD
3 JOIN OUR MAILING LIST
4 QUESTIONS?

Professor Scott Samuelsen
Secretariat, ILASS-Americas
UCI Combustion Laboratory
University of California, Irvine
Irvine, CA 92697-3550
Tel: (949) 824-5468
Fax: (949) 824-7423
E-mail: Info@ilass.uci.edu

A.2 U.S. National Combustion Meeting Copyright Statement for Section 4.2

Michigan Tech

Meng Tang <mengt@mtu.edu>

Inquiry about NCM copyright and possibility to update the manuscript?

Renfro, Michael <michael.renfro@uky.edu> Mon, Mar 27, 2017 at 10:42 AM
To: Meng Tang <mengt@mtu.edu>, "chih-jen.sung@uconn.edu" <chih-jen.sung@uconn.edu>

Meng,

I believe we could still replace your paper with an updated version as long as we received it very soon.

No, there is not a copyright transfer requirement for these papers.

Mike

From: Meng Tang [mailto:mengt@mtu.edu]
Sent: Monday, March 27, 2017 10:12 AM
To: Renfro, Michael <michael.renfro@uky.edu>; chih-jen.sung@uconn.edu
Subject: Inquiry about NCM copyright and possibility to update the manuscript?

Dear Dr. Sung and Dr. Renfro,

This is Meng and I'm the lead author of paper 2HC-0298. I have two inquiries that I would like to ask:

1. Is it possible to provide an updated manuscript at this time to reflect a change in the acknowledgement? We would like to add another sponsor in the acknolwedgement if possible.
2. Does the NCM paper require a copyright transfer form? My sponsor was asking if they need to sign these forms for the National Combustion Meeting.

Thanks for your time and your efforts in making the National Combustion Meeting possible!

Best regards,
Meng Tang

---------- Forwarded message ----------
From: **Combustion Institute** <info@combustioninstitute.org>
Date: 2017-02-27 13:53 GMT-05:00
Subject: Combustion Institute Submission PDF Submitted
To: Meng <mengt@mtu.edu>

Dear Meng Tang,

We are pleased to confirm that the PDF files of your complete manuscript to 10th US National Combustion Meeting has been received. The submission details are as follows:

Conference: 10th US National Combustion Meeting

Paper ID: 2HC-0298

Colloquium: Heterogeneous Combustion, Sprays & Droplets

Title: Experimental Spray Ignition and Soot Forming Characteristics of High Reactivity Gasoline and Diesel Fuel Using a Heavy-Duty Single-Hole Injector

Submission type: Oral Presentation

You will be notified in the near future regarding the presentation number and time slot.

Please be sure to check the conference website for event updates.

-The Combustion Institute

The Combustion Institute
5001 Baum Boulevard, Suite 644
Pittsburgh, PA 15213-1851

412.687.1366

--

Meng Tang, PhD Candidate

MTU Dept. of ME-EM

Phone: 906-370-8418

A.3 SAE International Copyright Statement for Chapter 5

400 Commonwealth Dr.
Warrendale, PA 15096

August 1, 2018

Meng Tang
MTU Dept. of ME-EM

Attn: Meng Tang

Dear Meng Tang:

Thank you for your request to reprint SAE Paper 2018-01-0304 reprint – Development of a Transient Spray Cone Angle Correlation for CFD Simulations at Diesel Engine Conditions.

Permission is granted as described in your original request received July 27, 2018, and subsequent correspondence. The conditions of the grant are outlined in the included republication agreement.

Indication of SAE International ownership of the excerpted content is required and should carry the following attribution statement *"© SAE International. Reprinted with permission. Further distribution of this material is not permitted without prior permission from SAE International."*

Please let me know if you have any questions regarding the terms of the permissions grant.

Best regards,

[redacted]

Rachel Sweeney
Intellectual Property and Content Licensing Manager, Content Management

SAE INTERNATIONAL
400 Commonwealth Drive
Warrendale, PA 15096
www.sae.org

SAE International Republication License Agreement

THIS PUBLICATION LICENSE AGREEMENT ("Agreement") is made on August 1, 2018, by and between SAE International, a Pennsylvania not-for-profit corporation having a principal place of business at 400 Commonwealth Drive, Warrendale, PA 15096-0001 USA ("Licensor"), and Meng Tang, a PhD Student with MTU Dept. of ME-EM ("Licensee").

WHEREAS, Licensee wishes to use the SAE Paper 2018-01-0304 in to be included in Licensee PhD Dissertation for MTU Dept. of ME-EM.

NOW, THEREFORE, in consideration of the premises and mutual covenants of the parties contained herein, it is hereby agreed as follows:

§ 1 Subject

The subject of this Agreement are the documents listed in Appendix A, which are published by Licensor (the "Licensed Materials") and which the Licensee wishes to include in a PhD Dissertation for MTU Dept. ME-EM
("Licensee's Product") published by Licensee.

§ 2 Rights & License

1. Licensor declares and Licensee acknowledges that Licensor is the owner of all rights related to the Licensed Materials and thus legally entitled to enter into this Agreement without limitation.
2. Licensor will indicate that ownership of aforementioned SAE International content by using the following attribution statement *"© SAE International. Reprinted with permission. Further distribution of this material is not permitted without prior permission from SAE International."*
3. Licensor grants to Licensee a non-exclusive, non-sublicensable, non-transferrable, revocable English-language only license to include the Licensed Materials in Licensee's Product, subject to the conditions in this Agreement. Use or translation into any other language is strictly prohibited without first obtaining additional licensing. Use of SAE International content in product customizations, derivatives and marketing collateral are expressly excluded. No public, open access to Licensed Materials, in whole or in part, is permitted.
4. This license is granted for the life of this product version only, including both numbered and maintenance updates, unless extended in writing by the parties. Upon termination all rights granted shall automatically revert to Licensor without further notice.
5. Upon termination, Licensee may retain copies of the excerpted material for (5) years within a secure archive or other such repository, after which Licensee shall destroy all files, copies, facsimiles and other replicas of the Licensed Materials in its possession, and will cease all distribution of the Licensed Materials.
6. All rights not specifically granted in this Agreement are reserved to the Licensor.

7. At termination, Licensee agrees that any and all rights and licenses granted in this Agreement shall automatically revert, transfer, and/or be assigned to the Licensor, and Licensee further agrees to execute any and all documents necessary to reflect Licensor's right, title, and interest in and to the copyright.
8. Notwithstanding anything else to the contrary herein, the license granted hereunder is a non-exclusive license and Licensor is free to enter into any agreement with another party for the transfer of rights related to the Licensed Materials at any time.

§ 3 Obligations

1. The preparation, publication, and distribution of the Licensee's Product shall be performed at the Licensee's cost and expense.
2. Licensee warrants that it will not alter, expand, or abridge Licensed Materials in any way. Should Licensor request, Licensee shall submit to the Licensor for approval all or part of the Licensee's Product prior to publication; thereafter, Licensee agrees to provide Licensor with access to the Licensed Materials upon request and without undo delay.
3. Licensee agrees to immediately suspend access to Licensed Materials upon awareness of a breach of the terms outlined in Section 2 above.
4. The Licensed Materials are provided "AS-IS" and Licensor has no liability or responsibility for errors or omissions in, or any decisions made by Licensee in reliance on, any information contained in the Licensed Materials or for outcomes relating to Licensee's modification or use of the Licensed Materials.

§ 4 Payments

1. Licensee agrees to pay Licensor a one-time licensing fee of $0.00 to include Licensed Materials in Licensee's Product as set forth in this Agreement.
2. Payment will be made by Licensee to Licensor upon full execution of this Agreement and can be made through SAE International's Customer Service at CustomerService@sae.org.
3. All payments shall be made to SAE International and shall be made in U.S. Dollars without any deductions. No taxes may be withheld and the complete sum transferred to the Licensor must be made payable in the United States. Payment may be made by valid credit card or check.
4. Inclusion of new, revised, reissued, or additional SAE publications requires a new agreement or an addendum to this Agreement.

§ 5 Miscellaneous Clauses

1. If Licensee at any time fails to fulfill or to comply with this Agreement in part or in whole, or if the Licensee goes into liquidation or bankruptcy proceedings, or if a receiver or other custodian is appointed for the Licensee, this Agreement shall terminate immediately without prejudice to the Licensor's right to recover any sums due.
2. Any dispute arising out of the Agreement that cannot be settled by amicable negotiation shall be settled according to and under the laws of the Commonwealth of Pennsylvania without regard to its conflicts of laws principles.
3. All rights and obligations described in this Agreement shall inure to the benefit of the legal successors and assigns of both parties.
4. This Agreement is the complete agreement between the parties and can be altered or nullified only by written statement signed by both parties.
5. Should a clause of this Agreement be or become void, this shall not affect the validity of the remaining clauses. Rather, the voided clause shall then be replaced by a new one that comes as close as legally possible to the parties' original intentions.

IN WITNESS WHEREOF, the parties have executed this Agreement as of the date first above written.

MENG TANG

BY: [redacted]

NAME: Meng Tang

TITLE: Research Assistant

DATE: 8/02/2018

SAE INTERNATIONAL

BY: [redacted]

NAME: Rachel Sweeney

TITLE: Intellectual Property and Content Licensing Manager

DATE: 8/01/2018

APPENDIX A

LICENSED MATERIALS

1. SAE Paper 2018-01-0304